UNIVERSITE DE PAU ET DES PAYS DE L'ADOUR

**THÈSE**

Présentée pour l'obtention du grade de

**Docteur de L'Université de Pau et des Pays de l'Adour**

Spécialité : **Géophysique**

par

**Muhammad Toqeer**

---

# Caractérisation de réservoir carbonaté par sismique réflexion 3D haute résolution

# Carbonate Reservoir Characterization by High Resolution 3D Seismic Reflection Survey

---

Soutenue publiquement le 05 Avril 2012

Membres du jury:

| | | |
|---|---|---|
| M. Hervé PERROUD | Professeur, Université de Pau et des Pays de l'Adour | Directeur de thèse |
| M. Dominique ROUSSET | Maître de conférence, Université de Pau et des Pays de l'Adour | Co-directeur de thèse |
| Mme. Béatrice DE VOOGD | Professeur, Université de Pau et des Pays de l'Adour | Président du Jury |
| M. Stéphane GARAMBOIS | Maître de conférence, HDR, Université J.Fourier - Grenoble | Rapporteur |
| M. Philippe Pezard | Directeur de Recherche (CNRS, Université de Montpellier 2) | Rapporteur |
| M. Evgeny Landa | Directeur, Organisme pétrolier de recherche appliquée (OPERA) | Examinateur |

**To**
*My Mother*
**and**
**to loving memory of my aunt**
*" Sughran Bibi"*

# Acknowledgements

## Résumé

Sur l'île de Majorque (Espagne), l'exploitation en continue de la nappe aquifère a favorisé la formation d'un biseau salé et l'épuisement de la ressource en eau potable. En 2002, un projet nommé ALIANCE, financé par l'Union européenne, a été lancé pour permettre une meilleure caractérisation des réservoirs. L'objectif est de concevoir un plan de gestion durable des ressources en eau dans les zones côtières aquifères sujets aux problèmes d'intrusion d'eau salée. Dans cet optique, un site expérimental près de la ville de Campos (Majorque) a été créé, avec la mise en place de plusieurs puits au sein d'un milieu karstique carbonaté. Des études pétrophysiques sur des échantillons ont été réalisées ainsi que différentes prospections géophysiques dans la zone saturée (tomographie puits à puits). Ce type d'études est utile pour déterminer certaines propriétés réservoirs telles que la porosité, mais sont limitées à la zone saturée au voisinage des puits. Ainsi, une étude sismique 3D haute résolution a été réalisée pour localiser les principaux réflecteurs, leurs répartitions sur la zone et imager les hétérogénéités du réservoir dans la zone non saturée. L'acquisition et le traitement de données sismiques lors de prospection de subsurface est une tâche difficile en raison de plusieurs facteurs, notamment logistique et technique. Cependant, cette acquisition 3D haute résolution a été optimisée pour imager une structure peu profonde, à savoir une centaine de mètres. Différentes stratégies de traitement de données ont été appliquées pour éliminer de manière efficace le bruit sur les données, et une technique de calcul de correction statique, basée sur l'inversion des temps de premières arrivées, a été mise au point. Différents attributs sismiques ont été extraits et utilisés pour la caratérisation du réservoir.

La propagation des ondes sismiques est limitée par la nature des roches carbonatées et la création d'ondes de Rayleigh. Un obstacle majeur rencontré lors du traitement des données sismiques a été la présence d'ondes de Rayleigh de fortes amplitudes, d'une part due à l'utilisation d'une source en surface et d'autre part en raison des hétérogénéités de petite tailles. Un "mute" de ces ondes de surface a été réalisé avant d'imager la structure profonde. De multiples problèmes d'interférences sont également dus aux nombreuses hétérogénéités, à l'atténuation rapide du contenu hautes-fréquences des signaux et au contraste d'impédance avec les couches sous-jacentes. L'interprétation finale nous amène à observer que le réflecteur principal est très irrégulier sur une zone d'étude de petite taille à l'échelle d'un réservoir. L'analyse de différents attributs sismiques révèle clairement des structures et hétérogénéités typiques des systèmes karstiques.

# Abstract

Continuous water extraction and intrusion of salt water in the coastal aquifer of the island of Mallorca (Spain) is depleting the fresh water aquifers. In 2002 a project named ALIANCE, funded by European Union, was initiated for better reservoir characterization and to devise the sustainable management plan of the water resources in coastal aquifers suffering from salt water intrusion. For this purpose an experimental site near the Campos town on the island of Mallorca (Spain) was developed. Several wells on the site were drilled and cored. Extensive studies are carried out to characterize the reservoir by studying the well cores. Different geophysical tomographic studies are also carried out for these drilled wells in the saturated zone. Laboratory study of cores, petrophysical studies and several tomographic studies were helpful to construct the reservoir porosity system and other reservoir properties. But these all studies are restricted to saturated zone and in the vicinity of the wells. High resolution 3D seismic survey is carried out on this site to locate the different characteristic reflectors, their spatial presence over the area and reservoir heterogeneity in the unsaturated zone.

Seismic data acquisition and processing for the shallow surveys is a difficult task due to number of factors including logistic and technical. Nonetheless high resolution 3D seismic survey is acquired with optimized parameters to image the required zone. Different data processing strategies are applied to get a noise free high resolution image. A technique for static correction calculation based on the delay time inversion is developed.

Energy penetration in the subsurface was hampered due to carbonate rock nature and forced generation of Rayleigh waves. The processing of the seismic data was difficult due to overwhelming high amplitude Rayleigh waves that are generated partly due to use of the surface source and partly due to the small scale heterogeneities. Rayleigh wave muting is performed to obtain the meaningful image. Due to heterogeneities, attenuation of high frequency content of the signals and impedance contrast of the underlying layers result in interference. Different seismic attributes are extracted and used for reservoir characterization. From the interpretation of data it is evident that even for this small area the shape of the main reflector varies considerably in the area. Seismic attributes reveal karsts and other structural heterogeneities in the area.

# Table des matières

# Table des figures

# Liste des tableaux

# Introduction

L'intrusion d'eau salée est un problème majeur pour les aquifères côtiers qui pollue les aquifères d'eau douce. De plus, le pompage extensif et le manque de gestion des puits dans l'extraction d'eau douce est additionnée à la gravité du problème. En 2002, le projet ALIANCE, financé par l'Union Européenne, a été initié afin de mieux comprendre la dynamique de l'intrusion d'eau salée et la pollution des aquifères d'eau douce, afin de développer de nouvelles méthodologies et pour concevoir une gestion durable des aquifères d'eau douce subissant l'intrusion d'eau salée. Pour répondre à ce problème, différents sites ont été sélectionnés et un de ces sites, situé sur l'île de Majorque en Espagne est complètement développé pour comprendre les hétérogénéités du réservoir, sa porosité et sa perméabilité.

Le site expérimental de Ses Stjoles, situé à proximité de Campos, dans la plateforme récifale de la Formation Llucmajor (Mallorque, Espagne) est très étudié, avec des projets en cours. Ce site est à la fois un exemple typique de carbonate karstique avec différents types de porosité et d'aquifère côtier subissant une intrusion d'eau salée. Il couvre une surface de 100m par 100m. De nombreux, 18, puits ont été forés jusqu'à une profondeur de 100m et carottés. Les carottes obtenues dans ce puits sont étudiées pour comprendre et évaluer les propriétés du réservoir. Les roches affleurant à proximité du site à Capo Blanco, ont été étudiées par Pomar (Pomar, L. & Ward, W. C., 1995; Pomar et al., 1983; Pomar, L. & Ward, W. C., 1994; Pomar, L., 1991; Pomar, L. & Ward, W. C., 1981) et d'autres géologues afin de déterminer le milieu de dépôt, les différentes unités lithologiques, et leur cadre stratigraphique en relation avec les variations du niveau marin. Pour comprendre la porosité et les processus affectant la porosité post-dépôt, ce site offre une opportunité unique d'avoir un aperçu des différents aspects du réservoir.

De nombreuses études de puits ont été menées pour comprendre les types de porosité, la distribution de la porosité, la perméabilité et d'autres propriétés du réservoir du site d'étude. Un modèle 3D de la porosité du complexe récifal a été développé grâce aux études en laboratoire de carottes provenant des puits, des études pétrophysiques et l'analogue de terrain(Jaeggi, 2006; Y. Maria-Sube., 2007; V.Hebert., 2011). Une description détaillée des lithofaciès rencontrés dans les puits carottés au site expérimental de Ses Sitjoles est également donnée le long des différentes propriétés des diagraphies. Des études détaillées supplémentaires pour la déduction du modèle de porosité à partir de carottage de forage, diagraphie et des descriptions détaillées des environnements de dépôt et les différents facteurs de contrôle de la création de porosité au cours des temps géologique et les autres hétérogénéités sont décrites en détail par (Y. Maria-Sube., 2007) et (V.Hebert., 2011).

L'exploration sismique est une manière élégante pour imager la sub-surface. La méthode de sismique réflexion mesure les temps doubles. De manière conventionnelle, la majorité des études d'exploration sismique est dédiée à l'exploration pétrolière. L'analyse des attributs sismiques avant et après sommation, l'inversion et la modélisation couplée avec des données intégrées permettent d'exploiter de nouveaux réservoirs sismiques et de prévoir de nouveaux puits dans le développement des domaines pétroliers. La physique des roches est d'importance majeure pour comprendre la compartimentalisation des réservoirs et les données de sismique 4D sont le moyen de plus efficace pour déterminer et planifier l'emplacement de nouveaux puits.

Mais l'exploration sismique fait également son chemin pour une application en sub-surface. La sismique de sub-surface est une branche émergeant de l'exploration sismique qui se fixe sur la sub-surface depuis 1 mètre de profondeur à approximativement quelques centaines de mètres. Le terme sub-surface est également un terme subjectif. Bien que les composantes de

la sismique de surface soient les mêmes que pour l'exploration sismique, ils diffèrent sur de nombreux aspects.

L'exploration sismique de sub-surface proche est utilisée pour de nombreuses applications incluant :

⋄ Les risques naturels et les investigations structurales de faible profondeur
⋄ La cartographie de la profondeur de la roche
⋄ Les études des nappes phréatiques
⋄ L'exploration minérale
⋄ La détection de zones de fracture
⋄ Le stockage de $CO_2$ et la surveillance

Les études de sismique réflexion pour des investigations de faible profondeur sont quelque peu difficiles et délicates à cause de nombreux facteurs incluant les hétérogénéités de la sub-surface, le bruit de fond et les couches de faible vitesse proches de la surface, parmi d'autres. Obtenir un échantillonnage spatial adéquat en évitant le moyennage spatial pour l'amélioration du rapport du signal sur bruit augmente les coûts des études. Mais d'autre part, les études sismiques de sub-surface permettent une meilleure imagerie de la sub-surface, la détection d'objets de petite taille et la caractérisation de la sub-surface peu profonde pour des thématiques géologiques, environnementales et géotechniques.

Comme décrit, l'acquisition de données sismiques pour la sub-surface est difficile et lourde. A cause de la faible longueur d'onde du signal sismique dans la sub-surface, même les petites hétérogénéités causeront de la dispersion et d'autres effets. La création d'ondes de Rayleigh est un autre problème en partie due à la source et en partie due aux karsts et aux autres caractéristiques liées. Les karsts peuvent causer diffraction, réflexion et réfraction des ondes de Rayleigh,ce qui rend plus difficile leur séparation des ondes réflechies qui permettent l'imagerie sismique.

Les roches carbonatées ont des caractéristiques uniques qui diffèrent de celles des roches silico-clastiques. La formation des roches silico-clastiques est due au dépôt de produits d'érosion, alors que les roches carbonatées sont formées par des processus chimiques et biologiques. Les roches carbonatées sont composées de débris biogènes. Les processus diagénétiques induisent une dissolution, une cimentation et la recristallisation du carbonate encaissant. Ces processus contribuent de manière constructive ou destructive à la porosité et à la perméabilité. De ce fait, il résulte de ces processus une grande variation de vitesse et de porosité dans les roches carbonatées. Les relations analytiques simples, applicables aux réservoirs silico-clastiques, comme la relation de Gardner, ne sont pas valides pour ces systèmes complexes.

La caractérisation des réservoirs carbonatés à travers la sismique est quelque chose de difficile comparé aux réservoirs sableux. Ceci est principalement dû aux hétérogénéités des réservoirs carbonatés. La détermination de la porosité à partir de la physique des roches n'est pas quelque chose de facile. Comme décrit par (Turhan, T. M., 1997), les carbonates produisent les défis suivants pour l'imagerie :

⋄ Les carbonates convient généralement un intervalle de vitesse plus large et donc une moins bonne résolution.
⋄ Un contraste d'impédance élevé est propice à la génération de multiples.
⋄ Les fortes vitesses des couches carbonatées peuvent résulter en une anisotropie et des hautes hétérogénéités de vitesses.
⋄ Les couches avec le pendage sous les couches carbonatées causent de la réfraction et

donc seuls les faibles angles des ondes réflechies sont enregistrés, l'image enregistrée a une largeur de bande étroite et apparaît spatialement brouillée.

La capacité à résoudre les caractéristiques de la sub-surface est contrôlée par la largeur de bande sismique. La résolution temporelle et spatiale aide à identifier les couches spatialement proches et à séparer deux points situés à proximité l'un de l'autre le long d'un même horizon. La résolution spatiale, qui est déterminée par la zone Fresnel, est aisément atteinte en réduisant intervalles sources et récepteurs.

Bien que des études géologiques étendues aient été menées sur le site de Campos dans le but de déterminer la porosité, les hétérogénéités lithologiques, de déterminer le niveau de la nappe (l'eau douce ), des zones de mélange et d'autres caractéristiques du réservoir, ces méthodes ont seulement déterminées les propriétés requises pour la caractérisation du réservoir dans la zone des puits. Bien que différents tomogrammes sismiques et électriques entre puits aient été réalisés, ces derniers sont restreints à la zone avoisinant les puits et dans la zone saturée.

Une étude de réflexion 3D à haute résolution est menée au site expérimental de Ses Sitjoles. Outre l'étude de réflexion 3D, une ligne sismique 2D et des études de réfraction sont également menées, pour la source et le bloc recepteur de la sismique réflexion 3D, pour déterminer la correction statique. Une étude VSP est réalisée sur le puits MC16 pour déterminer le profil de vitesse local. Des acquisitions spéficiques ont été implémentées pour les études de réfraction. Ceci ne va pas seulement améliorer la résolution spatiale, mais aussi permettre d'acquérir des données de haute densité et de haute couverture. L'étude sismique a été menée en vue de déterminer les hétérogénéités à petite échelle dans les séquences sous-jacentes et pour déterminer les réflecteurs majeurs et leur distribution sur le site de Campos. De plus, l'étude sismique va aider à combler le manque dans l'intégration de différentes données géologiques et géophysiques pour mieux caractériser les réservoirs. L'étude sismique va également tracer une ligne directrice à partir de l'acquisition des données pour l'interprétation des aquifères carbonatés côtiers. Pourtant, à cause de la résolution sismique, les hétérogénéités de petite taille, une porosité compréhensive et un modèle de perméabilité ne sont pas livrables, mais cela peut aider à délimiter l'aquifère, sa géométrie et les hétérogénéités de grande échelle, ce qui va aider à mieux comprendre des images d'ensemble de l'aquifère côtier et planifier de meilleures études. Une autre dimension de cette étude est le problème de l'efficacité des études sismiques pour les autres applications de faible profondeur dans les terrains carbonatés.

## Plan de la Thèse

Le premier chapitre de la thèse décrit de manière compréhensive les roches carbonatées, ses constituants, le développement et la dynamique des complexes récifaux avec les hétérogénéités résultantes, comme les karsts et les vacuoles etc. La géologie du site, les lithofaciès rencontrés dans le puits foré et différentes études sur ce site, à l'échelle du puits, sont décrites.

Dans le second chapitre, les principes de base de la technologie sismique sont décrits. Cela inclut les concepts théoriques et différents aspects de la sismique traitant de l'acquisition des données et de leur traitement. Différents aspects et les paramètres influençant l'acquisition des données sismiques sont décrits. La géométrie de l'acquisition sismique de terrain pour différentes études de réflexion et de réfraction et présentée. Le profil sismique vertical (VSP) et le profil de vitesse vertical calculé à partir des premières arrivées est présenté en chapitre 3.

La correction statique est conçue pour compenser l'effet de la faible vitesse de la couche d'altération superficielle et de son épaisseur, qui vont sinon induire des anomalies de temps de

trajet et donc des erreurs dans l'image sismique. Ceci constitue une des premières étapes après le pré-traitement des données. Il y a différentes méthodes de correction statique suggérées et employées à travers l'histoire de la sismique pétrolière. Nous avons proposé une méthodologie de calcul de correction statique basée sur l'inversion du temps de délai calculé à partir du premier temps d'arrivée. Cette méthodologie est appliquée pour des données synthétiques, et réelles 2D, 2.5D et 3D. Les résultats de la correction statique appliquée pour les données 2D sont comparés avec certaines méthodologies existantes, basées sur la première arrivée.

Le sujet du chapitre suivant est le traitement des données 2D et 3D. comme décrit plus tôt, les études de sismique peu profonde sont sujettes à du bruit généré par la source et ce problème devient pire pour l'étude des carbonates peu profonds. Pour les études sismiques peu profondes, le traitement est une étape difficile. Différentes stratégies sont appliquées pour le traitement des données 2D, dans le but d'estimer une optimisation des paramètres qui vont être utilisés pour le traitement des données 3D. Le traitement des données 3D est réalisé à partir de différentes techniques. Une attention spéciale est donnée à la préservation de l'amplitude et le traitement est réalisé en respectant l'hypothèse de "surface-consistency".

Le dernier chapitre traite de l'interprétation des données sismiques. L'extraction des attributs sismiques et leur analyse est une manière puissante d'améliorer les traits particuliers des données. Il y a différents types d'attributs, chacun étant utilisé dans un but particulier. Dans cette étude, un jeu d'attributs structuraux est appliqué pour différentes tranches de profondeur, pour étudier les hétérogénéités et d'autres caractéristiques structurales des données.

# Introduction

Saline water intrusion is major problem for coastal aquifers that is constantly polluting the fresh water aquifer. Moreover the extensive pumping and poor well management for fresh water extraction is adding to the severity of the problem. In 2002 a project ALIANCE, funded by European Union, was initiated to better understand the dynamics of saline water intrusion and pollution of fresh water aquifer, to develop the new methodologies for monitoring and to devise sustainable management plan of fresh water aquifers suffering from salt water intrusion. To address this problem different sites were chosen and one of site, located in the island of Mallorca, Spain is fully developed to understand the reservoir heterogeneity, porosity and permeability.

Ses Sitjoles experimental site near Campos within the Llucmajor Miocene reefal platform (Mallorca), Spain is studied extensively, with ongoing projects. This site is composed of heavily karstified carbonate rocks with different type of porosities. This site is a typical example of coastal aquifers suffering from salt water intrusion. This site covers an area of 100 x 100 m. Several wells, 18, are drilled to 100m and cored. The cores obtained from these wells are studied extensively to understand and evaluate the reservoir properties. The outcrop rocks near to the site, situated at Capo Blanco studied by Pomar ((Pomar, L. & Ward, W. C., 1995; Pomar et al., 1983; Pomar, L. & Ward, W. C., 1994; Pomar, L., 1991; Pomar, L. & Ward, W. C., 1981)) and other geologists in order to understand the depositional environment, different lithological units and their sequence stratigraphic framework with relation to sea level fluctuations to understand the porosity and post depositional porosity process, offers a unique opportunity to relate and gain insight of different aspects of the reservoir.

Several borehole studies are carried out to understand the porosity types, porosity distribution, permeability and other reservoir properties of the site. 3D porosity model of reefal complex is developed by the laboratory studies of cores encountered in the drilled wells at this site, petrophysical studies and its analogues to outcrop(Jaeggi, 2006; Y. Maria-Sube., 2007; V.Hebert., 2011). Detail description of lithofacies encountered in the drilled well at Ses Sitjoles experimental site is also given along with different wire-line properties. Furthermore detail studies for porosity model deduction from borehole cutting, wire line logging and detail description of depositional environment and different controlling factors for porosity generation through out the geological time and other heterogeneities are described in detail by (Y. Maria-Sube., 2007) and (V.Hebert., 2011).

Exploration seismology is an elegant way of subsurface imaging. Seismic reflection method measures the two way travel time. Conventionally much of the focus of exploration seismology is for hydrocarbon exploration. Seismic attributes analysis for pre-stack and post-stack data, inversion and modelling coupled with data integration helped in exploiting new seismic reservoirs and planning the new wells in the developed hydrocarbon fields. Rock physics is of vital importance to understand the reservoir compartmentalization and 4D seismic data is the lucrative way of continuous monitoring and planning new well locations

But exploration seismology is making its way in near surface applications also. Near surface seismology is an emerging branch of exploration seismology that focus on near surface from 1 meter to approximately few hundred meters. Near surface is itself a highly subjective term. Although the basic ingredients of near surface seismology are same as of exploration seismology yet it differs considerably in many aspects.

Near surface exploration seismology is applied for numerous application that includes :

- ◇ Geohazards and shallow structural investigation
- ◇ Mapping to bedrock depth
- ◇ Groundwater studies
- ◇ Mineral exploration
- ◇ Fracture zone detection
- ◇ $CO_2$ geological storage and monitoring

Seismic reflection survey for shallow investigation is somewhat difficult and cumbersome task due to many factors including the near surface heterogeneities, noises and near surface low velocity layer, among others. To avoid spatial aliasing, averaging and requirement of high fold data to improve S/N ratio increases survey cost. But on the other hand shallow seismic surveys deliver better subsurface imaging, detection of small scale objects and characterization of shallow subsurface for geological, environmental and geotechnical purpose.

As described the seismic data acquisition for near surface is a difficult and cumbersome task. Since due to shorter wavelength of seismic signal in near surface even small heterogeneities will cause dispersion and other effects. Rayleigh's wave generation is another problem partly due to surface related source and partly due to Karsts and other related features. Karsts and related features result in diffraction and Rayleigh waves reflection and refraction.

Carbonate rocks have unique attributes that are different from siliciclastic rocks. Formation of siliciclastic rocks is done by deposition of weathered rocks from somewhere else while carbonate rocks are formed in situ by biological and chemical processes. Carbonate rocks are composed of skeletal remain and other biological remains. Diagenesis at later stages results in dissolution, cementation and recrystallization of the parent carbonate rocks. These processes contribute constructively and destructively for porosity and permeability. So all these processes result in large variation of velocity and porosity of carbonate rocks. Simple analytical relation that are applicable to siliciclastic reservoir, such as Gardner's relation, are no longer valid for this complex system.

Carbonate reservoir characterization through seismic is somewhat difficult task as compared with sandstone reservoirs. This is mainly due to carbonate reservoir heterogeneities. Porosity determination from rock physics is not an easy task. As described by (Turhan, T. M., 1997) carbonate produces following imaging challenges such as :

- ◇ Carbonate have generally higher interval velocity and lower resolution.
- ◇ Higher impedance contrast in carbonates is prone to multiple generation.
- ◇ High velocity carbonate layers result in anisotropy and high-velocity heterogeneity.
- ◇ Dipping layer beneath carbonate layers cause in refraction and hence only limited angle of reflected waves are recorded, the recorded image have narrow bandwidth and appear spatially smeared.
- ◇ Pore geometry and bed will also affect the seismic imaging.

The ability of resolving the subsurface features is controlled by seismic bandwidth. Temporal and spatial resolution help to localise the closely spaced layers and separation of two close points along a single horizon. The spatial resolution, which is determined by first Fresnel zone, is simply attained by limiting the source and receiver interval.

Although extensive geological studies have been carried out at Campos site aiming to delineate the porosity, lithological heterogeneities, determination of fresh water table, mixing zone and other characteristic features of the reservoir, these methods only determine the required properties for reservoir characterization in the vicinity of the wells. Although different cross hole

tomograms and ERT are performed but these are restricted to the neighbouring wells and in saturated zone.

3D high resolution reflection survey is carried out at Ses Sitjoles experimental site. Apart from 3D reflection survey, 2D seismic line and refraction surveys are also carried out, for source and receiver block of the 3D seismic reflection block, to determine the static correction. VSP survey at well MC16 is performed to determine the local velocity profile. Efficient acquisition geometries are implied for refraction and reflection surveys to acquire the seismic data. This will not only improve the spatial resolution but also acquire high density and high fold data. To acquire high resolution seismic data, sledge hammer is used as an energy source and output of 5 sledge hammer is stacked for strong signals. Seismic survey is carried out to determine the mega scale heterogeneities in the underlying sequence and to determine the major reflectors and their distribution at Campos site. Also seismic study will help to fill the gap in integrating different geological and geophysical data for better reservoir characterization. The seismic survey will also set a guideline from data acquisition to interpretation in the carbonate coastal aquifers. Although due to seismic resolution, very small scale heterogeneities and a comprehensive porosity and permeability model is not deliverable but still it can help to delineate the aquifer boundaries, its geometry and small scale heterogeneities that will help to understand further overall image of the coastal aquifer system and planning new efficient surveys. Another dimension of this survey is the problem and efficiency of seismic surveys for other shallow applications in carbonate terrain .

## Thesis Outline

The first chapter of the thesis comprehensively describe the carbonate rocks, its constituents, development and dynamics of reefal complex with resulting heterogeneities, such as karsts and vugs, etc. Site geology, encountered lithofacies in the drilled wells, and different previous, borehole scale, studies at this site are described.

In the second chapter the basics of seismic technology is described. That includes the theoretical concepts and different aspects of seismic dealing with data acquisition and processing. Different aspects and influencing parameters of seismic data acquisition are described. Seismic field acquisition geometry for different reflection and refraction surveys is outlined. Vertical seismic profiling (VSP) and interval velocity profile calculated from first arrivals is outlined in 3rd chapter.

Static correction is aimed to mitigate the effect for the near surface weathering layer velocity and thickness that otherwise will result in false anomalies and erroneous imaging. This is among the very first step after pre-processing of the data. There are different methods of static correction suggested and employed thought the seismic petroleum history. We purposed a methodology of static correction calculation based on delay time inversion calculated from the first arrival picking. This purposed methodology is applied for synthetic data, 2D, 2.5D and 3D data. The results of static correction applied for 2D data are compared with some of the existing, based on first arrivals, methodologies.

Next chapter deals with the data processing for 2D and 3D case. As described earlier shallow seismic surveys are prone to source generated noises and this problem get worst for shallow carbonate surveys. For shallow seismic survey the processing is difficult task. Different strategies are applied for 2D data processing in order to estimate the optimum parameters that will be used for 3D processing. 3D data processing is performed with different techniques. Special

attention is given to amplitude preservation and the processing is performed respecting the assumption of surface consistency.

The last chapter deals with seismic data interpretation. Seismic attributes extraction and analysing is a powerful way to enhance the particular feature of the data. There are different types of attributes, each one is used for specific purpose. Here in this study a set of structural attributes are applied for different depth slices to study the heterogeneities and other structural features of the data.

## Résumé CHAPITRE 1

Les roches carbonatées sont d'origine chimique ou biogène. Les roches carbonatées sont divisées sur des critères minéralogiques en calcaires, minéraux calcitiques et dolomite. Les roches carbonatées sont formées à partir de processus chimiques et biochimiques complexes ayant lieu principalement en milieu marin. Plusieurs classifications sont proposées dans la littérature pour les roches carbonatées, mais les plus utilisées sont celles de Folk et de Dunham. La classification de Folk est détaillée et complexe et est utilisable en recherche. Elle est basée sur la nature des composants carbonatés de la roche ainsi que sur la nature de la phase de liaison, matrice ou ciment et leur ratio. Cette classification prend également en compte les aspects de la texture qui prennent en compte l'environnement et l'énergie de dépôt. La classification de Dunham est plus simple et largement utilisée par les géologues de terrain.

La porosité est un paramètre extrêmement important pour les réservoirs. La porosité dans les systèmes carbonatés est bien plus complexe en comparaison des systèmes silico-clastiques. La porosité primaire des roches carbonatées est altérée après son dépôt à cause de la diagenèse. La porosité inter-grain, la porosité intra-grain, la porosité de dépôt de sédiments boueux, de squelette et la porosité "fenestral" sont des types de porosité primaire. La porosité secondaire est créée et modifiée à cause de processus tels que la dissolution ou la dolomitisation.

La formation de récifs est due à l'interaction complexe de processus physiques, chimiques et biologiques. Ils constituent des réservoirs importants pour les hydrocarbures et les aquifères. Les récifs sont conditionnés par deux caractéristiques incluant une restriction latérale et des processus biologiques prononcés durant leur croissance. De nombreux processus, constructifs et destructifs, contrôlent et affectent la formation des récifs. De plus, la sédimentation et la cimentation affectent également le développement du récif ainsi que l'évolution de la porosité et ce à différentes étapes.

Le développement des karsts est dû à de nombreux facteurs liés les uns aux autres, incluant la conductivité hydraulique, l'enrichissement chimique de l'eau des nappes phréatiques, l'activité tectonique, les conditions paléoclimatiques et les variations eustatiques. Ces facteurs opèrent individuellement et/ou conjointement dans la formation des karsts. La direction d'écoulement des nappes phréatiques, la perméabilité, la lithologie et la surcharge de l'épaisseur de la roche sont étroitement liées avec la karstification. La formation des karsts est principalement d'origine météorique et sub-aérienne.

Les aquifères côtiers constituent une source importante d'eau pour des besoins variés. Le pompage continuel et les fluctuations du niveau marin résultent en une intrusion de l'eau de mer. Les aquifères côtiers caractéristiques sont contrôlés par un niveau piézométrique, un contraste de densité entre de l'eau douce et de l'eau de mer et le contexte géologique. La salinité dans les aquifères côtiers est due à des anciennes eaux marines riches en sel et à des intrusion d'eau de mer.

Le site de Sitjoles, situé à proximité de Campos en Espagne est un exemple typique d'aquifère côtier faisant face à de l'intrusion d'eau salée. Ce site expérimental est développé pour comprendre la dynamique de l'intrusion d'eau salée et sa contamination. Dans ce but, de nombreux puits sont forés et carottés. Ces carottes de forage sont précisément étudiées pour comprendre la distribution de la porosité dans ces aquifères côtiers. De nombreuses autres études de puits sont réalisées pour déterminer les différentes propriétés du réservoir à l'échelle du forage. Les distributions de faciès et d'épaisseur varient considérablement comme observées dans ces études de forage. Différentes études de forages ont révélées des structures karstiques

à différentes profondeurs. Des études tomographiques, de résistivité électrique et sismiques ont également révélé la présence de structures karstiques. Des études tomographiques entre les puits ont aidé à comprendre différentes corrélations de faciès dans certains puits.

# Carbonate Reservoir, Site Geology and Borehole Studies

## 1.1 Carbonate Rocks

Carbonate rocks are of chemical or/and biological origin. Carbonate rocks make 20 to 25 % of sedimentary rocks. Based on mineralogy carbonate rocks are divided into limestone, calcite mineral, and dolomite, dolomite mineral. Carbonate rocks are mostly composed of calcium ($Ca^{2+}$), magnesium ($Mg^{2+}$) and carbonate ($CO_3^{-2}$) ions. Calcium and Magnesium ions are present both in limestone and dolomite but magnesium is particularly important for dolomite. Principal carbonate minerals are grouped into calcite, dolomite and aragonite. The crystal system for principal carbonate mineral, calcite and dolomite group, and aragonite group is rhombohedral and orthorhombic respectively. Aragonite is a metastable polymorph of $CaCO_3$, having same chemical composition but different crystal structure, and converted rapidly to calcite under aqueous conditions. Majority of carbonate rocks are result of complex chemical or biochemical processes occurring in special marine environments, clear, warm and shallow water, where microbial activity and inorganic precipitation happens. The major factors for lime precipitation includes increase in temperature, intense evaporation, supersaturated water, marine upwelling due to pressure gradient, water mixing rich in $CO_3$ and low in $Ca^{+2}$, organic processes, ammonia production due to bacterial decay that will raise pH to increase carbonate concentration and photosynthesis, metabolism of microplanktonic flora, processes of $CO_2$ removal from water. Loss of $CO_2$ controlled by decrease in water pressure and increase in temperature, hence decrease in solubility, salinity and ionic strength of water will trigger the precipitation of calcium carbonate minerals. Calcium carbonate production rate is controlled by depth. Different algal production of $CaCO_3$ varies with depth in shallow and deep marine water.

Dolomites or dolomite rock, $CaMg(CO_3)_2$, are carbonate rocks that composed of more than 50% dolomite mineral. Dolomites occurs in close association with limestone as interbeds in stratigraphic units and with evaporates. Although dolomite is studied extensively but its origin is not well understood. Many dolomites that show the presence of limestone texture and structures, are secondary rocks formed by the diagenetic replacement of older limestone. But many fine crystalline dolomites lack the textural evidence and replacement and can not be proven to be originated by alteration of limestones. The unsatisfactory unexplained origin

of these fine-crystalline dolomites is referred to as dolomite problem. Scientist have not yet able to precipitate the dolomite in laboratory under normal temperature and pressure condition(Lumsden, D. N. & Lloyd, R. V., 1997). For the discussion of kinetics of dolomite formation see (Machel, G. G. & Mountjoy, E. W., 1986).

## 1.2 Classification of Carbonate Rocks

The classification scheme takes into account the objective, quantifiable description of the features as well as genetic and interpretive features, i.e, depositional environment and mechanism of formation etc. The classification of carbonate is based on texture, composition, mineralogy and combination of these. Several classification are reported in literature ranging from simple to complex. Only two Folk's (Folk, R. L., 1959, 1962) and Dunham's (Dunham, R. J., 1962) classification schemes along with the variants of these two gained popularity and are in wide spread use. These classification are based on grain (skeletal fragments, ooids, pellets, intarclasts and non carbonate detritus), matrix or carbonate mud and open pores or sparry-calcite-filled primary interparticle porosity. Below is the short description of above mentioned classifications along with classification criteria, advantages and disadvantages.

### 1.2.1 Folk Classification

This classification is compositional and textural (sorting, roundness, grain size). This classification being detailed and complex is used in research settings. Folk's classification is based on carbonate rock components (Bioclasts, Ooids, Peloids, Intraclasts, Micrite, Sparite etc) and the nature and ratio of matrix/cement. This classification, from composition point of view, divides the rock into *Allochemical* and *Orthochemical* groups. *Allochemical* rocks are those that contain grains brought in from elsewhere (i.e. similar to detrital grains in clastic rocks). *Allochemical* are divided into 4 members and each member is further divided into 2 sub members based on cement and matrix. *Orthochemical* rocks are composed of *in situ* crystallized carbonates.

Folk's classification also takes into account the textural aspects, i.e sorting and roundness that describes the depositional environment and energy settings. This aspect divides the rocks from low energy level to high energy level. Final component of Folk's classification relates to average grain or crystal size. Depending on the required detail, carbonate rock may be classified based on above three components i.e, biosparite or a rounded biosparite or a coarse calcarenite etc.

Folk's classification(Folk, R. L., 1959, 1962) offers many advantages. Because this classification is comprehensive, descriptive and genetic, environmental information is provided. It also describes the grain size, mineralogical composition, constituents and other features. It is very useful in academic research settings.

The drawbacks of this classification includes accurate naming, because microscopic work needed to identify small grains, their percentages with matrix and cement. Also It's not used extensively in field work and in industry because of required detailed microscopic work.

### 1.2.2 Dunham Classification

Dunham's classification(Dunham, R. J., 1962) is simple and widely used by field geologist and in petroleum industry. This classification is based on rock fabric, presence of biological binding, carbonate mud and grain versus matrix support. The main divisions of this classification are matrix-supported, lime mudstone and wackestone, grain supported, packstones and

grainstones, biological bounded, boundstone and crystalline limestone. Dunham's classification indicates the energy level of depositional environment at the time of deposition.

The main advantages of this classification include its objectivity and simplicity. Because this classification indicates the energy level during deposition hence it gives the genetic information. This classification is easily applied in the field and preliminary core analysis without microscope inspection.

The down side of this classification includes lack of detail compared to Folk's classification, lack of classification of diagenetically altered rocks. Its use is very limited in research setting. Another drawback is the difficulty in deciding whether a rock is grain or mud supported. This problem arises due to the apparent "float" of grains in two-dimensional view of three-dimensional fabric.

Besides of individual pros and cones these carbonate classifications, certain limitations exist that are hard to overcome for all classifications of carbonate. These classifications are suitable for primary depositional fabrics. Compaction, pressure dissolution and diagenesis can change the primary rock fabric and many fabric occur in limestones that are not covered by any classification system. Further problems in classification might arose due to impurities and admixtures of siliciclastics in limestone.

## 1.3    Classification of Carbonate Porosity

Carbonates have much more complex pore system as compared to the siliciclastics. This complexity is due to biological origin of carbonates and chemical reactivity during and at later stage of deposition. Biological process results in porosity within grains, fossil-related shelter porosity and growth framework porosity in reefs while chemical reactivity due to diagenetic processes, i.e, solution and dolomitization, result in secondary porosity. While carbonate porosity is developed and modified by aforementioned processes there are certain other intermediate processes by which porosity is developed, reduced, destructed and modified throughout the burial history.

### 1.3.1    Primary Porosity

In depositional reservoirs porosity is formed only by depositional processes and this porosity is classified as primary porosity. Since carbonate rocks are detrital, biogenic or chemical origin. There are many types of primary porosities in carbonate reservoirs. Here is the short description of primary porosities in carbonate reservoir.

*Integration porosity* developed in mud free carbonates at the time of deposition. The porosity in mud free carbonate sediments ranges from 40-50 % (Enos, P. & Sawatsky, L. H., 1981).

*Intragrain porosity* may originate in different ways, i.e, foraminifera, gastropodes, rudists etc. The microbal activity may increase the intragrain porosity, during and shortly after deposition (Perkins, R. D. & Halsey, S. D., 1971).

*Depositional porosity of mud bearing sediments :* Mud bearing carbonate sediments have higher porosity ranges. Packstones show the porosity range 44-60 % while wackstones show the porosity range from 60-78 % (Perkins, R. D. & Halsey, S. D., 1971). This high porosity in mud bearing sediments is due to the effect of shape and fabric.

*Framework and fenestral porosity :* In reefal environment the reef-building organisms play a vital role for framework porosity. Certain framebuilders such as scleractinian can construct an open reef framework that might enclose enormous volume of pore spaces during reef building

while coralline algae, stromatoporoids and sponges potentially build a close framework structure thus resulting in less framework porosity (James, N. P., 1962; Tucker, M. E. & Wright, V. P., 1990). During the reef complex development, boring organism such as clionid sponges and pelecypods can contribute to develop a substantial volume of porosity but this framework porosity tend to be filled quickly during early stage of reef development in depositional environment by varying size sediments that will eventually form a complex depositional pore system (Landa, L. S. & Moor, C. H., 1980; Moor et al., 1976).

### 1.3.2 Secondary Porosity

Secondary porosity is generated and modified due to processes such as dissolution and dolomitization. Fracturing increases the permeability rather then increasing the porosity(Lucia, F. J., 1995). diagenesis refers to all the post depositional but before metamorphism changes to the sedimentary rocks. All changes in grain size, shape, volume, porosity, chemical composition and change in sedimentary structures happens after the deposition. diagenesis may be of mechanical, biological, chemical origin or combination of these ones. Mechanical diagenesis through compaction might result in volume reduction, interstitial water expulsion and modification in grain packing thus changes and modifies the rock properties after deposition(Moor, C. H., 1989).
Bioerosion is the result of biological diagenesis. Bioerosion is of little significance to porosity change in the rock but it may result in large percentage of mud fraction in some depositional settings.
Chemical diagenesis is of significant importance for constructive and destructive changes in carbonate reservoirs. Chemical diagenesis operates through dissolution, cementation(precipitation), recrystallization and replacement. These processes can change, modify, create or destruct the carbonate reservoir porosity and properties. Chemical diagenesis seeks the equilibrium in water-rock system. Dissolution starts and continues until the saturation equilibrium is reached between rock and water. Extensive dissolution forms the karstic features. If water is supersaturated in $CaCO_3$ precipitation will be triggered and cementation will take place in the water-filled pores.
Porosity created and modified by dissolution is named as intercrystalline, moldic, vuggy and caverns originating from the same process but differ in size and shape. Different authors proposed different names to the same porosity type. Separate-vug poristy refers to moldic porosity by Lucia (Lucia, F. J., 1995). Similarly depending on the size Choquette and Pray (Choquette, P. W. & Pray, L. C., 1970) coined the terms vugs, channels and caverns.
Recrystallization changes the crystal morphology without changing the mineral composition. Whereas replacement completely changes one mineral to another one. For example dolomite replaces calcite and aragonite. Porosity enhancement with recrystallization or neomorphism in the form of microrhombic microporosity is reported by(Ahr, W. M.., 1989; Dravis, J. J., 1989; Moshier, S. O., 1989).

## 1.4 Reefs

Reefs form as the result of interrelationship of physical, chemical and biological processes. Due to diverse reef building organisms and diverse processes different type of reefs are formed which are large enough to have topographic relief. Reefs are characterized by two simple features, lateral restriction and pronounced biological processes during its growth. Although

14

in literature reef is ascribed to any discrete carbonate build up, but (Dunham, R. J., 1970) suggests the use of stratigraphic reefs and ecological reefs.

### 1.4.1 Reef Dynamics

Four important processes contribute to the reef building. These processes include constructive processes, destructive processes, cementation and sedimentation. These all factors play an important role in the formation of different types of reefs, their internal structures and porosity modification.

*Constructive processes* are biological processes by of reefs formation. Large individual or colonies of calcareous organisms form the reefs. In modern reefs these primary frame builders, see (Scoffin, T. P. & Garrett, P., 1974), are represented by scleractinian corals, crustose coralline algae etc while in ancient reefs scleractinian, rugose and tabulate corals, various calcareous algae and stromatolites. Reef formation is due to primary and secondary builders as well as other organisms. Major reef builds are due to abundant presence of aforementioned frame-building organisms, which happened to be only six or seven times during geological time scale(Longman, M. W., 1981; James, N. P. & Mountjoy, E. W., 1983), otherwise due to activities of sedimentary contributors, binders and precipitators only smaller reefal buildups and mounds occurred. Due to these microbial builders and their respective activities reefs of varying size cavities are formed.

*Destructive processes* include physical destruction and bioerosion. Physical destruction is due to the storm, wave and current activities. Due to these activities reef ecology and sedimentation is affected and consequent destruction of reefal buildups during geological record happened (Stoddart, D. R., 1969; Maragos et al., 1973). Bioerosion destroys the primary reefal fabrics. If rate of bioerosion is greater than carbonate production and sedimentation, complete destruction of reefal framework may occur (Jones, B. & Pemberton, S. G. J., 1988; Hein, F. J. & Risk, M. J., 1975). According to(Schroeder, J. H. & Zankl, H., 1974) bioerdoers can be classified int borers, raspers, crushers and burrowers. These bioerdoers destroy the reefal rocks in different ways and with different intensity.

*Sedimentation* supply to reefs is provided by mechanical breakdown of framework materiel by physical or biological processes, by decomposition of reef dwellers such as coralline algae, corals, foraminifera etc and supply from outside the reefs. Sediment supply to reefs may alter and modify the porosity, by multiple deposition and resulting sedimentary features and bioturbation(James, N. P. & Ginsburg, R. N., 1979; Watts, N. R., 1988). These internal sediments due to further biological, chemical and physical processes may become cemented and bored. This sediment material supply is generally in the reef-front and reef-crest but may occur in other parts of the reefs.

*Cementation* can provide strength and stability to reefs to make it wave resistant. Cementation process in reef is very important to understand the porosity distribution and modification within reef(Marshall, j. F., 1983; Lighty, R. G., 1983). Areas with high sea water flux are prone to cementation.

In nutshell the large scale factors that affect the reef morphology and development include biological, topographical and sea level changes due to tectonics, eustatic changes and subsidence.

15

## 1.5 Karst

Due to dissolution of carbonate rocks in carbonic rich water form karsts. Numerous factors play an important role in the development of karst including lithology, hydraulic conductivity, chemically enriched active ground water, palaeoclimates, tectonic activity and eustatic changes etc. Carbon cycle plays an important role in the development of karsts and associated features. Change in hydraulic gradient due to sea level change will favour solution activity and consequently formation of karsts and karst related features. The direction of ground water movement, permeability, lithology and overburden rock thickness bear an important relation with karstification. In vadose zone water moment through fractures will form vertically oriented pipes and sinks while its horizontal movement in phreatic zone will result in horizontally oriented cavities and cave system (Palmer, A. N., 1995; Loucks, R. G., 1999). Exposure of carbonate rocks and unconfined carbonate aquifer, due to recharge and discharge, will tend to enhance the karstification. Dissolution is a dominant active process for karstification in vadose and phreatic zones.

Dissolution process plays a vital role in the development of karst system and respective land-forms, hydrology and diamagnetic facies. These karst are developed in association with unconformities due to subaerial exposure (Choquette, P. W. & James, N. P., 1988).

According to (Esteban, M. & Klappa, C. F., 1983) karst is "*a diagenetic facies, an overprint on subaerially exposed carbonates, produced and controlled by dissolution, migration and precipitation of calcium carbonate in meteoric waters, occurring in a wide variety of climatic and tectonic settings and generating a recognizable landscape*".

Karst formation is mainly of the suabaerial meteoric origin. Karst formation may be *polycyclic* as well as *polygenetic*. Different karstification cycle will result in overprinting where each cycle might represent different process as discussed below.

- In modern coastal settings mixed meteoric-marine groundwater forms the karst by dissolution of emergent and shallow carbonate rocks (Stoessell et al., 1989).
- Karst porosity development in submerged continental shelves result from reflux of evolved meteoric waters (Stoessell et al., 1989; Fanning et al., 1981).
- Ascending hydrothermal fluids through the carbonate rocks form the megascopic karst dissolution features,i.e, caverns. Dissolution due to this process either overprint an existing karst feature or generate substantial porosity (Dublyansky, V. N., 1980; Egemeier,S. J., 1981; Bakalowicz et al., 1987; Muller, P., 1989).
- Karst formation by dissolution of connate fluid enriched in sulphuric acid, due to oxidation of $H_2S$ in evaporite-rich and/or mixing of water of different $H_2S$ (Hill, C. A., 1990, 1992).
- Karst like cavities may be formed by cold seawater-dissolution of extant carbonate platforms (Smart, P. L. & Whitaker, F. F., 1991).
- Intense intrastriatal dissolution of carbonate strata will result in solution-collapse features and formation of extensive breccias(Palmer , M. V. & Palmer, A. N., 1989).

The major types of karsts are of subaerial meteoric origin formed as the result of dissolution. Karstification in stratigraphic framework is due to subaerial exposure due to sea level drops, exceed of sedimentation rate to accumulation space, local tectonic uplift or due to eustatic falls.

## 1.6 Salinity and Salt Water Intrusion in Coastal Aquifers

Coastal aquifers are important source of water for domestic, industrial and agriculture purposes. Ecosystem is also largely supported by coastal aquifers. Continuous pumping and sea level fluctuation result in salt water intrusion and contamination of coastal aquifer. Coastal aquifer characteristics are controlled by hydraulic head due to sea, density contrast between fresh and see water, geological setting and resulting sedimentological characteristics. Ground water flow direction is towards the sea driven by head potential due to inland recharges. Periodic tidal fluctuation result in induced flow. Salt water wedge or floating freshwater lens is produced due to the isocones starting from the near coastline and penetrate to the lower boundary of the aquifer system.

Salinity in coastal aquifer is related to pre-Holocene marine water, ancient marine water and seawater intrusion. Pro-Holocene marine water salinity coastal aquifer are in area of Belgium and The Netherlands. According to (Groen et al., 2000) seawater in Surinam and other parts of NE angle of South America and Western Europe aquifers, replaced the fresh water in late Pleistocene times.

In some coastal areas dilution of ancient marine water concentrated in salt may be source of saline water. According to (Shavit, U. & Furman, A., 2001; Vengosh, A. & Ben-Zvi, A., 1994) saline water in Messinian (Miocene) is an example of this phenomenon in Israel. In Fuerteventura island diluted palaeowaters recharge the aquifer that cause water salinity through local permeable features(Emilio, C., 2002).

Apart from extensive fresh water pumping climate changes and sea level rise mostly contribute to the salt water intrusion and contamination of the fresh water aquifers. Sea level rise and climate changes impact the coastal aquifers in a number of different ways. This include sea water intrusion resulting in inland migration of fresh-saline water, seawater inundation and flooding of unconfined aquifers and perturbation in recharge and discharge pattern of aquifers due to rainfall and evapotranspiration. These parameters interplay differently depending on the particular site and surroundings.

Density contrast of fresh groundwater and sea water will result in see water intrusion. This density contrast also determines the rate and characteristic of intrusion. There exist a sharp boundary between fresh and saline water as well as existence of the transition zone. Dispersion and liquid mixing, due to diffusion and advection, are important phenomena in the transition zone. Density ratio of saline and fresh water, fresh water head and certain other characteristics of the aquifer play a vital role in the development of size and shape of the transition zone. Seawater movement toward this transition zone results in an extensive circulation of seawater and forms a large or thick mixing zone. The nature of circulation and formation of large mixing zone also depend on the homogeneity or heterogeneity of the aquifer(Khublaryan, M. G. et al., 2008).

## 1.7 Llucmajor Carbonate Platform

Mallorca Island, figure 1.1, formed through Late Miocene to early Pleistocene extensional faulting is, the biggest island of the Balearic archipelago in southern Spain, considered as NE continuation of Betic chain. Three NE-SW trending mountain ranges (Tramuntana, Randa and Levante system) are separated by two main depression. Three small basins, Palma, Inca and Sa Pobla, are situated on the western area separated from each other by NW-SE structures while

Llucmajor-Campos basin is situated in eastern area(Fontbote et al., 1983).
Llucmajor Carbonate Platform, depositional architecture and environment shown in figure1.2,
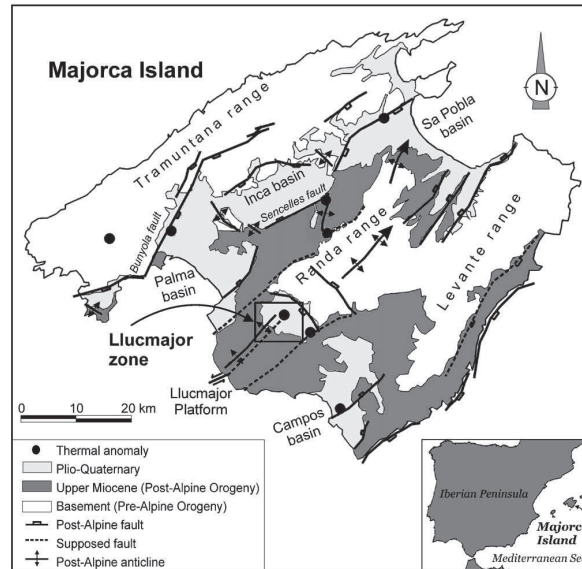


FIGURE 1.1 – Geological setting of Majorca Island (after(Arango et al., 2009)).

is 20 km wide late Miocene reefal platform situated in south of Mallorca. The well exposed sequence of rocks is extensively studied by Pomar. According to (Pomar, L. & Ward, W. C., 1995) four main lithofacies of progradational upper Miocene platform exposed at Cabo Blanco are :

1. Lagonal(back-reef) lithofacies :
   These facies are divided into inner and outer lagoonal. Mudstone and wackestone with vertical root molds, fecal pellets, benthic forminifera, bivalves, locally thin layers of monospecific gastropodes constitute the inner lagoonal deposits. Coarse skeletal grainstone and packstone, rhodoliths, echinoids, benthic foraminifera and coral fragments make the outer lagoonal deposits.

2. Reef-core lithofacies :
   are composed of skeletal grainstone and packstone within coral framework. Coral colony morphologies zonation occurred as a function of paleobathymetry. These morphologies range from dish-coral in lower part to branching coral in the middle part to massive-coral in the upper part of the reef-core.

3. Reef-Slope(fore-reef) lithofacies :
   In proximal setting the lithofacies are composed of coarse skeletal packstone with abundant mollusks, red-algaefragments, rhodoliths, coral debris and Halimeda. In distal-slope to open-shelf setting fine grained packstone is present.

4. Open-shelf(Shallow basin) lithofacies :
   Bioturbated, poorly bedded fine grained packstone with Planktonic foraminifera and deep water oyster are major constituent. Occasionally echinoids may also be founded.

These beds may be interbedded with biostromes of coarse grained red algae packstone with densely-stacked rhodoliths and laminar corals.
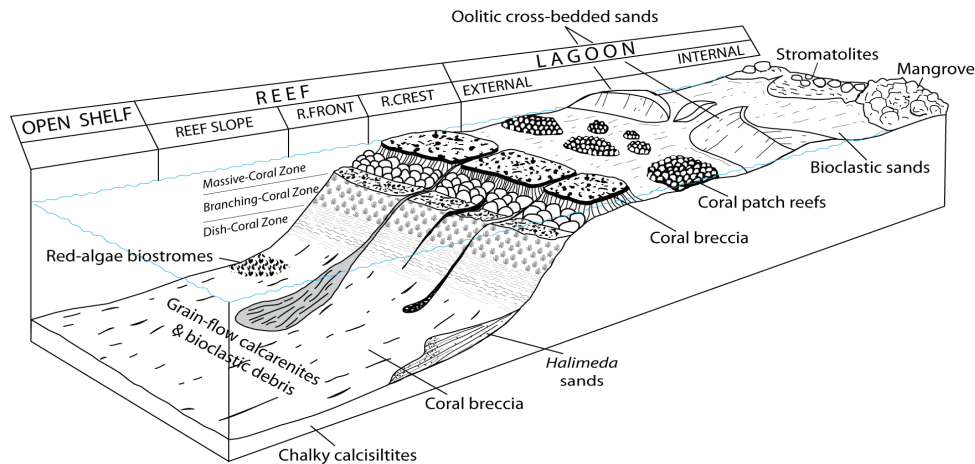


FIGURE 1.2 – 3D block illustrating the complex Llucmajor Miocene reefal platform and depositional environment(after(Pomar et al., 1983)).

Sea level changes and consequent variation in accommodation space plays an important role in the deposition and reservoir scale heterogeneities and this can be well understood by constructing the chronostratigraphic framework.

The basic building block of upper Miocene reef complex of Llucmajor platform, that is considered to be formed during third order sea level change (Pomar, L. & Ward, W. C., 1994), is composed of sigmoid(Pomar, L., 1991). Sigmoid stacks into large scale units of varying sea level fluctuations representing high frequency depositional frequency sequences (seventh to fourth order) that are considered as glacioeustatic in origin. Heterogeneity in lithofacies in this progradation platform is a function of accommodation space and basin floor morphology that controls carbonate production. Primary porosity is related to spatial and vertical depositional lithofacies that varies with each system tract. This porosity is mainly altered due to dolomitization and dissolution of aragonite component. Other diagenetic features include cementation of different origin, minor calcite replacement of aragonite component and thin subaerial crusts and mikrocarst in lagoonal units(Pomar, L. & Ward, W. C., 1981). Secondary porosity is mostly related to dolomitization that is related to third-order oscillation. Moldic porosity due to dolomitization of aragonite component result in major type of secondary porosity in almost all type of rocks present in Llucmajor reefal complex. In absence of aragonite component in inner lagoon rocks and in middle and outer lagoon rocks that are composed of benthic foraminifers, red algae and echinoids, secondary porosity is less pronounced. Further higher order cyclicity of sea level fall result in locally microkarstic features in some lagoonal layers.

## 1.8    Site Geology

This project was carried out at Ses Sitjoles site near Campos in Mallorca, Spain shown in figure 1.3. This site is composed of karstic carbonate coastal aquifer with brine water intrusion. This site was developed and studied to gain insight into hydrological properties of the coastal aquifer that are facing problem of salt water intrusion and thus contaminating the freshwa-
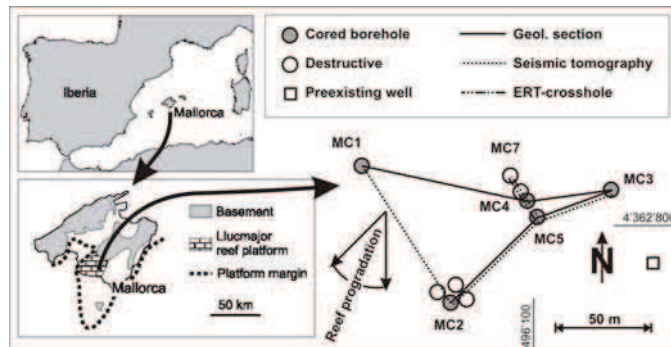
Figure 1.3 – Ses Sitjoles experimental site near Campos, within the Llucmajor Miocene reefal Platform (after(Jaeggi, 2006)).

ter aquifers. The main objectives of different geological and geophysical studies conducted on this experimental site include the understanding and determinations of the reservoir heterogeneities at different scale and their origin, porosity distribution, hydrological properties of the reservoir and preferential flow paths. The integration of different geological and geophysical studies will help to devise a long term monitoring, modelling and sustainable management of the aquifers.

This site is located approximately 6km inland and covers an area of 100mx100m. Different wells are drilled, on this experimental site as shown in the figure 1.3, down to 100m and cored. The water table is approximately at 37m. Based on the cores, figure1.4, of these drilled wells
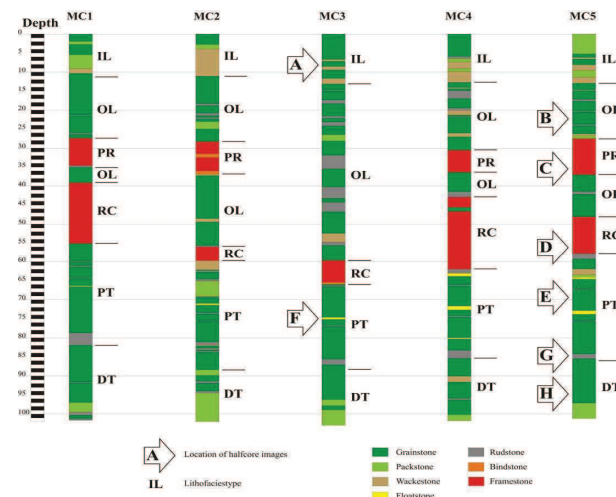


Figure 1.4 – The five borehole drilled at Campos site with sedimentary textures and indicated boundaries of lithofacies types inner lagoon(IL), outer lagoon(OL), patch reefs(PR), reef core (RC), proximal talus (PT) and distal talus (DT), (after(Jaeggi, 2006)).

main lithofacies units are delineated. The thickness of different lithological units varies considerably in these different drilled wells. Here is short summary of the encountered lithofacies

20

adapted from(Jaeggi, 2006).

1. Inner Lagoon :
   Consist of 10-13 meter thick sequence of oolithic grainstone occasionally with dense cal-crete hardpans and black pebbles and locally karstified soft lime stone having intrafossil or intergrain porosity. Texture is composed of micritic crusts and intergrain pore space is occluded by vadose blocky cement. The prominent formas are milliolids along with some red-algae and molluscs. This lithofacies type faced many cycles of transgression and regression and lacked direct connection to open marine environment.

2. Outer Lagoon :
   Consist of 30-46 meter tick sequence composed of skeletal grainstones and packstones with cementation of high biodiversity comprising of red algae, sessile and benthic foram genus, echinoids, oyster abundant molluscas etc. Micritic vadose cement is dominant but also patchy spar is present. Mainly moldic porosity due to latter alteration of aragonite is found and intergranuar porosity ranges only from 20 to 30 percent highly porous. Isolated patch reef consisting of Porites with extensive sponge and bivalve boring form dense, well cemented and diagenetically altered heterogeneities.

3. The Reef Core :
   Consist of 4-19m hick comprising of framestone and grainstone to packstone which act as internal sediments filling the most of the cavities and large channels within the reef. Moldic and non fabric selective vuggy pores constitute the porosity. The lower part of the reef is karstified.

4. Proximal Talus :
   is 20-30 m thick sequence mainly consist of white bioclastic and intraclastic, intensively bioturbated packstone to rudstone. The rock is better cemented with patchy blocky spur adjacent to the reef core while lower part is poorly cemented with micritic cement. Fractures occur towards the overlying reef. Porosity is of moldic origin occurring as large and elongated molds and small round shape molds. In lower part of the reef complex about 65m molding due to grain dissolution is extensive approximately 60 to 80 percent as compared to upper part, 5 to 40 percent only, and due to recrystallization reef components and matrix core are indistinguishable.

5. Distal Talus :
   is the lower most part encountered at the test site and consist of white strongly bioturbated and fine grained packstone and grainstone rock is homogeneous lacking macrofossils. Permeability is rather low due to lack of intergranular porosity although it exhibits highly well sorted moldic pores.

Figure1.5 shows the stratigraphic relationship between the exposed sequence at Cabo Blanco and the one of the well drilled in the site.
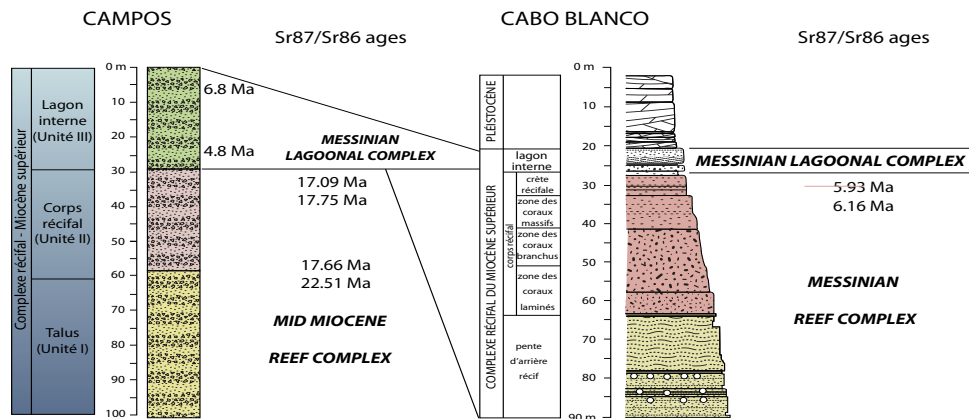
FIGURE 1.5 – Stratigraphic and diachronic relationship between sequences exposed at Cabo Blanco and drilled by ALIANCE near Campos (after(ALIANCE., 2007)).

## 1.9 Borehole Studies

For this study different down-hole techniques, the acoustic travel-time scan to assess the borehole wall heterogeneity, the impeller flowmeter (IFM) to determine the physical measurement of hydrodynamical active zone, the induction log to measure the electrical properties of the formation and full waveform sonic log to measure the acoustic properties of the formation, are used to characterize the different reservoir properties from cm scale to mega-scale. These all measures provide the valuable information at different scales. Below is the short description of each of the aforementioned down-hole technique to measure the borehole scale heterogeneities and porosity estimation.

### 1.9.1 Acoustic Travel Time Scans

Reservoir properties for very complex reservoirs need to establish with different tools and different methods of different scale. Every method has its pros and cons. Small scale heterogeneities and features are detected with imaging techniques including FMI, FMS and optical- and acoustic borehole televiewer(BHTV). Acoustic travel time scans are preferred over the other imaging tools due to full circumferential coverage and less sensitivity to borehole roughness and cavities.

To obtain the characteristic porosities, of different scales and origins, of the reservoir in different wells, acoustic travel time scans are acquired which continuously record the total optical porosity (TOP) of the borehole wall in the predefined window of 10cm length and 5cm scan increment. Detail description of processing, choice of window and scan increment is given in(ALIANCE., 2007). In figure1.6(top) peak (a) is due to leached core in outer zone. In reef core moderate karstification leads to the narrow peak (b) and region (c) is due to the extensive burrowing and moldic porosity in coarse grain sediments. In the lower part of distal talus homogeneity prevails except the peak(d) which is due to dissolution.

In MC3 all boundaries between the individual lithofacies are well pronounced. Due to the presence of sequence boundary consisting of wackstone characterized by low intergranular porosity and small molds, is marked by zero TOP in the interval (e). Open fractures dipping towards SW is marked by region (f).

Peak (g) in MC5 is due to the de-centred probe. The sequence boundary in PT is marked by vuggy zone on the top(h). The boundary PT/DT is not much pronounced as in other wells due to the presence of single molds and large burrows.
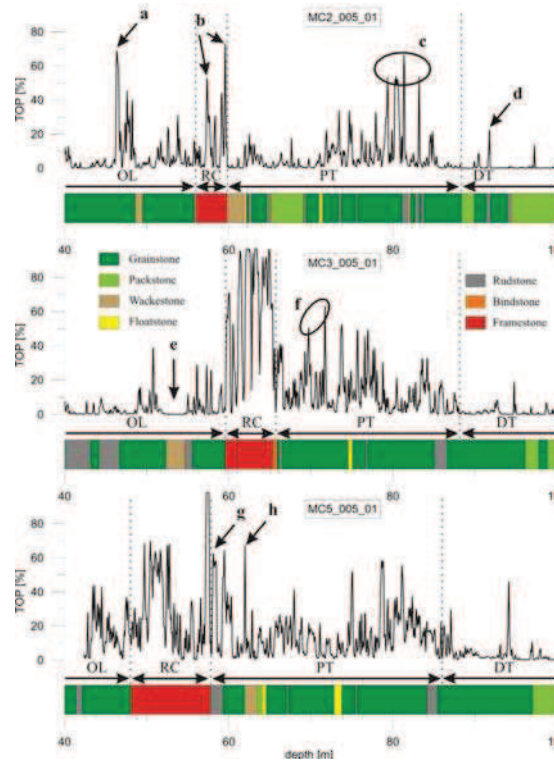


FIGURE 1.6 – Acoustic time scans, MC2(top), MC3(middle) and MC5(below) with 10cm window length and 5cm increment, correlated with cores obtained from the wells (after(ALIANCE., 2007)).

### 1.9.2   Impeller Fowmeter Logs

IFM is a powerful tool to characterize the hydraulic properties and identification of the major permeable groundwater pathways. For this study permeable features identified by IFM are interpreted and correlated with stratigraphy with the help of gamma logs, optical borehole televiewer logs(BHTV) and data from core description.

Impeller flowmeter is used to delineate the discrete, yielding flow at a certain depth is result in step on the log, and diffuse permeable feature, flow occurring continuously over a certain distance. These permeable feature are mostly secondary and tertiary in nature interconnected by karst. The field procedure for impeller flowmeter measurement is fully described in(ALIANCE., 2007).

In MC2 90% of the total flow has been recorded within 2.5m zone of karstified reef core. Three discrete permeable zone A-C occurred at leached coral zone and their hydraulic productivity is ascribed to the interconnected karstic channels. This karst development might happened during post depositional sea level lowstands, supported by sequence boundary that seems to be low permeable zone. The discrete permeable zone D might be due to extensive burrowing
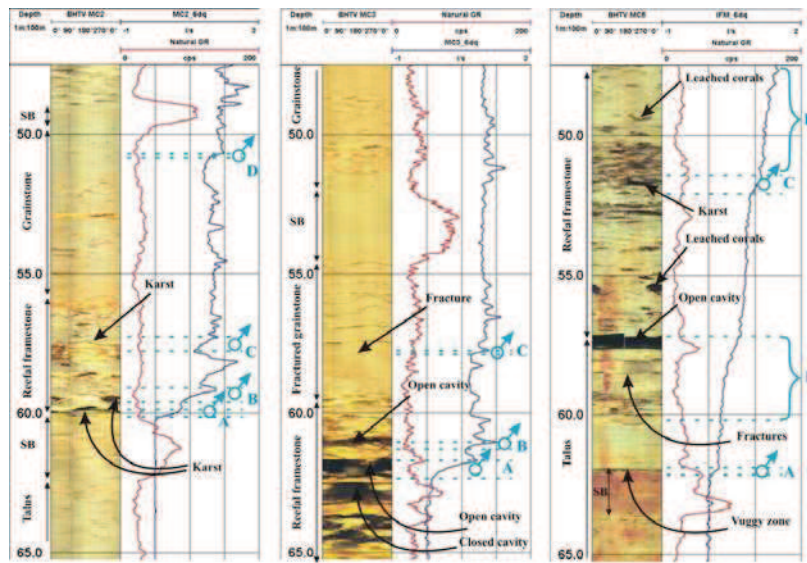
FIGURE 1.7 – Correlation of different discrete and diffuse permeable zone for well MC2(left), MC3(center) and MC5 (right). Gamma log (red line) and BTHV-images are also given for all the boreholes(after(ALIANCE., 2007)).

and overlying sequence boundary as it cannot be characterized clearly from core analysis and optical BHTV.

The Karst, upto 1m in height developed at the upper half of the reefal core, is best developed in MC3 borehole marked by two permeable features A and B yielding 80% of the total flow. The discrete permeable zone C, sandwich between sequence boundary and reef core, lies within a fractured zone.

In MC5 both discrete and diffusive permeable features occurred. A discrete permeable feature(A) present in grainstone to rudstone is underlain by sequence boundary which allowed the development of the vuggy zone. Two different zone of diffusive flow B, located in fractured zone below the reef core, and zone D, located in reefal framestone. Here in this borehole not only the karsts but well connected fractures also contribute to the flow as compared to the other boreholes where karsts and interconnected pores are exclusively responsible for the flow.

## 1.10   Induction Logs

Borehole electrical measurements have widely been used to deduce to the saturated porosity and lithological changes. For this study double spaced induction tool DIL38 has been used due to fact that it does not require the direct coupling with borehole. This fact well suited for the measurement in vuggy and badly cemented reefal carbonates. The calibration, field procedure and other related parameters are mentioned in(ALIANCE., 2007).

Total porosity, including primary, secondary and tertiary porosity, is determined from the joint analysis of induction and conductivity logs. Porosity values are relative rather than absolute due to the absence of cementation factor that is highly variable in the boreholes. Zone of rapid porosity increase that lies within mixing zone followed by low porosity zone. Due to 3 lost drill
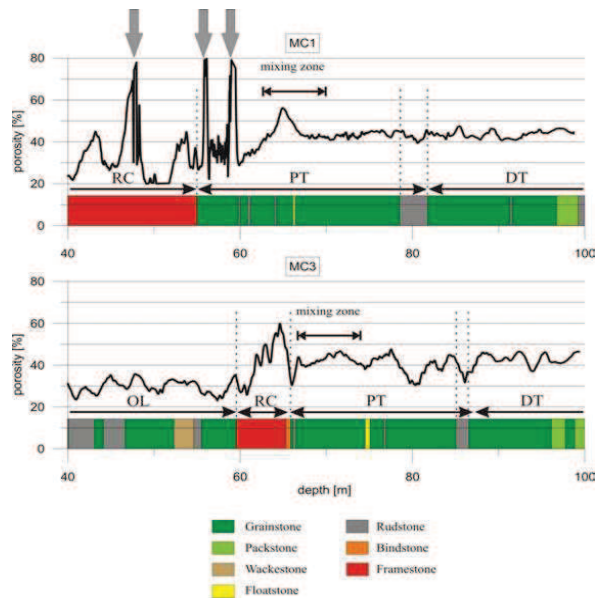
FIGURE 1.8 – Porosity from induction logs for boreholes MC1 and MC3 with correlation to geology observed on cores. Arrows indicate the lost of drill bit(after(ALIANCE., 2007)).
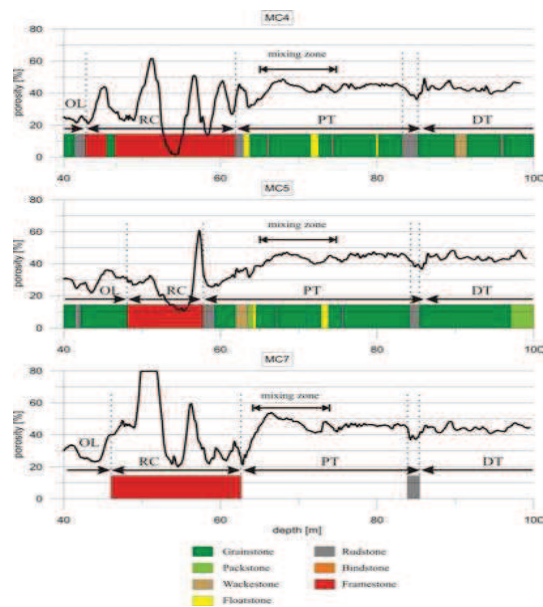


FIGURE 1.9 – Porosity from induction logs for boreholes MC4, MC5 and MC7 with correlation to geology observed on cores except for MC7. For MC7 due to unavailability of core material, geological correlation is based on BHTV image(after(ALIANCE., 2007)).

bits in well MC1 at depths 48m, 56m and 59m, marked by arrows in the fig6.2(top), the data is biased in this upper part. Porosity oscillates very little within the grainstone of proximal talus while porosity in rudstone of proximal talus is slight lower. The total porosity in the lower part of distal talus remain same as in the upper part of the proximal talus but with lower high frequency oscillations.

In MC3 boreholes reef core is overlaid by thick sequence of outer lagoon where porosity varies within range of 25-35%. Porosity is minimum in rudstone of outer lagoon sequence. Porosity is quite variable in reef core with altering zone of highly karstic filled with clays and dense recrystallized zones. In proximal talus low and high frequency oscillations are present due to the different rate of cementation of fractures. In distal talus high frequency oscillation are due to leached coral rubble and molds of other large fossils.

Boreholes MC4, MC5 and MC7, figure1.9, shows the almost similar characteristics for proximal and distal talus. The high porosity peaks are the karsts which exactly correlate with the core material at the same depth. The lower part of the proximal talus has quite uniform porosity of 45% that originates from the thin lenticular layers of reef rubble or from lager molds. The porosity is slightly less than 40% in basal rudstone due to better cementation of bioclastic material.

### 1.10.1   Full Waveform Sonic Logs

For this study full waveform sonic log is acquired for boreholes MC4 and MC5. The data acquisition and subsequent processing along with different effective parameters influencing the porosity calculation from sonic measurement are described in(ALIANCE., 2007). Figure1.10 shows the full waveform sonic log for boreholes MC4(top) and MC5(bottom). Three intervals of porosities are indicated by this figure, first interval of high oscillation from 3-100%, second part of low variability at an average porosity of 50-55% and finally an interval of average porosity of 40-45%. For MC5 same situation of porosity variation prevails but with higher fluctuation due to lower data quality and related cycle skip. The very high porosity values are due to dm scale cavities. The zone(a-e) corresponding to the low porosity values is due to the presence of dense and recrystallized rocks as seen on core material. The second interval of porosity values averaging 50-55% starts at the RC/PT boundary. The porosity shows the transitional behaviour of uppermost talus and further detail study in this zone, until a depth of 86.1m, show at least 5 porosity-plateaus that are geologically justified. The third interval of porosity with average value of 40-45% fits exactly with PT/DT boundary as described on the core material.
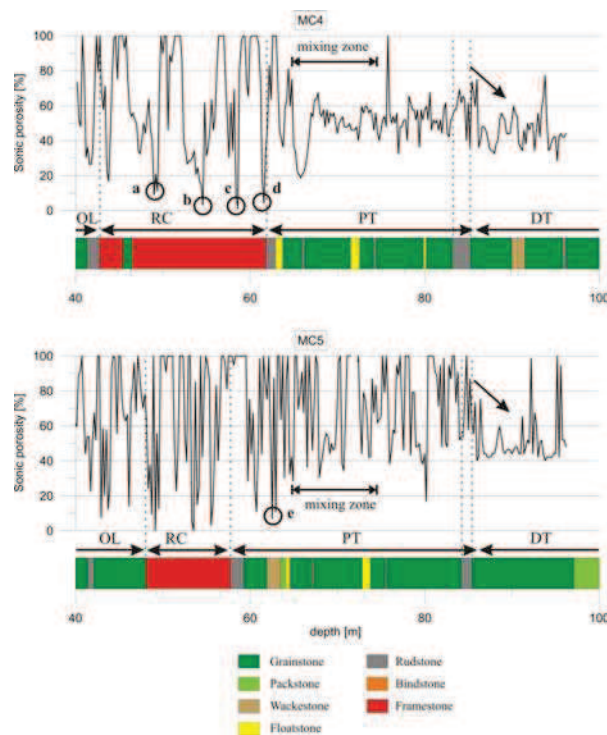


FIGURE 1.10 – Porosity deduced from full waveform sonic logs for boreholes MC4 and MC5 with correlation to geology observed on cores. Low porosity zones(a-e) correspond to recrystallized rocks. Inclined arrows indicate the prominent step in porosity at the transition PT-DT.(after(ALIANCE., 2007)).

## 1.11 Borehole Geophysical Surveys

Previously different geophysical surveys were carried out on this site. These surveys include the cross-hole electrical resistivity and seismic tomography to detect the small scale heterogeneities within and across the wells.

### 1.11.1 Electrical Resistivity Tomography

Standard resistivity logging tool are used to determine variation in electrical resistivity along the boreholes that offer many advantage over traditional borehole logging methods by taking into account the different electrode configurations that result in greater lateral penetration and thus obtaining more reliable results(Tsourlos et al., 2003). Single-hole and cross-hole electrical resistivity is performed for this study.

ERT gives the voltage values, for specified configure set up, which are measure of formation resistivity and geometry. Formation resistivity is the function of fluid resistivity, porosity, permeability, mineralogy, cementation and rock matrix. Data was acquired for different configura-
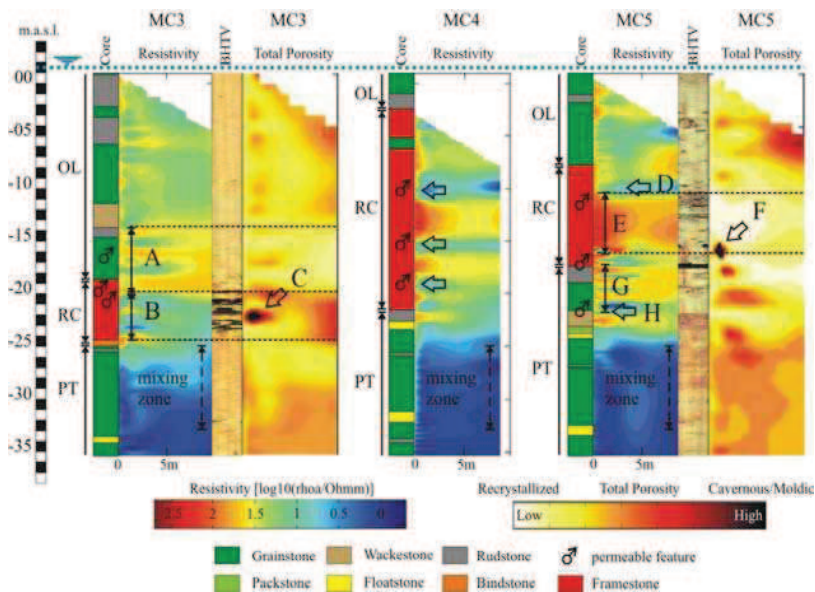


FIGURE 1.11 – Single hole, axial symmetric, ERT of boreholes MC3, MC4 and MC5 along with optical BHTV and permeable features from impeller flow meter (after(ALIANCE., 2007)).

tions such as Wenner, Schlumberger and dipole-dipole with a string of 50 electrodes spaced 1m apart from each other. For single whole tomography axial symmetry is considered. Cross-hole tomography is performed using cross-hole configurations with potential and current electrodes in one borehole. Numerical inversion maps the true resistivity distribution of the subsurface by minimizing the misfit of observed and model data to the RMS. For this study two cell size of 0.5m and 1m are tested for model resolution and 1m cell size is chosen because the accuracy of image is higher. Accuracy is higher close to the electrodes and vice versa. Furthermore ratio of borehole spacing and depth also affects the ERT accuracy.

Several features are recognised from the single-hole tomography panels as shown in figure 1.11. These zones are identified for different wells. Karstic features are mainly present within
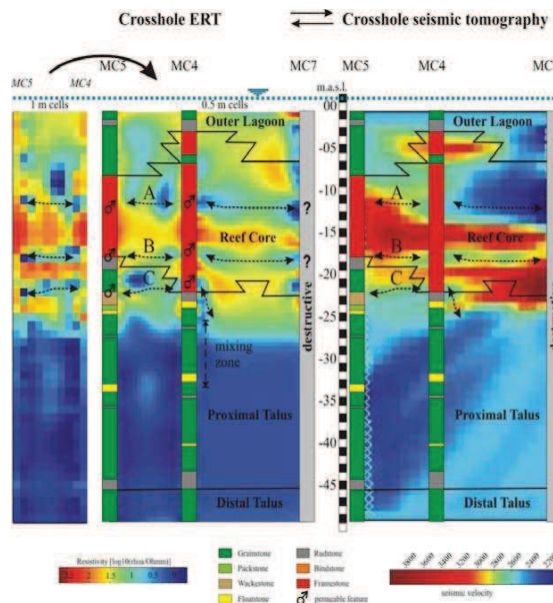
Figure 1.12 – Crosshole ERT for section MC5-4-7 with 0.5m cell-size (left) and section MC5-4 with 1m cell-size (middle) and cross-hole seismic tomogram for the same well (right) (after(ALIANCE., 2007)).

reefal complex marked by low resistivity zone as shown by arrows in MC4 and sometime occur as heterogeneity as indicated by D in MC5. Zone B at MC3 is recognised as composed of cavities of varying scale. Zone E is highly resistive zone. High resistive zones lie within reefal complex bounded by permeable karstic horizons. Zone A in MC3 and zone G in MC5 are sandwiched between sequence boundary and reefal core and these sequence boundaries are marked by intermediate resistivity values.

The purpose of cross-hole tomography is to correlate the low and high resistivity zones and distributed heterogeneous features of varying scale. The cross-hole tomography is for the MC5-4-7. A, B and C are low resistivity zones as shown in the figure 1.11. A and B corresponds to the Karst horizons with good lateral continuity.

**Seismic Tomography**

The main purpose of seismic tomography is to determine the velocity distribution and distinguish between high velocity and low velocity heterogeneities. High velocity is due to recrystallization, cementation and low rock matrix-scale porosity. Another target is porosity variation among and within different lithofacies. Seismic tomogram for MC2-5-3, MC5-4-7 and MC2-1 are acquired. The hydrophone streamer is located from 40m to 90 m depth except MC7 where hydrophone are present from 40m to 65M. Different velocities are observed depending on the rock type such that well cemented rocks have $V_p > 3000m/s$, grainstone of outer lagoon and the internal sediment of the reef core show value around $2600m/s$ while within talus values ranges from $2400m/s$ and $2600m/s$ depending on pore structure. Since seismic tomography has lower resolution as compared to sonic log only larger structures and overall trends are estimated. Seismic pseudo log represent, shown in figure 1.13, an averaged sonic log showing

29
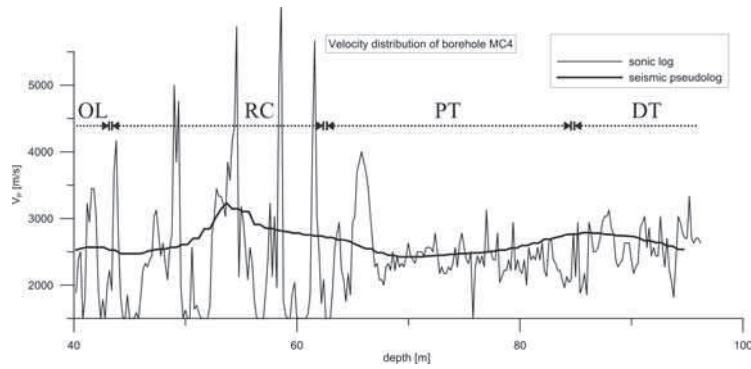
FIGURE 1.13 – Sonic log and seismic pseudo log velocity distribution for borehole MC4 (after(ALIANCE., 2007)).
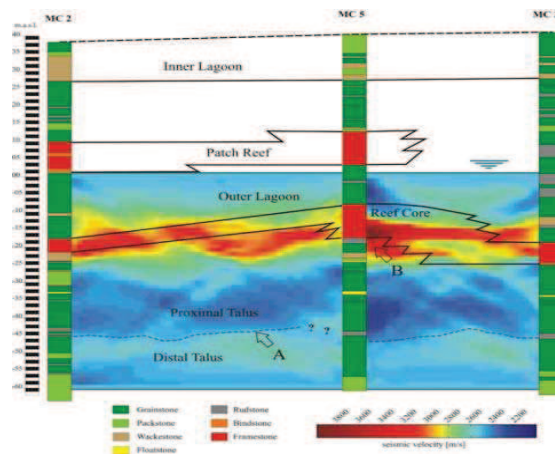


FIGURE 1.14 – Dip-section MC2-5-3 with seismic cross-hole tomogram. High velocity zone does not essentially correlate with the reefal geometry. Where A refers to high velocity boundary (after(ALIANCE., 2007)).
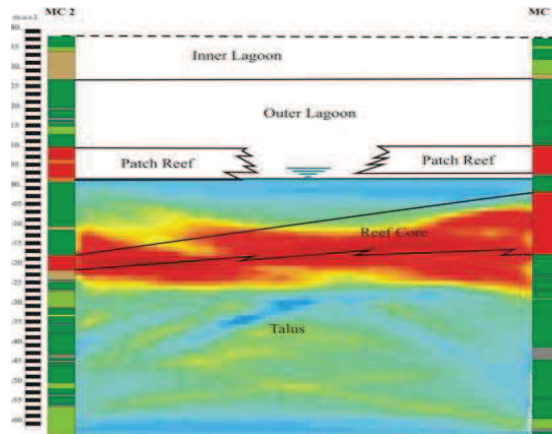
FIGURE 1.15 – Strike-section MC2-1 with seismic cross-hole tomogram (after(ALIANCE., 2007)).

overall trend such as higher $V_p$ values in well cemented and crystallized rock sections, comparative low values of $2400 m/s$ in proximal talus and sudden change at the Proximal and Distal Talus. The change of pore structure between proximal and distal talus result in slight velocity contrast between these two zones as shown in the figure 1.14. High velocity zone is persistent, fig 1.15, with variable thickness depending on the reef core belonging to respective system tracts. The base of this high velocity zone is located at 23m below the present sea level.

Figure 1.12 shows hat electric and seismic tomograms are comparable. High velocity and resistivity values are indicative of dense recrystallize rock. Karstic zones, karstic horizons and low velocity anomalies are well imaged by both methods. Seismic tomography shows the good lateral continuity and correlation between largely spaced boreholes while ERT shows more details for karstified zones where $V_p$ is overestimated. In upper part of the reef core ERT and seismic tomography are not coherent because of moderate differences in cementation, recrystallization and missing karstic features.

# Résumé CHAPITRE 2

L'exploration sismique constitue une méthode élégante d'imager la subsurface. Les ondes sismiques générées par une source adéquate et se propageant à la surface de la Terre, sont réfractées, réfléchies et transmises. Ces ondes sont enregistrées par des géophones. L'échelle d'investigation en exploration sismique varie en fonction de l'objectif. Traditionnellement, l'exploration sismique est utilisée dans la recherche d'hydrocarbures. Mais la méthode sismique s'applique également à la proche surface. Les principes de base de la méthode sismique appliquée aux investigations superficielles sont similaires à ceux de l'exploration sismique pétrolière.

Pour un milieu isotrope, l'équation d'onde décrit la propagation de l'onde sismique dans la Terre. Par ailleurs l'équation d'onde est également utilisée dans la modélisation et l'inversion. L'équation d'onde sismique est basée sur certaines hypothèses concernant l'élasticité du déplacement etc. L'équation d'onde sismique est dérivée de la loi d'Hooke combinée à la deuxième loi de Newton. La propagation de l'onde sismique dépend de la densité ainsi que des paramètres élastiques de Lamé. En présence d'anisotropie sismique on observe un changement dans le comportement de la propagation sismique. Le cas le plus simple d'anisotropie sismique se rencontre dans l'isotropie transverse (TI), possédant un unique axe de symétrie radial. Le milieu anisotrope d'un point de vue sismique est définit par 5 paramètres.

Une onde sismique se propage à travers des couches terrestres présentant des propriétés physiques différentes, les ondes incidentes sont partitionnées aux interfaces entre deux couches de propriétés différentes. Les conditions aux limites au travers de l'interface décident de la part d'énergie réfléchie et transmise. La résolution sismique, spatiale et temporelle, détermine la manière dont deux objets très proches peuvent être distingués l'un de l'autre. Le seuil de résolution temporelle se situe entre le quart et le huitième de la longueur d'onde dominante. L'absence d'une résolution verticale suffisante va donner lieu à des interférences ayant pour effet de fusionner deux couches très peu espacées en une couche unique. La résolution spatiale est définie quant à elle par la première zone de Fresnel. La résolution sismique dépend principalement de la fréquence centrale, de la largeur du spectre et de la géométrie d'acquisition. La résolution sismique peut se voir améliorée par différents types de traitements complémentaires. La vitesse sismique est influencée par de nombreux paramètres du milieu comme sa lithologie, sa porosité, son âge, la profondeur d'enfouissement, la température et la pression de pore, etc.

Il existe différents types de d'acquisition sismique. Les campagnes de sismique réflexion et réfraction sont réalisées à différentes échelles d'investigation et dans des buts variés. En sismique réfraction on s'intéresse exclusivement aux ondes sismiques réfractées : les résultats principaux de ce type de mesure concernent la détermination de l'épaisseur de la couche altérée, sa vitesse ainsi que la profondeur du substrat rocheux. Ces informations seront ultérieurement utilisées en vue de déterminer la correction statique.

La sismique réflexion s'intéresse à l'énergie sismique réfléchie par les différentes couches de la subsurface. Cette méthode est largement employée dans l'exploration des réservoirs pétroliers. La sismique réflexion s'utilise également pour des investigations superficielles. Différentes géométries d'acquisition sont employées.

Le dimensionnement est un autre aspect important dans l'exploration sismique. Les données sismiques peuvent s'acquérir en 2D ou 3D. La géométrie d'acquisition pour des données 2D est peu chère et flexible comparée à celle nécessitée pour les données 3D. Néanmoins, les don-

nées 3D offrent d'avantage d'informations et facilitent certaines phases du traitement du signal comme la migration 3D. L'interprétation 3D aide à la compréhension de la véritable géométrie des structures de subsurface, leur extension verticale et horizontale ainsi que leur orientation. Enfin, ces données peuvent être analysées dans toutes les directions et quelque soit l'intervalle temps/profondeur.

# Chapitre 2

# Exploration Seismology-Basic Concepts

The basic ingredients of exploration seismology are source of energy, geophones and recording unit. Seismic energy, based on objective and other considerations, is produce by dynamite, vibrator, sledge hammer etc. These waves travels through the underlying earth layers and at different interfaces, due to change in lithology, density and other physical parameter, partitioned and this energy either reflects, refract and transmit in the earth in different directions. Depending on the survey objectives different acquisition geometries are planned for an efficient data acquisition. Dimensionality is another important factor for seismic data acquisition and recording. 2D and 3D seismic surveys, reflection or refraction, are acquired for a range of objectives.

During the seismic recording not only the signals but different noises are also recorded. Signal term applies to the waveform of interest and all the unwanted signals are termed as noises. These noises are of different origin. The common noises are due to air waves, Rayleigh waves, other waves recorded at the time of recording such as traffic noises, noises recorded due to interference of power line etc. These noises are grouped into coherent and random noise. Different noise removal techniques are applied to get rid of them including filtering, muting and stacking.

Seismic sources are of important consideration for seismic energy generation. Different energy sources are used ranging from dynamite to sledge hammer. Seismic energy sources are broadly divided into impulsive and non impulsive categories. According to(R.E.Sheriff. & L.P.Geldart., 2001) an ideal source should have following characteristics (1) enough powerful so that energy can be detected after travelling large distance, (2) higher frequencies, (3) repeatable and does not create too much noise. Impulsive source energy comprised of explosive material used in boreholes. For borehole explosive source charge size and depth at which it is ignited is extremely important. Normally for land acquisition borehole charge is placed below the base of weathering layer so that energy can propagate rapidly and minimum loss of energy happens. Different impulsive sources for surface such as, thumper or weight dropper, land air gun and sledge hammer etc, are developed some of which are obsolete but other are still in use. Vibroseis is non impulsive controlled energy source that generates the waves of required frequencies, up-sweep, down-sweep or linear-sweep, for several seconds. When vibroseis is used as an energy source, additional processing is required such as cross-correlation with the sweep. The choice of seismic source depends on the site location and environmental considerations. Seismic energy activated by source creates the ground motion. This ground motion is conver-

ted to electrical energy by geophones and sent into recording equipment which digitize and record this energy in samples preserving the frequency, phase and amplitude of the signals. Exploration seismology is in extensive use for number of applications. This includes petroleum industry, geotechnical, environmental and shallow subsurface domain. Further choice of seismic source, geometry layout, type of survey is heavily site, cost and objective dependent.

## 2.1 Wave Equation

Seismic wave propagation through the earth is a complex phenomena. Seismic wave propagation, modelling and inversion is done by wave equation. Certain assumptions are made to derive a simplified wave equation. The most important condition is elastic displacement through the earth. This assumption may fail in the vicinity of source but works very well away from the source. Seismic wave equation is derived from the stress, strain, their relation to elastic moduli which is describe by Hooke's law and Newton's second law of motion (R.E.Sheriff. & L.P.Geldart., 2001; Throne Lay. & Terry C. Wallace., 1995; Yilmaz, O., 2001).
For a displacement vector $\mathbf{u} = (u, v, w)$ the wave equation for a homogeneous, isotropic elastic media can be written as(Throne Lay. & Terry C. Wallace., 1995) :

$$\rho \ddot{u} = (\lambda + \mu)\nabla\triangle + \mu\nabla^2 \mathbf{u} \tag{2.1}$$

Where $\rho$ is density and $\lambda, \mu$ are Lamé elastic properties.
Where

$$\nabla = \frac{\partial}{\partial x}\mathbf{i} + \frac{\partial}{\partial \mathbf{y}}\mathbf{j} + \frac{\partial}{\partial \mathbf{z}}\mathbf{k} \tag{2.2}$$

$$\triangle = \frac{\partial u}{\partial x} + \frac{\partial v}{\partial y} + \frac{\partial w}{\partial z} \tag{2.3}$$

and the Laplacian operator is

$$\nabla^2 = \frac{\partial}{\partial x^2} + \frac{\partial}{\partial y^2} + \frac{\partial}{\partial z^2} \tag{2.4}$$

The equation 2.1 can be split into P-wave and S-wave. By taking the divergence of equation2.1

$$\nabla.(\rho\ddot{u}) = (\lambda + \mu)\nabla^2\varphi \tag{2.5}$$

Since we are dealing in constant density medium the above equation may be written as(M.A. Slawinski., 2003) :

$$\rho\ddot{\varphi} = (\lambda + 2\mu)\nabla^2\varphi \tag{2.6}$$

and finally it can be written as :

$$\nabla^2\varphi = \frac{1}{V^2}\ddot{\varphi} \tag{2.7}$$

where

$$V = \sqrt{\frac{\lambda + 2\mu}{\rho}} \tag{2.8}$$

S-wave equation is obtained by taking the curl of equation 2.1

$$\nabla \times (\rho\ddot{u}) = (\lambda + 2\mu)\nabla \times \nabla\varphi - \mu\nabla \times \nabla \times \psi \tag{2.9}$$

In the constant density medium the above equation can be written as(M.A. Slawinski., 2003) :

$$\rho\ddot{\psi} = -\mu\nabla \times [\nabla \times \psi] \tag{2.10}$$

Finally above equation may be written as :

$$\nabla^2\psi = \frac{1}{V^2}\ddot{\psi} \tag{2.11}$$

Where

$$V = \sqrt{\frac{\mu}{\rho}} \tag{2.12}$$

Hence it shows that S-wave only respond to change in shape. Propagation of S wave is only limited to the solids.

When seismic source is ignited major part of energy travels through the earth body called body waves while rest of the energy travel along the free surface termed as surface waves. Body waves are further divide into P-wave and S-wave. P-wave travel along the direction of propagation and hence termed as compressional or longitudinal waves. In exploration seismology P-wave is in extensive use.

S-wave travel transverse to the direction of propagation. Hence this wave is also termed as transverse wave. S-wave is making its way in petroleum industry. Since S-wave only can travel through rock matrix. The combination of S-wave and P-wave used for the reservoir characterization and fracture identification etc.

Surface Waves on the other hand are of valuable interest in seismology and for geotechnical purposes. In exploration seismology the surface waves are nuisance. Surface waves are considered as coherent noise and eliminated.

## 2.2   Seismic Anisotropy

A medium is said to be an anisotropic medium if the intrinsic elastic properties change with direction measured at the same point(Winterstein, D. F., 1990). Transversely isotropic term refers to the the medium if elastic properties do not change in any direction perpendicular to the axis of symmetry. Two special case of seismic anisotropy extensively used in petroleum industry are vertical transverse isotropy and horizontal transverse isotropy. Transversely isotropic media has a single axis of rotational symmetry. Seismic signatures depends on the angle between propagation axis and symmetry axis.

In vertical transverse isotropy, figure2.1a, symmetry lies in vertical direction and arises due to the horizontal bedding and fracturing parallel to the bedding plane resulted from some dominant processes like depositional environment and regional stresses. Horizontal transverse isotropy, figure2.1b, or azimuthal anisotropy for which velocity changes laterally arises from tectonic processes and hence resulting from fractures in the direction other than the bedding direction.

For isotropic medium the stiffness matrix is given below. Because matrix is symmetrical therefore only 21 independent constants represent the elastic medium. Moreover for isotropic solid behaviour is completely defined by two independent elastic constants, $\lambda\&\mu$, the stiffness coefficient matrix reduces to the following special form .

$$C = \begin{bmatrix} C_{11} & C_{12} & C_{13} & C_{14} & C_{15} & C_{16} \\ C_{21} & C_{22} & C_{23} & C_{24} & C_{25} & C_{26} \\ C_{31} & C_{32} & C_{33} & C_{34} & C_{35} & C_{36} \\ C_{41} & C_{42} & C_{43} & C_{44} & C_{45} & C_{46} \\ C_{51} & C_{52} & C_{53} & C_{54} & C_{55} & C_{56} \\ C_{61} & C_{62} & C_{63} & C_{64} & C_{65} & C_{66} \end{bmatrix} = \begin{bmatrix} \lambda + 2\mu & \lambda & \lambda & 0 & 0 & 0 \\ \lambda & \lambda + 2\mu & \lambda & 0 & 0 & 0 \\ \lambda & \lambda & \lambda + 2\mu & 0 & 0 & 0 \\ 0 & 0 & 0 & \mu & 0 & 0 \\ 0 & 0 & 0 & 0 & \mu & 0 \\ 0 & 0 & 0 & 0 & 0 & \mu \end{bmatrix}$$

The stiffness tensor in subscript notation is written as

$$c_{ijkl} = \lambda \delta_{ij} \delta_{kl} + \mu(\delta_{ik}\delta_{jl} + \delta_{il}\delta_{jk}) \tag{2.13}$$

The stiffness tensor for transversely isotropic media with a vertical axis of symmetry is

$$C = \begin{bmatrix} C_{11} & C_{11} - 2C_{66} & C_{13} & 0 & 0 & 0 \\ C_{11} - 2C_{66} & C_{11} & C_{13} & 0 & 0 & 0 \\ C_{13} & C_{13} & C_{33} & 0 & 0 & 0 \\ 0 & 0 & 0 & C_{44} & 0 & 0 \\ 0 & 0 & 0 & 0 & C_{44} & 0 \\ 0 & 0 & 0 & 0 & 0 & C_{66} \end{bmatrix}$$

The stiffness tensor for transversely isotropic media with a horizontal axis of symmetry is

$$C = \begin{bmatrix} C_{11} & C_{13} & C_{13} & 0 & 0 & 0 \\ C_{13} & C_{33} & C_{33} - 2C_{44} & 0 & 0 & 0 \\ C_{13} & C_{33} - 2C_{44} & C_{33} & 0 & 0 & 0 \\ 0 & 0 & 0 & C_{44} & 0 & 0 \\ 0 & 0 & 0 & 0 & C_{55} & 0 \\ 0 & 0 & 0 & 0 & 0 & C_{55} \end{bmatrix}$$

Thomsen(Leon Thomsen., 1986) characterized the VTI medium completely in terms of five constants. P-wave, $\alpha_\circ$, and S-wave, $\beta_\circ$, velocities for the VTI medium are :

$$\alpha_\circ = \sqrt{\frac{C_{33}}{\rho}}$$

$$\beta_\circ = \sqrt{\frac{C_{44}}{\rho}} \tag{2.14}$$

Where the degree of anisotropy is defined by the $\varepsilon$, $\gamma$ and $\delta$ by combining the five constants.

$$\varepsilon = \frac{C_{11} - C_{33}}{2C_{33}}$$

$$\delta = \frac{(C_{13} + C44)^2 - (C_{33} - C44)^2}{2C_{33}(C_{33} - C44)}$$

$$\gamma = \frac{C_{66} - C_{44}}{2C_{44}} \tag{2.15}$$

Usually for sedimentary rocks these anisotropic parameters are of same order and have small values ($\ll 1$). Thus VTI medium is characterized by this *weak anisotropy* situation.
The three phase velocities in terms of these constants are written as :

$$
\begin{aligned}
V_P(\theta) &\approx \alpha_\circ(1 + \delta sin^2\theta cos^2\theta + \epsilon sin^4\theta) \\
V_{SV}(\theta) &\approx \beta_\circ(1 + \frac{\alpha_\circ}{\beta_\circ}(\epsilon - \delta)sin^2\theta cos^2\theta) \\
V_{SH}(\theta) &\approx \beta_\circ(1 + \gamma sin^2\theta)
\end{aligned}
\tag{2.16}
$$

Where :
$\theta$=Angle of wave vector relative to $x_3$ axis.
$V_{SV}$=Pseudo shear wave polarized normal to pure shear wave.
$V_{SH}$=Pure shear wave without polarization along symmetric axis.
$V_P$=Pseudo longitudinal wave.



(a)　　　　　　　　　　(b)
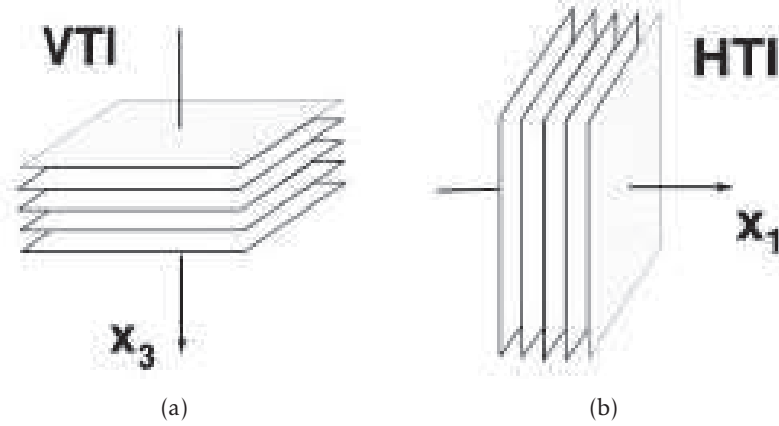
FIGURE 2.1 – a) Vertical transverse isotropy ; b) Horizontal transverse isotropy.

For Thomsen's parameter $\varepsilon = \delta$ a transversely isotropic medium becomes elliptically anisotropic(Vladimir, G. & Ilya, T., 2000), as shown in figure2.2. P-wave slowness surface and group-velocity surface will have an ellipsoidal shape while the SV-wave velocity, being independent of angle, is equal to $V_{so} = \beta_\circ$.
 Anisotropy requires special attention for seismic data processing. This includes the anisotropic velocity analysis, anisotropic NMO and DMO corrections and anisotropic migration.
Practical application of anisotropy in exploration industry includes fractured reservoir detection through share wave splitting and azimuthal variation of amplitude with offset to locate stratigraphic signatures etc.

## 2.3   Seismic Energy Partition at an Interface

When seismic waves travelling downward hit at an interface, boundary between two successive layers characterized by different material properties and hence elastic moduli, it partly reflect and partly transmit (refract) as shown in the figure 2.3. Seismic wave is characterized
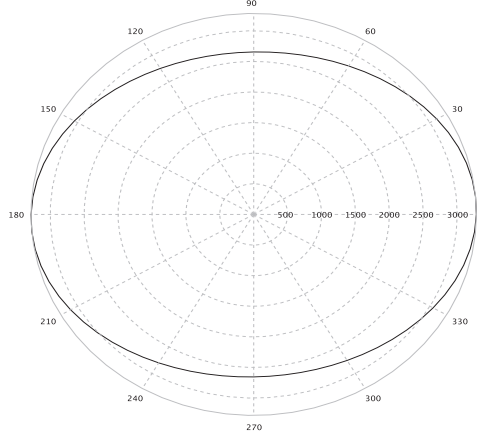
Figure 2.2 – For an elliptically anisotropic medium wavefronts will spread away from a point source in an ellipse rather than circles.

by ray parameter. According to Snell's law this energy partition behaviour is described mathematically as

$$\frac{sin\theta_1}{V_{p_1}} = \frac{sin\theta_2}{V_{p_2}} = \frac{sin\lambda_1}{V_{s_1}} = \frac{sin\lambda_2}{V_{s_2}} = p \qquad (2.17)$$

Where
$\theta_1$ and $\theta_2$ are angles for reflected and transmitted P-waves respectively
$\lambda_1$ and $\lambda_2$ are angles for reflected and transmitted S-waves respectively
$p$ is ray parameter.

Boundary conditions across the interface are very important. Boundary conditions decide the proportion of energy partition for reflection and transmission. Neighbouring points opposite to the interface have different value of normal stresses and at the interface stress field is continuous. Zeoppritz's equation relates the variation of reflection amplitude to the incident amplitude caused by acoustic impedance(R.E.Sheriff. & L.P.Geldart., 2001). Acoustic impedance is defined as

$$Z = \rho V_p \qquad (2.18)$$

Generally harder rocks have higher acoustic impedance. Smaller the acoustic impedance contrast across the interface greater proportion of energy will be transmitted and vice versa. At normal incidence the Zeoppritz's equation for transmission and reflection coefficients in terms of acoustic impedance is written as(R.E.Sheriff. & L.P.Geldart., 2001) :

$$R = \frac{Z_2 - Z_1}{Z_2 + Z_1} = \frac{\rho_2 V_{p2} - \rho_1 V_{p1}}{\rho_2 V_{p2} + \rho_1 V_{p1}} \qquad (2.19)$$

$$T = 1 + R = \frac{2Z_1}{Z_2 + Z_1} = \frac{2\rho_1 V_{p1}}{\rho_2 V_{p2} - \rho_1 V_{p1}} \qquad (2.20)$$
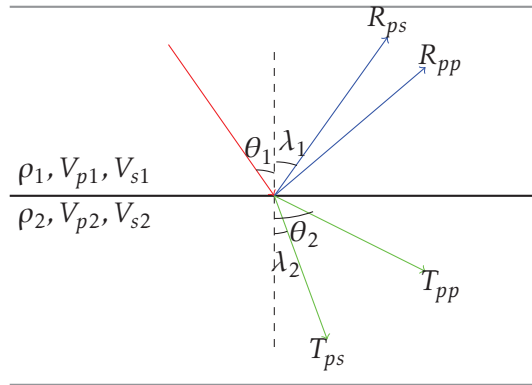
FIGURE 2.3 – Energy partition of an incident P wave shows reflected and refracted P and S waves.

and total energy is :

$$R^2 + T^2 = 1 \tag{2.21}$$

Where $Z_1$ and $Z_2$ are acoustic impedances for incident and refracting medium respectively. A negative value of R represents the phase change of 180°. Normal incidence formulas are valid for slight deviation from the normal ($\theta \leq 15$).

For small incident angles incident wave energy is almost reflected and transmitted as P-wave. As the incident angle increases the more energy is carried by reflected S-waves as compared to the P-aves(R.E.Sheriff. & L.P.Geldart., 2001).

## 2.4   Seismic Resolution

Seismic resolution refers to the fact how much two features can be distinguished and separated in seismic data. Seismic resolution applies both for vertically, vertical or temporal resolution, and horizontally, horizontal or spatial resolution. Seismic resolution is mainly controlled by spectral bandwidth.

### 2.4.1   Temporal Resolution

Vertical resolution helps to clearly distinguish two closely spaced reflectors on seismic section. The vertical resolution mainly controlled by seismic wavelet, its frequency content and bandwidth and impedance contrast. As higher frequencies are dissipated with increasing depth and increase in velocity so vertical resolution decreases with depth. The threshold of vertical resolution is between one-quarter and one-eighth of the dominant wavelength of the pulse(R.E.Sheriff. & L.P.Geldart., 2001). The dominant wavelength of the seismic pulse is $\lambda = v/f$, where $f$ and $v$ is dominant frequency and velocity respectively.

Thin bed tuning phenomena is observed due to constructive interference from the top and base of a reservoir when a bed or pinch out of one quarter thickness of the dominant wavelength embedded in a medium of different properties. Recording parameters and processing strategy, such as filtering, static correction and residual correction etc, also enhance the vertical resolution. For example deconvolution tries to enhance the vertical resolution by compressing the wavelet.

### 2.4.2 Spatial Resolution

The yardstick for horizontal resolution is Fresnel zone(Yilmaz, O., 2001). Lateral resolution is the recognition of two closely separated reflection points. Fresnel zone, figure 2.4, is defined as

*The subsurface area which reflects the seismic energy that arrives the earth surface within time delay equal to half of the dominant time period.*
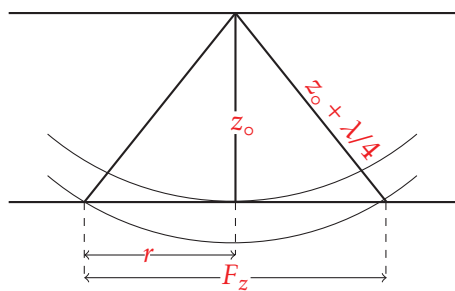


FIGURE 2.4 – 2D illustration of First Fresnel Zone.

The radius of Fresnel zone is given by

$$F_z = 2r = \sqrt{\frac{z_\circ \lambda}{2}} = \frac{v}{2}\sqrt{\frac{t_\circ}{f}} \qquad (2.22)$$

Where

$F_z$=First Fresnel Zone.
$z_\circ$=Depth of reflecting interface.
$t_\circ$=Two way travel time.
$f$=Dominant frequency.
$\lambda$=Dominant wavelength.

Two points that will be in this zone are generally indistinguishable at earth's surface. The shape and size of Fresnel zone not only depends on frequency but also on source-receiver position, velocity, dip, depth and curvature of reflecting zone. Smaller the Fresnel zone higher will be lateral resolution and vice versa (Jan, B. & Helbig, K., 1998),(Yilmaz, O., 2001).
Migration increases the spatial resolution, collapsing the diffractions, by focusing the seismic reflection energy into corresponding smaller Fresnel zones.

## 2.5 Seismic Velocity

Seismic velocity is a very important entity that plays role in seismic data processing, modelling and migration. Therefore understanding of seismic velocity is crucial. P-wave and S-wave

velocity is defined as

$$V_P = \sqrt{\frac{\lambda + 2\mu}{\rho}} = \sqrt{\frac{k + \frac{4}{3}\mu}{\rho}} \tag{2.23}$$

$$V_S = \sqrt{\frac{\mu}{\rho}} \tag{2.24}$$

Where
$k$=Bulk modulus
$\mu$=Shear modulus.
$\rho$=Density.
Apart from impedance contrast there are many factors that affect the seismic velocities. Seismic velocity is influenced by individual and combined factors. These factors include (R.E.Sheriff. & L.P.Geldart., 2001).

– Lithology
Lithology is very important factor that affect velocity. Different lithologies might have overlapping velocity ranges. This is due to differential compaction, age and porosity etc. So velocity solely not sufficient for lithology discrimination. Generally carbonate rocks have higher velocities than sand and shale.

– Porosity
Porosity is far most important factor affecting the velocity. The time average equation relating the velocity to porosity developed by Wyllie, Gregory and Gardner is

$$\frac{1}{V} = \phi\frac{1}{V_f} + (1 - \phi)\frac{1}{V_m} \tag{2.25}$$

This empirical equation does not take into account the structure of rock matrix, pores connectivity, cementation and burial history that might affect the velocity(R.E.Sheriff. & L.P.Geldart., 2001). This might give sometime poor misfit and erroneous velocity results in heterogeneous lithological environment.

– Burial depth and Pressure
Velocity increase with depth is coeval with increase in burial depth or overburden pressure. Due to increase in burial depth and pressure subsequent compaction result in porosity reduction, expulsion of pore fluids, especially in shale and clastic sediments. When the differential pressure remains constant velocity also remains constant even though overburden and fluid pressure change.

– Pore filling interstitial fluid
The pore spaces in porous rocks are filled with varity of fluid including water, gas, oil etc. This change the elastic moduli of the host rock and hence result in change in P-wave velocity and reflection strength. S-waves can not travel through the liquids. These changes are sometime evident by horizontal reflection strength on the time section such as bright and dim spots. The P to S wave ratio is also in use to distinguish the fluid filling the pore spaces.

– Age and Temperature
It is well proven fact that velocity increases in older rocks, this is due to longer burial

history, compaction and porosity reduction. Velocity decreases slightly with the temperature gradient for dry rocks but it varies considerably for heavy oil, tar and rocks saturated with these fluids(Wang, Z. & Nur, A., 1988).

Gardner's relation(Gardner et al., 1974) gives an analytical relationship between velocity and density which is expressed mathematically as

$$\rho = aV^{1/4} \tag{2.26}$$

Where a=0.31 when velocity is in m/s.

The near surface layer has generally very low velocity because of unconsolidated material. Low velocity layer has considerable velocity changes where seasonal changes are in action. For example areas with swear climatic condition will have different velocity distribution in different seasons due to pore fluid freezing and vice versa. Similarly in subarctic region near surface velocity changes according to climate(R.E.Sheriff. & L.P.Geldart., 2001).

## 2.6   Seismic Refraction Survey

Seismic refraction method is used to characterize the shallow earth layers, upto few meters. This include shallow layer depth, its velocity, geometry of the layer, its irregularity and contact with the underlying bed rock. Seismic refraction survey is not only a separate method but it also used to calculate the static correction for seismic reflection data and near surface velocity distribution. Seismic refraction method has long been in use for civil engineering, geotechnical applications and characterizing the aquifers. Seismic refraction methods are also in use to examine soil conditions by estimating the elastic constants.

Considering two layer case if the velocity of the shallow layer is less then the velocity of underlying rock then a wave attains a particular angle of incidence, critical angle, it result in critical refracted ray that travels along the interface with higher velocity. This situation is mathematically described by Snell's law, which is written as

$$\frac{sin\theta_c}{v_1} = \frac{sin90}{v_2} = \frac{1}{v_2} \tag{2.27}$$

The recorded first arrivals, either direct arrivals or refracted waves, are used for seismic refraction method. The seismic refraction acquisition is performed along a line by keeping the objective that recorded waves from the target layer are actually first arrivals at least for half of the line. The profile line length for refraction survey depends on the velocity distribution and thickness of the weathered layers.

Seismic refraction acquisition line length, geophone-shot interval and choice of source depends on the survey objective and target depth. Although seismic refraction profiles along the line are mostly used but other acquisition geometries exist for specific purposes. Reverse profile, split profile(Johnson., 1976) and single-ended (Cunningham.A. B., 1974) profile methods are commonly used.

Once seismic refraction data is acquired the next step is first arrival picking. Care must be taken for first arrivals picking by avoiding the direct arrivals and other noises. After first arrivals picking there exist different interpretation techniques based on picked first arrivals to deduce the required information. There are plenty of methods proposed by different authors to use the information of first arrival and acquire maximum information. These methods include intercept-time, delay-time, plus-minus method of Hagedoorn, ABC method, reciprocal

method and generalised reciprocal method among others(Mike Cox., 1999). Apart from these mere interpretation methods other techniques are proposed like tomography, inversion and hybrid methods.

There are certain difficulties and inherent problem of seismic refraction. This include the detection of hidden layers, blind zone, velocity inversion and most importantly an accurate first arrival picking. Steep dip and horizontal velocity gradient is another challenge for the accuracy of these aforementioned interpretation techniques. Depth conversion or depth determination by these interpretation techniques is another problem(Mike Cox., 1999).

## 2.7 Seismic Reflection Survey

Seismic reflection surveys are used to image the deeper subsurface. In petroleum industry these surveys are used to locate the structural and stratigraphic traps. Different acquisition geometries are applied for 2D seismic survey. Normally data acquisition is performed along a straight line. The acquisition geometries, figure 2.5, are either split-spread and the single-ended spread. Initially for each shot the seismic traces recorded for all the active gephones termed as shot gather.
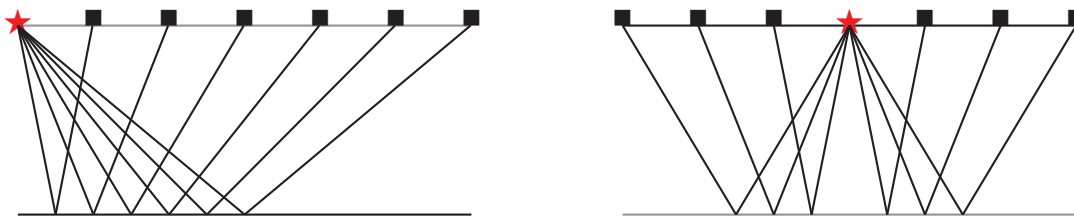


Figure 2.5 – Different acquisition geometries : single-ended(left) and split-spread (right). Where red star and black boxes represent source and receivers respectively.

Seismic trace is characterized by shot position, receiver position and subsurface reflection point. Normally for the horizontal layers the depth point is in between source and receiver and this point is called common depth point (CDP) or common midpoint (CMP), figure 2.6. Seismic survey are acquired and sorted into common depth or common mid point gathers. This means that same subsurface point is recorded for number of receivers and for numerous energy sources. Common depth point technique is very useful for seismic data processing. Because seismic signals are weak and noisy, the stacking process will not only enhance the strength of seismic signal but also result in cancellation of random noises that are out of phase for the same subsurface reflection point but recorded at different offsets.

Further CDP gather is also used for velocity analysis that determines the velocity for NMO correction. By NMO correction traces become equivalent to zero offset traces. For dipping interface common mid point and common depth point are not the same but dip move out (DMO) does the same job as normal move out (NMO) by also taking into account the dip factor. Hence even in dipping layer case the stacking will produce optimum results by improved S/N ratio stack section.

With the advent of technology sophisticated seismic recording instrument is developed. 3D seismic reflection surveys are becoming more and more important. For near surface reflection surveys similar acquisition techniques are being used.

44
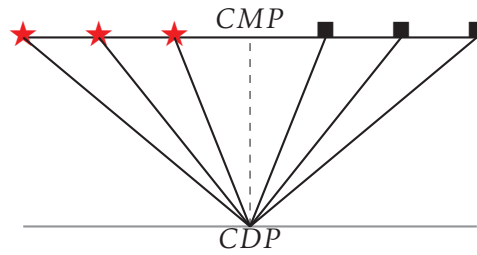
FIGURE 2.6 – Common mid point reflection profiling. Where red stars and black boxes represent sources and receivers respectively



(a)                                                                                    (b)
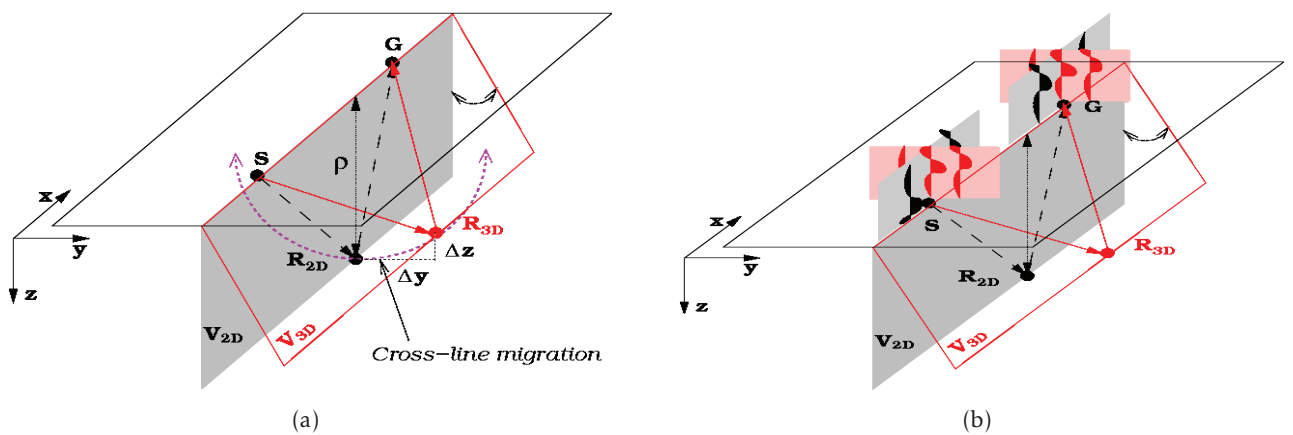
FIGURE 2.7 – (a) 2D versus 3D imaging of an out of plane diffractor. (b) 3D imaging result in exact imaging of position and propagation direction of the diffractor (after(Biondi., 2007)).

## 2.8  3D Seismic Survey

3D seismic surveys are aimed to acquire higher resolution data by recording the seismic waves representing the true 3D subsurface sampling rather than an area in a vertical plane. CMP gathers in 3D survey operate on an areal rather than linear distribution of shots and receivers. Seismic 3D surveys are common practice in petroleum industry but 3D shallow surveys are also becoming common as proposed by (Büker, F. et al., 1998) and then (Büker, F. et al., 2000).

3D seismic survey not only result in high quality data but also used in processing and 3D migration which is otherwise not possible in 2D surveys. The assumption made that for 2D survey earth is cylindrical with its axis orthogonal to the survey, in case when this assumption is true the 2D interpretative image will be true representation of 2D vertical section but if this assumption goes wrong, the interpretation image will produce distorted facts. Figure2.7(a) shows the discrepancy produced in 2D seismic interpretation while imaging 3D structure. The error will produce due to shape and position of 3D structure. The point diffractor, $R_{3D}$, is out of plane for 2D acquisition. The 2D migration will result in wrong positioning, $R_{2D}$, of the diffractor $R_{3D}$. Even 3D migration of this single reflected 2D line will produce ambiguity of diffractor position along the red semicircular curve perpendicular to the acquisition direction.

45

In 2D imaging the diffractor positioning error has both the cross-line direction component, $\Delta y$, and depth component, $\Delta z$. The analytical expression is independent of velocity and depends only on the apparent depth, $\Delta z$, of the reflector :

$$\Delta y + (d_r - \Delta z)^2 = d_r^2 \tag{2.28}$$

Hence the imaging of 3D data in case of constant velocity can be accomplished by imaging along the 2D lines followed by the cross-line migration. In case of variation in propagation velocity this aforementioned decomposition of 3D imaging will fail and proper 3D imaging and migration will be required as shown in figure 2.7(b).

3D seismic data also present some new challenges including higher dimensionality, data handling, right technique of processing and visualization to obtain an accurate image from optimization of resource, time and accuracy, are among others. Spatial sampling irregularity is another challenge that might create amplitude distortion that is included as coherent artefact in the image and will result in erroneous interpretation of seismic attributes and rock physical parameters.

3D seismic imaging not only helps in imaging 3D structure but also produce additional information concerning to 1D and 2D geological structures. 3D surveys bring wealth of information. Data can be visualized and extracted along time slices, horizons or in arbitrary directions. This will help to know the position and orientation of the particular features in 3D data. Furthermore seismic attributes are calculated from 3D data to better visualize, access and delineate the features of interest. Another important feature is extra information about rock properties and dimensional variation in properties such as velocity and anisotropy are better understood and answered by 3D. Success of 3D imaging also gave birth to time lapse seismic surveys for reservoir monitoring.

## 2.9  Near surface Seismology

Near surface seismology refers to the exploration of shallow part of the earth. This varies from less than 10 m to few hundred meters. Near surface seismology is rapidly evolving and growing field. Near surface seismology is being applied for numerous applications such as
  – Engineering and geotechnical
  – Environmental
  – Ground water
  – Mining

Near surface seismology face special challenges both technical and non-technical. Since near surface is composed of unconsolidated heterogeneous material that will create noises. These noises will have dispersive nature and result in noisy seismic section. The most significant difference between near surface and petroleum seismology is due to change of mechanical properties of medium under investigation. Due to near surface heterogeneities Rayleigh waves are very prominent and for 2D seismic reflection outside of 2D plane will severely affect the quality of acquired seismic data that will be difficult to process with traditional approach. For shallow surveys high horizontal and vertical resolution is another requirement which is not always achievable due to number of factors. Near surface moisture content variation might result in drastic change in recorded data quality notably change in amplitude and appearing and disappearing of certain events (Jefferson et al., 1998). Due to extreme velocity gradients conventional NMO fails and produce unsatisfactory results. Segregated processing of CMP

data will result in higher S/N ratio data(Miller, R. D. & Xia, J., 1998).
In non technical issues deployment of acquisition crew, logistic and cost are of big concern. Environmental consideration is another big issue. Because near surface seismology is often applied in the residential or populated area so it is difficult to address the community concern and use of a powerful explosive source.

## Résumé CHAPITRE 3

L'acquisition sismique a plusieurs domaines d'application. Le degré de réussite varie d'acquisition en acquisition et en fonction des objectifs. Ce degré de réussite dépend de la localisation du site, du aux caractéristiques et à la réponse de la proche sub-surface. L'exploration sismique en proche sub-surface est rendue difficile par un certain nombre de facteurs parmi lesquels la couche superficielle à faible vitesse, les hétérogénéités, l'aliasing spatial des ondes de Rayleigh et le bruit de la source jouent un grand rôle.

En cherchant à éviter l'aliasing spatial, en améliorant le rapport signal sur bruit par le moyennage et la couverture élevée des données, le coût de l'acquisition sismique a augmenter. Dans l'acquisition de données de sismique superficielle les principales limitations concernent la conception d'une géométrie d'acquisition efficace, la logistique et les coûts résultants. Le choix de la source d'énergie sismique est également restreint par les considérations environnementales et économiques. Dans le cas 3D la couverture des mesures n'est pas aussi régulière que dans le cas 2D et pour des raisons pratiques, la couverture 3D est considérée comme équivalente à la moitié de la couverture 2D. La distribution de couverture dans le cas 3D varie avec l'offset, le plus grand pourcentage étant réservé aux offsets lointains, les plus petits aux offsets proches.

Pour cette étude, différentes acquisitions sismiques ont été conduites en sismique réflexion et réfraction. L'acquisition de sismique réflexion en 3D est le principal objectif de cette campagne d'acquisition. De plus, les acquisitions 3D de sismique réfraction sont effectuées sur les mêmes blocs de source et blocs de récepteurs utilisés dans la sismique réflexion 3D. Le profil sismique 2D est situé sur la diagonale du bloc 3D. Les acquisitions en sismique réfraction sont utilisées afin de déterminer la correction statique par la technique d'inversion des délais, basée sur les premières arrivées. Les variations topographiques sont régulières dans le secteur de mesures.

Le profil sismique vertical est enregistré dans le puit MC16. Le modèle de vitesse d'intervalle est construit à partir du pointé des premières arrivées. Il est utilisé pour la migration et la génération de sismogrammes synthétiques.

**Chapitre** $3$

# Seismic Data Acquisition

## 3.1    Overview of Seismic Data Acquisition

Seismic reflection surveys, 2D and 3D, for shallow investigation are successfully applied for broad range of objectives such as to detect fracture zones, mapping of water aquifers, glacial study, landslide and slope stability. The degree of success varies from survey to survey based on objective and site geology. Seismic reflection survey for shallow investigation is somewhat difficult and cumbersome task due to many factors including the near surface low velocity layer, heterogeneities and source generated noises among others. High frequency for shallow survey is of great importance. In case of dominant low frequency interference between first arrivals and reflection wavelet occurs at all offsets. Other annoying factors like spatial aliasing of ground rolls, interference of air coupled waves etc will create artefacts (Steeples, D. W. & Miller, R. D., 1998). Avoiding spatial aliasing, averaging and requirement of high fold data to improve S/N ratio will increases survey cost. But on the other hand shallow seismic survey deliver better subsurface imaging, detection of small scale objects and characterization of shallow subsurface for geological, environmental and geotechnical purposes. Seismic reflection and refraction surveys are normally composed of data acquisition, processing and interpretation. Although seismic processing helps to obtain an optimal subsurface picture by suppressing noises, by applying filtering, muting, static and dynamic corrections and finally migration but certain acquisition parameters setting will result in relatively good quality and adequately sampled data. Seismic interpretation results will depend on acquisition strategy in general and processing techniques in particular.

For shallow seismic data acquisition main limitations are efficient field geometry, logistics and resulting cost. Selection of seismic energy source is site dependent. There is fair range of seismic energy sources. For shallow seismic surveys dynamite is not commonly used because of environmental and cost considerations. For small scale land seismic surveys different energy sources are developed and successfully employed. Target depth, frequency content, amount of energy and cost decide the fate of seismic survey. For 3D surveys cost, portability and acquisition time are of major concern.

Subsurface sampling is another important factor that conveys information about aliasing. Offsets sampling in a CMP gather for 2D data reflects the effective acquisition geometry. According

to(Yilmaz, O., 2001) to avoid aliasing the relation between signal sampling and bin size is :

$$b \leq \frac{V_{min}}{4 f_{max} sin \xi_{max}} \tag{3.1}$$

Where $b$, $V_{min}$, $f_{max}$ and $\xi_{max}$ is subsurface CDP bin size, minimum velocity of the target reflector, maximum frequency and maximum dip to be imaged respectively. Generally for higher frequency signals smaller bin size is required for appropriate spatial sampling(Vermeer, G. J. O., 1999). Fold and offset distribution is also very important. For different shot-receiver pairs recorded traces have different azimuths and offsets but share the same subsurface position. Due to range of offsets and azimuths random noise incorporated in these signals is cancelled after summation owing to out of phase. Fold represents the total number of traces reflected from the same subsurface point in 2D case and belongs to same bin for 3D case. Fold for 2D case has a regular offset distribution containing equal number of near, mid and far offsets. According to(Chaouch, A. & Mari, J. L., 2006) fold contribution for 3D case varies with offset, highest fold percentage is for far offsets while lowest for near offsets. Shallower events will be only on a portion of near offsets traces hence stacking will produce low fold stack for shallower events. For 3D fold distribution is lower as compared to 2D therefore for practical reasons 3D fold is considered as one half of the 2D fold.

## 3.2 Seismic Field Data Acquisition

To study the Campos site, 2D and 3D reflection surveys are carried out. Furthermore refraction surveys are conducted for the receiver and source block of 3D reflection survey. For all type of surveys 24 bit recording units, Geometrics and DMT, are used. Single component geophones of 14Hz frequency are used. A constant gain of 18db is applied. Sledge hammer is used as an energy source for all types of surveys. The recording parameters for 2D reflection line are given in the table3.1. Figure3.1 shows the acquisition layout of 2D line as the function

Table 3.1 – 2D seismic Line acquisition and recording parameters

| | |
|---|---|
| Total number of receiver lines | 1 |
| Total number of receivers | 116 |
| Receiver line length | 115m |
| Total number of source lines | 1 |
| Total number of sources | 115 |
| Source line length | 114m |
| Sampling Interval | 0.250 ms |
| Recordring Length | 0.5s |

of the topography. The acquisition and recording parameters for 3D reflection block, refraction of receiver block and refraction of source block are given in the table 3.2, table3.3 and table3.4 respectively. The acquisition geometry for 3D reflection block is shown in the figure3.2. 2D seismic line is on the diagonal of the 3D reflection block. Further refraction surveys are carried out for the receiver and source block. Theses refraction surveys are aimed to determine

the static correction of the sources and receivers, termed as source block and receiver block respectively, used for3D reflection survey blocks. Figure 3.3(a) and figure 3.3(b) show the acquisition geometry for receiver block refraction survey and topography respectively. Figure 3.4(a) and figure 3.4(b) show the acquisition geometry for source block refraction survey and topography respectively. The topography over the survey area is smooth, varies upto 200cm, evident from 2D line topography profile, source and receiver blocks topography images.
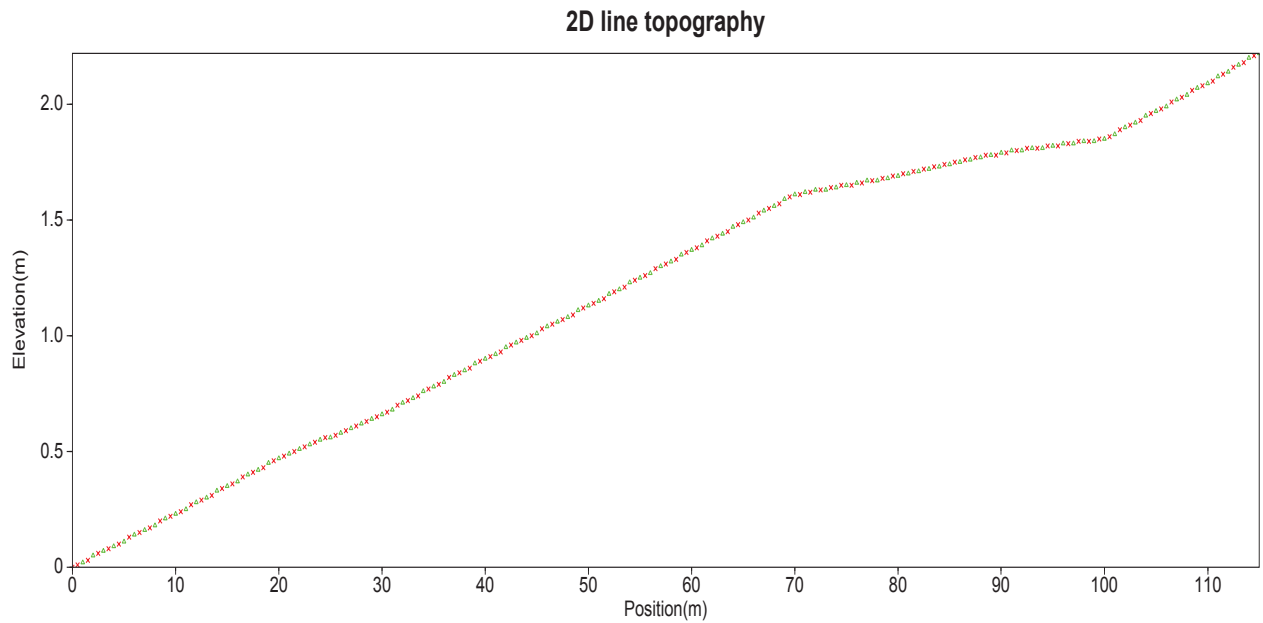


FIGURE 3.1 – 2D Line acquisition layout as a function of topography (green and red colors indicate the receiver and source respectively).

**Reflection Acquisition Layout**
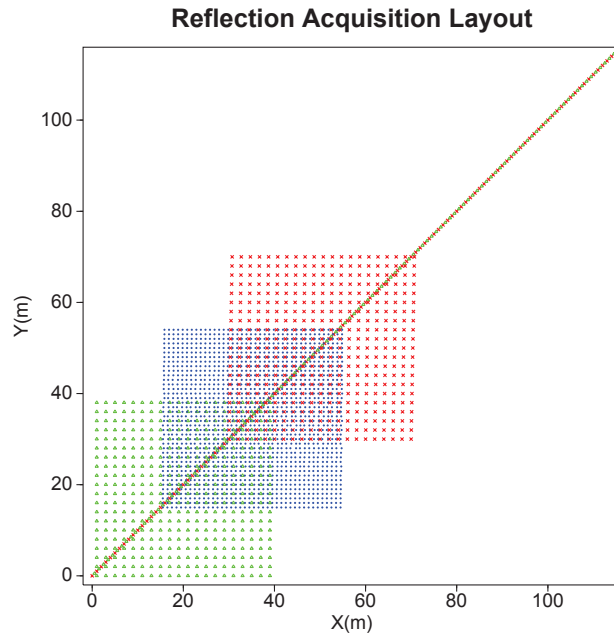


Figure 3.2 – Seismic Reflection Geometry, 2D and 3D, (green color corresponds to the receivers while red and blue colors indicate source and CMP respectively).

Table 3.2 – Acquisition and recording parameters for 3D reflection block

| | |
|---|---|
| Total receiver lines | 20 |
| Total receivers per line | 20 |
| Receiver line length | 38m |
| Total receivers | 400 |
| In-line distance | 2m |
| Cross-line distance | 2m |
| Total source lines | 21 |
| Total sources per line | 21 |
| Source line length | 40m |
| Total shots | 441 |
| In-line distance | 2m |
| Cross-line distance | 2m |
| Sampling Interval | 0.25ms |
| Recording Length | 512ms |
| Recording delay time | 40ms |

(a)                                                    (b)
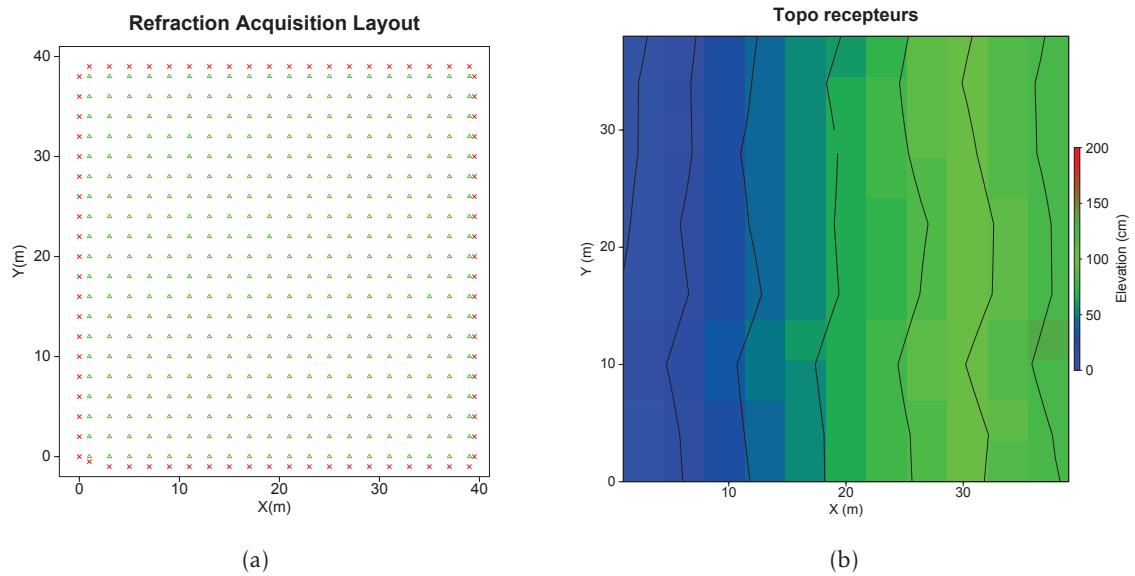
Figure 3.3 – (a) Refraction geometry for receiver block (where green and red color corresponds to the receivers and sources respectively).(b) Topography of the receiver block.

Table 3.3 – Acquisition and recording parameters for the refraction of receiver block

| | |
|---|---|
| Total receiver lines | 20 |
| Total receivers per line | 20 |
| Receiver line length | 38m |
| Total receivers | 400 |
| Receiver line length | 38m |
| In-line distance | 2m |
| Cross-line distance | 2m |
| Total source lines | 4 |
| Total sources per line | 20 |
| Source line length | 40m |
| Total shots | 80 |
| Sampling Interval | 0.25ms |
| Recording Length | 512ms |
| Recording delay time | 40ms |

(a)                                                    (b)
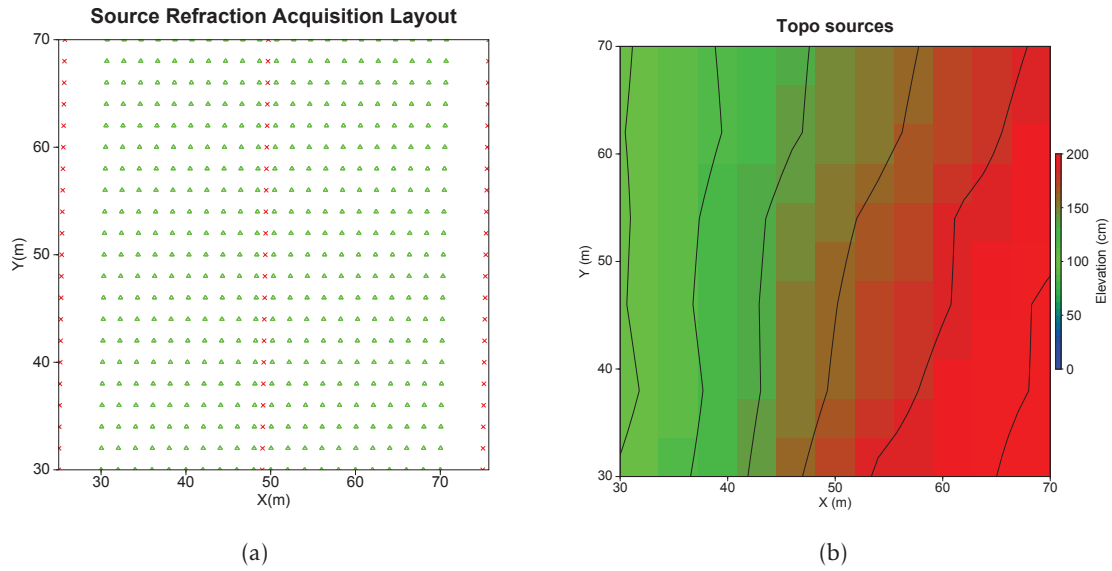
FIGURE 3.4 – (a) Refraction geometry for source block (where green and red color corresponds to the receivers and sources respectively). (b) Topography of the source block.

TABLE 3.4 – Acquisition and recording parameters for the refraction of source block

| | |
|---|---|
| Total number of receiver lines | 21 |
| Total number of receivers | 441 |
| Receiver line length | 45m |
| Total number of source lines | 3 |
| Total number of sources | 63 |
| Source line length | 41m |
| Sampling Interval | 0.250 ms |
| Recordring Length | 0.5s |

## 3.3 Data Binning

Binning is the process of assigning the traces, for 3D reflection surveys, to specific bin according to midpoint between source and receiver. It thus helps in sorting the data, from shot gather to cdp gather and vice versa, and facilitate for further seismic processing by ensuring the surface consistency. Binning is performed by the superposition of regular grids onto the midpoint plane. All the traces belonging to a specific bin are assigned the effective midpoint coordinates equal to the coordinates of central point of the cell. The nominal bin size is determined on the basis of acquisition parameters and may vary in in-line and cross-line directions. For a regular 3D acquisition geometry nominal fold represents the total traces that belong to each bin. For this study a square of 1m dimension is used for binning. So all the traces from 441 sources are assigned in 1600 bins. Figure3.5(a) shows the binning of the 3D reflection block and Figure 3.5(b) is the CMP fold after binning.



(a)                                                      (b)
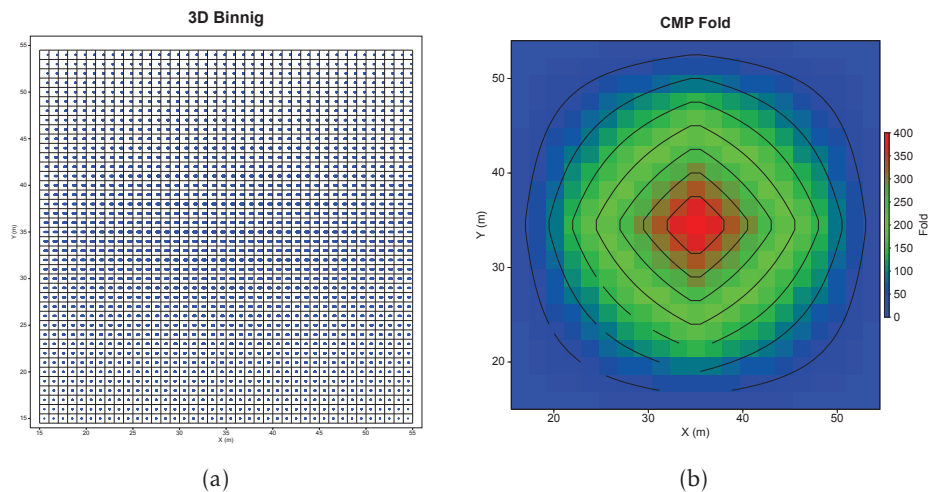
FIGURE 3.5 – (a)Binning for 3D reflection block.(b) CMP fold for 3D reflection block

## 3.4 Vertical Seismic Profiling

Vertical seismic profile is an important and perhaps most valuable tool in borehole seismic for wavefield recording at seismic frequency bandwidth. VSP provides the travel time from surface source to the receivers in the well. Normally for classical VSP, source is located at or near the surface and sonde is deployed in the borehole. There are different acquisition geometries for VSP including zero-offset, near offset and far offset. Other source-receivers configuration includes cross-well and reverse VSP. In cross-well VSP, energy source and sonde are deployed in different wells while for the reverse VSP, energy sources are in the well and recording instrument is on the surface(Ronald et al., 1996). Both up-going and down-going waves are recorded in VSP as compared to surface seismic reflection surveys and other borehole measurements. Figure3.6 shows up and down going raypaths and depth travel-time diagram for near offset VSP. These events are processed and isolated to get the final VSP stack, corridor stack, that can be directly tied to the surface seismic.
Application of VSP includes the exact location of reflectors thus calibration of the seismic

events to the geology, seismic to well tie, differentiation between the primary reflection events and multiples, reflection properties of different events, high resolution imaging in the vicinity of the well and velocity information of the subsurface among the others.



(A)

(B)
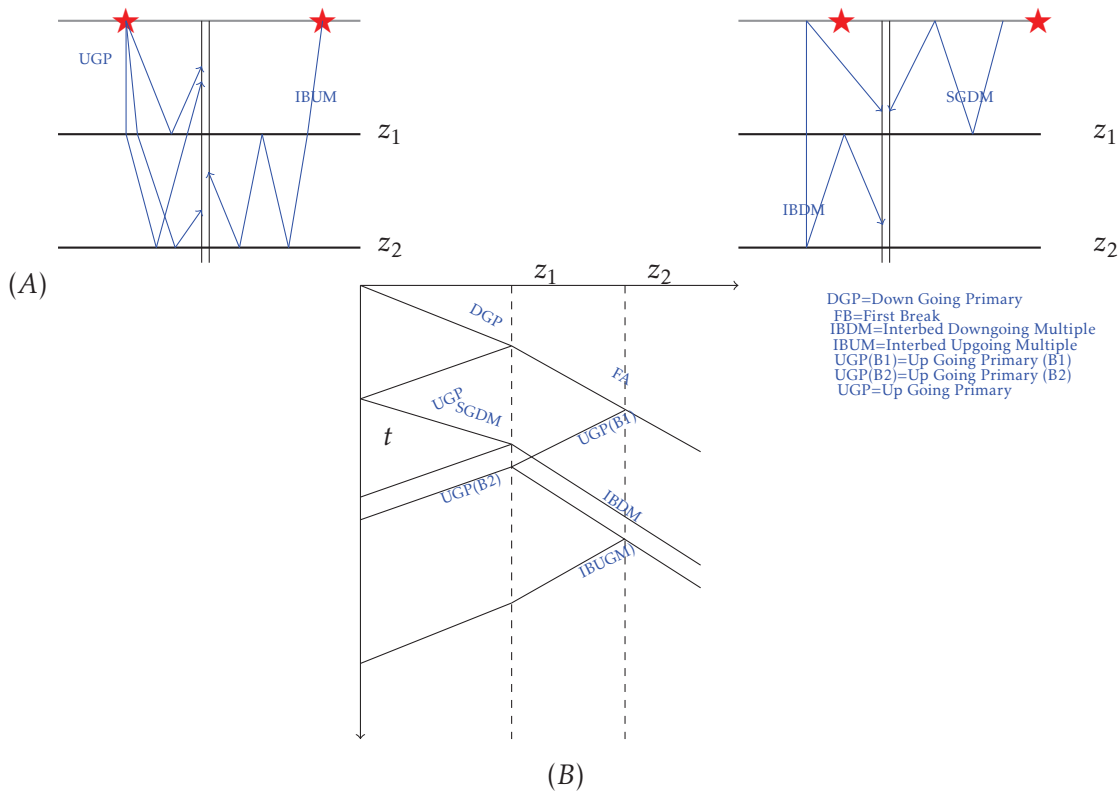
FIGURE 3.6 – A). Up-going and down-going raypaths for a near-offset VSP.(B) Depth travel-time diagram. The surface generated down-going multiples will be recorded at all geophones whereas inter-bedded multiples generated between layers $z_1$ and $z_2$ will only be recorded for the geophones below the layer $z_1$. Up-going reflections from layer $z_1$ will be recorded only for geophones located above layer $z_1$. Geophones located at interface will record the up-going and down-going primaries. First break curve represents the down-going primaries except head waves. Down-going multiple appear parallel to the down-going primary. An up-going primary(B1) will generate a reflected down-going multiple at an interface $z_1$ that consequently might generate an inter-bedded up-going multiple at interface$z_2$ (after (Hinds et al., 1989).)

For this study near-offset VSP is acquired for borehole MC16. The source offset is 2m and recording instrument (sonde) is clamped every 50cm in the well. Figure3.7(left) is the depth-traveltime seismogram, vertical component, acquired for this field study. In this section down-going and up-going waves are clearly distinguishable. First arrivals are picked, black curve, to estimate the subsurface velocity. Sudden fall of first arrival at 2200cm depth is due to presence of cavity in the borehole, that is also evident from the average velocity profile (black dots) in the figure3.7(center). By observing slope of the best fit lines of first arrivals at different levels, the interval velocity model of the subsurface is constructed as shown in the figure3.7(right).

The lower part of the figure is compared with the sonic log value that globally show the same trend. From this interval velocity profile the average velocity is calculated and superposed in the middle figure, red curve. It shows the very good fit that is the evidence of the accuracy of interval velocity model.

**MC16 hz offset 2m component Z**

**MC16 average velocity**

**MC16 interval velocity**
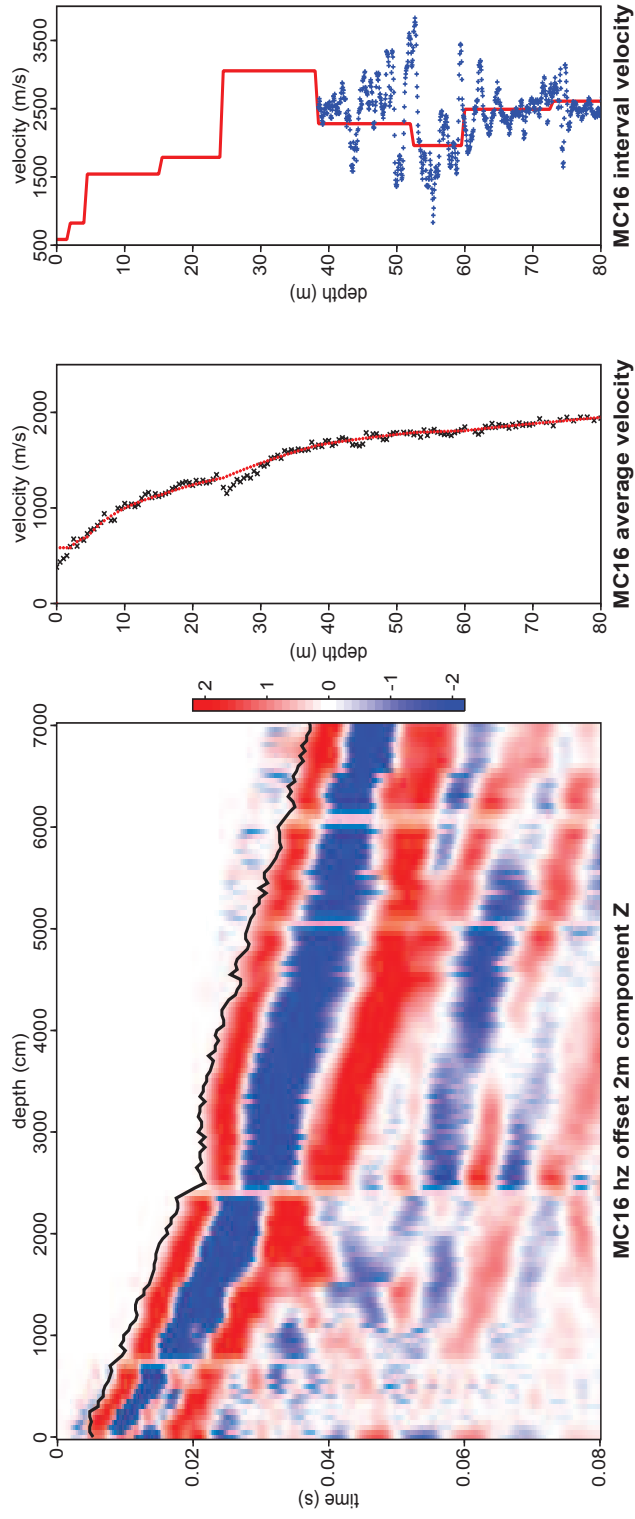
FIGURE 3.7 – Vertical component of VSP where black line is the first arrival curve(left). Average velocity calculated from the first arrivals (black stars) and average velocity,red curve, calculated from the velocity model (center). Velocity model deduced from the slopes of different parts of first arrival curve(right) where sonic measurement (blue curve) is superposed on the velocity model.

## Résumé CHAPITRE 4

Jusqu'à une certaine profondeur, les couches de proche sub-surface sont composées de matériel non consolidé. Les ondes sismiques se propageant à travers ces couches superficielles non consolidées auront besoin de davantage de temps pour les traverser. Il est important de pallier à cet effet. L'idée de la correction statique revient à appliquer un décalage constant en temps en vue d'amener les données enregistrées à une niveau bien défini en compensant l'irrégularité de la topographie (élévation statique), la vitesse et l'épaisseur de la couche altérée. Si la correction statique n'est pas appliquée cela peut entraîner la dégradation des données, l'apparition d'anomalies de temps de trajet, des problèmes dans la résolution et l'inversion de phase. Il existe plusieurs techniques de correction statique basées sur la première arrivée, la tomographie de réfraction ou des méthodes hybrides. La première rupture de pente correspond aux prémices des premières arrivées générées par la réfraction de l'énergie sismique à la base de la couche altérée.

Le concept à la base de la sismique réfraction est décrit par la loi de Snell-Descartes. Lorsque qu'un rai sismique rencontre une interface géologique, il est réfracté en fonction du contraste de vitesse entre les couches ($V_2 > V_1$). Il existe différentes méthodes pour calculer la correction statique, basées sur la première arrivée avec prise en compte du temps d'arrivée, plus-minus ou GRM ("generalized reciprocal method"). Dans ce chapitre, une méthode de calcul de correction statique basée sur l'inversion des délais est proposée. La technique d'inversion des délais permet de calculer des temps d'arrivées individuels pour les sources et les récepteurs. Pour un cas à deux couches, le temps corrigé peut s'écrire en termes de délais à la source et aux récepteurs sous la forme

$$t_{S_i R_j} = \delta t_{S_i} + \delta t_{R_i} \tag{3.2}$$

Les temps d'arrivées sont calculés pour toutes les premières arrivées pointées et réorganisés en matrice. Le système d'équation linéaire décrivant l'inversion des délais s'écrit comme

$$M[\delta t_{S_M|R_N}] = [t_{S_M R_N}] \tag{3.3}$$

Où :

$M$      matrice de configuration basée sur les points de tir et les récepteurs actifs correspondants.

$t_{S_M R_N}$      vecteurs des temps corrigés correspondant.

$\delta t_{S_M|R_N}$      vecteur des temps d'arrivée recherchés sur l'ensemble des tirs et des récepteurs.

Afin d'augmenter le rang de la matrice et de stabiliser le processus d'inversion, l'hypothèse de consistance spatiale est invoquée, selon laquelle les délais des sources et des récepteurs doivent être égaux lorsqu'ils partagent une même localisation de surface. La méthode de correction statique proposée ici est appliquée à des données synthétiques et des cas 2D, 2.5D et 3D. Par 2.5D on entend ici un ensemble de lignes 2D parallèles. Cette méthode d'inversion des délais est comparée à d'autres méthodes existantes pour un cas en 2D.

Dans un cas 3D, l'anisotropie de vitesse sera également prise en compte en faisant l'hypothèse d'une anisotropie elliptique pouvant être totalement décrite par 3 mesures de vitesse à 45° d'intervalle en notation tensorielle. Cette méthode donne la vitesse azimutale pour chaque paire source/récepteur. Les premières arrivées calculées des temps d'arrivées individuels, après inversion des délais, sont systématiquement comparés aux premières arrivées observées. La méthode proposée est validée par la correspondance des premières arrivées observées avec celles calculées. Des comparaisons complémentaires sont effectuées afin de vérifier la validité

de cette méthode, dont les principes, les applications et les résultats sont présentés dans ce chapitre.

# Static Correction

## 4.1 introduction

Near surface layers, up to certain depth, are composed of unconsolidated loose material. Seismic waves propagating through these shallow unconsolidated layers will take longer time to traverse them. It is important to mitigate this effect. The idea of static correction is to apply the constant time shift to bring the recorded data on a well defined datum by compensating the irregular topography (elevation static), weathering velocity and weathering layer thickness.

What happen if we do not apply the static correction ? This will produce seismic resolution problem, both temporal and spatial, phase inversion, problem of miss ties with well or different vintage data and false structural or stratigraphic anomalies that will create problem at the final stage of data interpretation. It will smear the quality of processed data due to static anomalies. For high-resolution shallow reflection survey its importance lies in the fact that time shifts are comparable to the dominant period of reflection. Thus static corrections, if calculated and applied correctly, will enhance the data quality and assist in the further processing steps.

Static correction is the first processing step for the seismic data processing. The forthcoming processing steps accuracy will depend on how correctly static correction is applied. The need of static correction has been judged long time ago. Static correction application is coeval to seismic exploration methods. There are many methods of static correction reported in seismic data processing. These methods are based on first arrival analysis, refraction tomography and hybrid method. Our technique is based on the first arrivals.

First break is the onset of first arrivals which are the manifestation of refracted energy at the base of the weathering layer (head waves), depending on the velocity and thickness of the soil superficial layers. Static correction computations based on first arrival include slope-intercept method, time-delay (plus-minus) method, or generalized reciprocal method. All these methods have certain advantages and inherent shortcomings. But the legacy of all first arrival based methods lies in the accomplishment of Snell's law due to velocity contrast ($V_2 > V_1$).

In this paper, we present a data driven approach for static correction calculation. This approach, which is based on first arrival times picking, belongs to the delay time calculation family of static correction calculation. It also corresponds to a new implementation of the concept of least-squares method for static correction calculations, as described by (Yilmaz, O., 2001). To validate our technique, we compared the results with analytical calculations for a 2D synthetic example. Then the 2D static correction results for a real case were compared with computa-

tion by delay time and generalized reciprocal method. Finally, this technique was applied to compute the static corrections for a 2.5D and a 3D real cases.

## 4.2 Refraction Statics

Seismic waves, ignited by a source, travel through the earth layers and interfaces and are recorded at different geophones placed on the surface. These waves include direct waves, head waves and reflected waves. Direct waves travels along the earth-air interface straight from source to receiver. Snell's law describes the key concept of the seismic refraction. When a seismic ray hit the geological interface, it is refracted depending on the velocity contrast of the layers. Mathematically it is described as :

$$\frac{sin\theta_i}{sin\theta_r} = \frac{V_1}{V_2} \tag{4.1}$$

where $\theta_i$ and $\theta_r$ are the incident and refracted ray angles to the interface normal respectively. If the velocity of the lower layer $V_2$ is greater than that of the upper layer $V_1$, there will be a point where the refracted angle reach 90 degree, then a head wave, or critically refracted wave, will travel along the interface with the velocity of the lower layer. For the 2 layers case with an horizontal interface, the total travel time of a critically refracted head wave may be written as :

$$t = \frac{2zcos\theta_c}{V_1} + \frac{X_{S_iR_j}}{V_2} \tag{4.2}$$

where $\theta_c$, named critical angle, is given by $\theta_c = sin^{-1}(V_1/V_2)$ and $z$ is the upper layer thickness. Equation 4.2 is a linear equation for source-receiver distance (offset) $X_{S_iR_j}$ (figure 4.1), where first and second coefficients are the intercept time and the inverse of the underlying layer velocity respectively. The minimum source-receiver distance for recording the head-wave, named critical distance, corresponds to a reflection at the critical angle. However, direct waves will be the first arrivals until the source-receiver distance reaches the so-called crossover distance, where head wave and direct wave arrive at the same time. After the crossover distance, refracted waves will be the first arrivals. For an earth model made of a set of horizontal layers, the travel time $t_n$ for a wave critically refracted along the $n^{th}$ interface can be written as :

$$t_n = \sum_{k=1}^{n-1} \frac{2z_kcos\theta_{kn}}{V_k} + \frac{X_{S_iR_j}}{V_n} \tag{4.3}$$

Similarly, for a model made of planar dipping layers, the above equation can be expressed as (Johnson., 1976) :

$$t_n = \sum_{k=1}^{n-1} \frac{h_k(cos\alpha_k + cos\beta_k)}{V_k} + \frac{X_{S_iR_j}sin\beta_1}{V_1} \tag{4.4}$$

where
$\theta_{kn} = sin^{-1}(V_k/V_n)$
$\alpha_k = \theta_{kn} - \gamma_k, \beta_k = \theta_{kn} + \gamma_k$
$\gamma_k$     Dip of the $k^{th}$ interface
$z_k$     normal thickness of the $k^{th}$ layer
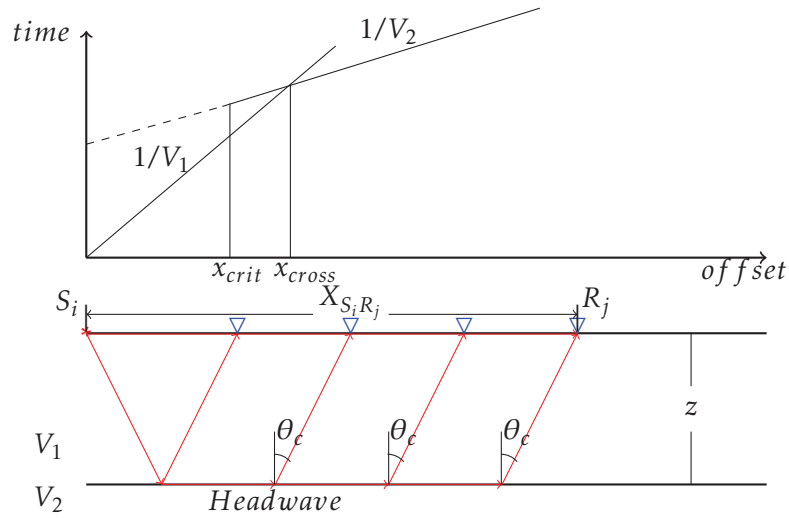
Figure 4.1 – Refraction principal for first arrivals : $x_{crit}$ and $x_{cross}$ correspond respectively to the critical and crossover distances.

$h_k$      vertical thickness of the $k^{th}$ layer

$V_k$      velocity of the $k^{th}$ layer

The so-called *Intercept-Slope* method consists of obtaining by linear fitting the coefficients from first-breaks offset-time graphs, and then deducing from these coefficients the depth, dip and velocity of each layer, so a superficial earth model can be setup to compute vertical travel-times and therefore the searched-for static correction times. Note that for dipping layers, both forward and reverse shooting is required to resolve all coefficients. However, this approach cannot take into account irregular interfaces.

## 4.3   Delay Time Method

Delay time method for statics estimation was proposed by (Gardner, L. W., 1939). The total travel time from a source $S_i$ to receiver $R_j$ shown in figure 4.2 is given by

$$t = \frac{S_i B}{V_1} + \frac{BC}{V_2} + \frac{CR_j}{V_1} \tag{4.5}$$

where $V_1$ and $V_2$ are the weathering layer and refractor velocities respectively. Referring to the figure 4.2, the equation 4.5 may be written in terms of source and receiver delay times as :

$$t = \frac{X_{S_i R_j} cos\gamma}{V_2} + \delta t_{S_i} + \delta t_{R_j} \tag{4.6}$$

where :

$\delta t_{S_i} = t_{S_i B} - t_{AB}$      Delay time for source

$\delta t_{R_j} = t_{CR_j} - t_{CD}$      Delay time for receiver

These source and receiver delay times represent the delay of seismic waves due to propagation through the weathered layer. It can be shown that for a dipping interface, delay-time is related
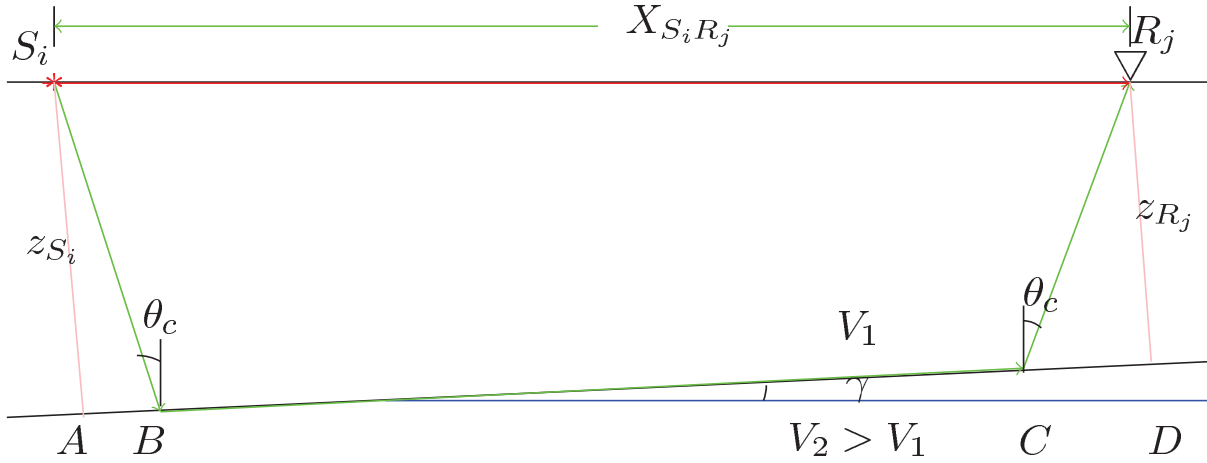
FIGURE 4.2 – Ray paths for the delay-time method.

to the layer thickness ($z$ normal, or $h$ vertical) by the relation :

$$\delta t = \frac{z cos\theta_c}{V_1} = \frac{h cos\theta_c cos\gamma}{V_1} \tag{4.7}$$

Delay times cannot be deduced directly from the traveltime equation 4.6 since they appear summed for source and receiver. (Hagedoorn, J. G., 1959) proposed the plus-minus method to calculate individual delay times, which is shortly described below.

### 4.3.1  Plus-Minus Method

Hagedoorn or plus-minus method is used to estimate the delay times and refractor velocity. It requires forward and reverse shooting. Referring to figure 4.3, the reciprocal travel-time between forward and reverse shot points can be written in terms of delay times as :

$$t_{S_f S_r} = \frac{X_{S_f S_r} cos\gamma}{V_2} + \delta t_{S_f} + \delta t_{S_r} \tag{4.8}$$

where $X_{S_f S_r}$ is the distance between forward and reverse shot points, and $\delta t_{S_f}$, $\delta t_{S_r}$ are the delay times for forward and reverse shot points respectively. The traveltime from the forward shot point to the receiver is given by

$$t_{S_f R} = \frac{X_{S_f R} cos\gamma}{V_2} + \delta t_{S_f} + \delta t_R \tag{4.9}$$

while for the reverse shot point, it is given by

$$t_{S_r R} = \frac{(X_{S_f S_r} - X_{S_f R}) cos\gamma}{V_2} + \delta t_{S_r} + \delta t_R \tag{4.10}$$

Hagedoorn's minus term, intended to determine velocity $V_2$, can be obtained by taking the difference between equation 4.9 and equation 4.10 :

$$t_{S_f R} - t_{S_r R} = \frac{2X_{S_f R} cos\gamma}{V_2} - \frac{X_{S_f S_r} cos\gamma}{V_2} + \delta t_{S_f} - \delta t_{S_r} \tag{4.11}$$

64
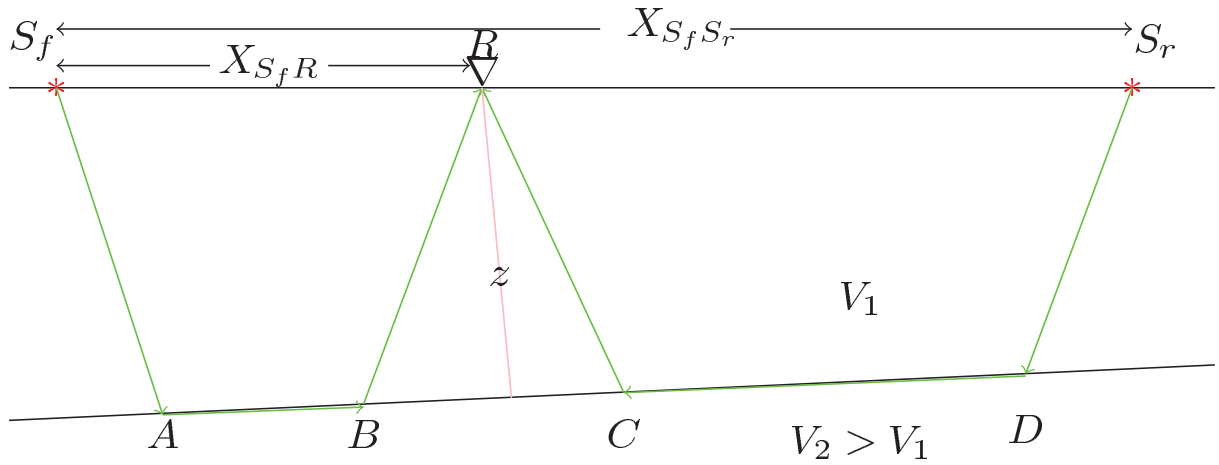
FIGURE 4.3 – Ray paths for the plus-minus method.

This equation corresponds again to a linear relationship for source-receiver distance $X_{S_f R}$ whose slope and intercept-time can been obtained by linear fitting to provide estimates of $\theta_c$ and $\gamma$.

Adding equation 4.9 and 4.10 yield the plus term :

$$t_{S_f R} + t_{S_r R} = \frac{X_{S_f S_r} cos\gamma}{V_2} + \delta t_{S_f} + \delta t_{S_r} + 2\delta t_R \tag{4.12}$$

By substituting equation 4.8, the delay time for the receiver can be obtained :

$$\delta t_R = (t_{S_f R} + t_{S_r R} - t_{S_f S_r})/2 \tag{4.13}$$

This delay time can then be used to obtain a local estimation of normal thickness $z$ or vertical thickness $h$ (see eq. 4.7) of the weathering layer at the receiver position R, provided that $V_1$ has been determined using direct arrivals. The plus-minus method is well fitted for 2D linear acquisition, where forward and reverse shots are available. It assumes than the refractor interface can be locally approximated by a plane.

## 4.4 Generalized Reciprocal Method

To overcome the aforementioned limitation of plus-minus method, (Palmer, D., 1980) has proposed the Generalized Reciprocal Method (GRM), in which rays emerging from approximately the same refractor point (figure 4.4) arrive at different receivers separated by a distance $\triangle X$, to be determined. GRM also requires the forward and reverse refraction arrival times, but is suitable for more general interfaces shape, lateral velocity changes and moderate dips. GRM can detect the presence of hidden layers and velocity inversions. In a first step, a velocity analysis function is computed to obtain both velocity and a best estimate of distance $\triangle X$. Then, generalized time depth values are calculated at each receiver positions. The velocity analysis function is defined as

$$t_v = (t_{S_f R_1} - t_{S_r R_2} + t_{S_f S_r})/2 \tag{4.14}$$

where :

$t_{S_f R_1}$     Travel time from source $S_f$ to receiver $R_1$
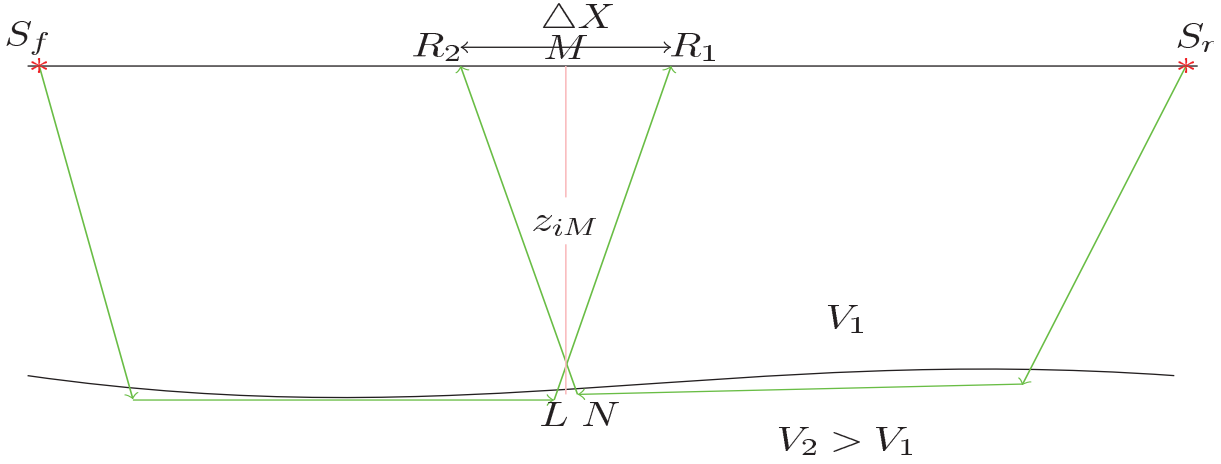
FIGURE 4.4 – Ray paths for the Generalized Reciprocal method.

$t_{S_r R_2}$    Travel time from source $S_r$ to receiver $R_2$
$t_{S_f S_r}$    Travel time from source $S_f$ to source $S_r$

The generalized time depth ($t_M$), the one way travel time to the refractor is

$$t_M = \frac{1}{2}[t_{S_f R_1} + t_{S_r R_2} - (t_{S_f S_r} + \frac{\triangle X}{V_n'})] \tag{4.15}$$

where $V_n'$ is the apparent refractor velocity for the $n^{th}$ layer. The velocity function is applied to the center of the two receivers $R_1$ and $R_2$, at location M. The optimum value occurs when points L and N are coincident (see figure 4.4), i.e, when the rays recorded at receivers $R_1$ and $R_2$ emerges from the same subsurface location. For this optimum value, the velocity function shows minimum lateral velocity changes and time-depths reveal maximum details.

## 4.5   Delay Time Inversion Methodology

The above methods rely on the availability of forward and reverse shots, to recover refractor depths in between these shots. They are well suited for 2D land seismic acquisition, where reverse shots can be simulated from common-receiver gathers. However, they cannot easily be extended to a real 3D seismic dataset, with the variety of possible source-receiver configurations. Our purpose here is to generalize the delay-time method for arbitrary 3D sources/receivers configurations. We consider a set of seismic shots $(S_i)_{i=1,M}$ for which first-breaks have been picked at receivers $(R_j)_{j=1,N}$. This set could be constituted from a selection of high-quality shots from the whole dataset, such as any receiver would be covered at minimum twice. The delay time inversion technique is based on general equation 4.6 which can be rewritten with a corrected time in the following manner :

$$t_{S_i R_j} = t - \frac{X_{S_i R_j} cos\gamma}{V_2} = \delta t_{S_i} + \delta t_{R_j} \tag{4.16}$$

To calculate the corrected time, knowledge of $V_2$ (bedrock velocity) is mandatory. It could be obtained together with the weathering layer velocity, critical angle and refractor dip from linear

66

data subsets by using the *Intercept-Slope* method. Note that these estimations could be azimuth dependent in 3D. From Snell's law :

$$V_2 = \frac{V_1}{sin\theta_c} \tag{4.17}$$

where critical angle, $\theta_c$, is calculated as :

$$\theta_c = \frac{1}{2}(sin^{-1}(\frac{V_1}{V_{22}}) + sin^{-1}(\frac{V_1}{V_{21}})) \tag{4.18}$$

and refractor dip as :

$$\gamma = \frac{1}{2}(sin^{-1}(\frac{V_1}{V_{22}}) - sin^{-1}(\frac{V_1}{V_{21}})) \tag{4.19}$$

$V_{21}$ and $V_{22}$ are the bed rock velocities obtained from pairs of positive and negative offsets and corresponding first arrivals respectively.
The system of linear equations for delay time inversion can be written as :

$$M[\delta t_{S_M|R_N}] = [t_{S_M R_N}] \tag{4.20}$$

where :
$M$      configuration matrix based upon shot points and corresponding active receivers
$t_{S_M R_N}$      vector of corresponding corrected times
$\delta t_{S_M|R_N}$      vector of searched-for delay times for all shots and all receivers.
The configuration matrix $M$ and linear system are built in the following manner :
The upper part of matrix $M$ links for each measured first-break the corresponding shot with the active receiver, it has as many lines as measured first-break times, and as many columns as the total number of shots and receivers. However, its determinant is null, even if all receivers were active at least for one shot. In the case where no first-break were measured at a given receiver (e.g. killed trace), a column of zeros appears that should be removed from matrix $M$, so the corresponding delay-time will not be recovered. In the same way, a receiver with only one measured first-break cannot be correctly resolved, thus the corresponding column is also removed.

$$
\begin{array}{c}
\begin{array}{cccccccccc}
S_1 & S_2 & S_3 & \ldots & S_M \mid R_1 & R_2 & R_3 & \ldots & R_N
\end{array}\\[2pt]
\begin{array}{c}
S_1\\ S_1\\ S_1\\ \ldots\\ S_2\\ S_2\\ S_2\\ \ldots\\ \ldots\\ \ldots\\ S_M\\ S_M\\ S_M\\ --\\ S_1\\ S_2\\ S_3\\ \ldots\\ \ldots\\ \ldots\\ S_M
\end{array}
\left(
\begin{array}{ccccc|cccc}
1 & 0 & 0 & \ldots & 0 & 1 & 0 & 0 & \ldots & 0\\
1 & 0 & 0 & \ldots & 0 & 0 & 1 & 0 & \ldots & 0\\
1 & 0 & 0 & \ldots & 0 & 0 & 0 & 1 & \ldots & 0\\
\ldots & \ldots & \ldots & \ldots & \ldots & \ldots & \ldots & \ldots & \ldots & \ldots\\
0 & 1 & 0 & \ldots & 0 & 0 & 1 & 0 & \ldots & 0\\
0 & 1 & 0 & \ldots & 0 & 0 & 0 & 1 & \ldots & 0\\
0 & 1 & 0 & \ldots & 0 & 0 & 0 & 0 & \ldots & 0\\
\ldots & \ldots & \ldots & \ldots & \ldots & \ldots & \ldots & \ldots & \ldots & \ldots\\
\ldots & \ldots & \ldots & \ldots & \ldots & \ldots & \ldots & \ldots & \ldots & \ldots\\
\ldots & \ldots & \ldots & \ldots & \ldots & \ldots & \ldots & \ldots & \ldots & \ldots\\
0 & 0 & 0 & \ldots & 1 & 0 & 0 & 0 & \ldots & 0\\
0 & 0 & 0 & \ldots & 1 & 0 & 0 & 0 & \ldots & 0\\
0 & 0 & 0 & \ldots & 1 & 0 & 0 & 0 & \ldots & 1\\
-- & -- & -- & -- & -- & -- & -- & -- & -- & --\\
1 & 0 & 0 & \ldots & 0 & -1 & 0 & 0 & \ldots & 0\\
0 & 1 & 0 & \ldots & 0 & 0 & -1 & 0 & \ldots & 0\\
0 & 0 & 1 & \ldots & 0 & 0 & 0 & -1 & \ldots & 0\\
\ldots & \ldots & \ldots & \ldots & \ldots & \ldots & \ldots & \ldots & \ldots & \ldots\\
\ldots & \ldots & \ldots & \ldots & \ldots & \ldots & \ldots & \ldots & \ldots & \ldots\\
\ldots & \ldots & \ldots & \ldots & \ldots & \ldots & \ldots & \ldots & \ldots & \ldots\\
0 & 0 & 0 & 0 & 1 & 0 & 0 & 0 & \ldots & -1
\end{array}
\right)
\left(
\begin{array}{c}
\delta t_{S_1}\\ \delta t_{S_2}\\ \delta t_{S_3}\\ \ldots\\ \delta t_{S_M}\\ --\\ \delta t_{R_1}\\ \delta t_{R_2}\\ \delta t_{R_3}\\ \ldots\\ \delta t_{R_N}
\end{array}
\right)
=
\left(
\begin{array}{c}
t_{S_1 R_1}\\ t_{S_1 R_2}\\ t_{S_1 R_3}\\ \ldots\\ t_{S_2 R_2}\\ t_{S_2 R_3}\\ t_{S_2 R_4}\\ \ldots\\ \ldots\\ \ldots\\ t_{S_M R_{N-2}}\\ t_{S_M R_{N-1}}\\ t_{S_M R_N}\\ --\\ 0\\ 0\\ 0\\ \ldots\\ \ldots\\ \ldots\\ 0
\end{array}
\right)
\end{array}
$$

The lower part of matrix M implements the hypothesis of spatial consistency, that is source and receiver delay times should be equal when they share the same surface location (here for the case $N = M$ and $S_i$ at the same location as $R_i$, $i = 1, N$). These extra constraints on the searched-for delay times allow to increase the matrix rank, and therefore to stabilize the inversion. A coefficient greater than 1 can also be used there to enforce these constraints.

Least square inversion of the above equation is given as :

$$[\delta t_{S_M|R_N}] = (M^T M)^{-1} M^T [t_{S_M R_N}] \tag{4.21}$$

with $M^T$ = Transpose of matrix M. Once solved, the obtained delay times permit to re-compute the first-break times, for comparison with the observed ones. The quality of the inversion results can then be assessed from the residuals.

## 4.6   Application to Synthetic Data

For synthetic data preparation, a 2D dipping layer model was used, as shown in figure 4.5. Forward and reverse shots were simulated, with 21 receivers at 2.5 m interval, corresponding to minimum and maximum offset of 0 m and 50 m respectively. The calculated first arrival times were perturbed with random noise to simulate a picking uncertainty of ±1 time sample. Figure 4.6 shows the interface depths obtained after the delay-time inversion, together with the model forward and reverse shots first-arrival times and their comparison with re-calculated first-arrival times after inversion. As it may be observed, the fit between model and calculated first-arrival times is very satisfying, with a residuals RMS close to the time sampling step. The model parameters (depths, dip and velocity) were also accurately recovered. The inversion procedure is thus validated by this synthetic test, so it can now be applied to real data.
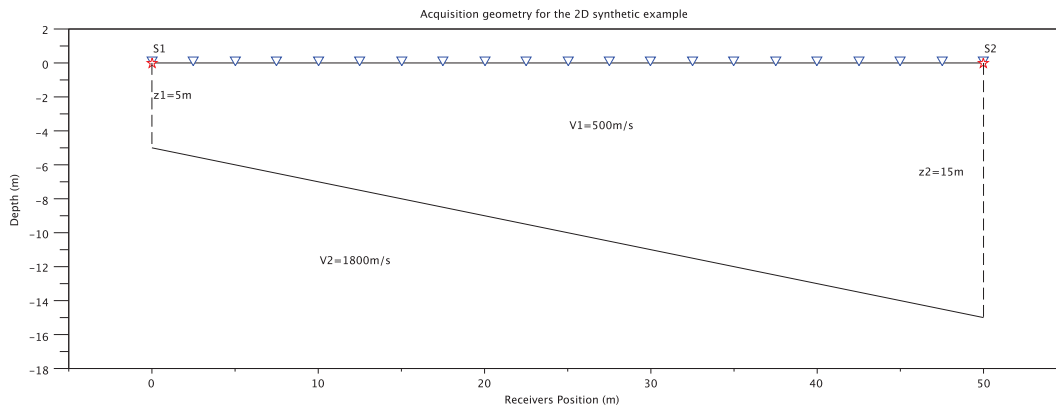


FIGURE 4.5 – Acquisition geometry for the 2D synthetic example, with blue triangles for receivers and red stars for sources.
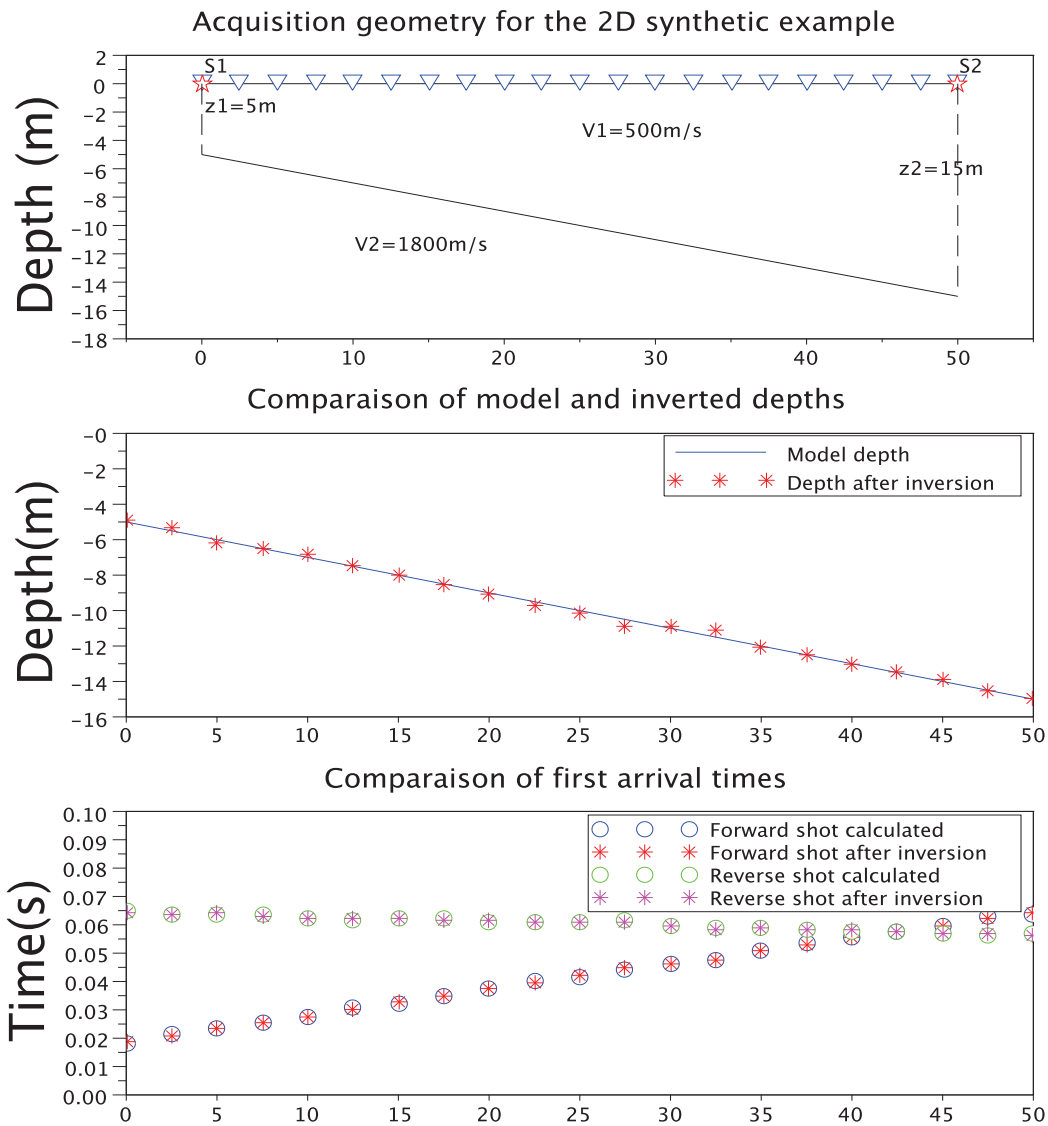
**Figure 4.6** – Results of delay-time inversion for the 2D synthetic example ; (top) Comparison of model depth (blue line) with depths obtained from the delay-time inversion (red stars) ; (bottom) Comparison of first arrival times calculated from the model parameters (open circles) with first arrival times re-calculated after delay-time inversion (stars), for both forward and reverse shots.

## 4.7   Application to 2D field data

We have applied the delay time inversion method for a 2D seismic line with split-spread acquisition geometry, 116 fixed receivers, and sources at midpoint in between receivers. Inter receiver distance is 1m so the source-receivers minimum offset is 0.5m. Maximum offset was chosen to ensure good quality first-breaks picking, limited to the first refractor. Figure 4.7 shows the first arrival picking and regression analysis to determine the velocity from picked first arrivals.
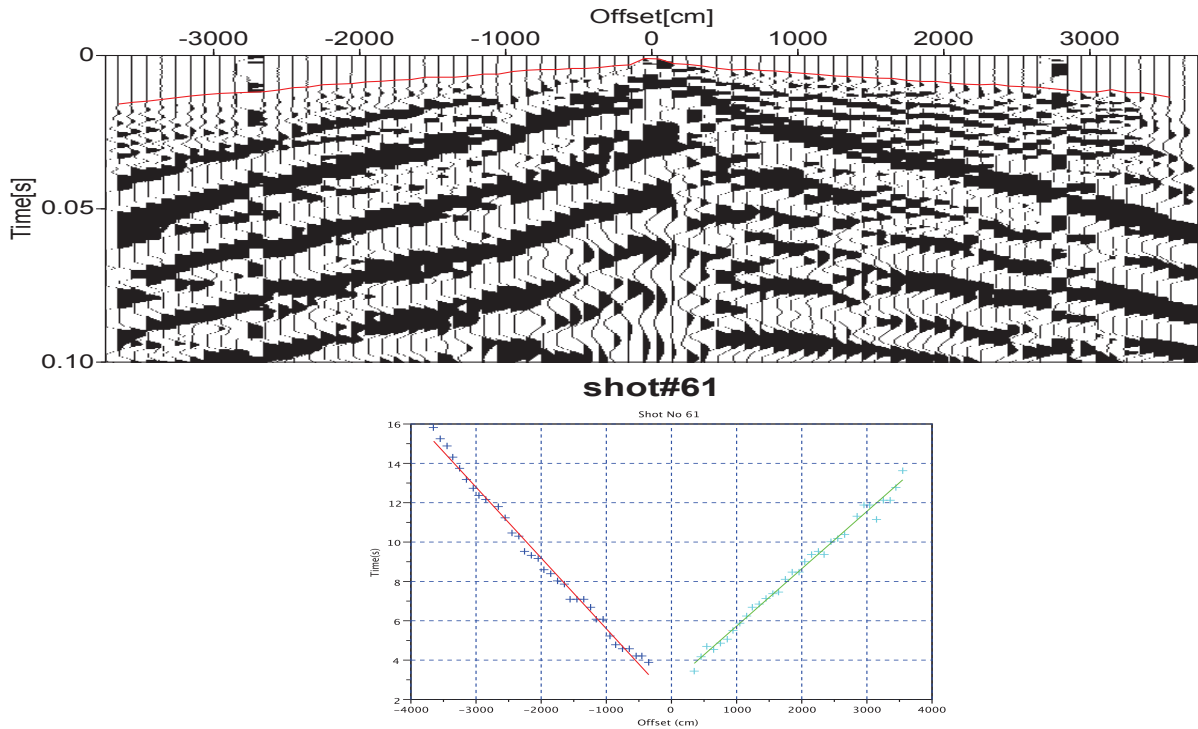


FIGURE 4.7 – First arrival picking, above, and best fit line, by linear regression, through the picked first arrivals.

Figure 4.8 shows the 2D seismic line acquisition geometry and the first arrivals plot corresponding to active receivers for a selection of shots.

Surface consistency was achieved by imposing in the configuration matrix that sources delay time be equal to neighbouring receivers delay time, distant by 0.5m. For the non-selected source points, delay-time was obtained by interpolation from neighbouring receivers. Figure 4.9 shows the comparison of observed first arrivals and calculated first arrivals after delay time inversion, which reveal a very good consistency. For the 633 picks, the residual distribution has a zero-centered gaussian shape, with a RMS residual equal to 0.4 ms. To determine the weathering static correction for receivers in terms of receivers delay time we may write :

$$Rwstat_j = \frac{-h_{R_j}}{V_1} + \frac{h_{R_j}}{V_2} = \frac{-h_{R_j}}{V_1}(1 - sin\theta_c) \qquad (4.22)$$

71
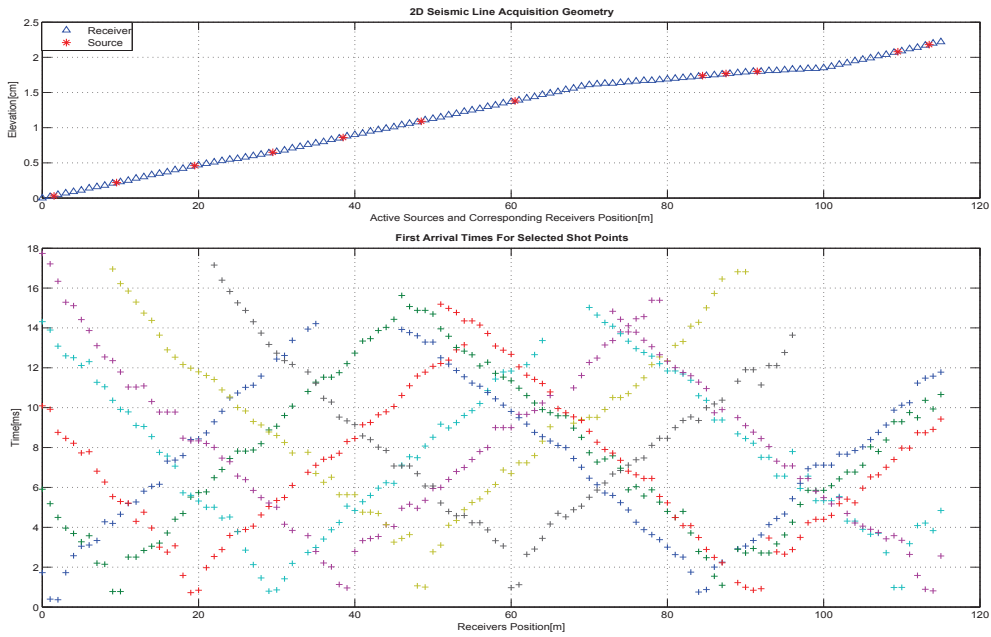
FIGURE 4.8 – Elevation of the sources (red) and receivers (blue), and first arrivals dataset for selected shot points along the 2D receiver line.
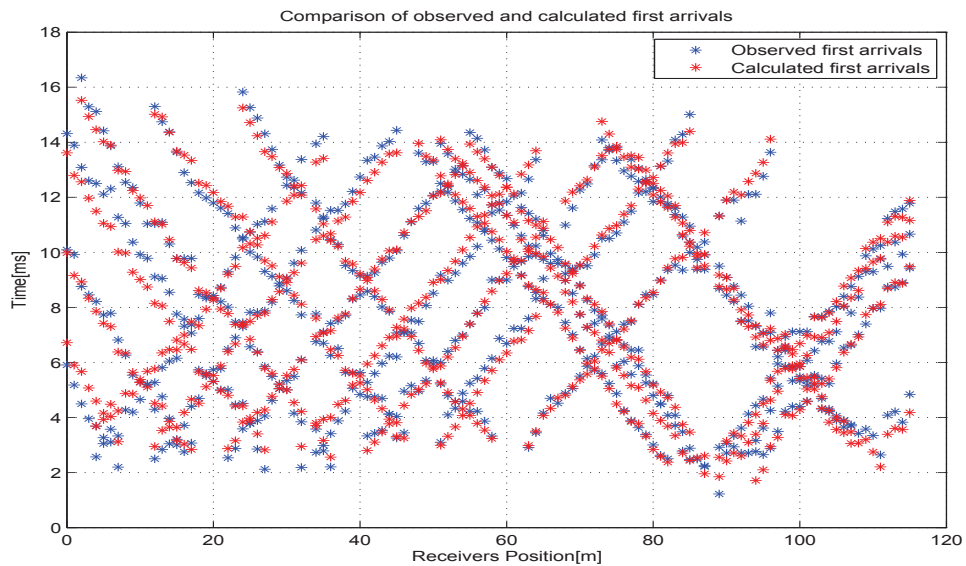


FIGURE 4.9 – Comparison of observed (blue) and calculated (red) first arrivals after delay time inversion for the 2D experiment.

It can therefore be written in a velocity-independent manner, using the delay-time obtained after inversion, together with critical angle and dip :

$$Rwstat_j = -\delta t_{R_j} \frac{1 - sin\theta_c}{cos\theta_c cos\gamma} \qquad (4.23)$$

The total static correction for receiver $R_j$ at surface elevation $E_{R_j}$ and replacement velocity $V_2$ is :

$$Rtstat_j = \frac{(E_{datum} - E_{R_j})}{V_2} - \delta t_{R_j} \frac{1 - sin\theta_c}{cos\theta_c cos\gamma} \qquad (4.24)$$

Similarly the weathering static correction for sources in terms of sources delay time is given by :

$$Swstat_i = -\delta t_{S_i} \frac{1 - sin\theta_c}{cos\theta_c cos\gamma} \qquad (4.25)$$

Hence the total static correction for sources at surface elevation $E_{S_i}$ is :

$$Ststat_i = \frac{(E_{datum} - E_{S_i})}{V_2} - \delta t_{S_i} \frac{1 - sin\theta_c}{cos\theta_c cos\gamma} \qquad (4.26)$$

Figure 4.10 shows the comparison of these static corrections determined successively using the delay time plus-minus method, the generalized reciprocal method, and our delay-time inversion method. We can observe that the order of magnitude and the general trends are similar but there exist significant differences for some location, that may produce significant changes in seismic processing results.
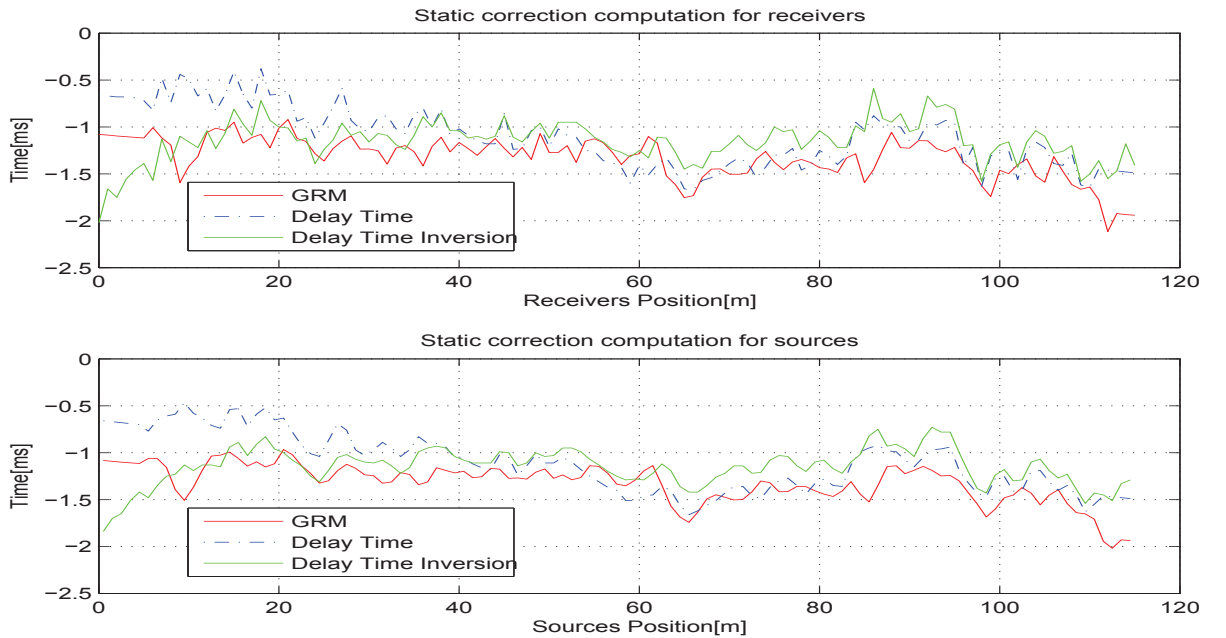


FIGURE 4.10 – Comparison of estimated static corrections for the 2D line sources and receivers, based on GRM, delay-time plus-minus and delay-time inversion methods.

## 4.8 Application to 2.5D data

The purpose of our technology is to handle 3D seismic configurations. According to geometry of acquisition, it could be divided into sets of parallel 2D lines, what we called 2.5D, or to complete 3D patterns. The first case is considered here, and the last in the next section. For the application of the delay time inversion technique to calculate the statics correction for 2.5D data, we consider a set of parallels 2D lines extracted from a 3D high-resolution seismic acquisition which comprised a square of receivers, made of 20 in-lines and 20 cross-lines, spaced every 2m, and sources points regularly distributed around the receivers square, as shown in figure 4.11. First arrivals were picked from pairs of shots located at the extremities of each receiver line, in both in-line (figure 4.12) and cross-line (figure 4.13) directions, within a chosen range of offset (from 4 m to 32 m) for optimal picking conditions. Critical angle, refractor velocity and dip were determined independently using the *Slope-Intercept* method for each in-line or cross-line receiver line, and proved to be variable, pointing towards limited spatial heterogeneities but significant azimuthal anisotropy. The first arrivals picks were also arranged in a matrix corresponding to the specific receiver number to ensure spatial coverage. When less than 2 picks are available at a given receiver, it generates a loss of rank in the configuration matrix $M$, so these receivers (mainly located on the borders and in the square corners) were removed for the inversion. Geometrical surface consistency was also introduced by implementing the linear condition that average source points delay time should be identical to average receivers delay time.
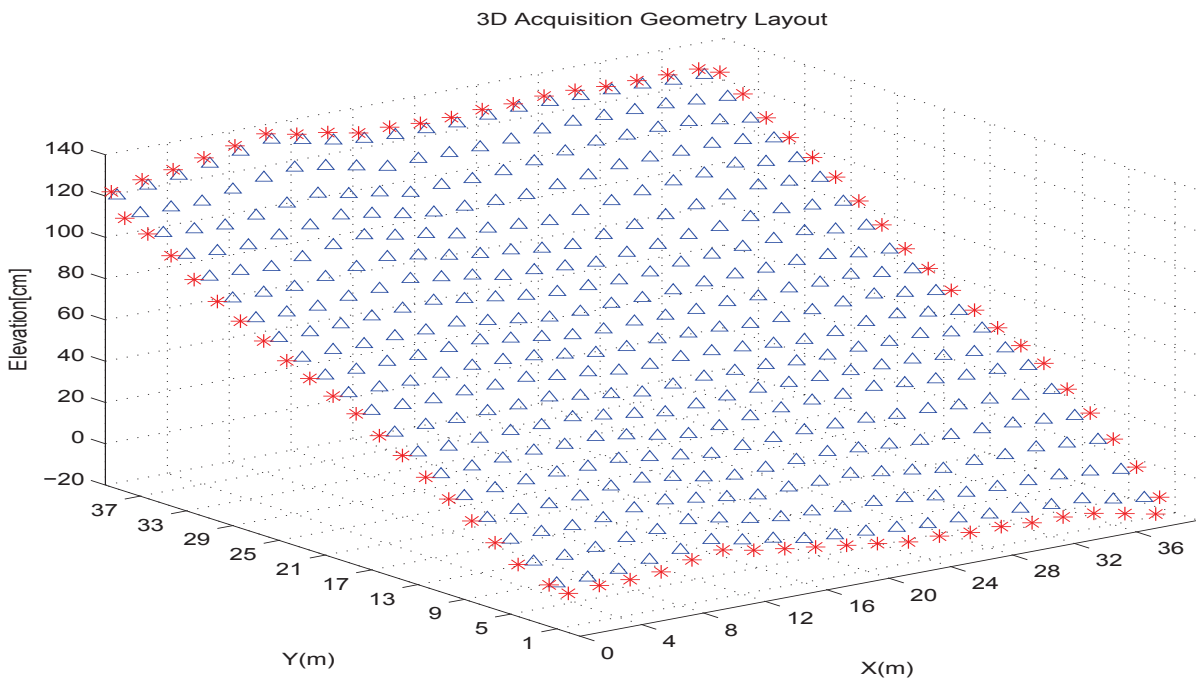


Figure 4.11 – Elevation of sources (red) and receivers (blue) for the 3D seismic experiment.

Figure 4.14 shows the observed and calculated first arrivals after delay time inversion. It reveals close relationships between them, what is confirmed by a residuals RMS of 0.28 ms for 976 picks. To calculate the static corrections for the sources and receivers, the same formulas are used as for the 2D case, using specific critical angle, replacement velocity and dip averaged at each receiver position.

Offset[cm]

shot#20

Offset[cm]
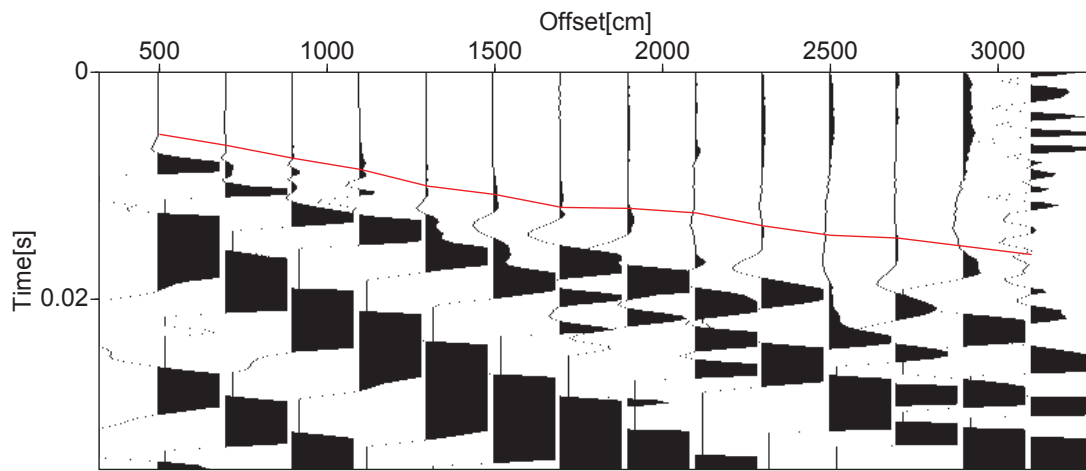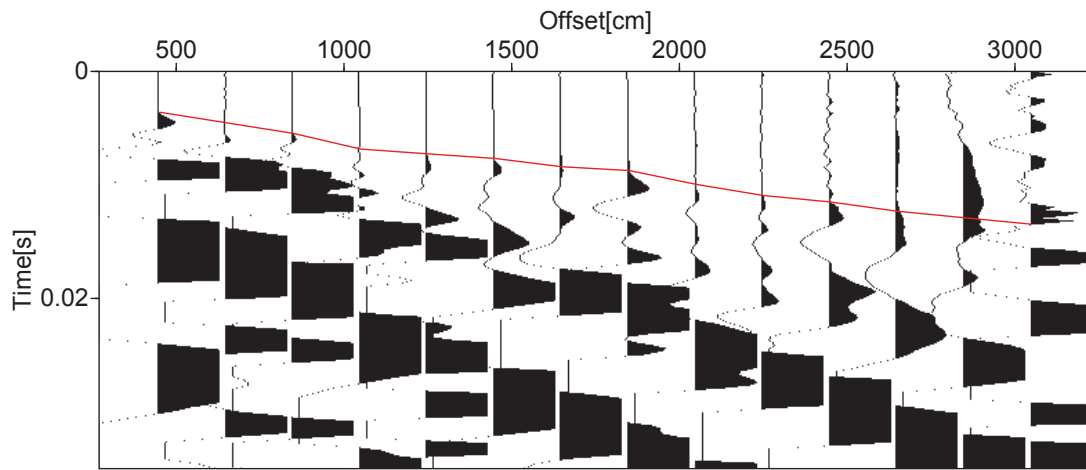
shot#41

Shot No 20 and 41
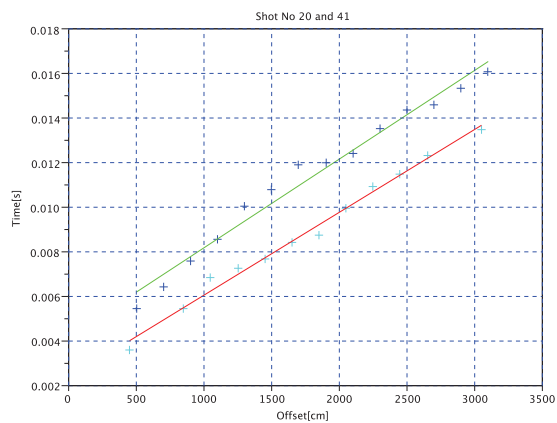
FIGURE 4.12 – First arrival picking and best fit line, by linear regression, through the picked first arrival for forward and reverse Inline.
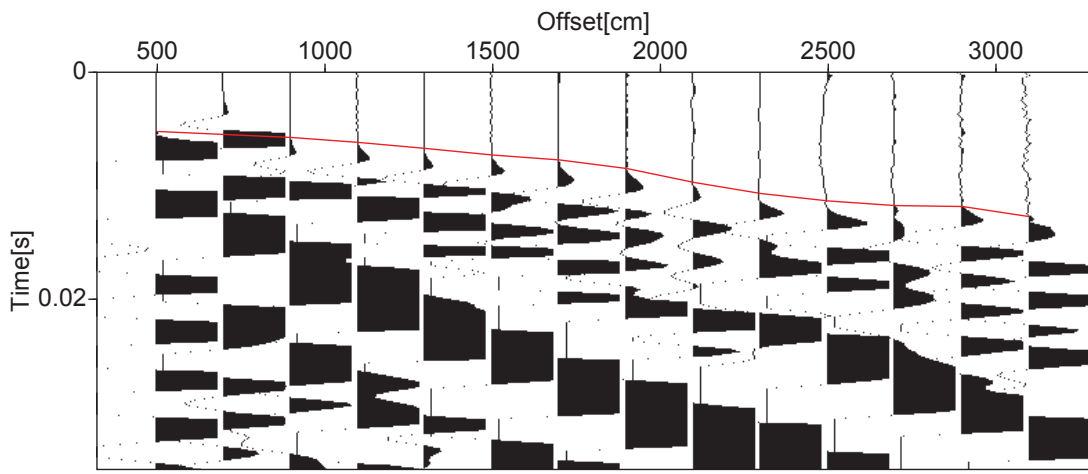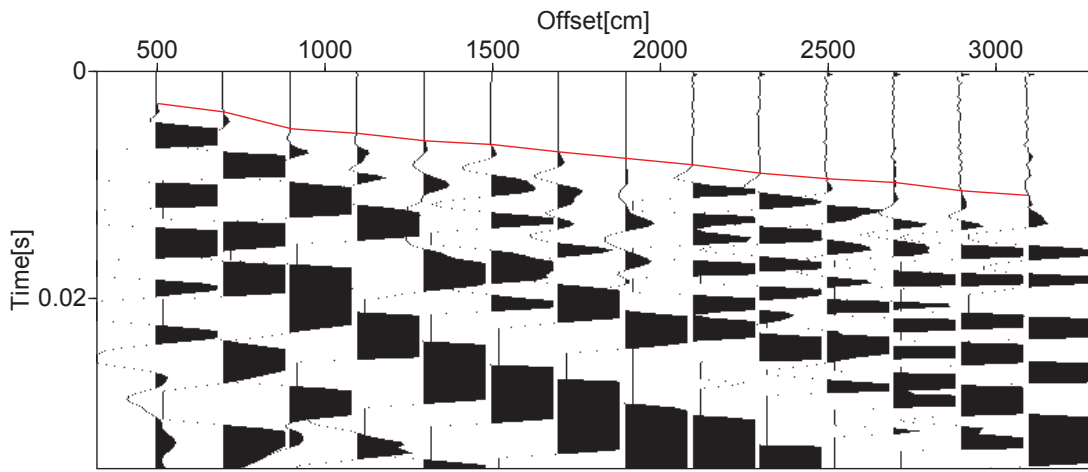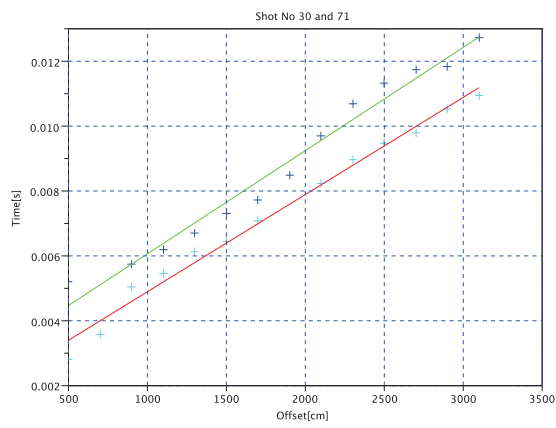
FIGURE 4.13 – First arrival picking and best fit line, by linear regression, through the picked first arrival for forward and reverse crossline.
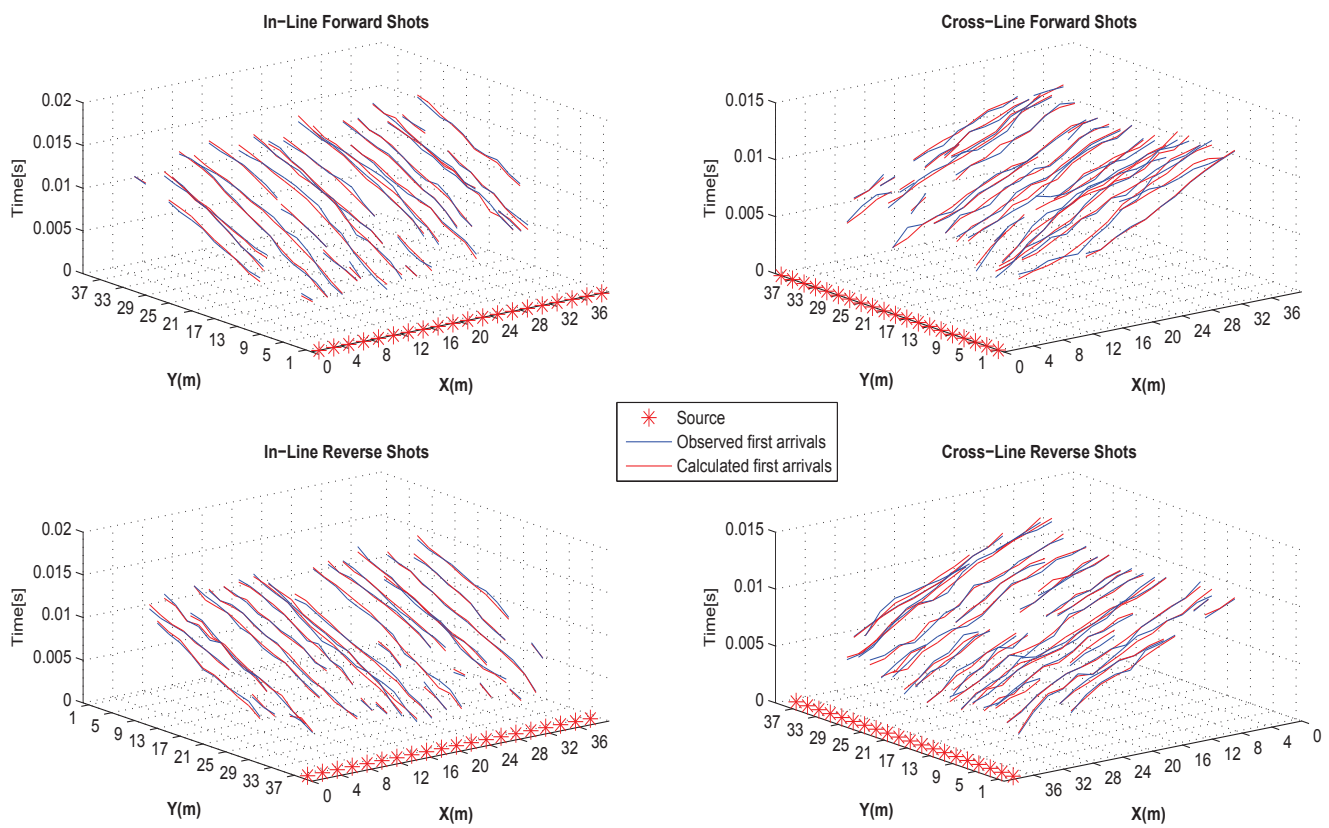
FIGURE 4.14 – Comparison of observed and calculated first arrivals after delay time inversion for the 2.5D dataset, in both in-line and cross-line directions.

## 4.9　Application to 3D data

The same but complete dataset was considered for the 3D case application. As indicated above, we have to deal with a further complexity, since we have observed azimuthal velocity anisotropy in the 2.5D case. This means that a different velocity has to be used for time correction for each source/receiver pair having a different azimuth. As a first order approximation, we assume elliptical anisotropy, so it can be completely described from 3 velocity measurements at 45 degrees interval using a tensorial notation. The three velocity measurements are available as the averaged in-line, cross-line, and diagonal velocity, obtained in the 2D and 2.5D cases, since the 2D dataset was recorded in the diagonal of the 3D square. To obtain the velocity for any azimuth, we first constructed the squared-slowness 2nd order symmetric tensor S for the in-line/cross-line coordinate system :

$$S = \begin{bmatrix} \frac{1}{V_a^2} & \frac{1}{V_{ab}^2} - (\frac{1}{V_a^2} + \frac{1}{V_b^2})/2 \\ \frac{1}{V_{ab}^2} - (\frac{1}{V_a^2} + \frac{1}{V_b^2})/2 & \frac{1}{V_b^2} \end{bmatrix}$$

where $V_a$, $V_b$ and $V_{ab}$ are respectively velocity along in-line, cross-line and diagonal axes. The velocity in azimuth $\phi$, measured from the cross-line axis, will thus be obtained using :

$$V(\phi) = 1/\sqrt{U(\phi)^T S U(\phi)} \tag{4.27}$$

$$U = \begin{bmatrix} sin\phi \\ cos\phi \end{bmatrix}$$
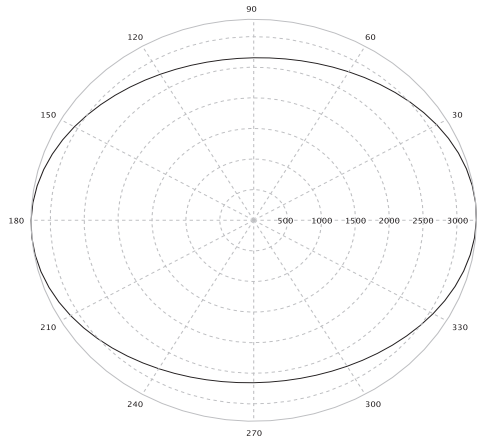


Figure 4.15 – Elliptical refractor velocity according to source/receiver azimuth.

Figure 4.15 shows the elliptical azimuth-dependent velocity obtained. On the other hand, only

79

limited velocity variation was observed between parallel receiver lines, so the area could be considered as homogeneous and anisotropic. Furthermore, only small dips, always less than 2 degrees, were detected in the 2.5D case, so the dip can be considered as negligible. We have therefore assumed for the 3D processing a fixed but azimuthally anisotropic refractor velocity and no dip. Corrected times were calculated for each source/receiver pair using the corresponding azimuthal velocity. For the delay-time inversion, we have selected 12 shots from the total number of 80 shots, and made the picking for all good-quality first arrivals in the same offset range as in the 2.5D case (4 to 32 m). The selection of shots ensures a sufficient coverage at each receiver, except in the square corners, and limits the cumbersome task of first-break picking. To take full account of azimuthal effects, we have selected for configuration matrix $M$ construction, only receiver positions where first-breaks from at least 3 different shots are available. The same geometrical surface-consistency condition was applied as in the 2.5D case. Figure 4.16 shows the comparison of observed and calculated first arrivals after delay time inversion, with a residuals RMS of 0.51 ms for 2524 picks. The gaps in the graphs correspond to receivers not picked for each specific shot. For source/receiver static corrections computations, the same formulas were used as for the 2D and 2.5D cases, with a global averaged refractor velocity and zero dip. The results obtained for the 3D case will be discussed in the following section, and compared with the 2D and 2.5D results.
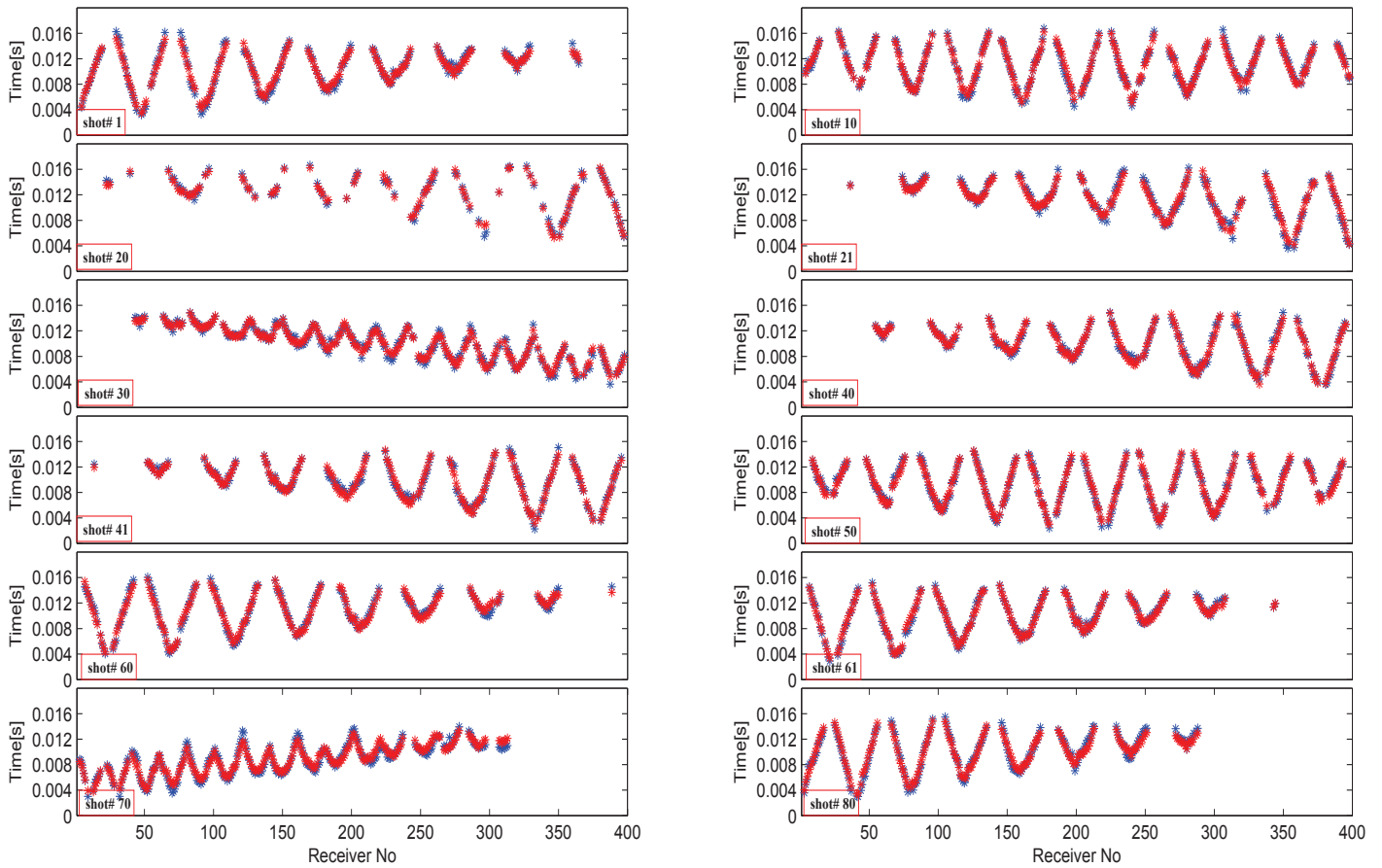
FIGURE 4.16 – Comparison of observed (blue) and calculated (red) first arrivals after delay time inversion for selected shots of the 3D experiment.

## 4.10 Application to 2.5D source block data

To determine the static correction for source block, the refraction data is acquired for 21 parallel lines. Each line consist of 21 receivers with inter-receiver distance of 2m. For each line 3 sources are used, two at line extreme ends and third one at the center. The refraction data is acquired for each line individually. So at the end data along 21 lines with total 63 sources is acquired (figure 4.18a). First arrivals are picked for all shots for a range of offsets. Figure 4.17 shows the first arrival picking for two sources located at the opposite end of the same line and consequent linear regression analysis that is used for local velocity and dip determination. For each line the critical angle, refractor velocity and dip is determined individually by using the *Slop-Intercept* method. Picked first arrivals are arranged into a matrix corresponding to the field geometry. Only those receivers are included in the inversion process where first arrivals are picked more than once. Surface consistency is achieved by applying the constraint that source delay time for each central shot is equal to the sum of delay times of immediate neighbouring

81

receivers on the both sides of source. Figure 4.18(b) shows the trace fold map where blue values correspond to low fold values( less than two) that are excluded from the inversion process. While red anomalous values on the same position in the figure 4.18(c) are the zero values corresponding to those low fold values.The static correction values have the same range as for receiver block 2D, 2.5D and 3D case. This is due to fact the source block is adjacent to receiver block and topographic variations are almost same. This also shows that the low velocity layer thickness and distribution is quite regular in this area. Figure 4.18(d) shows the residual values. Figure 4.19 shows the comparison of observed and calculated first arrivals that are in good agreement.
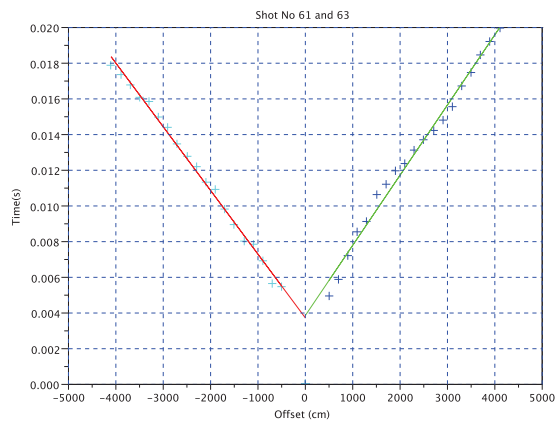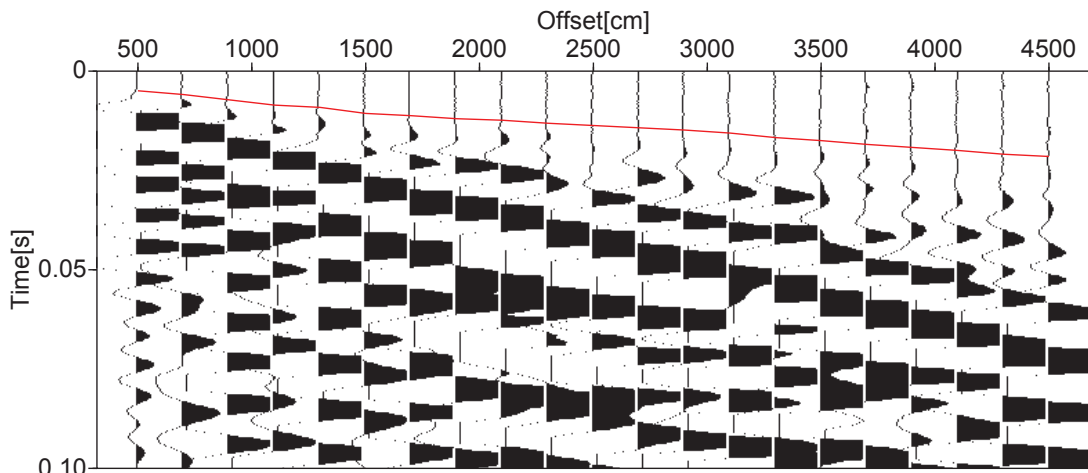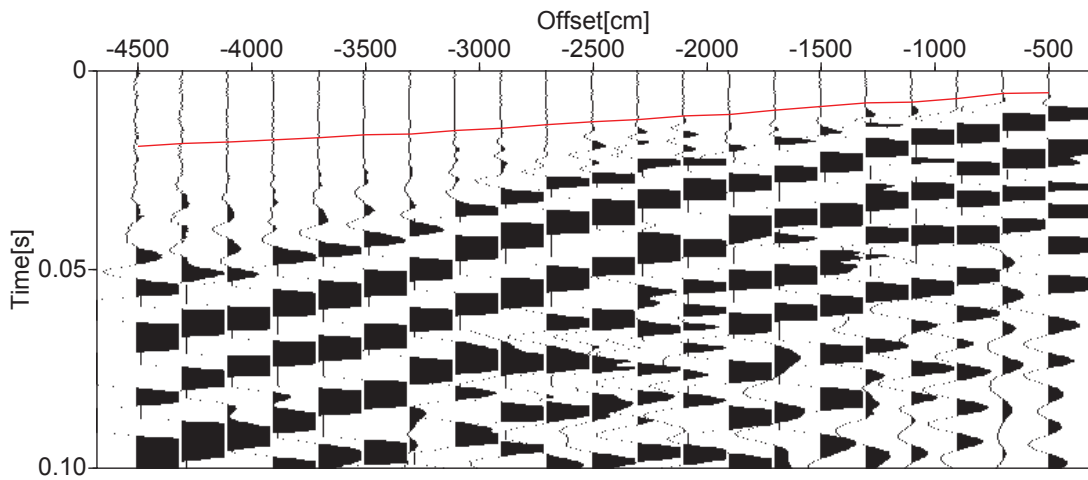
FIGURE 4.17 – First arrival picking and regression analysis for source block.

Source Refraction Acquisition Layout

(a)



Fold for source block

(b)



statics for source block

(c)



Source Residual(Residual=0.4ms) N=1078
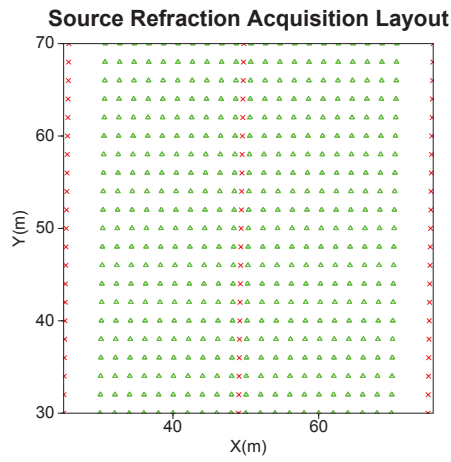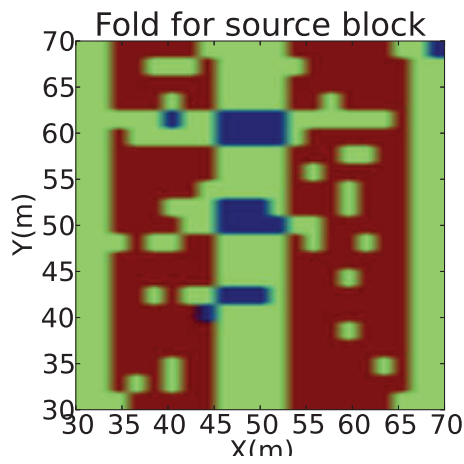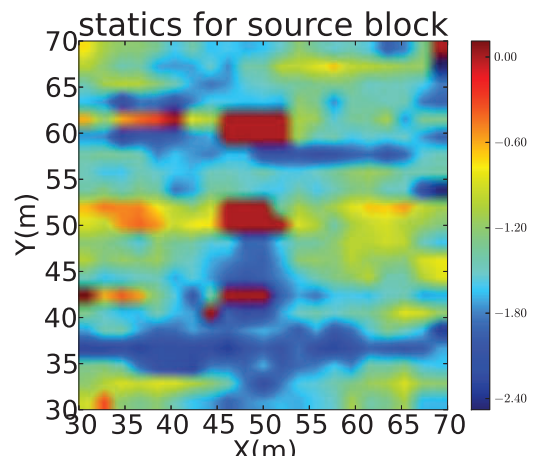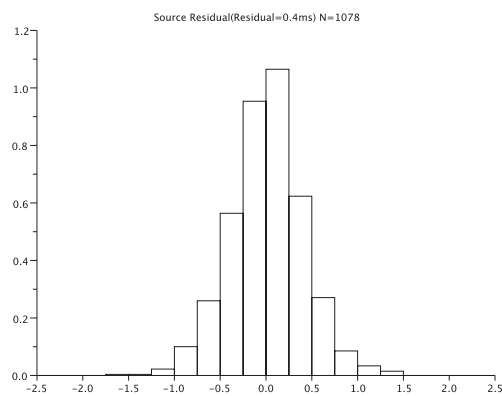
(d)

FIGURE 4.18 – a) Refraction acquisition geometry of source block ; b) trace fold for source block ; c) static correction map for source block ; d) residuals histograms.

84
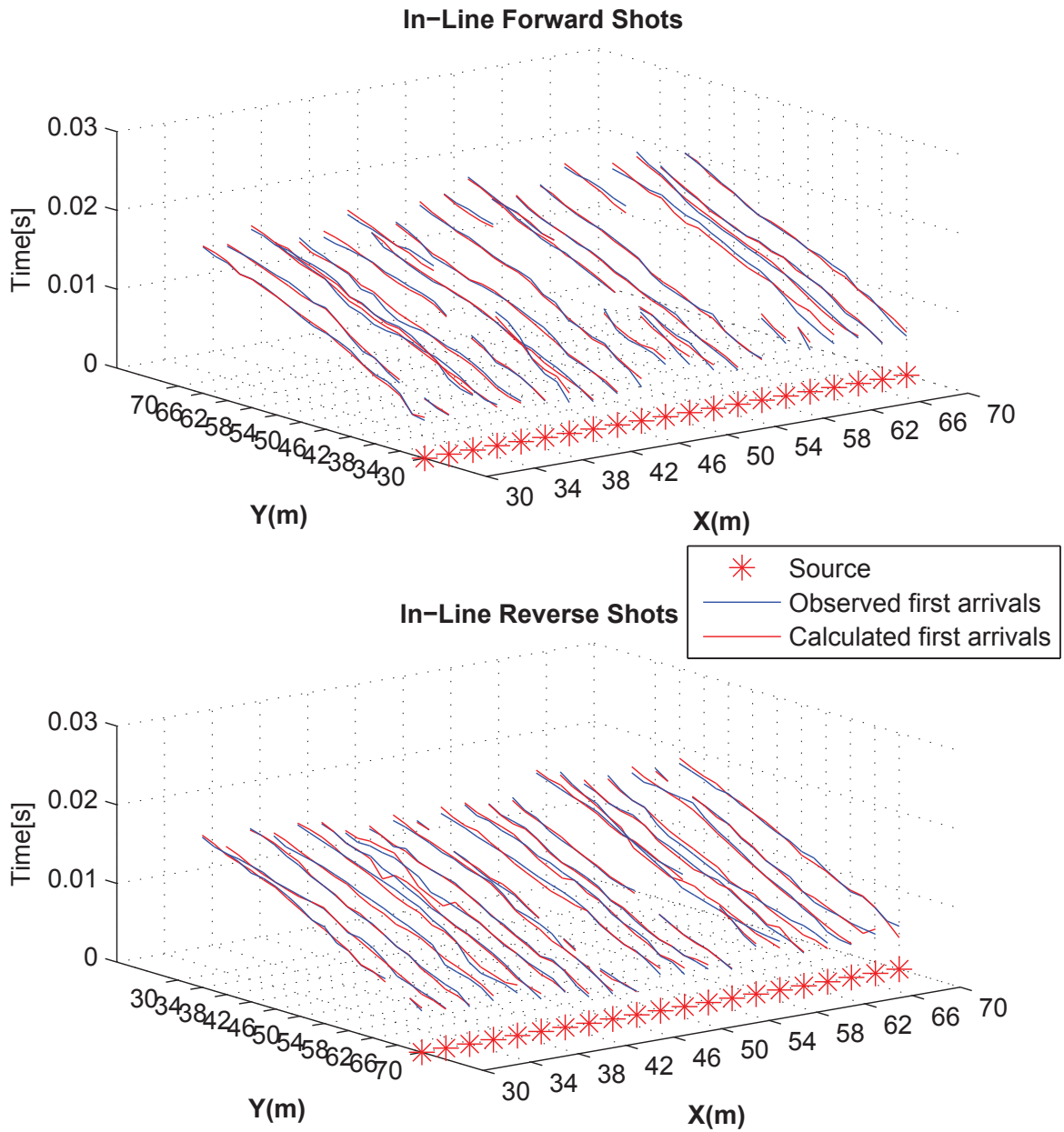
FIGURE 4.19 – Comparison of observed and calculated first arrivals after delay time inversion for the 2.5D source block dataset.

85

## 4.11   Discussion

To establish the interest of this new static correction technique, two comparisons can be made. The first one was to compare with static corrections obtained with previous methodologies, such as the delay time plus-minus method, or the GRM method. This was shown for the 2D case, where the three methods can be used from the same first-break picks set (figure 4.10). It appears both a generally good agreement, specially with the GRM results, but also localized differences that could reach 1 ms, that could be significant for very high resolution shallow seismic experiments. As this new method does not require specific parameters determination, as in GRM, and takes into account in the same manner all available first-break picks, it appears more general, and more easy to implement, even in the 2D case, although it was mainly conceived in view of the 3D case. A second comparison can be made between the 2D, 2.5D or 3D static corrections determinations obtained for the same receivers in the real data applications shown above, since all the experimental data came from the same site and the 2D line has been acquired along the diagonal of the 3D square. It means that for the receivers located on the square diagonal, we have results issued from the 3 cases. Figure 4.20 shows the static corrections estimations obtained for these specific receivers, except in the square corners where the 2.5D and 3D inversions did not provide results. All static corrections values lie within a narrow 1.5 ms interval, the 2D values being the more stable, and the 2.5D the more variable, slightly offset from the general trend. The 3D values lie between the two other sets. The origin of the 2.5D values shift can be understood by the comparison of the full sets obtained in the 2.5D and 3D cases, as shown in figure 4.21. The top row shows the shot/receiver configurations, the second the receiver first arrivals fold maps, and the third the receivers static corrections maps. The left column corresponds to the 2.5D case, the right one to the 3D case. As can be seen, the 2.5D case requires much more shots, but provides lower receiver fold, especially on the square borders. On the other hand, in the 3D case, much higher fold is achieved with a small number of shots. As a consequence, it appears large border effects in the 2.5D case, with a band over two receiver lines with low values (displayed in yellow to red colors on the corresponding static corrections map), while such border effects are not seen on the 3D static correction map, except in the square corners. As we have enforced the constraint of similar averaged static corrections value in the inversion process, it means that these border low values are compensated by higher values in the rest of the square, as compared with the 3D case. Nevertheless, the problem of static corrections is concerned with relative differences between receivers rather than the absolute value, which will anyway depends upon the datum level choice. As far as the residuals are concerned (figure 4.22), we obtained in all cases zero-centered gaussian distributions, but with variable widths and RMS values, the best RMS being obtained in the 2.5D case (0.28 *ms*), then the 2D case (0.41 *ms*), and finally the 3D case (0.51 *ms*). We think that this situation is related with the velocity information available to compute the first arrival corrected times in the linear system to solve. In the 2.5D case, a local velocity was obtained and used for each pair of forward and reverse shots, so the observed data could be very well fitted. The residual RMS is then similar to the time sampling step, which is the best that could be achieved, as shown in the synthetic data case above. In the 2D case, a global (averaged) velocity was obtained and used for the whole receiver line, so it becomes more difficult to fit all observed data, if it exists some velocity variation along the line, what is evidenced by the observed velocity variations between the 2.5D receiver lines, although limited. Finally, in the 3D case, a further complexity arises, since we have used there again a global velocity, averaged but also azimuthally anisotropic,

that corresponds to an even stronger approximation, and therefore even more difficulties to fit the observed data. However, we could hope that this situation is compensated by the higher data fold (close to 3 times more data), so the inversion results stay reliable.
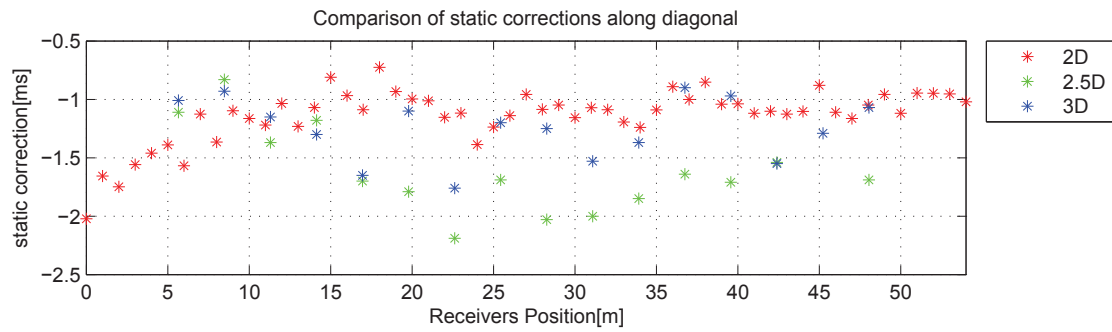


FIGURE 4.20 – Comparison of delay times and static corrections obtained through the 2D, 2.5D and 3D seismic experiment.

(a)

(b)

(c)

(d)

(e)

(f)
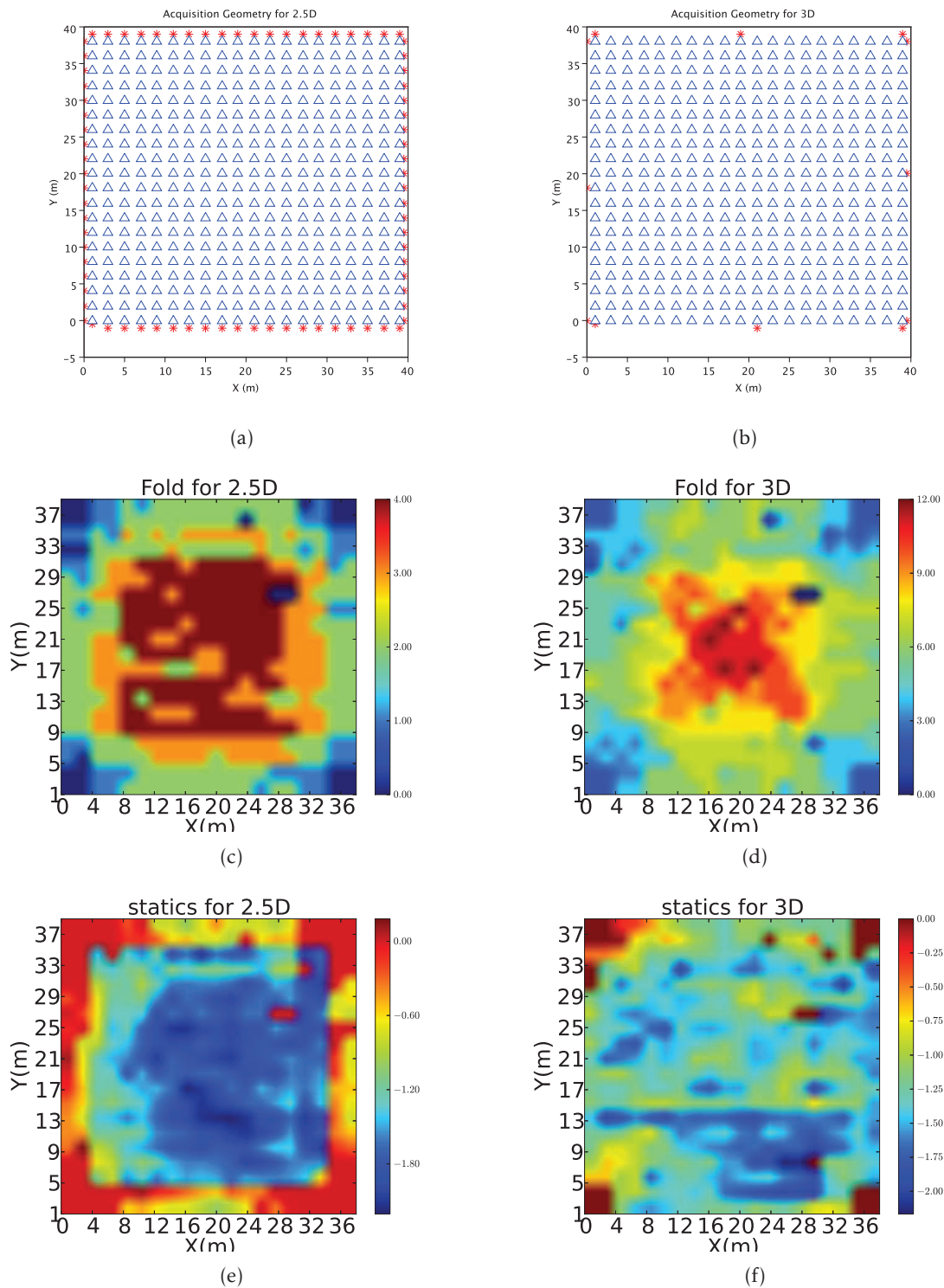
FIGURE 4.21 – a) 2.5D acquisition geometry ; b) 3D acquisition geometry ; c) trace fold for 2.5D ; d) trace fold for 3D ; e) static correction map for 2.5D case ; f) static correction map for 3D case.
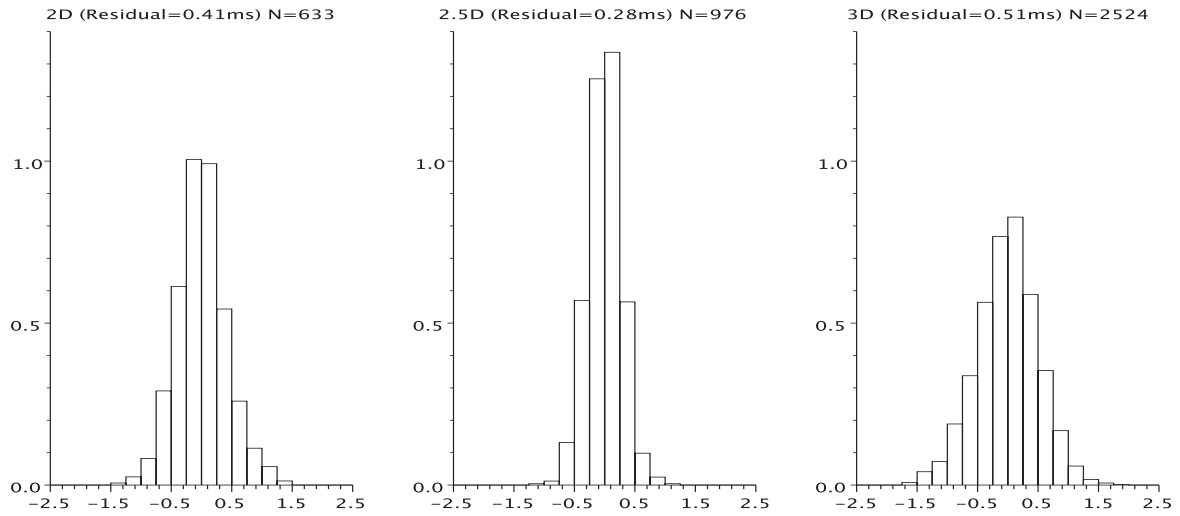
FIGURE 4.22 – Residuals histograms for the 2D, 2.5D and 3D cases.

## 4.12   Conclusion

In this paper, we propose a new implementation of delay time least-squares inversion, in order to provide accurate static corrections for the weathered layer compensation in land seismic records. This new implementation provides similar results as previous methodologies in 2D, in a more easy way. It can also be generalized to the 3D case, both deprecated to 2.5D or fully 3D. It is based upon first-break picking, but this new implementation facilitates this cumbersome task, since only good quality picks can be selected, and the amount of picks can be limited so that just enough data is available at each receiver. There are no limitations on geometry, as long as there exists some constrains between sources and receivers due to surface consistency, that could be expressed as linear relationships between their delay times. If not, the configuration matrix will yield to an ill-conditioned matrix for inversion. This new method has been applied to synthetic and real datasets, and was able in each case to simulate in a very satisfying manner the picked first-arrivals travel-times. It also appears that a preliminary detailed refractor velocity analysis is required, using first-arrival linear trends, like in other approaches. It allows to formulate the static corrections without having to formally express the weathered layer velocity and depth, but rather the delay-time and refraction critical angle. In the real data applications, total static corrections have been proposed, including topographical effects, to include in the subsequent data processing flow, which is beyond the scope of this paper.

# Résumé CHAPITRE 5

Le but du traitement des données sismiques est d'améliorer le rapport signal/bruit et de relier l'image sismique en temps à la section sismique en profondeur à la plus grande résolution possible. Le traitement des données sismiques nécessite de nombreuses étapes distinctes sans être néanmoins disjointes. Ces différentes étapes dans le traitement ont pour but d'améliorer et/ou d'éliminer certaines caractéristiques de la forme d'onde. A cet effet, on utilise des techniques mathématiques, statistiques ou hybrides variées de manière individuelle ou jointe. La donnée sismique est transformée d'un domaine dans l'autre afin d'en éliminer ou d'en améliorer certains traits plus facilement reconnaissables, et pour les évènements gênants plus facilement supressible, dans ce domaine particulier.

Pour la plus grande part, le traitement des données sismiques consiste à supprimer, filtrer, corriger de manière statique ou dynamique et migrer les données. Pour les acquisitions superficielles, le traitement est une tâche compliquée qui nécessite un soin tout particulier du fait de la couche à faible vitesse, la résolution et l'interférence du bruit avec les réflexions. La séquence de traitement est assez similaire que l'on se place en 2D ou en 3D, mais dans le cas 3D d'avantage de données doivent être traitées. Certaines étapes du traitement fonctionnent mieux en 3D qu'en 2D, comme la migration.

Les campagnes de sismique superficielle sur carbonates comparées à leur équivalent clastique posent des problèmes supplémentaires. Les couches de carbonates altérées situées proches ou au niveau de la surface prévient la pénétration d'une grande part de l'énergie sismique par l'effet de réflexion ou de propagation forcée dans la direction horizontale. Et l'énergie ayant pénétrée est elle-même grandement réfractée sur de grande distance avant d'avoir atteint la base de la couche de carbonates. La couche à faible vitesse en surface génère un important "ground-roll", masquant les réflexions de basse amplitude.

L'onde de Rayleigh pose aussi un sérieux problème dans cette étude. Tout d'abord, la ligne sismique 2D est traitée selon différentes stratégies pour se débarrasser de cette onde de Rayleigh. Les paramètres optimaux sont utilisés dans le traitement du bloc 3D. Des opérations de filtrage et de suppression sont menées en vue d'éliminer l'onde de Rayleigh. La suppression est préférée au filtrage.

Le traitement est effectué de manière à être cohérent avec la surface. La déconvolution compresse les ondelettes et résulte en l'amélioration de la résolution temporelle. L'équilibrage spectral << *spectral balancing* >> correspond à une déconvolution précédée par l'application d'un filtre passe-bande. L'équilibrage spectral est préféré dans le cas d'une acquisition de terrain avec sources en surface. La correction statique résiduelle est appliquée pour compenser le faible décalage en temps. La correction statique résiduelle permet un équilibrage en amplitude ainsi que l'alignement des phases et des temps. Pour cette étude, la méthode de maximisation des sommes en puissance, maximisation de la puissance après sommation des traces sur la fenêtre de temps analysée, a été utilisée.

Parmi les phases de traitement complémentaires, on compte l'analyse des vitesses et la correction NMO. Cette approche de traitement est qualifiée de traitement conventionnel. La technique de sommation de surface commune de réflexion (CRS) est basée sur un nombre plus élevé de paramètres dans l'équation des temps de propagation. Cette technique orientée par les données permet d'obtenir une résolution plus importante et un très grand rapport signal sur bruit à offset nul. Les résultats apportés par ces deux techniques sont très proches.

La migration sismique est le procédé permettant la suppression des évènements diffractant,

le repositionnement des évènements sismique sur la section sismique et l'amélioration de la résolution spatiale en concentrant l'énergie sur la zone de Fresnel. Différents algorithmes de migration sont appliqués et la migration $<< Split - Step >>$ de Fourier (migration en profondeur à zéro offset) donne des résultats satisfaisants. La vitesse est très importante dans la migration sismique. Le modèle de vitesse d'intervalle déduit des premières arrivées au puits MC16 est utilisé pour la migration. En présence d'une faible variation latérale des vitesses et en réalisant de mesures directes de la vitesse d'intervalle par VSP, cette méthode est une bonne candidate pour la migration, comparée aux vitesses de sommation obtenues par l'analyse des vitesses, ou aux informations relatives aux vitesses fournies par la méthode CRS.

# Seismic Data Processing

## 5.1   Seismic Data Processing

Seismic data processing is the next stage after data acquisition. Seismic data acquisition strategies, if resulted in adequate spatial and temporal sampling, will facilitate the seismic data processing. Preprocessing stage is composed of geometry setting of the field records, QC, bad trace killing, binning and sorting. Geometry setting is very important process since it assigns every trace the required information that will be further used in data processing.

Seismic data processing is aimed to enhance the S/N ratio and to relate the time section to the true subsurface depth image with highest possible resolution. Seismic data processing consist of many individual yet related steps to process the data. Different steps are aimed to enhance or/and to eliminate the certain characteristic of waveforms. For this purpose different mathematical, statistical or hybrid techniques are used individually and jointly. Seismic data is transformed from one domain to another domain to eliminate or enhance different features partly due to the easy recognition and suppression of annoying events in that particular domain.

Mainly seismic data processing consist of muting, filtering, different static and dynamic corrections and migration. For shallow surveys the processing is a complicated task and great care should be given because of low velocity layer, resolution and interference of noise with events. Processing sequence both for 2D and 3D is similar but in 3D case more data has to be processed as compared to 2D. Certain processing steps work better with 3D as compared to 2D such as migration etc.

Shallow seismic surveys for carbonate poses additional problem as compared to clastic counterparts. Carbonate layers near or at the surface hamper a large part of energy from penetration due to reflection or forced propagation into horizontal direction. Even the penetrated energy is severely refracted over large area by the time it reach to the carbonate layer base. The low velocity surface layer generates strong horizontal ground rolls that mask the low amplitude reflection events.

Since in this project we are interested in the shallow part, seismic data is processed to 0.1s which is approximately equivalent to 100m. For this study different processing strategies are used and compared. Raw shot from 2D line and along the diagonal of 3D seismic block are shown in figure 5.1 and figure 5.2 respectively. From these shots different seismic events are evident but noise is overwhelming in these shots. The processing starts with first arrival pi-

cking, to calculate the static correction that is described in previous chapter. After first arrival picking and static correction top mute is applied to get rid of noise that is evident from the figure 5.1. 2D seismic line is first processed to decide the different processing parameters and strategies that will be used for 3D reflection block.

Since the seismic data is noisy therefore special attention is given to the amplitude correction and preservation, both laterally and temporally, during processing. The aim is to apply the amplitude corrections in a balanced way.

In this chapter main seismic processing steps are described both for 2D seismic line and 3D reflection block.
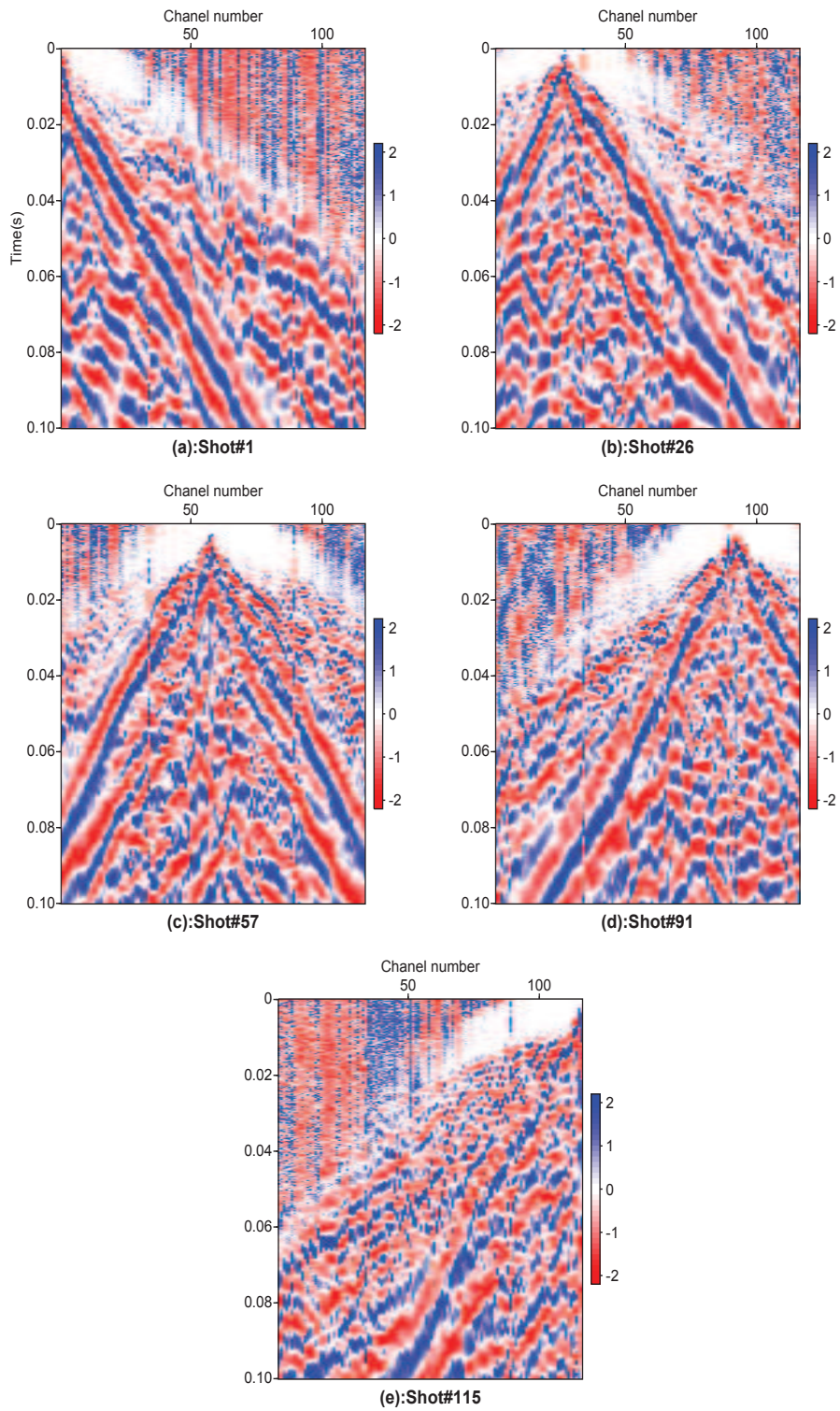
Figure 5.1 – Different raw shots for 2D seismic line. Rayleigh waves of varying amplitudes arriving at different times for different shots mask the low amplitude reflection events.
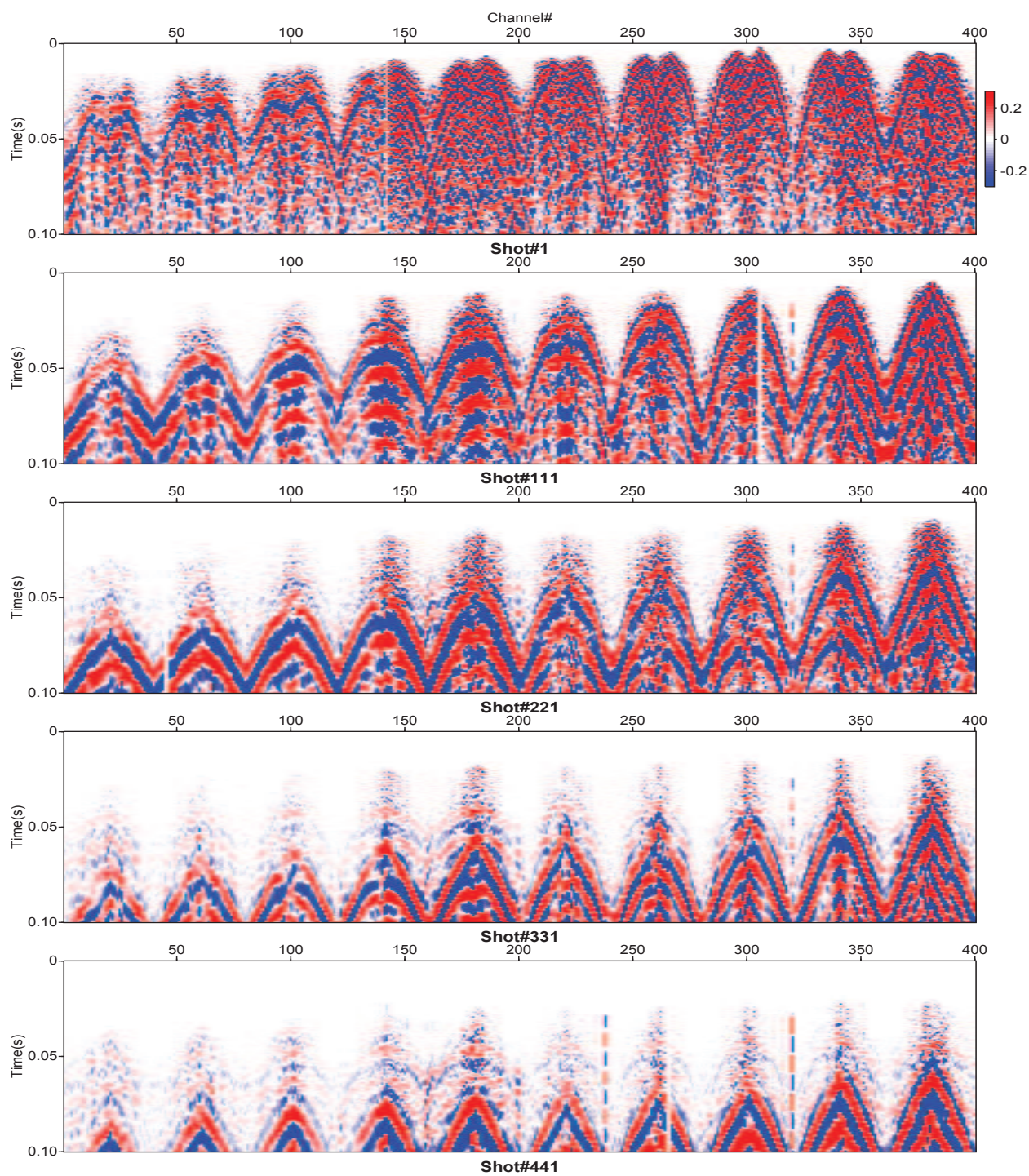
FIGURE 5.2 – Raw shots along the diagonal of 3D reflection block. High amplitude Rayleigh waves made the primary events invisible within different time range.

## 5.2   Elimination of Rayleigh waves

Rayleigh waves or ground rolls characterised by high amplitude, low frequency and low velocity, travel along the free surface with particle motion being elliptical in a plane perpendicular to the surface and parallel to the direction of propagation. The amplitude of Rayleigh waves decrease exponentially from the source below the surface and most of the energy contained within one wavelength of the surface. Rayleigh waves are dispersive in heterogeneous medium due to its mechanical and geometrical properties and presence of small scale scatters. In vertically heterogeneous media different frequencies propagate with different phase velocities at different depths. Seismic source at or near the surface generates surface waves that dominate on the seismic section.

Surface waves are both blessing and curse depending on scale and mode of investigation. In global seismology surface waves are of supreme interest and extensively used to describe the velocity of crust and mantle structure of the earth through tomography. For near surface application, engineering and geotechnical, surface waves are in extensive use to determine the near surface properties.

Figure 5.1 shows the different raw shots of 2D seismic line. Here Rayleigh waves are very dominant and have strong amplitude. These waves are reflective and dispersive due to medium heterogeneity and their generation may also be attributed to the surface source. Moreover these waves arrive at different time for different shots. These high amplitude waves mask the reflection events.

For 3D Rayleigh wave problem is even worst. Figures 5.2 shows the Rayleigh waves arrival for different raw shots, along the diagonal of 3D reflection block, with varying amplitude. For the first shot the Rayleigh waves completely masked the data for the first few milliseconds while for the rest of shots Rayleigh waves arrive at the later time progressively and different reflection events can be recognised having lower energy. Furthermore its frequency bandwidth is similar to that of P-wave reflection events and this fact make it difficult to filter the Rayleigh waves. Rayleigh waves velocity change gradually depending on the offset and azimuth from the shot point.

In exploration geophysics surface waves are regarded as coherent noise. For near surface reflection surveys the surface waves dominate and mask the reflection events partly due to near surface heterogeneities, rapid change in lateral and vertical properties of the layer, and partly due to use of surface source.

There exist many approaches that tend to remove the ground rolls. The simplest approach is to find the domain that maps the signals and noises into distinguished events where those events are muted or filtered. Such techniques include FK filtering(Yilmaz, O., 2001; Embree et al., 1963), linear and hyperbolic $\tau - p$(Spitzer et al., 2001) and Karhunen-Loeve transformations(Liu, X., 1999; Montagne, R. & Vasconcelos, G. L., 2006). In FK filtering the data in t-x domain is transformed to frequency-wavenumber domain and since ground rolls are linear events in t-x domain they are mapped into lines in frequency-wavenumber domain and are filtered by using a 2D band pass filtering. $\tau - p$ transformation transfer the data from t-x domain to intercept time-slowness domain where events are separated and mapped to different locations and noises can be rejected by band pass filtering.

Statistical techniques are in use for ground roll elimination including Principal component analysis, Singular value decomposition and its various variants(Kendall et al., 2005; Bekara, M. & Baan, M. V., 2007) and Eigenimages. Other methods for ground roll filtering are based

on wavelets transform(Deighan, A, J. & Watts, D. R., 1997), curvelt transform(Yarham et al., 2006), Wiener filtering(Karsli, H. & Bayrak, Y., 2008) and time-derivative filtering(Melo et al., 2009).

These waves are difficult to filter or eliminate. Several techniques are in use to get rid from surface waves and each technique has its own pros and cones. Bandpass filtering is not a solution for these Rayleigh waves elimination. $F-K$ filtering is limited in the processing of shallow surveys. Muting can be very effective but it will also mute the reflection events. For this study both high bandpass filtering and muting are applied. High bandpass filtering will result in loss of low frequency content of the data, figure 5.3(central column) and figure 5.4d, for 2D and 3D case respectively, and this prove meaningless but muting will result in the partial loss of primary reflections in the region, as shown in figure 5.3(3rd column) and figure 5.4b. But in this study muting is proved more efficient due to preservation of low frequency content. 2D seismic line is processed with both choices of Rayleigh wave filtering and muting. Later in this chapter the final stacked sections are shown processed with Rayleigh wave muting and filtering. Based on the processing results of the 2D seismic line, the choice of Rayleigh wave muting is opted.

## 5.3   Deconvolution and Spectral Balancing

Deconvolution is the process of decomposing observed time series into its constituents(Manuel & Enders, 1979). Deconvolution compresses the wavelet and result in enhancement of temporal resolution yielding the representation of subsurface reflectivity. Since many frequency components in seismic signal fall within the same frequency as of primary reflection so their undesired effects can not be replaced just by frequency filtering and deconvolution plays an important role to get rid of them. Similarly shot multiples and reverberations generated by source coupling can be suppressed successfully.

When the input signal is known, Wiener filter converts the input signal into an output signal by minimizing the least square error between the actual and desired output signal. Spiking deconvolution is applied when desired output of the Wiener filter is a spike. Since spike is composed of all the frequencies with same amplitude, applying whitening will result in better spike. Spectral balancing is deconvolution preceded by bandpass filtering. Spectral balancing is preferred in the case of land acquisition using surface sources resulting in complexly organised frequencies(Tufekcic et al., 1981).

Figure 5.5 and figure 5.4 shows the result of spectral balancing, applied for Rayleigh wave muting and filtering, and corresponding frequency spectra for a shot and cdp for 2D and 3D case respectively.
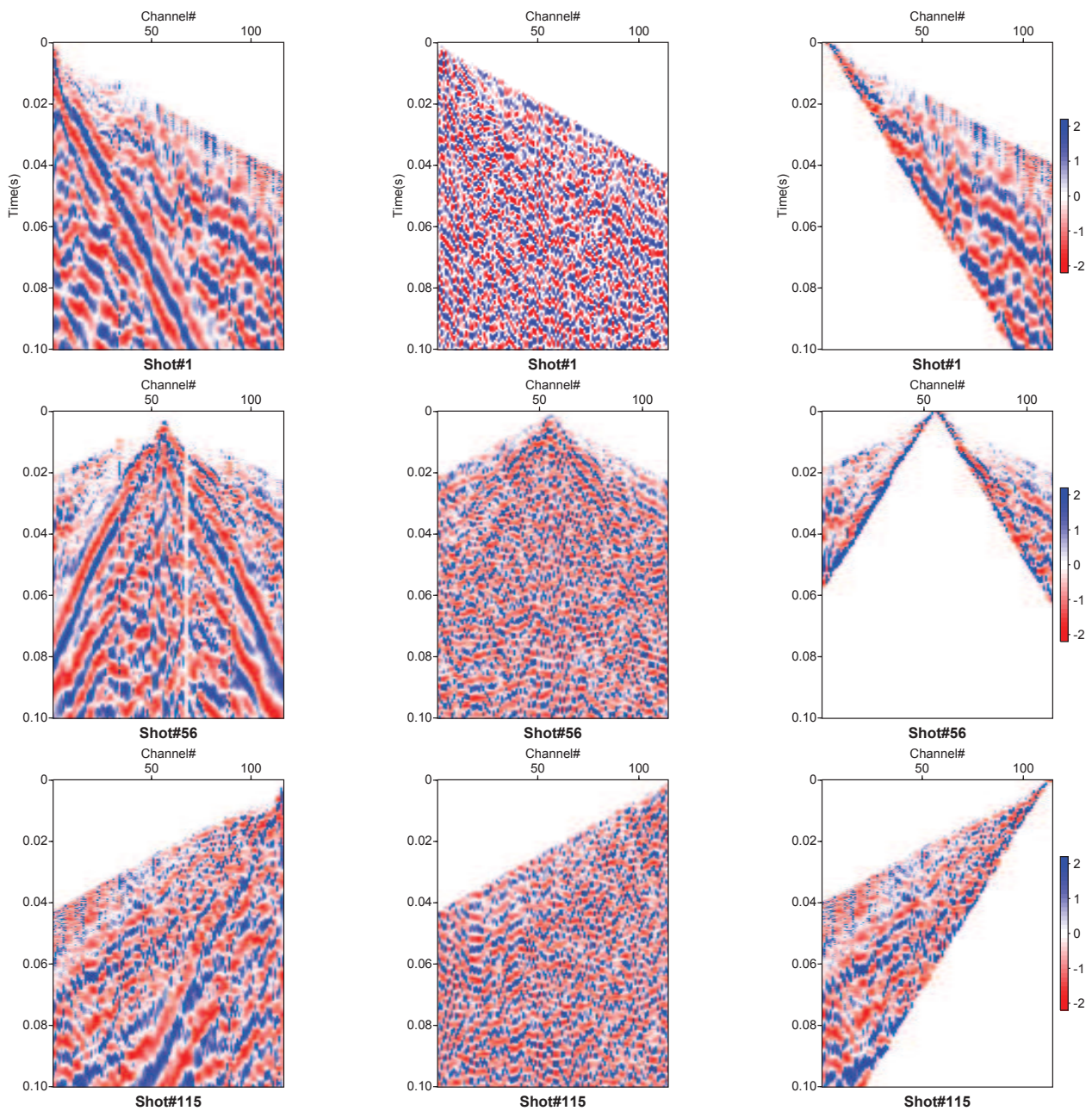
FIGURE 5.3 – Comparison of different processing strategies for Rayleigh wave elimination in 2D case. Raw shots after top muting and static correction (left column). After high band pass, (125-140-300-350) Hz, filtering (central column). After Rayleigh wave muting (right column). Seismic events are more clear and visible after Rayleigh wave muting compared to high pass filtering.
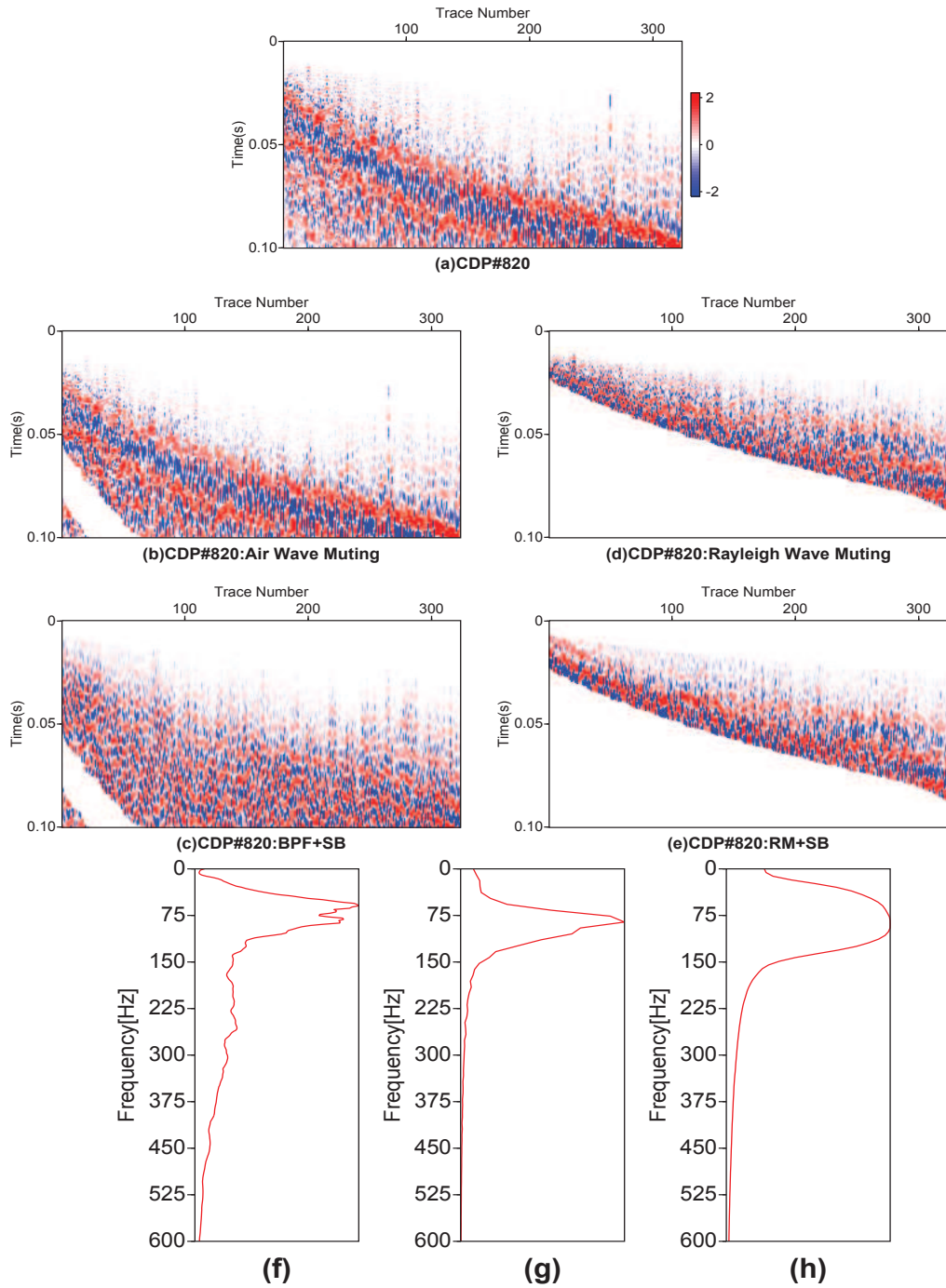
FIGURE 5.4 – Comparison of different processing strategies for Rayleigh wave elimination. a) Original cdp after static elevation correction ; b) Air Wave muting of (a) ; c) Band Pass filtering, (60-80-120-150)Hz, and Spectral Balancing of (b) ; d) Rayleigh wave muting of(a) ; e) Spectral balancing ,(20-30-120-150)Hz, of (d) ; g) Frequency spectrum of (a) ; h) Frequency spectrum of (c) ; g) Frequency spectrum of (e).
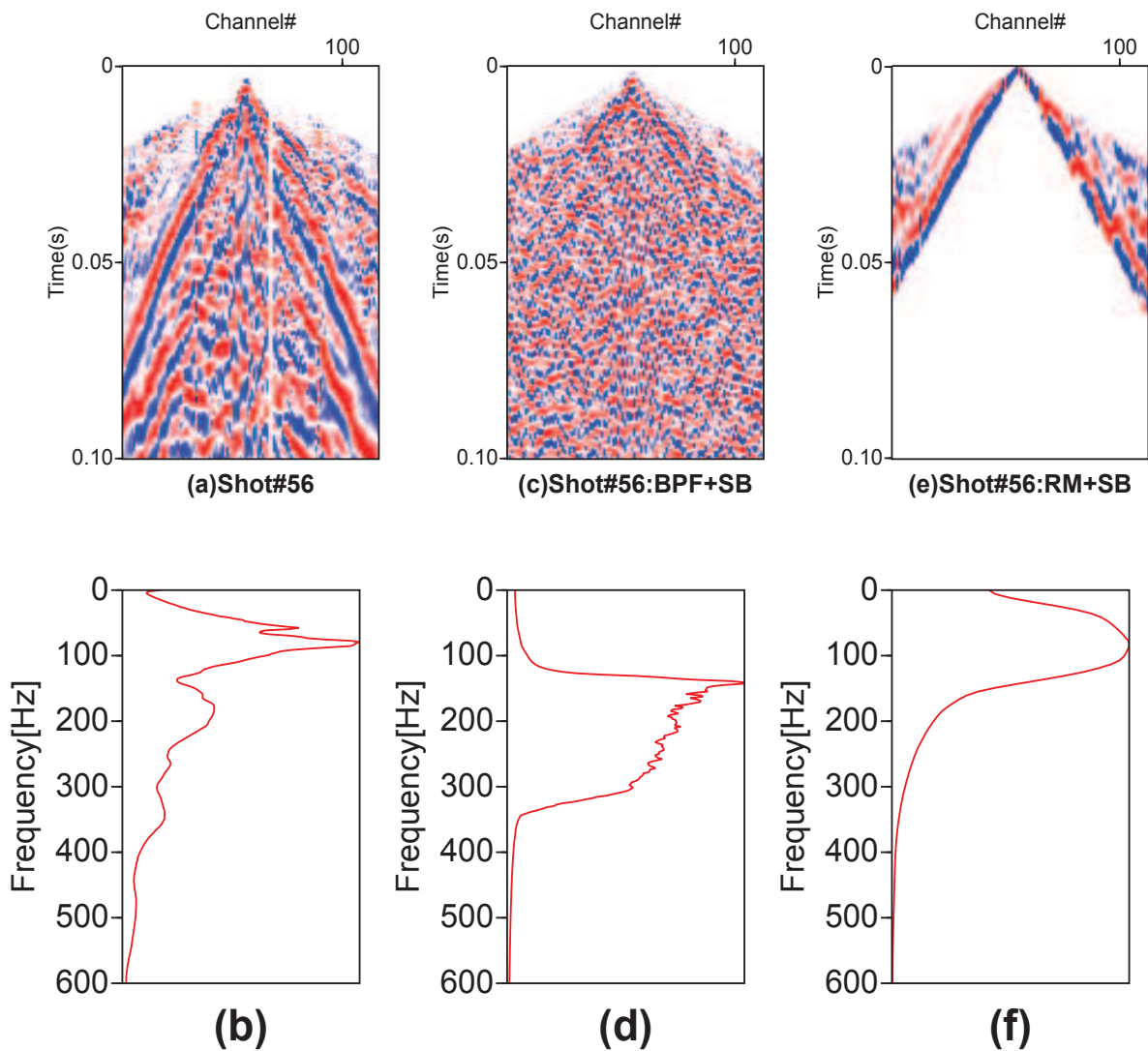
FIGURE 5.5 – a)Shot#56 after top muting and static correction ; b) Frequency spectrum of (a) ; c) Spectral Balancing of (a) ; d) Frequency spectrum of (b) ; e) Rayleigh wave muting and spectral balancing ; f) Frequency spectrum of (e).

## 5.4   Velocity analysis and NMO correction

For NMO correction the $V_{NMO}$ or stacking velocity is determined by velocity analysis, from CMP gathers, based on the semblance measure of the multi trace correlation (Neidell, N. & Taner, M, T., 1971). Velocity spectrum (Taner, M. T. &  Koehler, F., 1969) is used to determine stacking velocities over a narrow time window for a range of velocities by means of semblance. The semblance coefficient is defined as

$$S_c = \frac{\sum_{j=k(i)-W/2}^{k(i)+W/2} (\sum_{i=1}^{M} f_{i,j(i)})^2}{M \sum_{j=k(i)-W/2}^{k(i)+W/2} \sum_{i=1}^{M} f_{i,j(i)}^2} \tag{5.1}$$

Where $f_{i,j(i)}$ is the amplitude of $j^{th}$ sample of $i^{th}$ trace in the ensemble of M traces. W is the window size. The semblance is calculated along the surfaces $k(i)$.

Accuracy of $V_{NMO}$ or stacking velocity is influenced by numerous factors including S/N ratio, dip and depth of the reflector, spread length, time gate length, data bandwidth, stacking fold, velocity range and offset range etc.

Normal Move Out (NMO) correction is aimed to flatten the constant-offset section to zero-offset section by taking into account the respective offsets and subsurface layers velocities. For dipping layers DMO does the same job as NMO by also taking into account the corresponding events dips. For the horizontally stratified medium and considering the small spread approximation, maximum offset in the spread is smaller than the maximum target depth, the NMO equation is

$$t_x^2 = t_\circ + \frac{x^2}{V_{NMO}^2} \tag{5.2}$$

Where $x$, $t_\circ$, $V_{NMO}$ is the source-receiver offset, zero offset time for a normal incident ray and the NMO or stacking velocity respectively. Equation 5.2 is a hyperbolic travel time equation. NMO correction is the difference between the travel time of a reflected wave at an offset $x$ and zero offset travel time at that position. Mathematically it is written as

$$\triangle t_{NMO} = t_x - t_\circ = t_\circ [ \sqrt{1 + (\frac{x}{t_\circ v_{NMO}})^2} - 1 ] \tag{5.3}$$

NMO correction depends on the velocity and offset . For shallow and large offset NMO correction result in frequency distortion called NMO stretching. This produce the wavelet whose dominant period $T_\circ$ becomes greater than its original period $T$ (Yilmaz, O., 2001). Mathematically it can be described as

$$\frac{\triangle f}{f} = \frac{\triangle t_{NMO}}{t_\circ} \tag{5.4}$$

Where $f$ and $\triangle f$ is the dominant frequency corresponding to dominant period $T_\circ$ and change in frequency respectively. NMO stretching may be responsible for high frequency component of the amplitude spectrum. NMO stretch muting may be helpful to reduce frequency distortion as proposed by (Miller, R, D., 1992) but will result in reduced stacking fold for shallow events.

Recently non stretch NMO technique is introduced by (Perroud, H. & Tygel, M., 2004).
For 2D seismic line velocity analysis is carried out for several cdps. Figure 5.6 and figure 5.7
show the velocity analysis and NMO correction along with stacked section for 2D and 3D case
respectively. Note the cdp before and after NMO correction and how events are aligned in the
corresponding stacks.
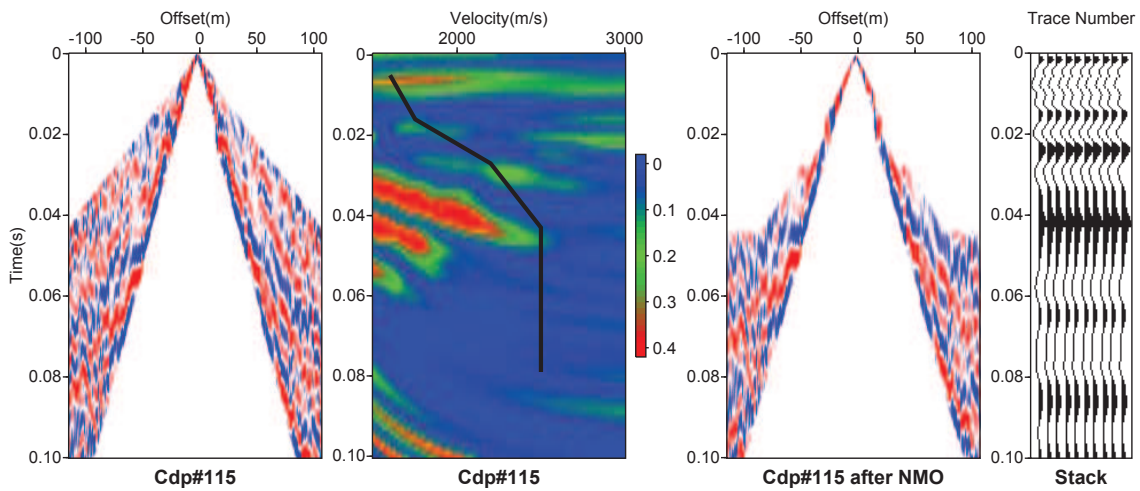


FIGURE 5.6 – Velocity analysis, NMO correction and stacked cdp for 2D case.
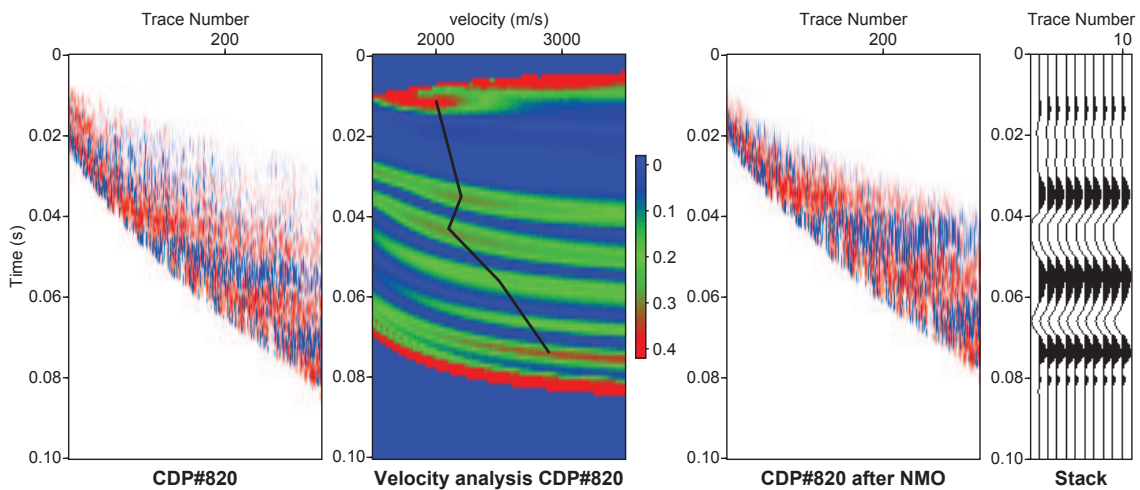


FIGURE 5.7 – Velocity analysis, NMO correction and stacked cdp for 3D case.

## 5.5 Residual Static Correction

Residual static correction, applied to compensate small time shifts or small wavelength statics that are not fully corrected in static correction due to complex subsurface velocity variations, will lead to an improved final stack section. Residual static correction is not only simple time shift but, based on surface consistency assumption is based on the fact that delay times are function of sources and receivers locations on the surface rather than raypaths in the subsurface, also includes phase and amplitude component.

There are different methods available for calculation of residual static correction but in this study stack power maximization method(Ronen, J. & Claerbout, J. F., 1985), maximization of the power of the sacked trace over the time window being analysed, is used for residual static correction. For a specific source point range of time shifts are applied and the one that produce highest stack power is chosen, this process is repeated for all the sources and receivers for a line to obtain the surface consistent residual static correction. This method involves the creation of two supertraces, from common shot gather under consideration and other one from the stacked traces of the common shot gather. Consider the shot and stack supertraces denoted by $F(t)$ and $G(t)$ respectively. The stack power of sum of these two traces over a time window t is given by :

$$P(\Delta t) = \sum_t [F(t - \Delta t) + G(t)]^2 \tag{5.5}$$

Where $\Delta t$ is the trail static shift applied to shot supertrace $F(t)$.
By expanding above equation

$$P(\Delta t) = \sum_t F^2(t - \Delta t) + \sum_t G^2(t) + 2 \sum_t F(t - \Delta t)G(t) \tag{5.6}$$

Here first two terms are the powers of the the respective supertraces while third term is the cross correlation of the supertraces.

For 3D case large residual correction values are observed as shown in last row of figure5.8, green color, calculated by stack power maximization method. Although the global trends for weathering correction calculated by delay time inversion (red lines) and residual static correction (green lines) are same but the magnitude of residual correction is many order greater than weathering correction. The first column of figure 5.8 shows the comparison of elevation static, static correction and residual correction for the cdp processed after Rayleigh wave filtering. While the second column shows the same cdp processed with Rayleigh wave muting and compared with elevation correction, static correction and residual correction. Not how for, figure 5.8f, the cdp amplitude, time and phase alignment after residual static correction is improved as compared to the elevation and static correction.
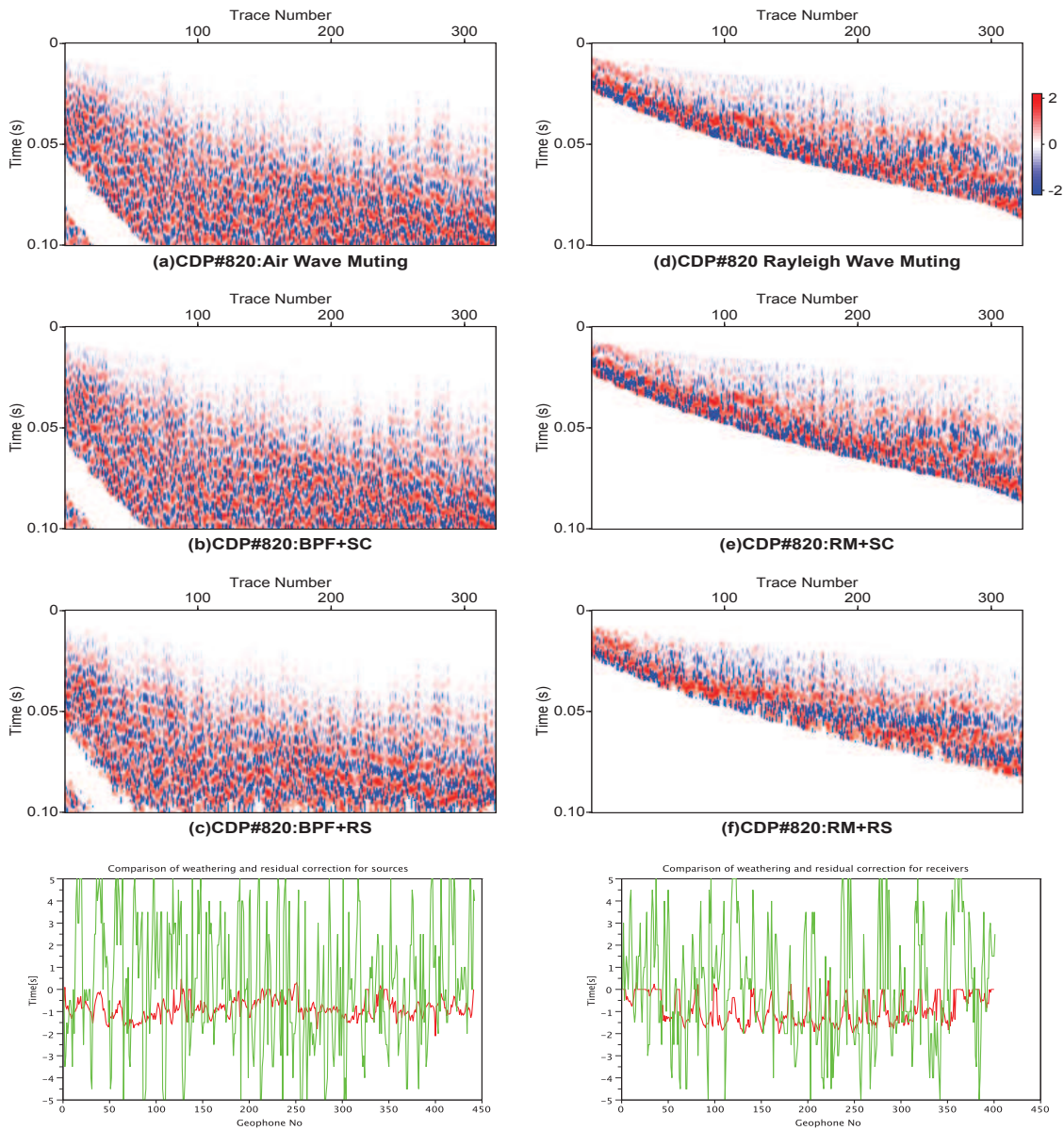
FIGURE 5.8 – Comparison of processing with and without residual static correction ; a) Air wave muting ; b) High bandpass filtering, (60-80-120-150)Hz, and static correction ; c) High bandpass filtering, (60-80-120-150)Hz, and residual static correction ; d) Rayleigh wave muting ; e) Rayleigh wave muting and static correction ; f) Rayleigh wave mute and residual static correction (Note how events are amplitude balanced, phase and time aligned after surface consistent residual correction). Comparison of weathering correction and residual static correction for sources and receivers, where green and red lines represent the residual correction calculated by stack power maximization method and weathering corrections calculated by delay time inversion methodology.

## 5.6   Common Reflection Surface Stack

CRS methodology, proposed by (Müller et al., 1998), is based on the several parameters travel-time equation. It is data driven technique to obtain high resolution, high S/N ratio zero offset stack data that correctly takes into account the location, orientation and curvature of the subsurface reflector. CRS method uses the available data, requires minimum *a priori* information and is fully data driven. CRS works with stacking operator and stacking parameters. For 2D zero offset case 3 stacking parameters are required while for 3D zero offset case 8 parameters are required(Mann, J., 2002). CRS is a model independent seismic reflection imaging technique formulated by paraxial travel time formulas (Jäger, R., 1999; Müller, T., 1999) that rely on the hypothetical wavefronts described by (Hubral, P., 1983). These hypothetical wavefronts correspond to the exploding reflector and explosion of a point source, as shown in figure 5.9.
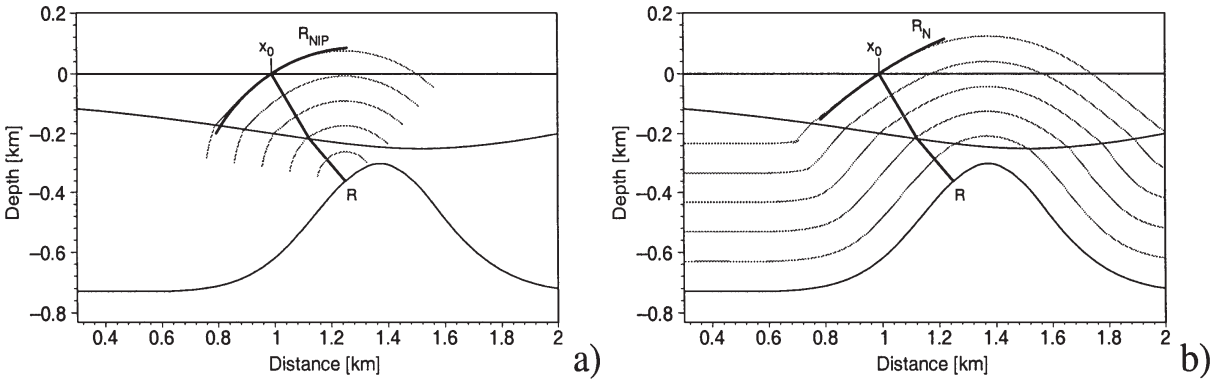


FIGURE 5.9 – a) NIP wave for point source R. b) Normal wave for the exploding reflector at R ( after (Jäger et al., 2001)).

The CRS stacking operator, travel time surface, for a point $P_o = (x_o, t_o)$ for 2D ZO section is given by (Schleicher et al., 1993; Tygel et al., 1997)

$$t^2(x_m, h) = [t_o + \frac{2 sin\alpha}{v_o}(x_m - x_o)]^2 + \frac{2t_o cos^2\alpha}{v_o}[\frac{x_m - x_o)^2}{R_N} + \frac{h^2}{R_{NIP}}] \tag{5.7}$$

Where h, $x_m$, $v_o$ and $t_o$ is half-offset, midpoint, near surface velocity and zero offset time respectively. The attributes, that define the wavefront in the observational plane, $\alpha$, $R_{NIP}$ and $R_N$ are the angle of emergence, radius of curvature of NIP wave and radius of curvature of the normal wave respectively. CRS stacking operator fits an actual reflection event in the multi-coverage data through three stacking parameters $\alpha$, $R_{NIP}$ and $R_N$. For fast implementation of the algorithm a three one parametric search is performed instead of one three parametric search (Mann et al., 1999).

Consider the case $x_m = x_o$ when equation 5.7 reduces to well known CMP hyperbola equation

$$t^2_{CMP}(h) = t^2_o + \frac{2t_o h^2 cos^2\alpha}{v_o R_{NIP}} \tag{5.8}$$

This formula becomes

$$t^2_{CMP}(h) = t^2_o + \frac{4h^2}{v^2_{NMO}} \tag{5.9}$$

105

where

$$v_{NMO}^2 = \frac{2v_\circ R_{NIP}}{t_\circ cos^2\alpha} \tag{5.10}$$

For $h = 0$ equation 5.7 reduces to

$$t_{ZO}^2(x_m) = [t_\circ + \frac{2sin\alpha}{v_\circ}(x_m - x_\circ)]^2 + \frac{2t_\circ cos^2\alpha}{v_\circ R_N}(x_m - x_\circ)^2 \tag{5.11}$$

For plane normal waves emerging from the surfaces, $R_N = \infty$ the above equation becomes

$$t_{ZO}(x_m) = t_\circ + \frac{2sin\alpha}{v_\circ}(x_m - x_\circ) \tag{5.12}$$

For $v_{NMO}$ calculation coherence analysis is applied using $NMO$ travel time by using semblance as proposed by (Neidell, N. & Taner, M, T., 1971)

$$S_c = \frac{\sum\limits_{j=k(i)-W/2}^{k(i)+W/2} (\sum\limits_{i=1}^{M} f_{i,j(i)})^2}{M \sum\limits_{j=k(i)-W/2}^{k(i)+W/2} \sum\limits_{i=1}^{M} f_{i,j(i)}^2} \tag{5.13}$$

Where $f_{i,j(i)}$ is the amplitude of $j^{th}$ sample of $i^{th}$ trace in the ensemble of M traces. W is the window size. The semblance is calculated along the surfaces $k(i)$.

CRS method implementation is two stage process. First stage consist of three successive parameter search tested for specific gather in the data and will result in initial stack. In second stage an optimized CRS stack is obtained by three parameter search for whole data by using the input from the initial stack.

## 5.7   Comparison of the results

Figure5.10(a) and (b) shows the final stacks obtained after conventional processing and CRS methodology respectively. Both stacks convey almost the same information although one can observe the minor difference between these two. In both cases the required imaging is not possible owing to the lack of low frequency content.

Figure5.10(c) and (d) shows the stacks of same 2D line, processed by Rayleigh wave muting, after applying conventional and CRS approaches. These both figures gives the good results as compared to the figure5.10(a) and (b) because of the presence of low frequency content. Here the main reflectors are clearly visible.

Figure5.11(a) shows the coherency attribute and velocity distribution of the whole 3D block. Coherency values are weak in upper and lower time section but occasionally very strong values are observed in the 0.02 to 0.04s time window. Similarly velocity distribution is fairly distributed and does not show much lateral variation. The same velocity profile is observed by the classical velocity analysis.

Figure5.11(b) shows the stacks obtained after the classical and CRS methodology. Both stacks correctly shows the reflectors on the time section but the reflectors are sharp in the classical

106

approach.

Figure5.12 shows the coherency attribute, velocity and final stack for the in-line and cross-line with obvious difference of in-line and cross-line and their respective attributes.

Although both processing strategies result in stacked data of alike features, the stack data resulted from conventional processing is opted for migration and further for interpretation. Although theoretically CRS should produce higher quality stacked data compared to the conventional processing but in this case it is not true. This might be ascribed to the low signal/noise ratio data, low coherency of the data as evident from the figure 5.11(a). This low coherency might affect the consequent CRS processing.

The resulting images, both from NMO and CRS stacks, not only reveal main quasi horizontal events but also some diffraction patterns that are overprinted on them, with steeping events that can be followed on in-line and cross-line sections. Therefore migration appears to be necessary to focus such events followed by interpretation using attribute analysis. Migration is discussed in the next section while attribute analysis is discussed in next chapter.

**(a) NMO Stack after Rayleigh wave filtering**



**(b) CRS Stack after Rayleigh wave filtering**



**(c) NMO Stack after Rayleigh wave muting**



**(d) CRS Stack after Rayleigh wave muting**
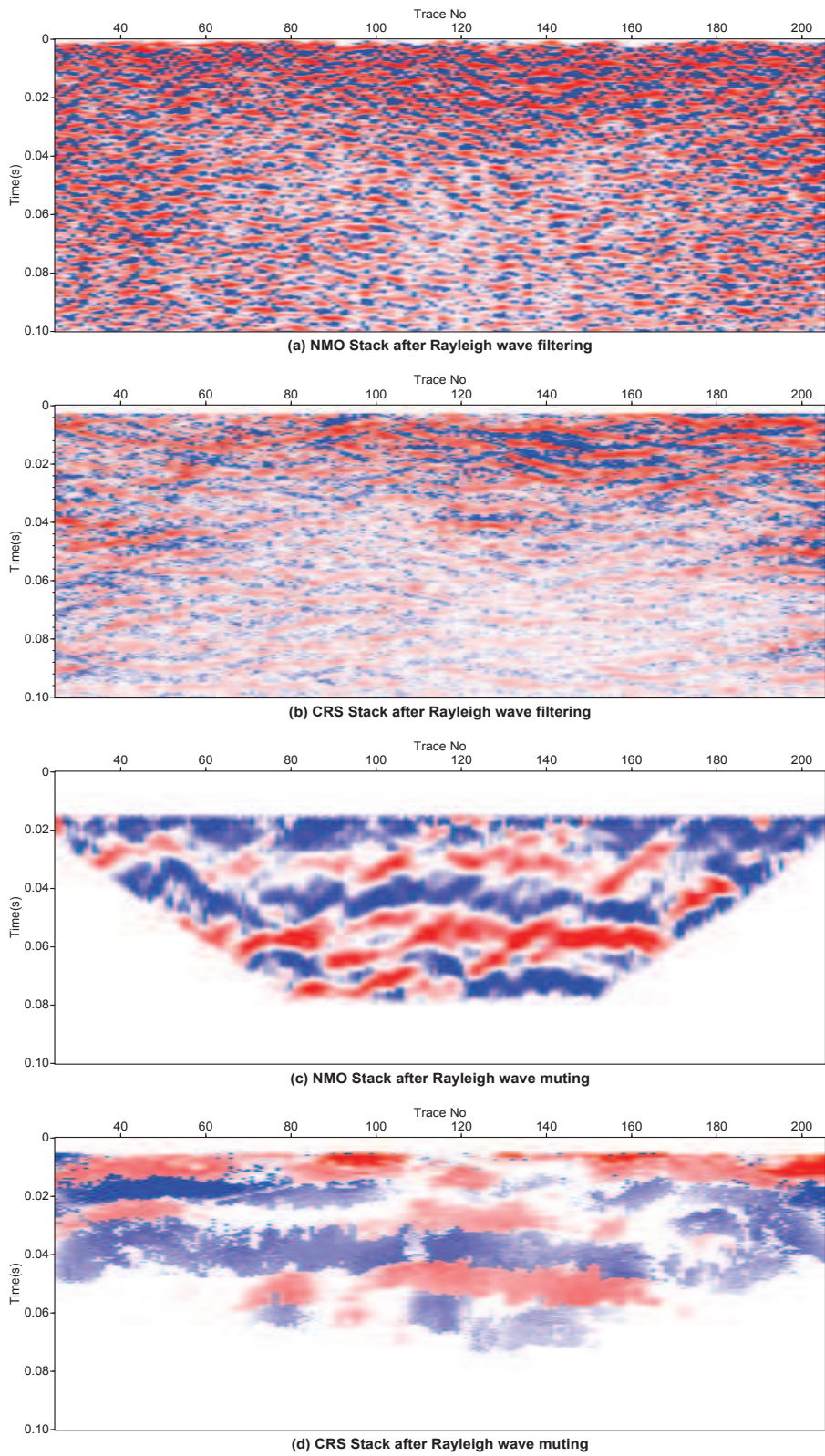
FIGURE 5.10 – Comparison of NMO and CRS stack for 2D case.
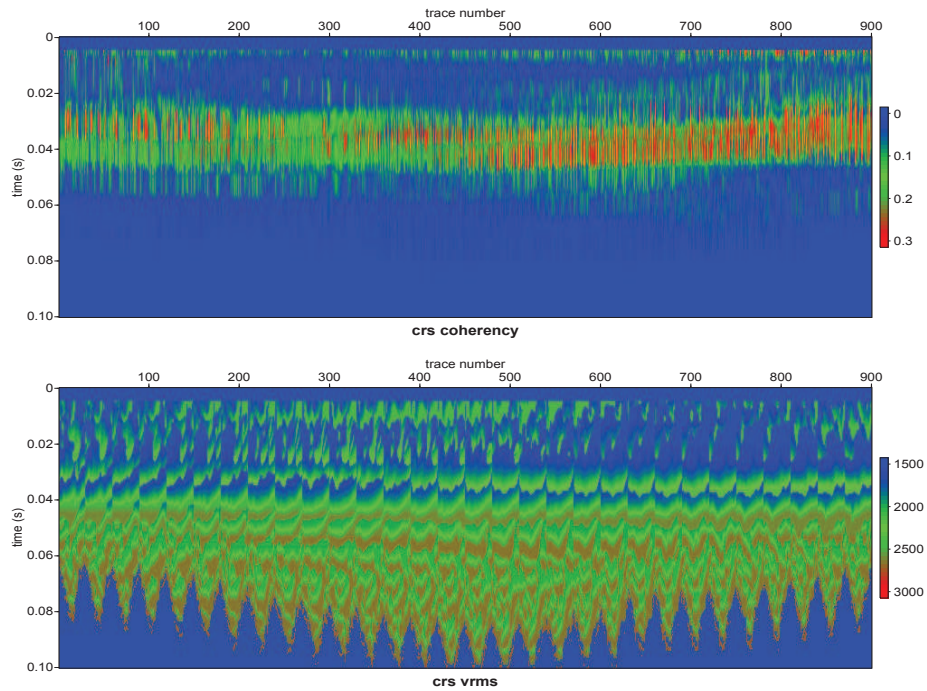
(a)
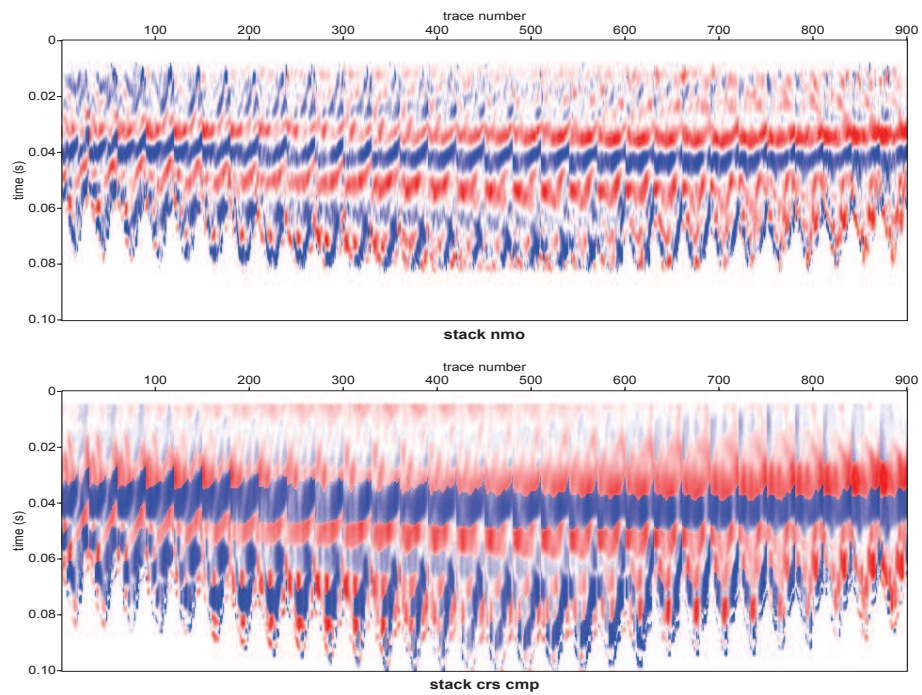


(b)

FIGURE 5.11 – a) Coherency attribute (above) and Vnmo Velocity(below). b) NMO stack (above) and CRS stack (below)
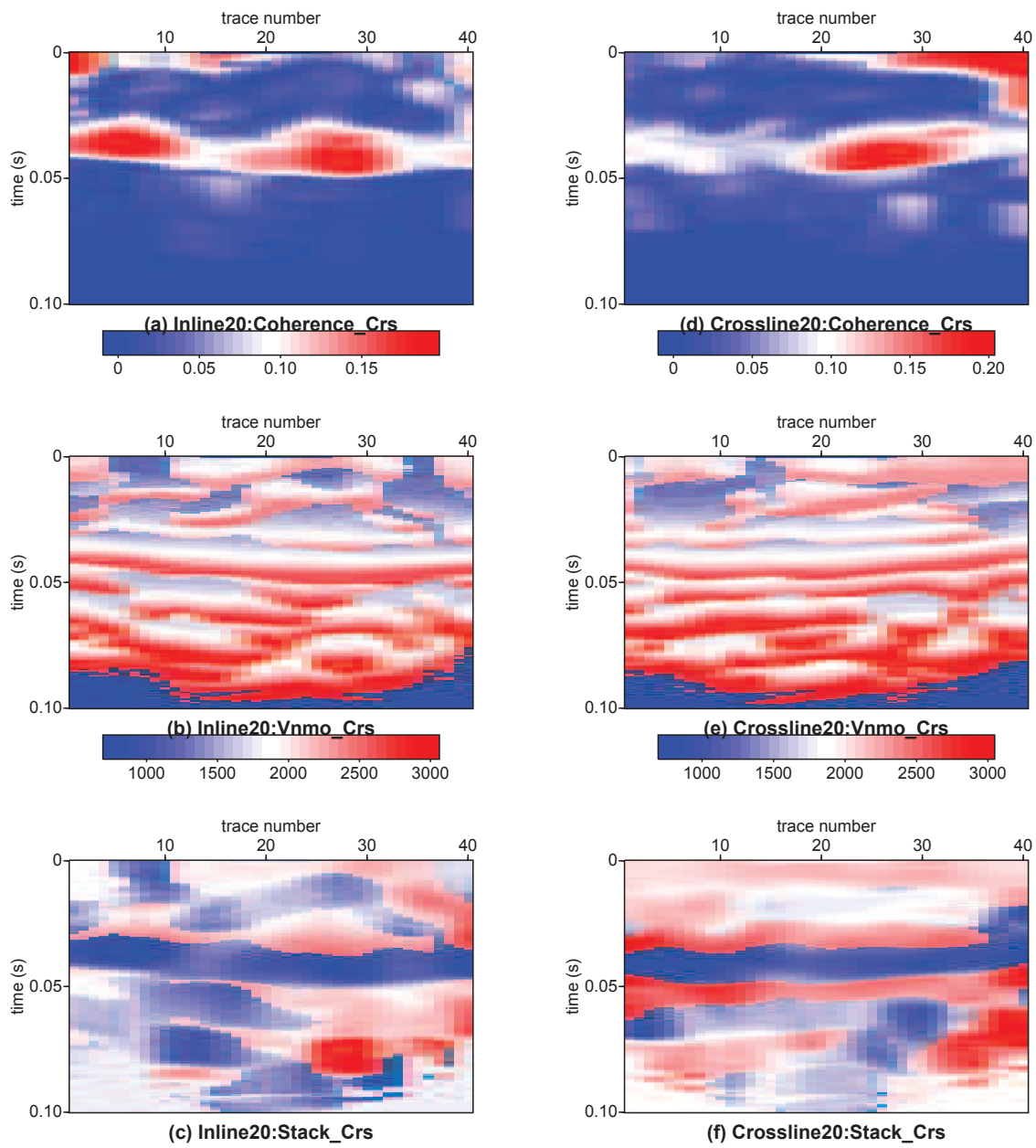
Figure 5.12 – CRS attributes and stacked Inline and Crossline

110

## 5.8  Migration

Theoretically each reflection event on the seismic section is the mid-point of an appropriate CMP gather. But in reality this scenario is not honoured due to subsurface structural features and dipping layers. Due to this reflection events on the seismic section are displaced temporally and spatially. Moreover structural and stratigraphic heterogeneities result in lateral and vertical velocity variations and diffractions contaminates the seismic signals. Migration is the process to collapse these diffracting events, repositions the seismic events on the seismic section to their appropriate position in the subsurface and improves the horizontal resolution by focusing the energy over the Fresnel zone. There are several techniques for seismic data migration. These seismic migration techniques can be grouped into integral or summation methods and differential methods. The Kirchoff migration belongs to integral methods while reverse time and finite difference migration belongs to second type. These migrations algorithms are solved in space time(t,x), frequency space(f,x) wavenumber time(t,k) or any combination of these methods. These techniques can be grouped into Kirchoff type, Finite difference and Frequency wavenumber. Every migration technique plays its role with inherent pros and cones. Seismic velocity is an important parameter for migration. There are several type of seismic velocities. Accuracy of velocity for seismic migration is of vital importance. Normally for seismic migration stacking velocities are used deduced from velocity analysis. In this study interval velocity extracted from VSP survey is used for migration, figure 5.13a.



(a) Vint as a function of depth        (b) Vint and Vrms as a function of time
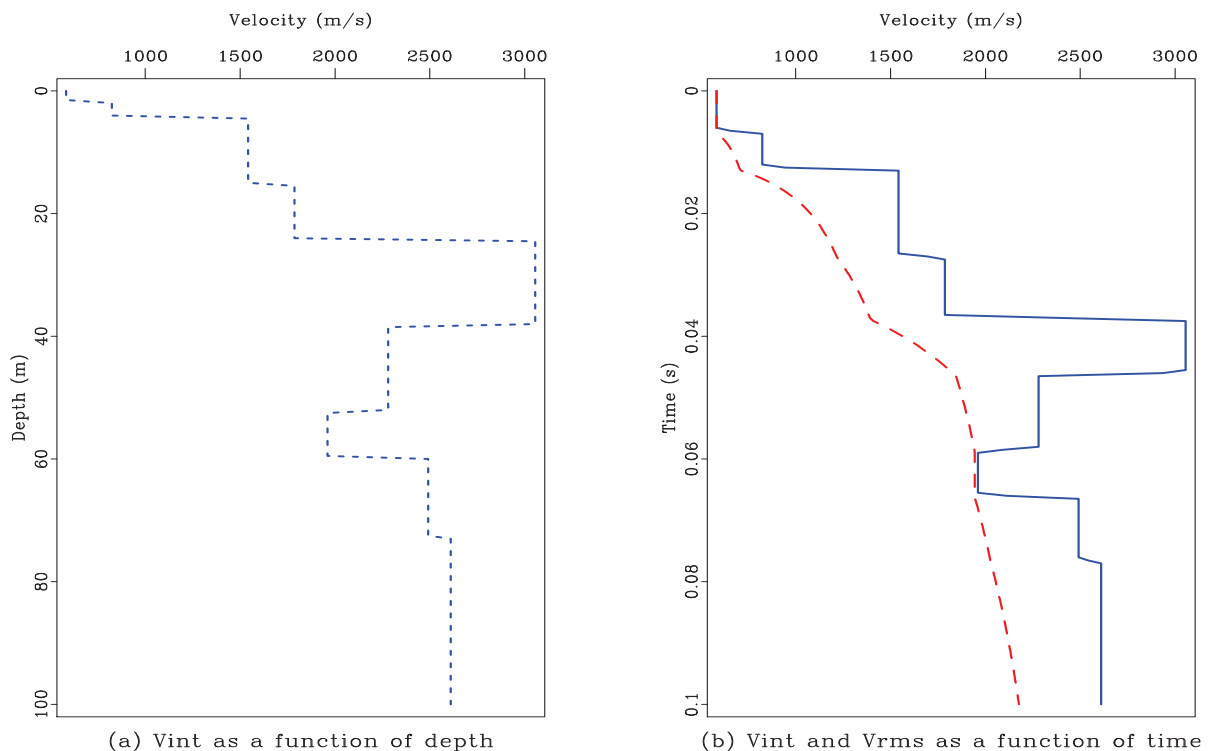
FIGURE 5.13 – Velocity models.

111

This interval velocity is then converted to root mean square velocity by using the Dix formula

$$V_{int} = \sqrt{\frac{(V_{rms,n}^2)t_n - (V_{rms,n-1}^2)t_{n-1}}{t_n - t_{n-1}}} \tag{5.14}$$

Seismic interval velocity is the average velocity of a particular depth interval while root mean square (rms) velocity is the weighted average velocity for stratified earth from surface to the $n^{th}$ layer. Figure 5.13a shows the interval velocity as a function of depth while interval and root mean square velocities as the function of time are shown in figure 5.13b. For Stolt and Stolt-Strech rms velocity is used while for split step Fourier migration(zero offset depth migration) interval velocity is used.

### 5.8.1 Stolt Migration

Stolt migration technique proposed by (Stolt, R. H., 1978) is performed in *f-k* domain based on exploding source model. Consider the scalar field component, $p(x,y,z,t)$, resulting from an exploding source. This component satisfies the scalar wave equation :

$$\nabla^2 p(x,y,z,t) - \mu^2 \frac{\partial^2}{\partial t^2} p(x,y,z,t) = 0 \tag{5.15}$$

Applying the forward Fourier transformation with respect to x, y and t coordinates

$$\frac{\partial^2}{\partial z^2} P(k_x,k_y,z,\omega) = (k_x^2 + k_y^2 - (\frac{\omega}{v})^2) P(k_x,k_y,z,\omega) \tag{5.16}$$

This transformation along x and y coordinates is only valid if the velocity is constant in both directions.
where, $\omega = 2\pi f$, is angular frequency and wavenumber, $k_z$, is defined as :

$$k_z = \mp \sqrt{(\frac{\omega}{v})^2 - k_x^2 - k_y^2} \tag{5.17}$$

Where

$$P(k_x,k_y,z,\omega) = \iiint p(x,y,z,t) e^{(ik_x x + ik_y y - i\omega t)} dx dy dt \tag{5.18}$$

The general solution of equation 5.16 is :

$$P(k_x,k_y,z,\omega) = A(k_x,k_y,z,\omega)e^{ik_z z} + B(k_x,k_y,z,\omega)e^{-ik_z z} \tag{5.19}$$

Since we are only dealing with upcoming waves and for zero offset time data $p(x,y,0,t)$. The inverse Fourier transformation of above equation will represent the migrated data at depth z at time t=0

$$p(x,y,z,0) = \iiint P(k_x,k_y,0,\omega)e^{-i(k_x x + k_y y + k_z z)} dk_x dk_y d\omega \tag{5.20}$$

Stolt migration is based on single constant velocity that's why it is not very efficient most of the time but it is computationally very fast and can be used as first hand check or residual migration.

112

### 5.8.2 Stolt Stretch Migration

Stolt stretch migration is the variant of Stolt migration. In this method vertically varying velocity is being used instead of constant vertical velocity. According to (Fomel, S. & Vaillant, L., 2001) stolt-stretch comprised of following

   – Stretch the time variable
   – Interpolation of the stretched time to the regular gird
   – Double forward Fourier transformation
   – Stolt migration
   – Inverse Fourier transform
   – Inverse stretching or shrinkage of the time axis

### 5.8.3 Split Step Fourier Migration

Split-step Fourier migration, developed on the basis of vertical wavenumber , was propose by (Stoffa et al., 1990) . This method is based on phase-shift migration (Gazdag, J., 1978). First phase shift is applied in frequency-wavenumber domain that uses the constant reference slowness and second phase shift is applied in frequency-space domain that uses the perturbation. This method takes into account the laterally and vertically varying velocities by use of reference slowness and perturbation respectively. Consider the acoustic wave equation of a constant density medium :

$$\nabla^2 p - \mu^2 \ddot{p} = 0 \tag{5.21}$$

Where $p = p(x, y, z, t)$ and $\mu = \mu(x, y, z)$ is pressure and medium slowness respectively. Where $\mu(x, y, z)$ is half of the propagation velocity as required by exploding reflector model (Loewentha et al., 1996).
By taking the Fourier transformation of above equation

$$\nabla^2 P + \omega^2 \mu^2 P = 0 \tag{5.22}$$

where $P(r, z, \omega) = \int_{-\infty}^{\infty} p(r, z, t) \exp^{-\iota \omega t}$ and r is the horizontal position vector, $r = |r| = \sqrt{x^2 + y^2}$
Decomposing the slowness field into reference slowness, which is mean slowness, and perturbation which varies with reference to this mean slowness

$$\mu(r, z) = \mu_\circ(z) + \triangle \mu(r, z) \tag{5.23}$$

putting  5.23 into  5.21 we get

$$\nabla^2 P + \omega^2 \mu_\circ^2 P = -S(r, z, \omega) \tag{5.24}$$

Thus inclusion of $S(r, z, \omega)$ transformed the homogeneous equation  5.22 into inhomogeneous equation.
The Fourier transform the previously migrated upgoing wave field at depth $z_n$, $P_u(r, z_n, \omega)$ to wavenumber space

$$\tilde{P}_u(k_r, z_n, \omega) = \int_{-\infty}^{\infty} P_u(r, z_n, \omega) \exp^{-ik_r \cdot r} dr \tag{5.25}$$

Where $k_r = |k_r| = \sqrt{k_x^2 + k_y^2}$ is horizontal wave vector.
Next apply the phase shift by using the reference slowness for all frequencies and wavenumber on the vertical wavenumber

$$\tilde{P}_l(k_r, z_n, \triangle z, \omega) = \tilde{P}_u(k_r, z_n, \omega) \exp^{-ik_{z_\circ} \triangle z} \tag{5.26}$$

113

Where $k_{z_o} = \omega\mu_o\sqrt{1 - (k_r/\omega\mu_o)^2}$ and $\mu_o^2$ is the average slowness for small interval $\triangle z$. Inverse Fourier transform of the phase shifted data is

$$P_l(r, z_n, \triangle z, \omega) = (\frac{1}{2\pi})^2 \int_{-\infty}^{\infty} \tilde{P}_l(k_r, z_n, \triangle z, \omega) \exp^{-ik_r \cdot r} dk_r \qquad (5.27)$$

Next apply the second phase shift which corresponds to the perturbation in slowness in the same small interval $\triangle z$ that result in

$$P_u(r, z_{n+1}, \omega) = P_l(r, z_n, \triangle z, \omega) \exp^{-\iota\omega\triangle\mu(r,z)\triangle z} \qquad (5.28)$$

To obtain the migrated data for the current depth over all the frequencies of interest integrate the above equation

$$p(r, z_{n+1}, 0) = (\frac{1}{2\pi})^2 \int_{-\omega}^{\omega} P_u(r, z_{n+1}, \omega) d\omega \qquad (5.29)$$

## 5.9 Application of migration for field data

In the onward discussion the original and deconvolved sections are compared. Before applying the migration the smoothing/deconvolution is performed by estimating the prediction error filter followed by the helix deconvolution, the idea was introduced by(Claerbout J.F., 1998). This smoothing will improve the efficiency and accuracy of the migration by avoiding the sparse values that otherwise might be taken as dips and diffracted events. Figure5.14 shows the data before and after deconvolution. Observe the smoothness of the data after deconvolution.

Figure 5.15 show the Inline#30 migrated with stolt, stolt stretch and split step Fourier migration. For stolt migration 1800m/s velocity is used while for the stolt strech velocity profile shown in figure 5.13b is being used. For split step Fourier migration 3D velocity model is constructed from the interval velocity profile deduced from VSP shown in figure 5.13a. For split step Fourier transformation the interval velocity only varies vertically while it is constant in inline and crossline direction. This is also evident from the velocity acquired as an attribute from CRS method. As one can observe the stolt and stolt stretch methods do not migrate the data well but split step Fourier migration migrated the data. Figure 5.15 (right column) shows the original and migrated inline after deconvolution. Figure 5.16 shows crossline#30 with all aforementioned migration methods. Finally figure 5.17 shows the migrated 3D block obtained after split step Fourier migration. Figure 5.17(c) and figure 5.17(d) show the migrated data before and after deconvolution. The deconvolved migrated block clearly shows the prominent reflection events.

114
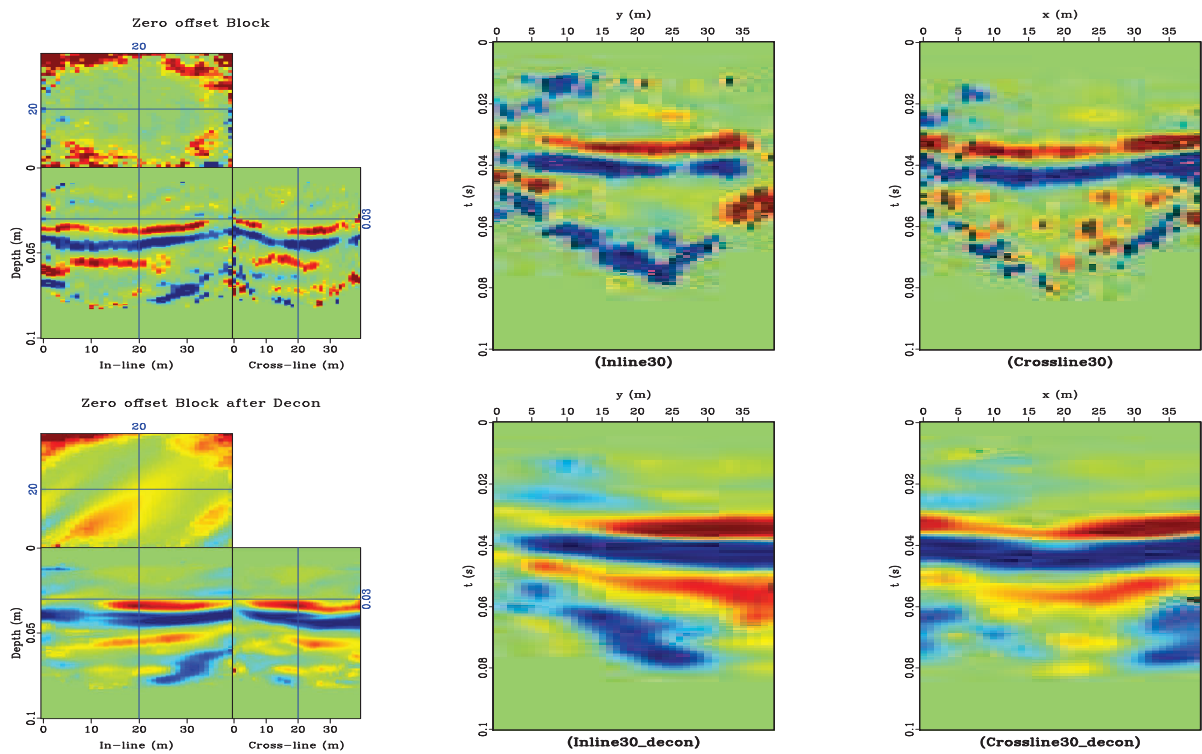
FIGURE 5.14 – ZO stack data, crossline and inline (Upper row). Same data after deconvolution (Lower Row).

115
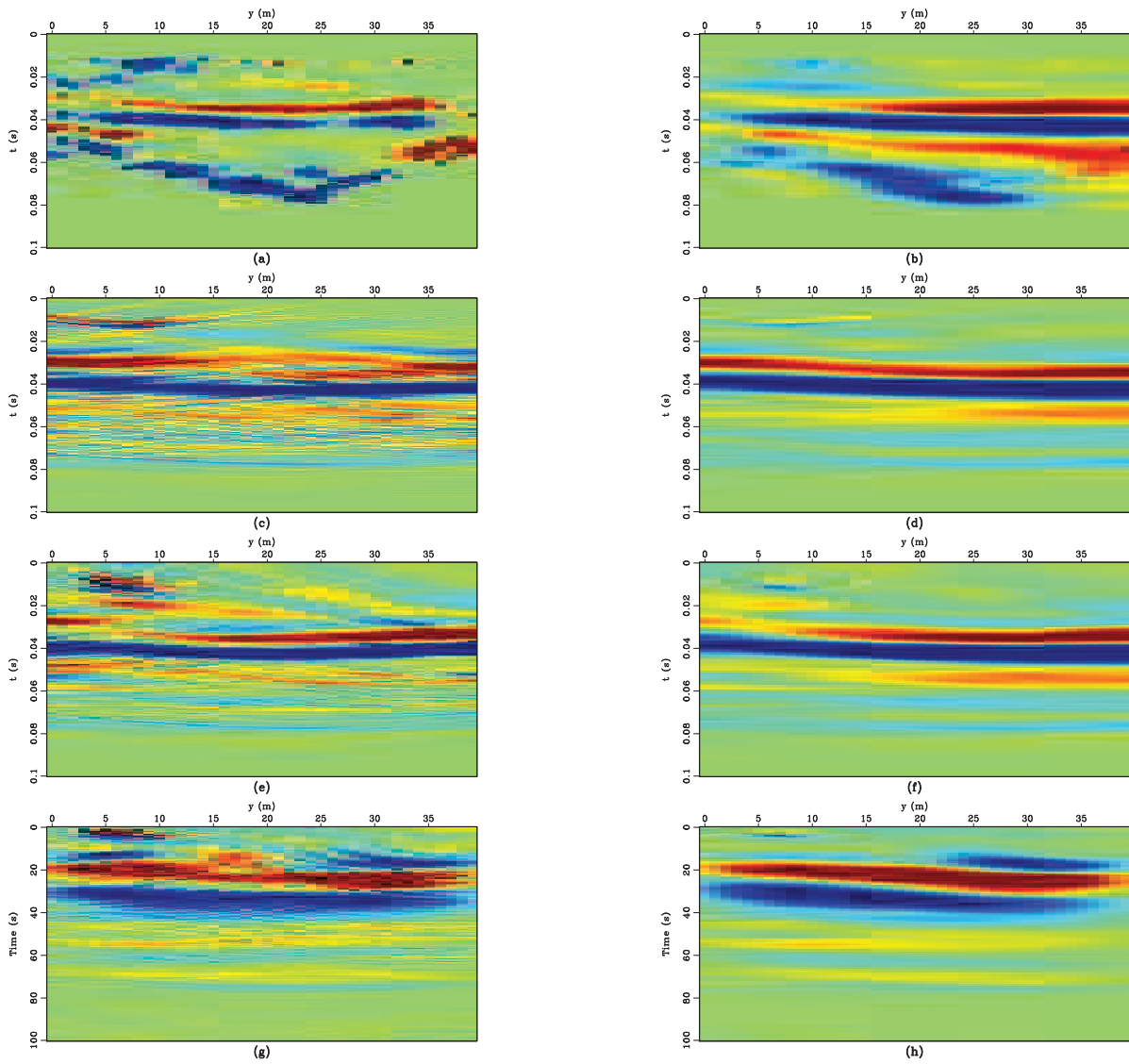
FIGURE 5.15 – a) Inline#30 ; b) Deconvolved inline#30 prior to migration ; c) Stolt migration of (a) ; d) Stolt migration of (b) ; e) Stolt-stretch migration of (a) ; f) Stolt-stretch migration of (b) ; g) ZO migration of (a) ; h) ZO migration of (b).
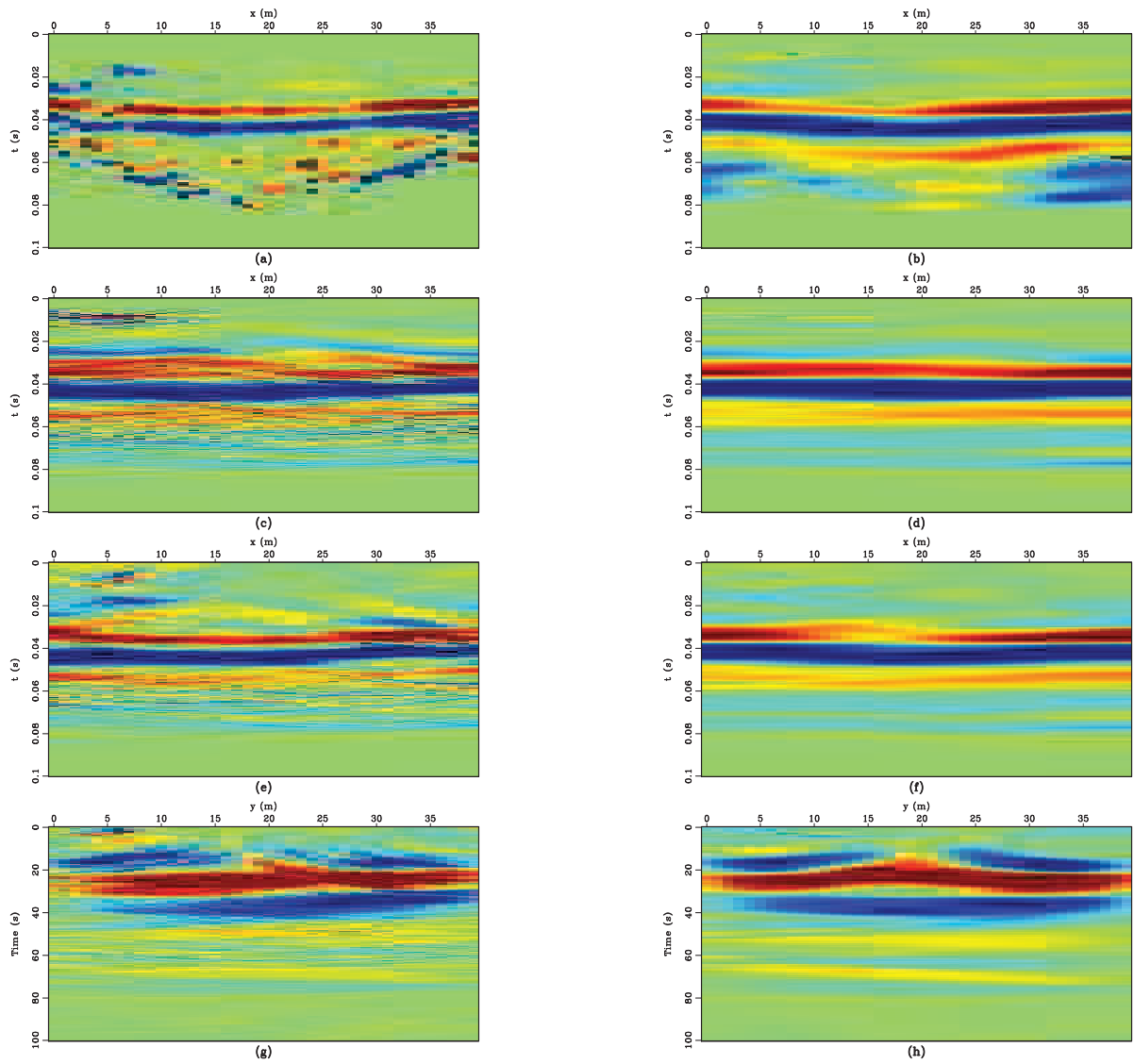
FIGURE 5.16 – a)Crossline#30 ; b) Deconvolved crossline#30 prior to migration ; c) Stolt migration of (a) ; d) Stolt migration of (b) ; e) Stolt-stretch migration of (a) ; f) Stolt-stretch migration of (b) ; g) ZO migration of (a) ; h) ZO migration of (b).
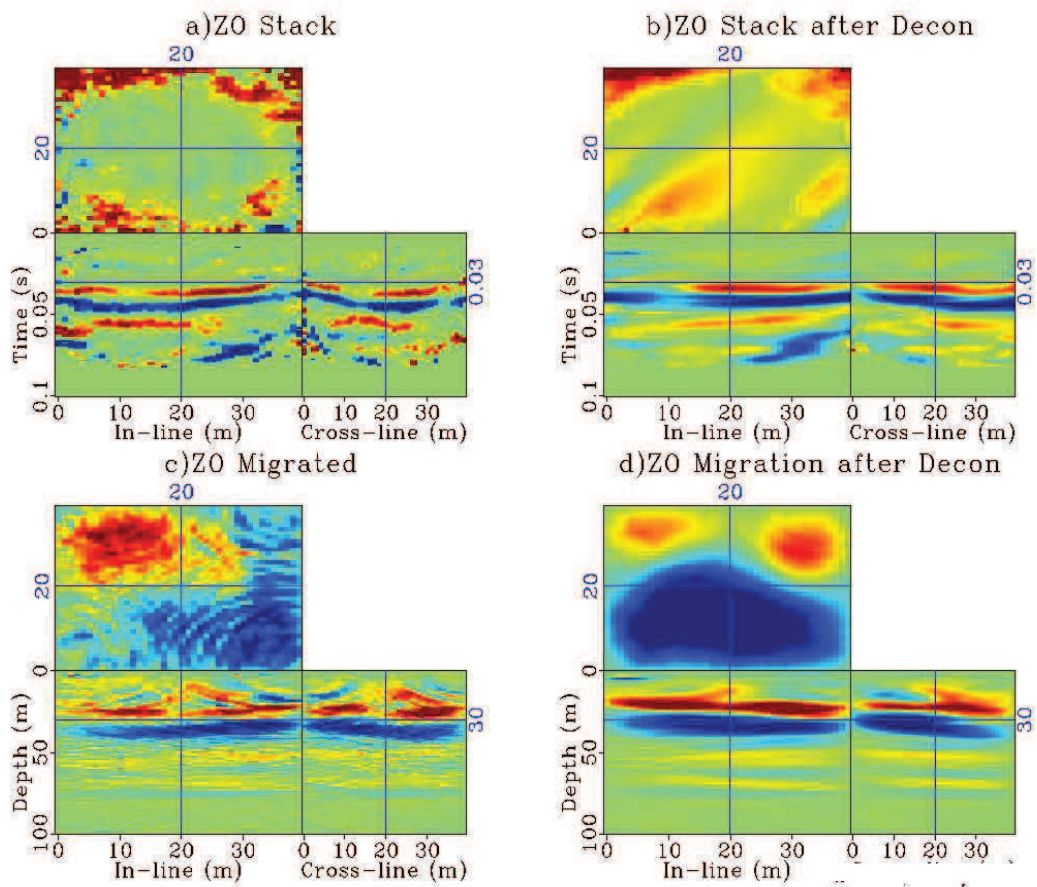
FIGURE 5.17 – a) Zero Offset stack data ; b) Zero offset stack data after deconvolution ; c) Migration of zero offset data ; d) Migration of deconvolved zero offset data.

## Résumé CHAPITRE 6

On appelle attributs sismiques les mesures quantitatives issues des données sismiques. Les attributs sismiques sont utilisés pour mettre en lumière et extraire les différents objets d'intérêt. Il existe différents attributs sismiques, chacun d'eux ayant un usage spécifique. Ces attributs peuvent s'appliquer aux données avant ou après sommation. Ces attributs opèrent sur les représentations temps/profondeur, les sections longitudinales ou transverses à la ligne d'acquisition ainsi que sur les différents horizons. Différents schémas de classification sont proposés dans la littérature sismique concernant des attributs dépendant de nombreuses propriétés.

L'inspection visuelle des différentes sections longitudinales et transverses montre la position et la forme des réflecteurs. Leurs positions varient selon les directions longitudinales et transverses. La pénétration de l'énergie est entravée par le réflecteur principal de plus haute impédance. De la même façon, différentes caractéristiques sont mises à jour pour différentes tranches en profondeur. L'horizon principal est pointé de façon semi-automatique. Cet horizon n'est pas régulier et présente un coin à l'extrémité de l'acquisition. Différentes sections longitudinales et transverses situées au niveau de l'horizon font état d'un changement dans la position et la forme de l'horizon pointé.

Un sismogramme synthétique 1D est généré en se basant sur un modèle de convolution. Pour calculer le contraste d'impédance on utilise le profil de vitesse d'intervalle construit à partir des premières arrivées au puits MC16 et associé à une densité constante. A partir d'ondelettes de Ricker centré sur différents pics fréquentiels on génère différents sismogrammes synthétiques 1D. Ces sismogrammes synthétiques montrent la position des réflexions principales et les interférences.

Différents attributs sont calculés par utilisation du programme OpendTect afin de délimiter les karsts et les reliefs karstiques. Les attributs de similarité fournissent des résultats insatisfaisants car ils dépendent uniquement de la cohérence de la forme d'onde. Les pentes sont calculées pour chaque échantillon dans le cube de données 3D et sont enregistrées comme pentes longitudinales et transverses. L'attribut rayon de courbure, utilisant les pentes calculées, laisse apparaître de nombreux reliefs karstiques à différentes profondeurs. Ces reliefs karstiques sont plus prononcés en zone saturée qu'en zone de vadose. On retrouve également des reliefs karstiques à proximité des deux puits localisés dans le cube 3D de sismique réflexion.

```
 ┌──────┐
 │      │6
 Chapitre
```

# Data Interpretation

## 6.1   Seismic Attributes for Reservoir Characterisation

Seismic attributes represent the particular features of the seismic data. These features are detected by individual or combination of attributes such as energy, amplitude, similarity, coherency and curvature amongst others. Literally exploration industry is burst of attributes. These attributes are applied in different manners to elaborate different structural and stratigraphic features, petrophysical properties, reservoir location, its architecture and heterogeneity and rock/pore fluid properties. Attributes enhance a particular feature and can be used only for that purpose such as different structural features are delineated by coherency, dip, azimuth and curvature attributes. Similarly amplitude attributes are manifestation of stratigraphic features. Attributes may be extracted from prestack and post stack data. These attributes operates on seismic section, time slices or depth slices and horizons. Meta attributes are intelligent combinations of individual attributes that are used for further analysis, modelling and inversion such as porosity detection through supervised or unsupervised neural networking. Logically any seismic attribute can be defined that bear objectivity.

As the attribute grows in number several authors classified the attributes in different group. The attributes are divided into geometrical and physical groups(Taner et al., 1994). Azimuth, dip and continuity constitute the geometrical group of attributes and helps in visibility of geometrical features of subsurface such as fault and discontinuities among others, while physical group consists of phase and frequency and these helps out in determining the physical parameters of lithology. Another scheme proposed by (Brown, A. R, 2004) that classified the attributes into time, amplitude, frequency and attenuation with further subclasses that operates both in pre and poststack data. In this scheme time attributes provide information on structure while amplitude attributes provide information about stratigraphy and reservoir. Another classification is proposed by (Chen, Q. & Sidney, S., 1997) based on wave kinematic, wave dynamic and geological reservoir features. Similarly classification of (Barnes, A. N., 1997) based on complex trace analysis is worth mentioning. Another more general classification is proposed by (Liner et al., 2004) dividing the attribute in general and specific classes. General class is composed of attributes that are measures of geometrical kinematic, dynamic or statistical features. These general attributes are based on physical or morphological character of the data representing the geology or lithology. Reflector amplitude, reflector time, reflector dip and azimuth, spectral decomposition, complex trace attributes, coherence and AVO fall in general attribute group.

These attributes are generally applicable to all the basin while specific attributes are only applicable in one case but not in another one. These attributes are sum, product or derivatives of fundamental attributes.

The understanding, conceptual development and extraction of attributes is owing to advent of digital recording and workstation. The quality and different types of attributes are indebted to modern recording and computational power. Every decade brought new attributes with improved quality. During analogue recording, notably 1950-1960, geometrical attributes, structural elevation, dip, thickness and discontinuities, were used to be successfully extracted but their correlation between lines were somewhat difficult and erroneous. These attributes were 2D. During the decade of seventies digital recording started and this brought amplitude related attributes in the exploration industry along with improved quality seismic data recording. Bright spots associated with gas become another exploration target gradually. Bright spot phenomena also includes dim spot, flat spot, polarity reversals and frequency losses. Seismic display in color mode with variable density and grey scale along with other colors proved another important milestone that helped a lot to locate amplitude related attributes ans subtle geometrical features. Variable area color scheme was first proposed by (Balch, A. H., 1971). Nigel Anstey and his team mates at the same time working at Seiscom Ltd developed innovative color display scheme. They successfully applied the color scheme to show interval velocity, reflection strength and frequency content. In the same decade complex trace attributes such as instantaneous envelope, instantaneous phase and instantaneous frequency came into limelight. These Instantaneous attributes are helpful to delineate change in acoustic impedance, rock/fluid content, reflector continuity and hence subtle structural features, attenuation and thin-bed tuning etc. This complex trace analysis latter give birth to seismic stratigraphy. This seismic stratigraphy helped to understand and delineate the depositional environment and processes.

3D seismic data acquisition and processing make the seismic attribute worthwhile. 3D seismic technology not only highly improved the data quality but also give new life to seismic attributes. Different seismic attributes were used for structural, stratigraphic matters. Automated Horizons were tracked which reduces the time and improved the accuracy.

## 6.2 Data Interpretation

Figure 6.1 shows every fifth in-line and cross-line sections through the 3D data cube. This figure shows the different reflectors, continuous and discontinuous, of varying shape. These reflectors are more pronounced in the central part. The reflectors shape and position along the in-line and cross-line directions vary considerably. This shape and position variation of reflectors is the manifestation of the subsurface heterogeneities. Reflectors shape and position variations is not smooth as shown in the successive in-line and cross-line panels. Even at the center of the cube the reflector shape and position change rapidly in cross-line direction. Different reflectors are present beneath this pronounced reflector. Although data was acquired with high frequency content but the presence of noise and subsequent processing to get rid of these noises limited the resulting frequency bandwidth. The dominant wavelength is approximately 20 m in this case. Therefore interference occurred and these reflectors are not sharply defined. Due to strong shallow reflectivity and small scale scatters, enough energy is not penetrated below this main reflector. The main reflector of pronounced reflectivity corresponds to the reefal complex in vadose zone.

Figure 6.2 shows the different depth slices from the data cube. These figures are showing the heterogeneities of the subsurface. Certain events are appearing and disappearing in these depth slices. Moreover the shape of heterogeneous bodies are also evident.

Figure 6.3a shows the picked horizon around 25m. This horizon is semi-automatically picked as the zero crossing surface. This reflector is not flat and is shallow in the central part, wedge shaped, while towards the side of survey it is deeper and smooth. Figure 6.3b shows the horizon through cross-line section where green color line shows the horizon position on this cross-line. It also shows the shallowness of the horizon at the central part. In figure 6.3c two in-line sections at different positions through the horizon indicate the horizon position. Notice the bump on the in-line#28 compared to the in-line#15. Similarly in-line and cross-line sections are shown through the shallow part of the horizon in the figure 6.3d.

To understand the origin of this strong reflection event, synthetic seismogram is constructed from the VSP, of borehole MC16, velocity profile.
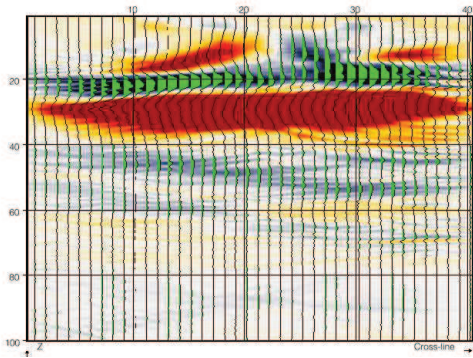
(a) Inline#1
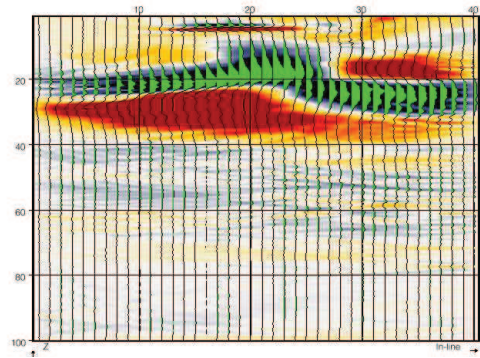
(b) Crossline#1
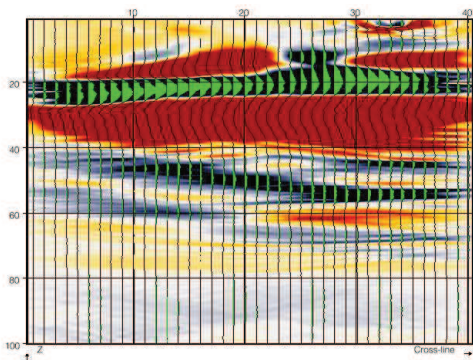
(c) Inline#5
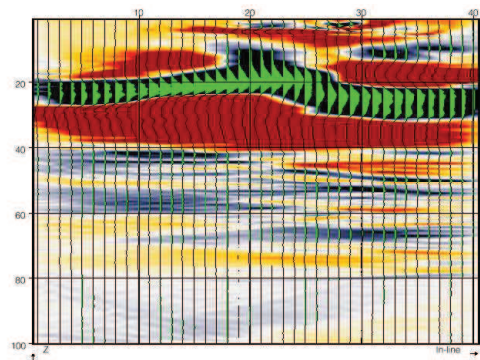
(d) Crossline#5
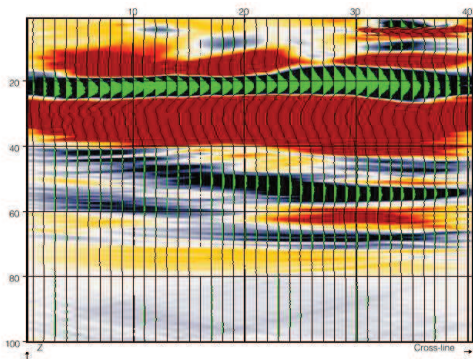
(e) Inline#10
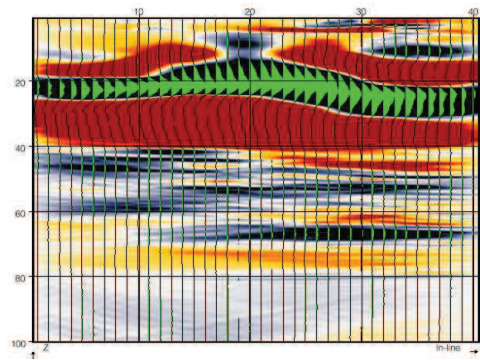
(f) Crossline#10
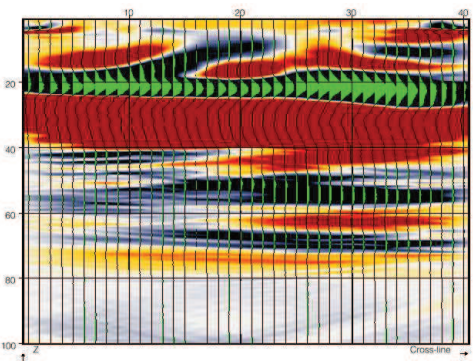
(g) Inline#15

(h) Crossline#15

123
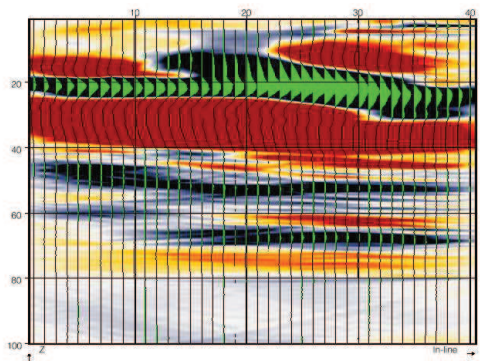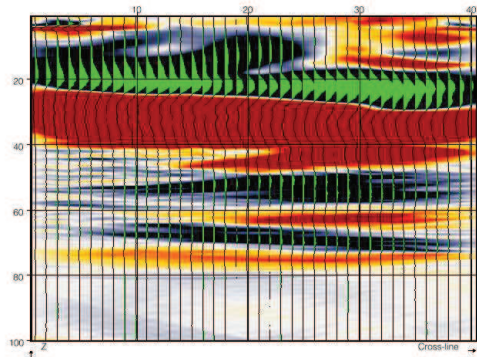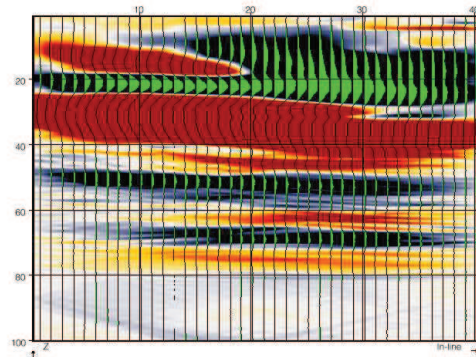
(i) Inline#20


(j) Crossline#20
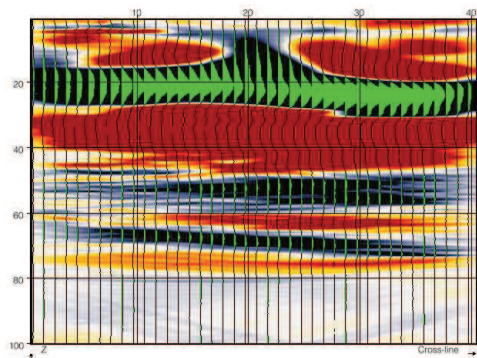

(k) Inline#25
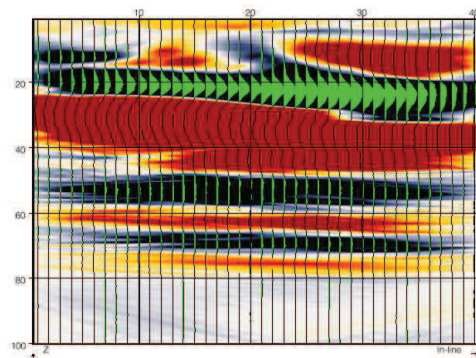

(l) Crossline#25
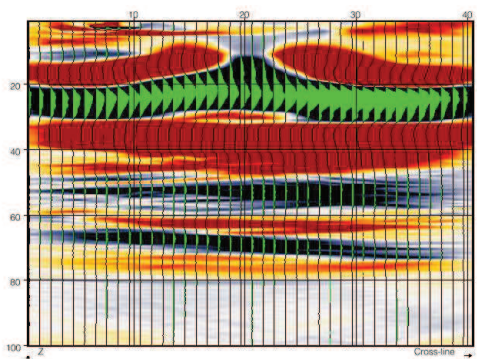

(m) Inline#30


(n) Crossline#30

124

(o) Inline#35

(p) Crossline#35

(q) Inline#40
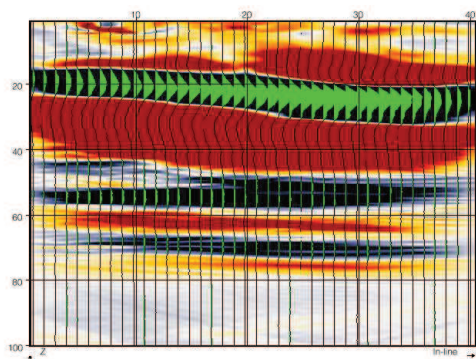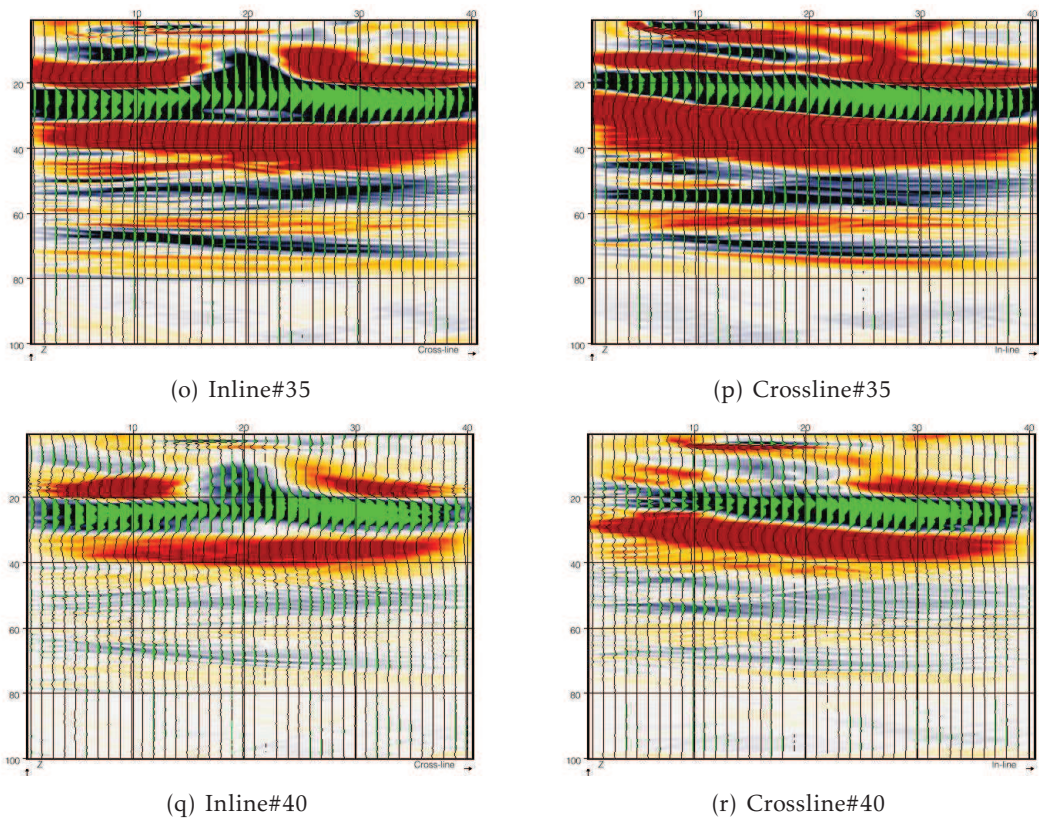
(r) Crossline#40

Figure 6.1 – In-lines and cross-lines from the migrated data cube.
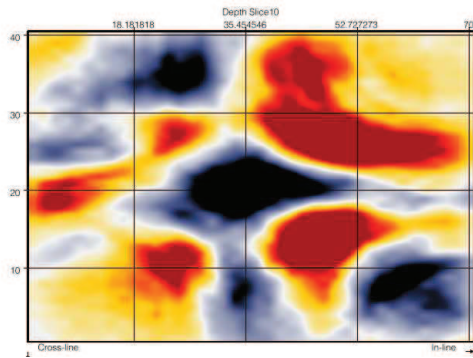
(a) Depth Slice#20
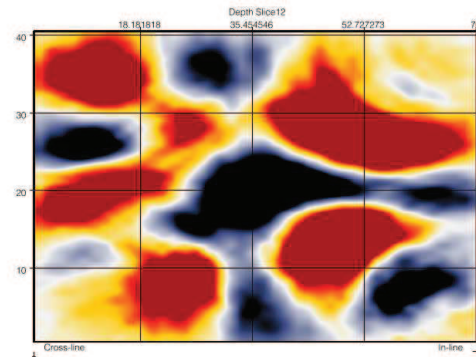
(b) Depth Slice#22
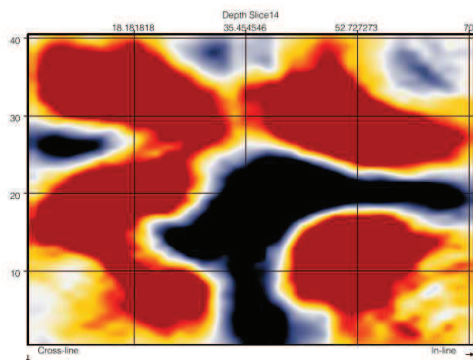
(c) Depth Slice#24
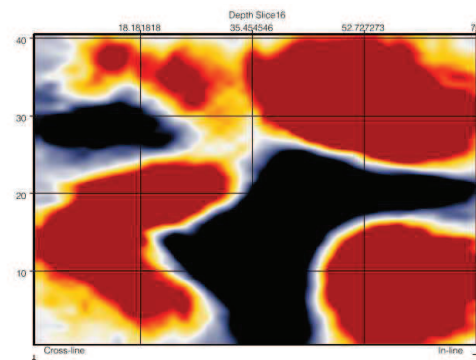
(d) Depth Slice#26
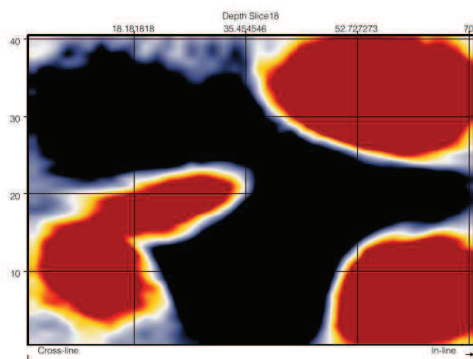
(e) Depth Slice#28
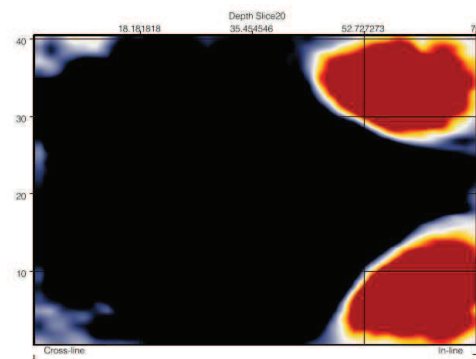
(f) Depth Slice#30
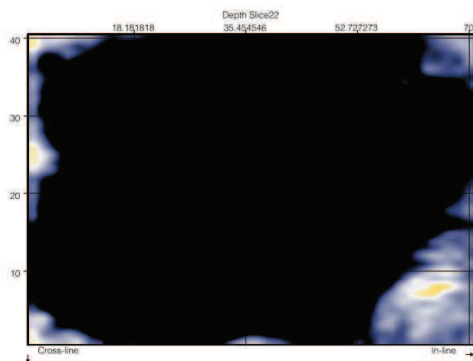
(g) Depth Slice#32
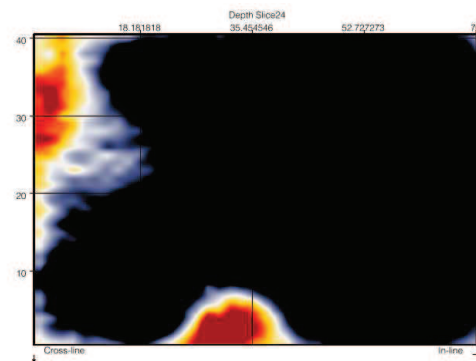
(h) Depth Slice#34

FIGURE 6.2 – Different Depth Slices.
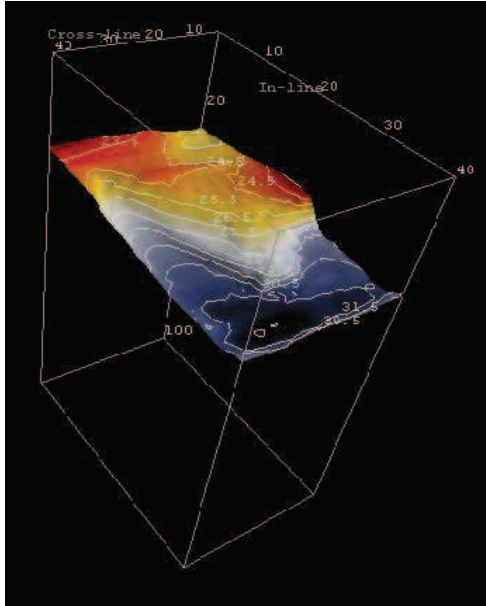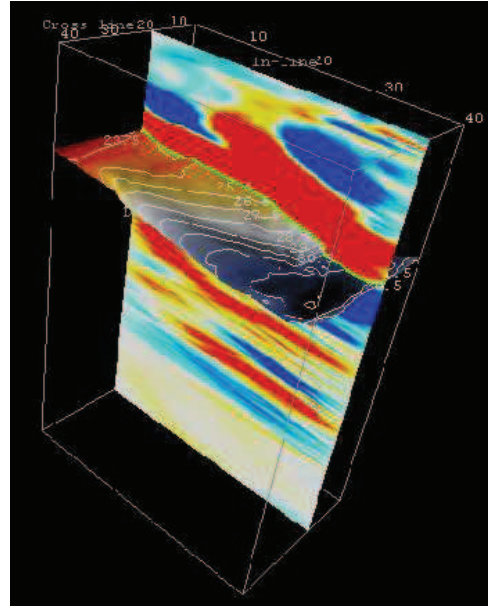
(a)　　　　　　　　　　　　(b)
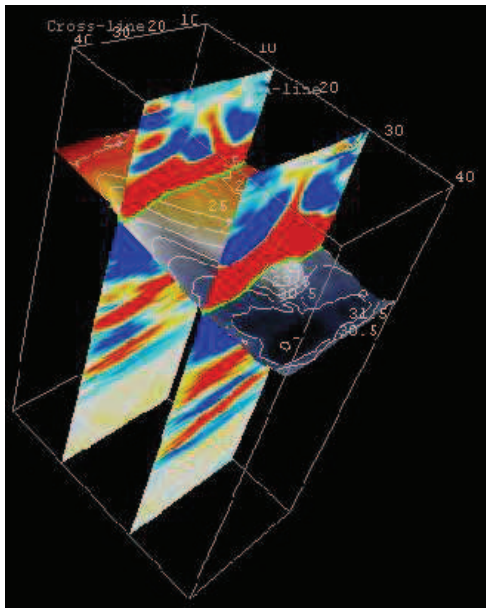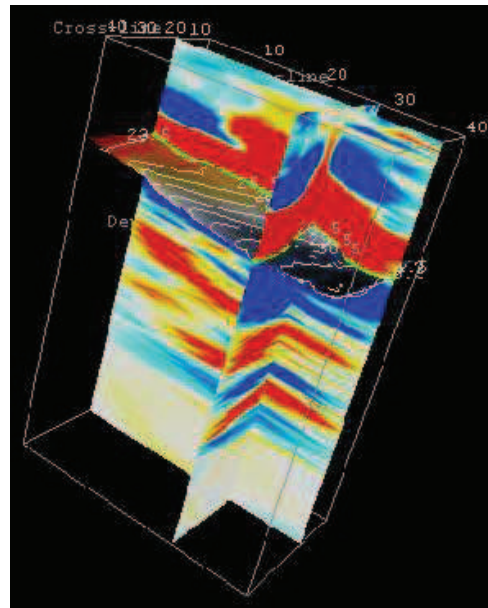
(c)　　　　　　　　　　　　(d)

Figure 6.3 – a) Main horizon ; b) horizon through cross-line section ; c) horizon through different in-line sections ; d) horizon through in-line and cross-line sections.

127

## 1-D Synthetic Seismogram

Synthetic seismogram is the simulation of earth response (reflectivity) convolved with a source wavelet of known properties. Synthetic seismogram is constructed and compared with the migrated poststack seismic image to evaluate the main reflector positions in depth section and the vertical resolution.

Convolution model is used to generate 1-D synthetic seismogram. Convolution model is sim-
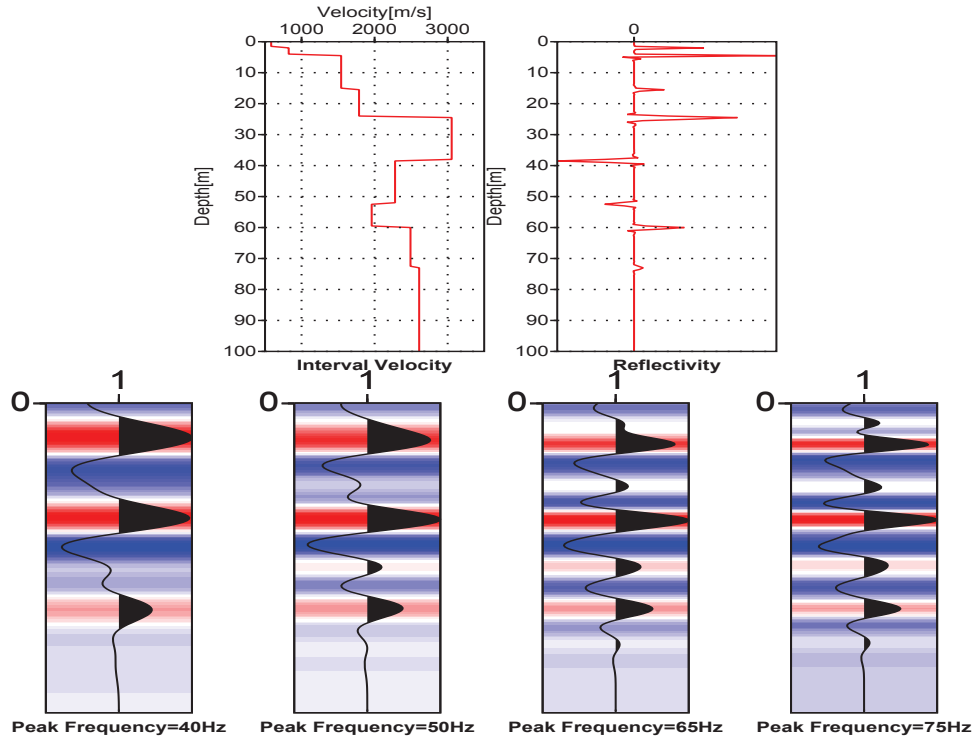


FIGURE 6.4 – In time domain the interval velocity, reflectivity and synthetic seismogram generated with Ricker wavelet of different peak frequencies.

ply the convolution of the wavelet, $w(t)$, and reflectivity, $r(t)$. Synthetic seismogram computation by convolution model is defined as

$$S(t) = w(t) * r(t) \qquad (6.1)$$

For normal incident ray paths reflectivity is defined as

$$r = \frac{I_{i+1} - I_i}{I_{i+1} + I_i} \qquad (6.2)$$

where $I = \rho v$ is the acoustic impedance, simple multiplication of velocity and density. For synthetic seismogram generation, Ricker wavelet defined by peak frequency is used. Velocity profile derived from VSP, of MC16 borehole, first arrival picking and constant density, $\rho = 2.8 g/cm^3$, is used to calculate the impedance.

128
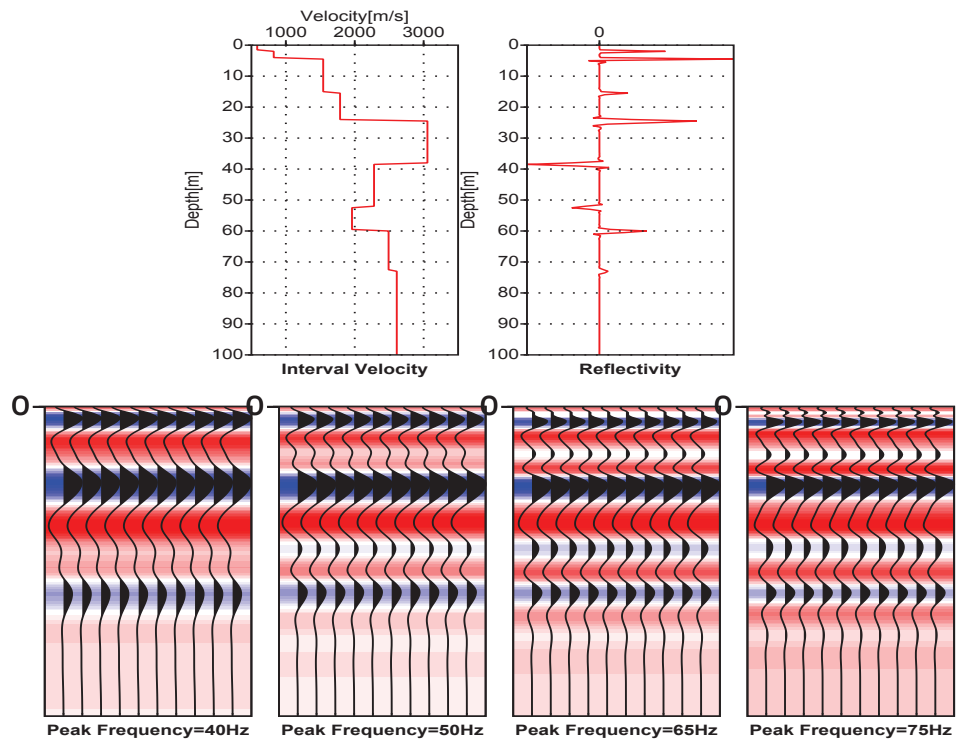
FIGURE 6.5 – In depth domain Interval velocity, reflectivity and synthetic seismogram generated with Ricker wavelet of different peak frequencies.
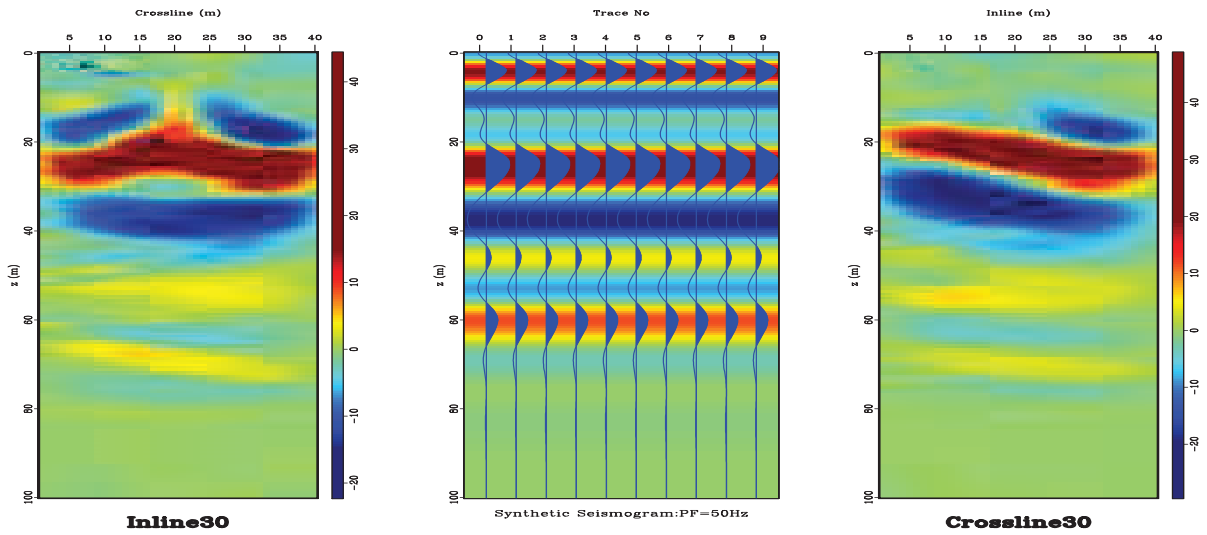


FIGURE 6.6 – Comparison of In line and cross line with synthetic seismogram.

129

Figure 6.4(top row) show the interval velocity and reflectivity in time domain while the figure6.4 (bottom row) shows the different wavelets using the same reflectivity profile but Ricker wavelets of different peak frequencies. The waveform sharpness and increase in vertical resolution are due to the peak frequencies of Ricker wavelet. Figure 6.5(top row) shows the interval velocity and reflectivity to generate the 1-D synthetic seismogram in depth domain. For all the synthetic seismogram same reflectivity profile is used while Ricker wavelet of different peak frequencies are used. Different synthetic seismograms show the change in waveform shape and the vertical resolution as a function of the peak frequency. Figure 6.6 shows the comparison of synthetic seismogram, generated with Ricker wavelet of peak frequency of 50Hz, with in-line and cross-line. This shows a consistent behaviour, with the main positive signal due to discontinuity in velocity profile at 25m.

## 6.3   Attribute Analysis

Attributes are used to extract the different features. Since in this case our objective is to locate the different structural heterogeneities. This will lead us to use the structural attributes that will help for delineating structural heterogeneities. Amplitude dependent attributes will not work in this case because they are more sensitive to fluid/rock saturation. In small scale shallow studies the attribute extraction and its analysis is difficult particularly due to low signal to noise ratio and data quality generally.

For this study different structural attributes are applied for different depth slice. Two of the depth slices are in vadose zone while the third depth slice and depth zone is located in saturated zone. In the following sections, all the attributes are shown after clipping and symmetrical around zero. This will help in clear visual and inspection of attributes. The color scheme show the relative amplitude rather than absolute values. Similarity or coherency is the first step to delineate the structural features. In next section similarity attribute is defined and result are shown and described why this fails to convey the required information. OpendTect software of dGB Earth Sciences is used for all the attribute analysis.

## 6.4   Similarity Attribute

Similarity attribute is basically a measure of alikeness of the traces. Similarity attribute, introduced by(de Rooij, M.. & Tingdahl, K., 2002), is based on the euclidean distance between traces. Mathematically similarity between two traces is defined as

$$S_{T_{m,n-1},T_{m,n+1}}(t) = 1 - \frac{\sqrt{\sum\limits_{k=-N}^{N} [T_{m,n-1}(t+k) - T_{m,n+1}(t+k)]^2}}{\sqrt{\sum\limits_{k=-N}^{N} [T_{m,n-1}(t+k)^2]} + \sqrt{\sum\limits_{k=-N}^{N} [T_{m,n+1}(t+k)^2]}} \qquad (6.3)$$

Similarity is one minus the euclidean distance between traces normalized to the sum of traces lengths. Different statistical properties of similarity can be obtained such as average, minimum, maximum, median and variance etc. These statistical output are based on neighbouring similarities.

For example minimum similarity along an in-line, figure6.7, can be written as.
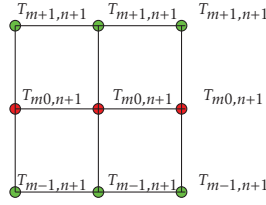
FIGURE 6.7 – Sketch for similarity attribute analysis. Red row is referenced in-line. Where m and n denote number of traces and samples respectively.

$$Min_{S_{T_{m,n-1},T_{m,n+1}}}(t) = Min[S_{T_{m,n-1},T_{m,n+1}}(t), S_{T_{m+1,n},T_{m-1,n}}(t),$$
$$S_{T_{m+1,n-1},T_{m-1,n+1}}(t), S_{T_{m-1,n-1},T_{m+1,n+1}}(t)] \tag{6.4}$$

Other output statistical are defined in the similar manner.

Similarity attribute is used to detect and map the structural discontinuities. Similar traces in waveform and amplitude will have higher similarity and vice versa. Traditionally similarity is used to map the faults, fractures, reef, sinkholes, channel boundaries, mud volcanoes and salt domes etc on time slice and horizon. Similarity offers unbiased visualization of features. Figure 6.8 shows the depth slices along with different similarity statistical output. The respective outputs, average and minimum similarities, show the same trend as the original depth slices. Red color show the higher similarity. These similarity attributes does not provide the required information to isolate the structural features. This is due to the fact that similarity only takes into account the amplitude in the particular window and does not take into account the dips that are sensitive to structural heterogeneities. This led us to calculate the attributes that uses the dip information.

(a) Depth Slice#18  (b) Depth Slice#23  (c) Depth Slice#42

(d) Average Similarity  (e) Average Similarity  (f) Average Similarity

(g) Minimum Similarity  (h) Minimum Similarity  (i) Minimum Similarity
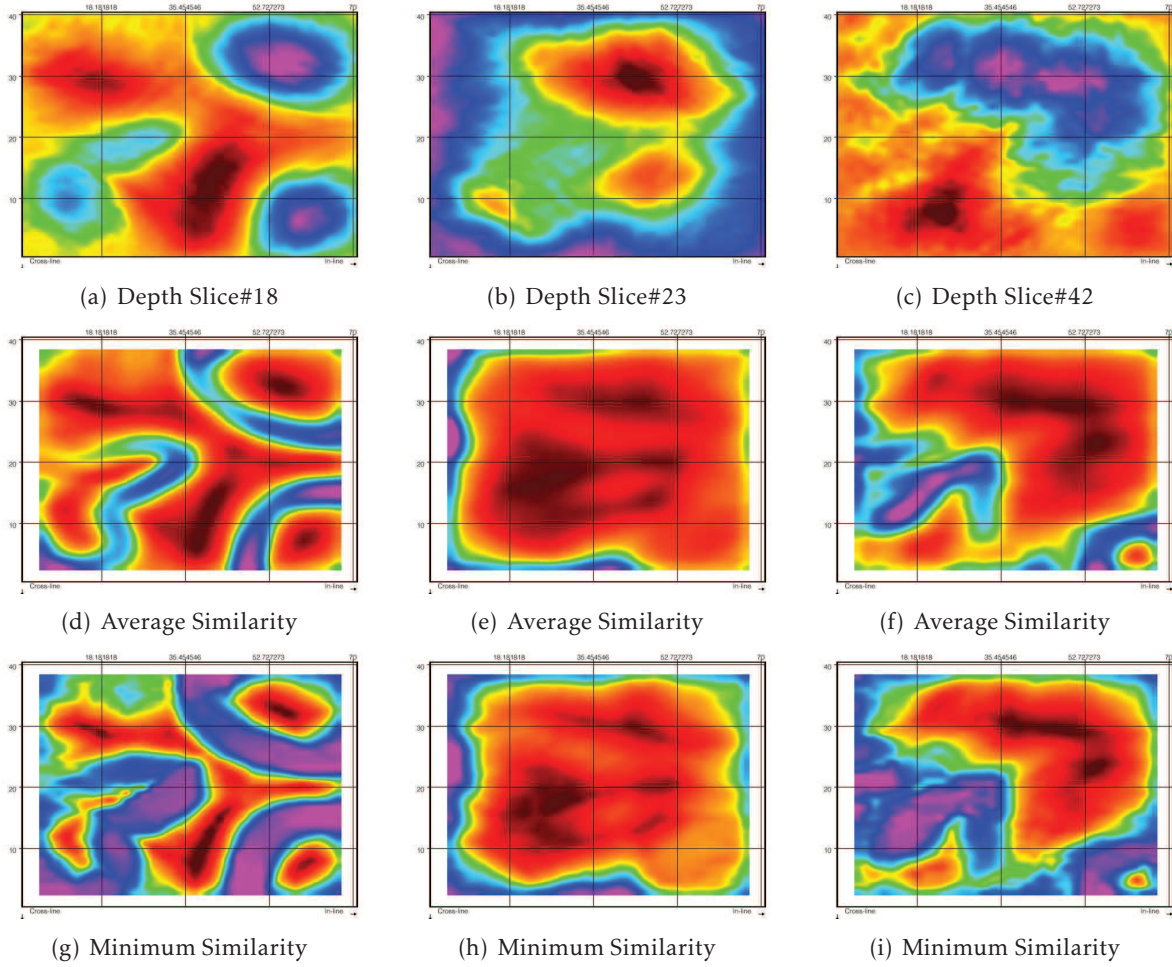
FIGURE 6.8 – Different Depth slices (top row), average similarity of the corresponding depth slices (middle row) and minimum similarity of the corresponding depth slices (bottom row). Red color show the higher similarity while purple color indicate the lower similarity.

## 6.5  Dip Calculation

Dip is defined as the ratio of time difference and distance between two points :

$$p = \delta t/d \tag{6.5}$$

For 3D seismic data in time domain, the dip is defined along x and y dimension.

$$p_x = \delta t/\delta x \tag{6.6}$$
$$p_y = \delta t/\delta y \tag{6.7}$$

Similarly for 3D seismic data in depth domain, the dip is defined along x and y dimension.

$$p_x = \delta z/\delta x \tag{6.8}$$
$$p_y = \delta z/\delta y \tag{6.9}$$

The dips in terms of apparent angle dips $\theta_x$ and $\theta_y$ shown in figure6.9, assuming constant velocity, is defined as(Marfurt, K. J., 2006).

$$p_x = \frac{2tan\theta_x}{v} \tag{6.10}$$

$$p_y = \frac{2tan\theta_y}{v} \tag{6.11}$$

There exists several method to calculate the volumetric dip and azimuth from stacked data.
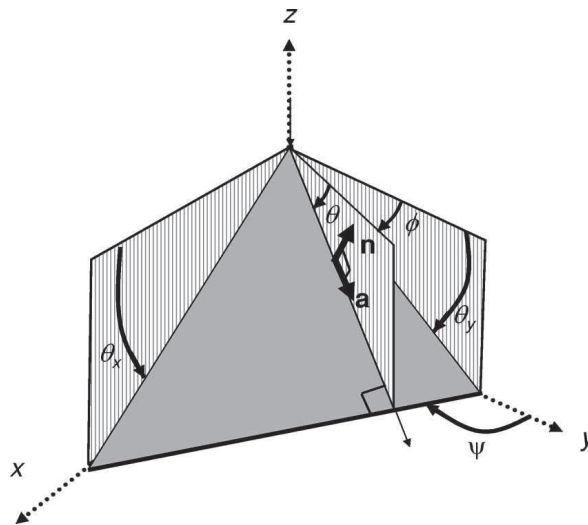


FIGURE 6.9 – Nomenclature for defining the dips. Where **n** is unit vector normal to the reflector, **a** is unit vector dip along the reflector, $\theta$ is the dip magnitude, $\Phi$ is dip azimuth, $\psi$ is dip strike. $\theta_x$ and $\theta_y$ are the apparent dips in $xz$ and $yz$ plane respectively(after(Marfurt, K. J., 2006)).

But frequently used techniques are based upon aligning the phases derived from the complex trace analysis proposed by(Luo, et al., 1996) and (Barnes, A. E., 1996), direct scanning for the most coherent reflectors proposed by(Marfurt et al., 1998) and using gradient structure tensor proposed by(Bakker et al., 1999) and (Hocke, C. & Fehmers, G., 2002).

Dip is calculated for each sample in the data cube. The dip calculated for each sample in the data cube is stored as in-line and cross-line dip component. This dip calculation is used as an input for certain attributes that will be described in the next section.

The dip calculation and subsequent attribute calculation is performed by OpendTect software. For dip calculation BG steer algorithm is used with one trace step out for in-line and cross-line. Further vertical and lateral median filter is applied to get rid of noises that might result in erroneous outputs. In-line and cross-line dips are projected in in-line and cross-line directions respectively. These dips are stored as $mm/m$. These dips are used latter for different attribute calculation.

Figure 6.10 shows the in-line and cross-line dips for different depth slices. The dip will cause either due to dipping beds or structural heterogeneities. The first row of the figure 6.10 shows the depth slice#18 and corresponding in-line and cross-line dips. There are strong to moderate

in-line dips on the hole depth slice. Similarly strong cross-line dips are only localized in the part of the depth slice#18. Similarly the dip components are shown for the other depth slices.



(a) Z#18

(b) Inline dip

(c) Crossline dip

(e) Z#23

(f) Inline dip

(g) Crossline dip

(i) Z#42

(j) Inline dip
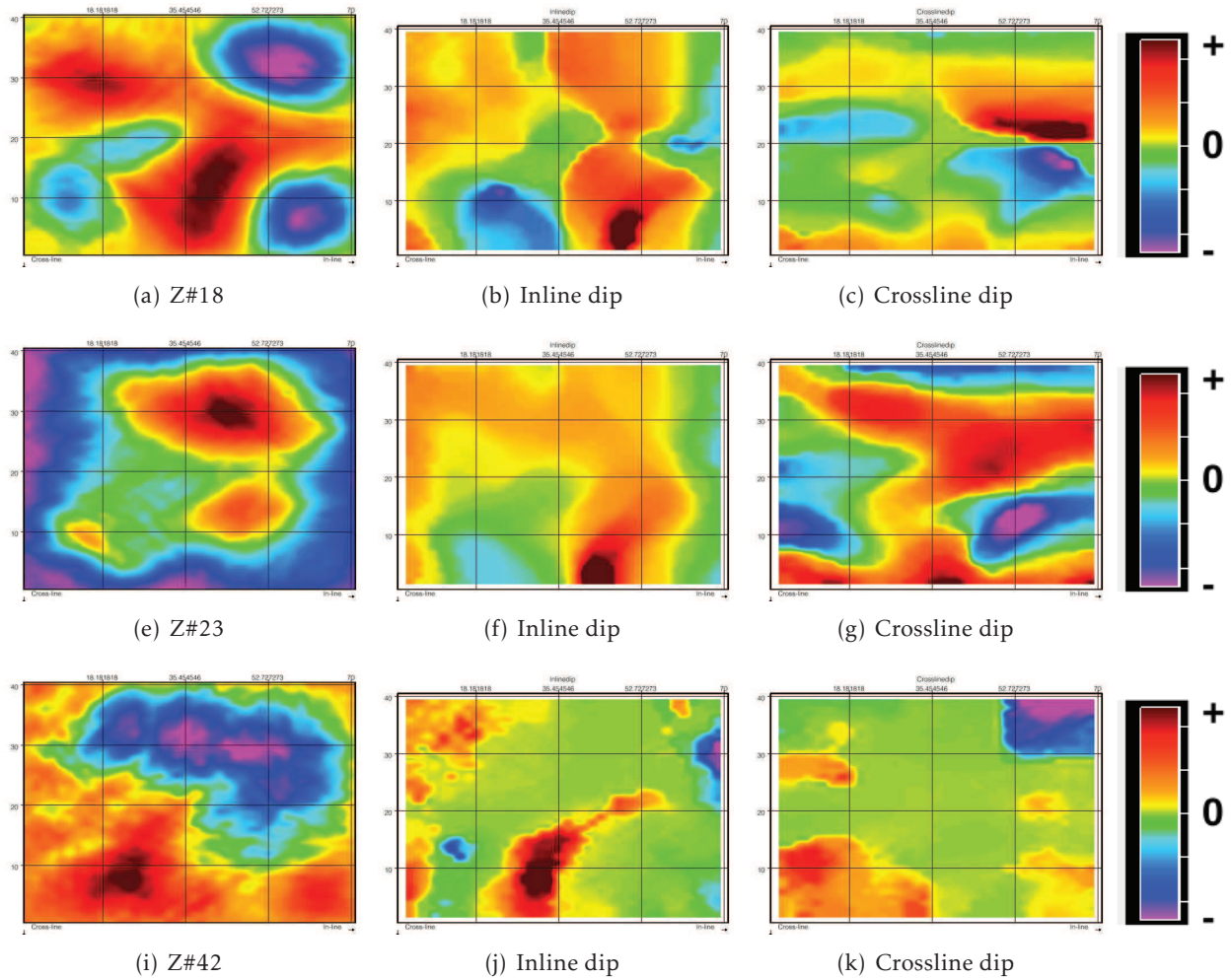
(k) Crossline dip

FIGURE 6.10 – Depth slices (left column), corresponding in-line (central column) and crossline dips (right column). Purple, green and red colour indicate the negative, zero and positive values respectively.

## 6.6 Curvature Attributes

Curvature is the measure of a curve deviation from a straight line or rate of change of direction of a curve. In terms of derivative curvature may be written as

$$K = \frac{\frac{d^2y}{dx^2}}{(1 + (\frac{dy}{dx})^2)^{3/2}} \tag{6.12}$$

Curvature is second derivative of two way travel time or depth surfaces. The concept of curvature calculation is defined in the figure 6.11a, the curvature related to the different events. For an anticline structure curvature is positive, diverging arrows, while for synclinal structure curvature is negative, converging arrows. For a straight line or constant dipping event curvature is zero, parallel arrows.

For a 3D body, figure 6.11b, an infinite number of curvature can be extracted. But a useful subset of curvature outputs include normal curvatures, defined by plane which are orthogonal to the surface. The calculation of curvature for gridded surface involves the least square fitting



(a) Curvature for 2D case          (b) Curvature for 3D case
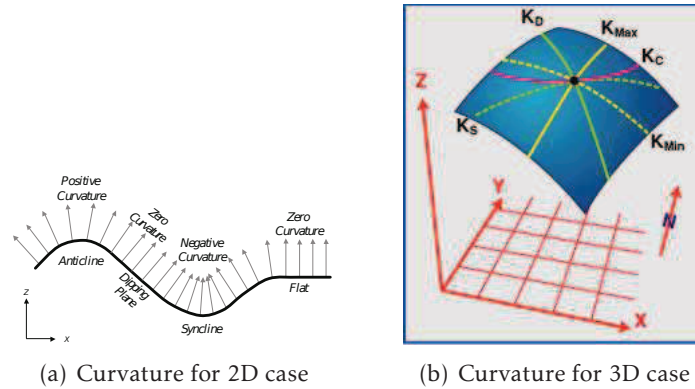
FIGURE 6.11 – (a) Definition of curvature for 2D ; b) Curvature definition for 3D case. Where X and Y are in-lines and cross-lines respectively while Z is depth axis. $K_{min}$,$K_{max}$, $K_d$ and $K_S$ stand for minimum, maximum, dip and strike curvature respectively. (after(Roberts, A., 2001)).

of the quadratic surface

$$y = ax^2 + by^2 + cxy + dx + ey + f \tag{6.13}$$

where the coefficients are calculated from the dip values as calculated in previous section. There are different curvature outputs calculated from the coefficients and then combination of these curvature outputs result in new curvature attributes. Based on different combination of these normal curvatures, important curvature properties related to different surfaces are extracted. Below is the list of some of the curvature attributes from(Roberts, A., 2001), used for this study.

– Mean Curvature

Mean Curvature is the average of any two orthonormal curvatures through the surface. In terms of the coefficients it is defined as

$$K_m = \frac{a(1 + e^2) - cde + b(1 + d^2)}{(1 + d^2 + e^2)^{3/2}} \tag{6.14}$$

135

– Gaussian Curvature
Gaussian curvature is the product of principal curvatures and calculated as :

$$K_g = \frac{4ab - c^2}{(1 + d^2 + e^2)^2} \qquad (6.15)$$

Gaussian curvature itself is not very effective attribute but it is used to derive other curvature attributes.

– Maximum Curvature
Maximum curvature is calculated from the mean and Gaussian curvature as

$$K_{max} = K_m + \sqrt{k_m^2 - k_g} \qquad (6.16)$$

– Minimum Curvature
Minimum curvature is derived from the combination of mean and Gaussian curvature

$$K_{min} = K_m - \sqrt{k_m^2 - k_g} \qquad (6.17)$$

This curvature attribute is useful for the delineation of structural heterogeneities.

– Most Positive Curvature
Most positive curvature is defined as

$$K_{Mpos} = (a + b) + \sqrt{(a - b)^2 + c^2} \qquad (6.18)$$

– Strike Curvature
Strike curvature in terms of coefficients is written as

$$K_s = \frac{2(ae^2 - cde + bd^2)}{(d^2 + e^2)\sqrt{(1 + d^2 + e^2)}} \qquad (6.19)$$

Strike curvature is extracted perpendicular to the dip curvature, i.e along the strike.

– Curvedness
Curvedness is the measure of the amount of total curvature present in the surface.

$$K_n = \sqrt{\frac{K_{max}^2 + K_{min}^2}{2}} \qquad (6.20)$$

– Contour Curvature
Contour curvature is defined as

$$K_c = \frac{2(ae^2 - cde + bd^2)}{(1 + d^2 + e^2)^{3/2}} \qquad (6.21)$$

Contour curvature closely resemble to strike curvature.

– Shape Index
Shape index is derived from the combination of minimum and maximum curvatures.

$$S = \frac{2}{\pi} tan^{-1} \left( \frac{k_{max} + k_{min}}{k_{max} - k_{min}} \right) \qquad (6.22)$$

Shape index is the quantitative measure of the shape describing the local morphology of the surface.

In figure 6.12 different curvature attributes are displayed for depth slice#18. Minimum curvature attribute indicates several interesting features. The ellipse on left side of minimum curvature shows a collapse feature because lower curvature value is surrounded by higher curvature values. This feature is typical to the karstic formations. The other circles also show the similar feature but with more regular shape. Contour curvature also indicates the local elongated dissolved feature that might possibly formed due to several diagenetic episodes. Rest of the attributes convey information concerning to surface roughness with local highs.

Similarly in the case of depth slice#23, figure 6.12, the minimum curvature indicate a low curvature feature surrounded by high curvature feature. This also indicates some irregular collapse feature. Rest of the attributes dictate minor structural relief but not prone to the typical karst related feature. For depth slice#23 significant karst or karst related features are not found.

For depth slice, figure 6.14, two pronounced features on the minimum curvature are evident. The ellipse show karstic feature, but feature in the rectangle is difficult to interpret. This feature seems to be a channel formed due to karsting or dissolution. Another interpretation might be the series of dissolution features aligned in a row. The same feature is also well recorded on the strike and contour curvatures. On this attributes it is more clear and share the same spatial position. The continuity fact suggest an interconnected karst channel. The ellipse on strike and contour curvature is indicative of large scale irregular vuggy features that are affected by different diagenetic episodes.

Further analysis is carried out on the neighbouring depth slices of the depth slice#42 as shown in the figure 6.15. These figures show the elongated channel feature that begins at 40m and continue until 42m. This continuity of elongated channel on successive depth slices indicate the feature connectivity in depth. This connectivity in depth is possible due to water percolation over the continuous time period or leeching. Other sparse isolated features are also evident on the successive depth slices. These features are restrictive in nature and locally developed with no continuity.
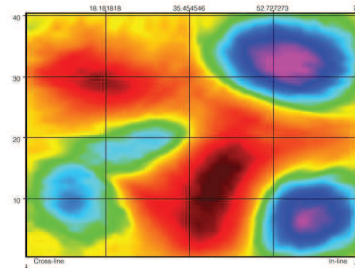
(a) Depth Slice#18
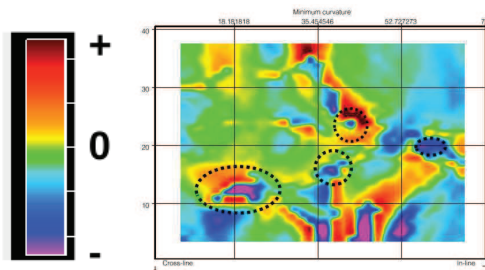


(c) Minimum Curvature
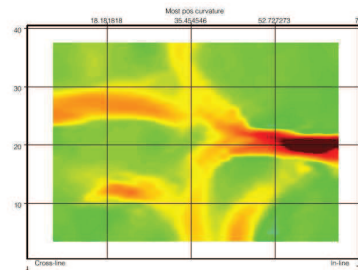


(d) Most Positive Curvature
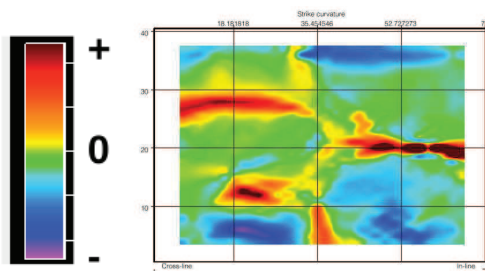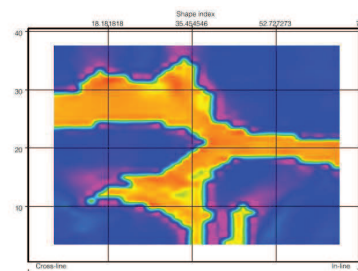


(f) Strike Curvature
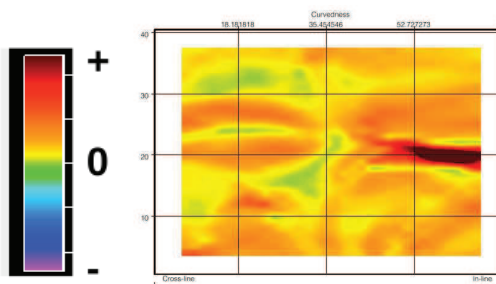


(g) Shape Index
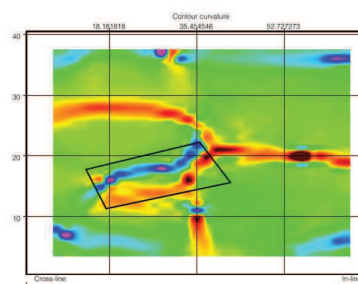


(i) Curvedness



(j) Contour Curvature

FIGURE 6.12 – Depth slice#18 and different curvature attributes.
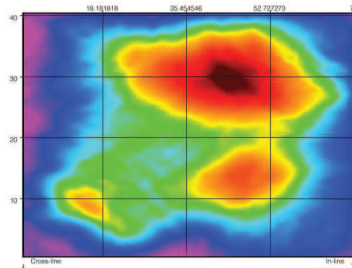
(a) Depth Slice#23
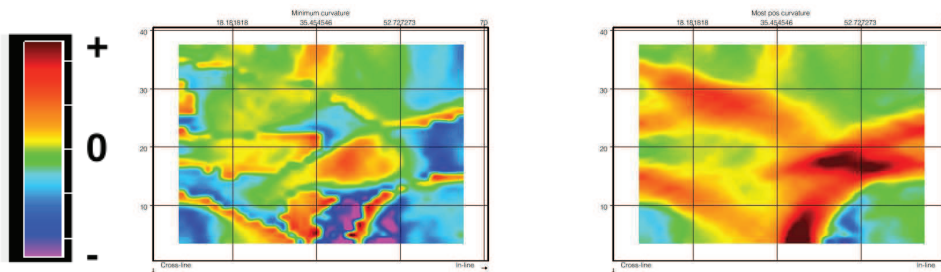


(c) Minimum Curvature



(d) Most Positive Curvature
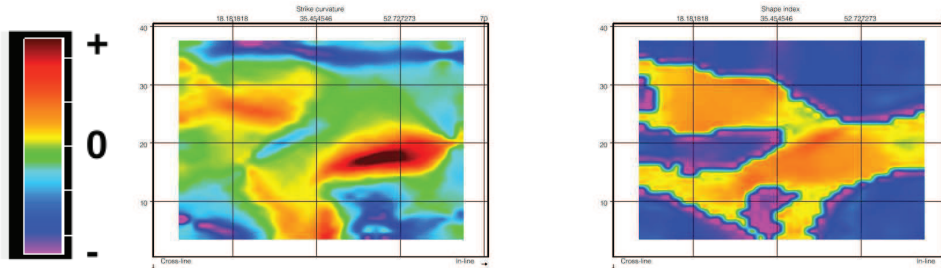


(f) Strike Curvature
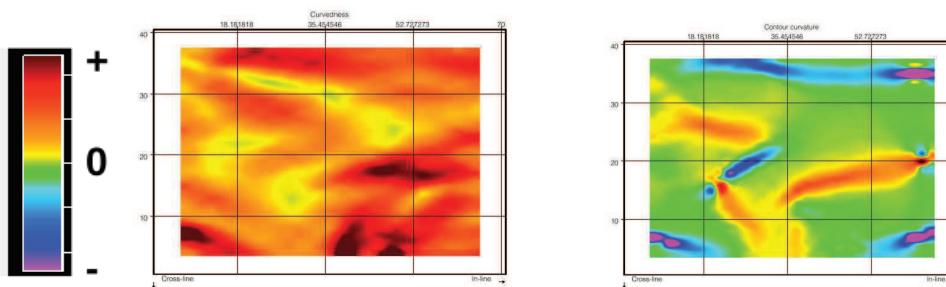


(g) Shape Index



(i) Curvedness



(j) Contour Curvature

FIGURE 6.13 – Depth slice#23 and different curvature attributes.
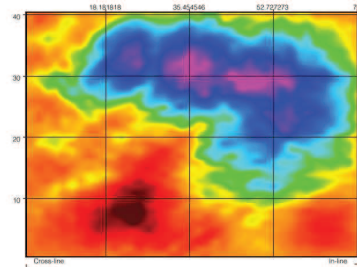
(a) Depth Slice#42
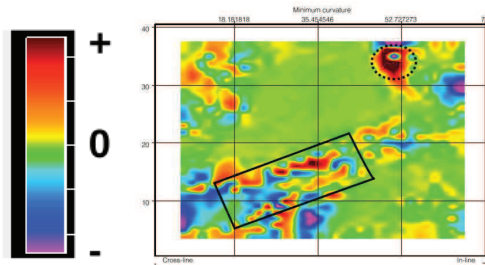


(c) Minimum Curvature
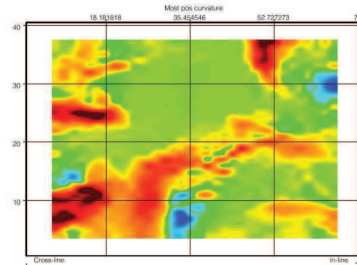


(d) Most Positive Curvature
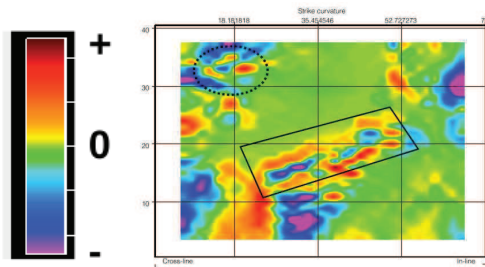


(f) Strike Curvature
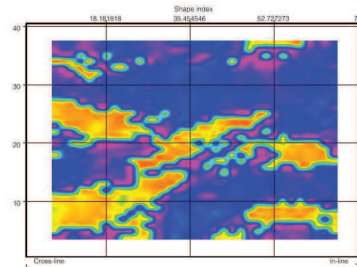


(g) Shape Index
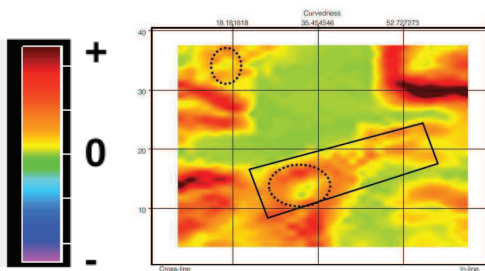


(i) Curvedness
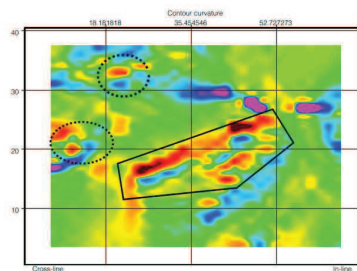


(j) Contour Curvature

Figure 6.14 – Depth slice#42 and different curvature attributes..

(a) Z#39     (b) Contour Curvature#39     (c) Strike Curvature#39     (d) Minimum Curvature#39

(f) Z#40     (g) Contour Curvature#40     (h) Strike Curvature#40     (i) Minimum Curvature#40

(k) Z#41     (l) Contour Curvature#41     (m) Strike Curvature#41     (n) Minimum Curvature#41

(p) Z#42     (q) Contour Curvature#42     (r) Strike Curvature#42     (s) Minimum Curvature#42

(u) Z#43     (v) Contour Curvature#43     (w) Strike Curvature#43     (x) Minimum Curvature#43
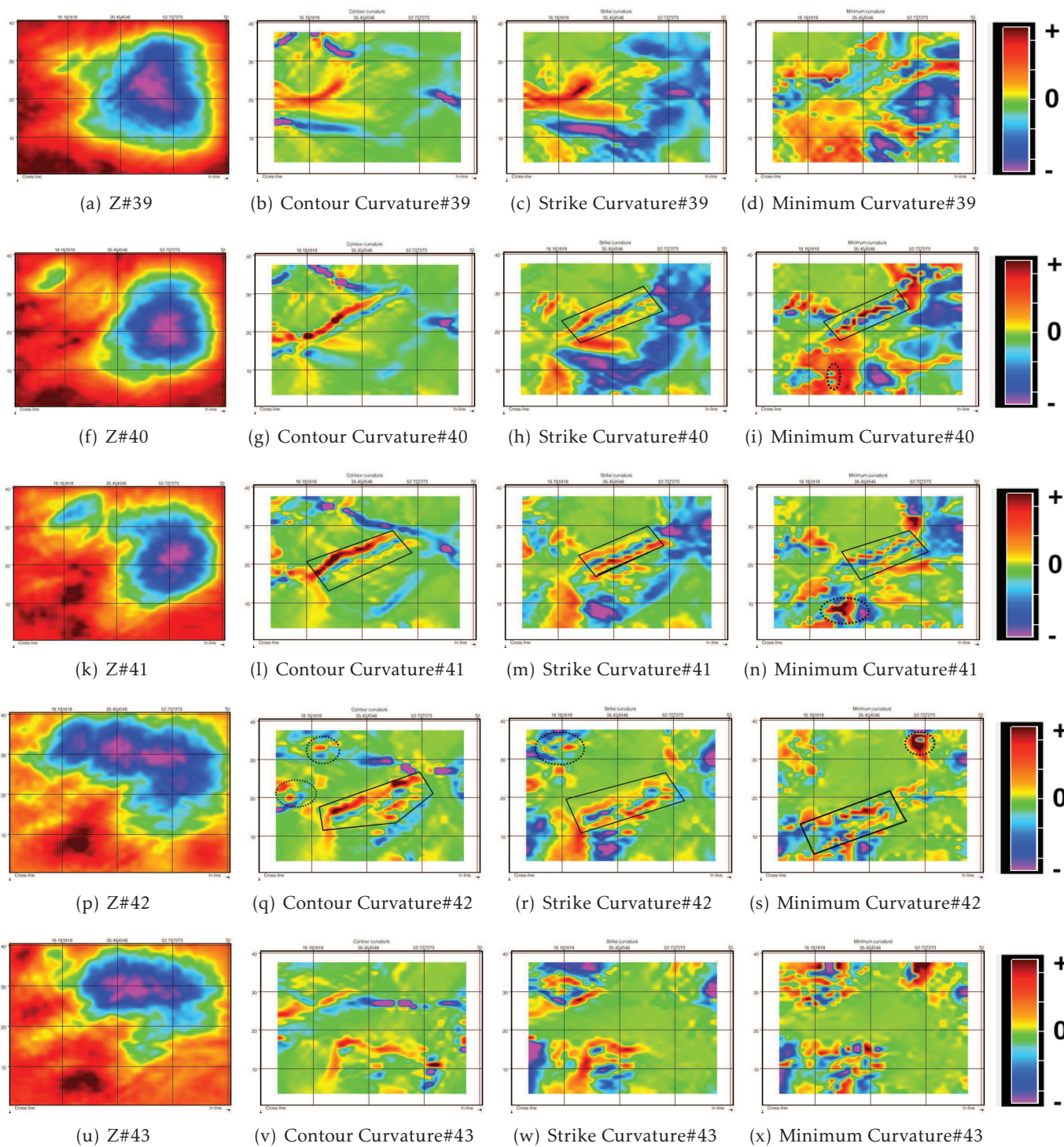
FIGURE 6.15 – Different depth slices and corresponding curvature attributes.

141

## 6.7 Conclusion

Figure 6.16 shows the seismic acquisition layout and different wells. The cluster of wells in the extreme below left are extensively studied for borehole porosity and heterogeneity. There are only two well in the vicinity of 3D seismic survey. Although these wells show the similar physical rock properties, i.e density etc, but the lithofacies thickness in these wells vary considerably. Different structural features are only present in certain wells. These variations encountered in different boreholes despite of the small distance among the boreholes indicate the complexity of the area.
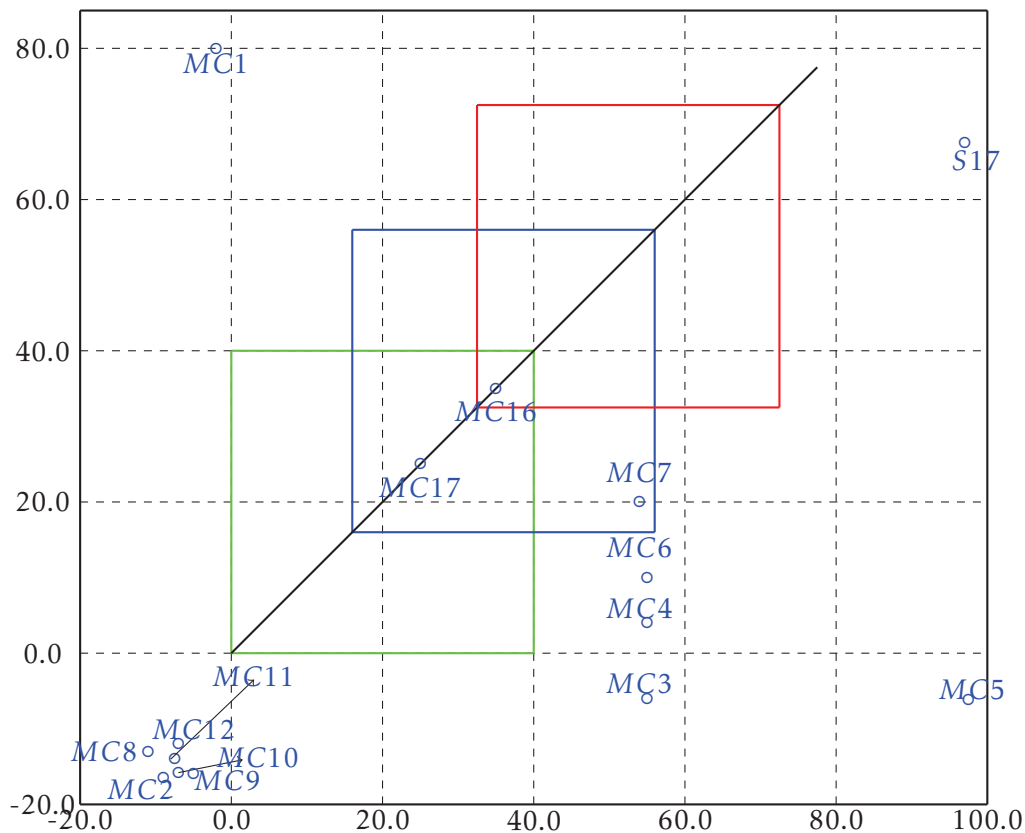


FIGURE 6.16 – Sketch of 2D and 3D reflection survey. Where green, blue and red colour square shows the outer limit of receivers, CMPS and sources for 3D reflection survey. 2D line is at diagonal of 3D reflection survey layout. Different drilled borehole position is also shown.

Figure 6.17a shows the interval velocity derived from MC16 well. Different layers of varying thickness and P-wave velocity are shown. Third layer from 17 to 24m composed of limestone inter bedded with shale. From 24m to 60m the rock sequence composed of coral reef is characterized by different velocities. This massive coral reef is further divided into three zone characterized by the velocity variation. The first coral reef unit is characterized by 1750m/s velocity, second unit has the highest velocity of 3000m/s and third one of 2300m/s velocity. The highest velocity zone is characterized by little karstification. Second and third zone are also marked

142

by the karsts and cavities. The water table is at 37m. Second unit is partly in vadose zone and partly in phreatic zone. While zone below the massive coral reefal unit is saturated with the mixed water.

Figure 6.17b show the optical images of borehole MC16 and MC17. These borehole are located



(a)                    (b)
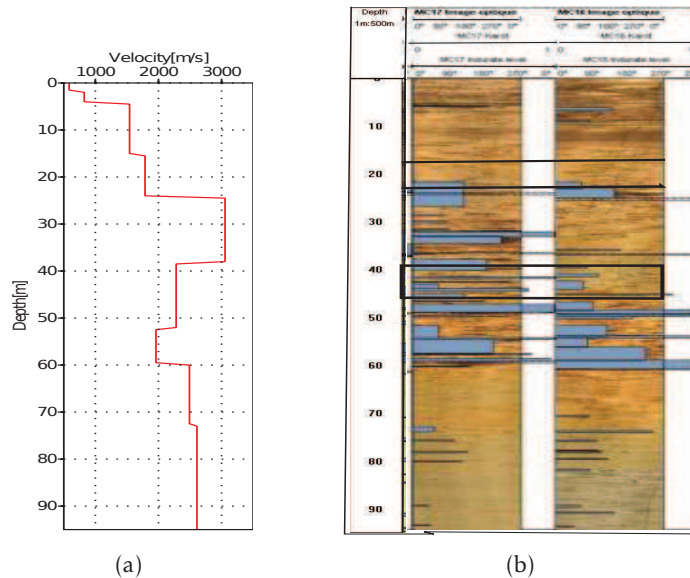
FIGURE 6.17 – a) Interval velocity profile deduced from first arrival picks ; b) Optical image and gamma ray wire-line log from well MC16 and MC17. Blue color indicate the interpreted karsts. Solid black color and rectangle indicate the depth slices used for attribute analysis. The position of these boreholes is shown in the figure6.16.

at the 2D seismic line and 3D seismic reflection block. Several karstic features are marked by blue colour squares on both boreholes. Note that despite of few meters distance between these two boreholes, the karstic features are not necessarily present in both wells at same depth. In borehole MC17 the karstic features in the depth range 28m to 38m are present and MC16 well is void of that. But the karstic features are pretty similar in the 52m to 58m interval.

By curvature attribute the different karstic features at different depths are identified. At depth slice 18m karstic features are detected but are not very pronounced. Similarly at 23m some karstic features are detected. But these karstic features are most prominent in the depth interval from 41m to 44m. These features are spatially continued upto several meters.

Although curvature attribute helped to identified different karstic features but due to low vertical resolution only large scale dissolution features are detected. Small scale features detection needs higher vertical resolution seismic data.

# Conclusion

Cette étude porte sur la caractérisation d'un réservoir carbonaté comprenant des intrusions d'eau salée. Ce site est utilisé comme un site expérimental. Auparavant, des études en puits ont été effectuées. Ces études ont été utiles pour obtenir des propriétés détaillées du réservoir mais les résultats sont uniquement valides à proximité des puits. L'acquisition 3D en sismique réflexion est effectuée pour mettre en évidence les hétérogénéités du réservoir. Bien que la résolution obtenue avec la sismique réflexion soit faible comparativement à l'échelle du puits, elle peut nous permettre de comprendre le réservoir à grande échelle. De plus, les attributs sismiques ont un intérêt particulier.

Une bonne planification de l'acquisition des données sismiques a une importance vitale. Pour cette étude, l'acquisition de données 3D en sismique réflexion a été préparée de façon à obtenir un échantillonnage spatial adéquat en évitant le moyennage spatial. En utilisant un dispositif d'acquisition optimisé, la qualité des données est également améliorée. Avec un intervalle de 1 mètre pour le binning, la couverture spatiale obtenue est élevée. L'objectif est d'acquérir des données entre la proche surface et 100 m de profondeur.

Les niveaux proches de la surface composés de matériaux altérés de faible vitesse et d'épaisseur variable pourront induire des retards significatifs des temps de trajet. Des corrections statiques sont appliqués pour minimiser les effets dus à ce niveau superficiel à faible vitesse. Sans l'application de corrections statiques, le traitement des données conduirait à produire une image éronnée. Les acquisition 3D en réfraction ont également permis de déterminer et d'appliquer des corrections statiques basées sur les délais Une méthode de correction statique basée sur l'inversion des délais est proposée. Les premières arrivées sont utilisées pour cette inversion. Cette technique d'inversion des délais est comparée aux méthodes de corrections statiques existantes pour les cas en 2 dimensions. Cette technique est appliquée pour déterminer les corrections statiques de données réelles en 2.5D et 3D. Un autre paramètre important, l'anisotropie de vitesse, a été déterminé et pris en compte pour l'inversion des délais.

Les données acquises présentent un bruit important et un faible rapport signal/bruit. La pénétration de l'énergie est difficile, ceci est du à la nature très dures des roches carbonatées. Les hétérogénéités du sous-sol favorisent la présence des ondes de Rayleigh. Les diffractions sont produites par des hétérogénéités de petites dimensions. Pour obtenir un traitement des données efficace, plusieurs stratégies ont été appliquées pour éliminer le bruit. Le filtrage passe-haut des données n'est pas efficace. Le mute des ondes de Rayleigh permet d'améliorer l'image mais induit la perte d'une partie du signal. Les techniques de traitement conventionnels et modernes (CRS) donnent presque le même résultat. Un traitement $<< Surface\ consistent >>$ est appliqué pour améliorer le rapport signal/bruit en préservant les amplitudes. Ensuite, le migration est appliquée pour focaliser les diffractions.

Les données ainsi traitées montrent plusieurs réflecteurs. Mais, la nature très dure des roches carbonatées et l'utilisation d'une source en surface ne permet pas la propagation suffisante d'énergie en profondeur. Ainsi, en l'absence d'un contenu haute fréquence dans le signal, la résolution verticale est limitée. L'étude de différents inlines et crosslines montrent une faible pénétration de l'énergie et des interférences. Des sismogrammes synthétiques 1-D ont été générés en utilisant une ondelette de Ricker à différentes fréquences afin d'expliquer la résolution verticale. A cause des interférences proches de la surface, les réflecteurs ne sont tous pas précisement définis. Cependant, l'horizon principal pointé montre l'irrégularité de la subsurface. Ce réflecteur de haute impédance est compris entre deux niveaux de plus faible impédance.

Les attributs sismiques apportent des informations complémentaires sur les données. Il existe de nombreux attributs sismiques mais chaque attribut est sensible à des caractéristiques spécifiques. Pour extraire des attributs, la qualité des données doit être bonne. Dans cette étude, un ensemble attributs a été utilisé. Comme l'objectif est de déterminer les hétérogénéités structurales, karsts, zones de dissolution et vacuoles, un ensemble d'attributs géométriques et structuraux ont été utilisés. Seuls les résultats relatifs à l'attribut de courbure se sont révélés intéressants et montrent la présence de karsts et de possibles chenaux connectés dans la zone saturée. Ces observations sont confirmées par les images optiques obtenus dans les forages localisés à proximité du bloc 3D.

D'autre attributs liés à l'amplitude ne présentent pas de caractéristiques particulières. Les structures de trop petite taille ne peuvent pas être détectées à cause de la faible résolution verticale. Bien que cette étude donne différents résultats, la faible pénétration de l'énergie et la faible résolution verticale n'ont pas permis d'obtenir tous les résultats attendus.

Les résultats obtenus pourraient être améliorés si une technique plus efficace que le mute pouvait être appliquée pour éliminer les ondes de Rayleigh, bien que les ondes de Rayleigh soient dans la même gamme de fréquence que les ondes réfléchies. Ceci pourrait être l'objectif d'une future étude dans un contexte de réservoirs carbonatés superficiels.

# Conclusion

This study is carried out to characterize the carbonate reservoir facing with salt water intrusion. This site is developed as an experimental site. Previously extensive bore hole studies were carried out. These studies are helpful for detail reservoir properties but the results are only valid in the vicinity of the boreholes. 3D seismic reflection survey is carried out to delineate the reservoir heterogeneities. Although seismic survey resolution is low comparatively to the borehole scale but this helps to understand the reservoir on the bigger scale. Further seismic attributes are of particular interest.

Proper planning of seismic data acquisition is of vital importance. For this study 3D seismic reflection surveys is carefully planned to get adequate spatial sampling, avoiding spatial averaging and acquisition foot prints. By implying the optimized data acquisition layout will also result in better data quality. High spatial coverage is attained after data binning at 1m interval. The objective was to acquire the data for shallow subsurface down to 100m.

Near surface layer composed of weathering material will cause significant travel time delay due its low velocity and thickness. Static correction is applied to mitigate the effect of subsurface low velocity layer and its thickness. Without static correction application the consequent processing will result in erroneous image. 3D refraction surveys are also conducted to determine the static correction based on delay time and applied. A method of static correction is proposed based on delay times inversion. First arrivals are used for delay time inversion. This proposed delay time inversion technique is compared with exiting methods of static corrections for 2D case. This technique applied to determine the static correction for 2.5D an 3D real data. Another important parameter, velocity anisotropy, was determined and taken into account for subsequent delay time inversion.

The acquired data has strong noise and low signal/noise ratio. Due to harder nature of carbonate rocks energy penetration was difficult. Near surface heterogeneities contributed to the Rayleigh waves generation. Diffractions were produced due to small scale heterogeneities. For an efficient processing of the data, several strategies are applied to get rid of the noise. High pass filtering alone does not help to get significant image. Muting of Rayleigh waves prove worthy. But muting also results in the loss of data. Conventional and modern data processing techniques gave almost the same result. Surface consistent processing is applied to get a high signal to noise ratio data by preserving the amplitude. Further migration is applied to collapse the diffractions.

The processed data show many reflectors. But as mentioned earlier due to hard rock nature of carbonates and use of surface energy source, enough energy was not penetrated. Consequent data processing and in the absence of higher frequency content of the signal the vertical resolution is limited. Inspection of different in-lines and cross-lines indicate the low energy penetration and interference. 1-D synthetic seismogram is generated using the Ricker wavelet of different peak frequency in order to explain the vertical resolution. Due to interference subsurface reflectors are not sharply defined. Zero crossed picked horizon shows the complexity of the subsurface reflector. This high impedance reflector is embedded between two layers of lesser impedance.

Seismic attributes enhance the particular features of the data. There exist abundance of seismic attributes but each attribute is sensitive to specific data features. For attribute extraction data quality should be good. For this study a set of attributes is used. Since the aim was to determine the structural heterogeneities, karsts, vugs, dissolution features etc, so a set of geo-

metrical or structural attributes is used. Only the result of curvature attribute are interesting. Different curvature attribute indicate the presence of karsts and possibly connected channels in the saturated zone. These observations are confirmed with the optical images of the boreholes located in the vicinity of 3D block.

Other amplitude related attributed does not show any remarkable feature. Due to low vertical resolution small scale features can not be detected. Although this survey deliver results in many ways but optimum result is not derived due to lower energy penetration, lower vertical resolution and total data volume. Apart from higher resolution the total data volume is also important because attributes operate in lateral and vertical windows by taking into account the traces and samples respectively.

The extent of studied data volume could be improved if a better technique than muting could be developed to get rid of Rayleigh waves, although Rayleigh waves share the same frequency spectrum as that of reflected events. This should be the purpose of the future research, as the same situation would exist in the shallow carbonate reservoirs.

# Bibliographie

Ahr, W. M.., 1989. Early diagenetic microporosity in the Cotton Valley Limestone of East Texas, *Sediment. Geol.*, **54**, 275–292.

ALIANCE., 2007. Advanced Logging Investigations of Aquifers iN Coastal Environments, *FINAL SCIENTIFIC REPORT (01/2002 to 07/2005)*.

Arango, C., Marcuello, A., Ledo, J., & Queralt, P., 2009. 3D magnetotelluric characterization of the geothermal anomaly in the Llucmajor aquifer system (Majorca, Spain) , *J. of Applied Geophysics*, **68**, 479–488.

Bakalowicz, M. J., Ford, D. C., Miller, T. E., Palmer, A. N., & Palmer, M. V., 1987. Thermal genesis of dissolution caves in the Black Hills, South Dakota, *Bull. Geol. Soc. America*, **99**, 729–738.

Bakker, P., Van Vliet, L. J., & Verbeek, P. W., 1999. Edge-preserving orientation adaptive filtering , *Proceedings of the IEEE-CS Conference on Computer Vision and Pattern Recognition*, pp. 535–540.

Balch, A. H., 1971. Color sonograms : A new dimension in seismic data interpretation , *Geophysics*, **36**, 1074–1098.

Barnes, A. E., 1996. Theory of 2-D complex seismic trace analysis, *Geophysics*, **61**, 264–272.

Barnes, A. N., 1997. Genetic classification of complex seismic trace attributes, *SEG Expanded Abstracts*, **67**, 1151–1154.

Bekara, M. & Baan, M. V., 2007. Local singular value decomposition for signal enhancement of seismic data, *Geophysics*, **72**, V59–V65.

Biondi., B. L., 2007. *3D seismic imaging*, Society of Exploration Geophysicist, Tulsa, Ok.

Brown, A. R, 2004. *Interpretation of three-dimensional seismic data* , *6th ed*, American Association of Petroleum Geologists.

Büker, F., Alan G. Green., & Heinrich Horstmeyer., 1998. Shallow 3-D seismic reflection surveying, Data acquisition and preliminary processing strategies, *Geophysics*, **63**, 1434–1450.

Büker, F., Alan G. Green., & Heinrich Horstmeyer., 2000. 3-D high-resolution reflection seismic imaging of unconsolidated glacial and glaciolacustrine, *Geophysics*, **65**, 18–34.

Chaouch, A. & Mari, J. L., 2006. 3-D Land Seismic Surveys : Definition of Geophysical Parameters, *Oil & Gas Science and Technology - Rev. IFP*, **61**, 611–630.

Chen, Q. & Sidney, S., 1997. Seismic attribute technology for reservoir forecasting and monitoring, *The Leading Edge*, **16**, 445–456.

Choquette, P. W. & James, N. P., 1988. *Introduction*, *In : Paleokarst*, Springer-Verlag, New York.

Choquette, P. W. & Pray, L. C., 1970. Geologic nomenclature and classification of porosity in sedimentary carbonates, *Am. Assoc. Pet. Geol. Bull.*, **54**, 207–250.

Claerbout J.F., 1998. Multidimensional recursive filters via a helix, *Geophysics*, **63**, 1532–1541.

Cunningham.A. B., 1974. Refraction data from single-ended refraction profiles, *Geophysics*, **39**, 292–301.

de Rooij, M.. & Tingdahl, K., 2002. Meta—attributes the key to multivolume, multi attribute interpretation, *The Leading Edge*, **21**, 1050–1053.

Deighan, A, J. & Watts, D. R., 1997. Ground-roll suppression using the wavelet transform, *Geophysics*, **62**, 1896–1903.

Dravis, J. J., 1989. Deep-burial microporosity in Upper Jurassic Haynesville oolitic grainstones, *East Texas Sediment. Geol.*, **63**, 325–341.

Dublyansky, V. N., 1980. Hydrothermal karst in the alpine folded belt of southern parts of U.S.S.R, *Kras i Speleologia (Poland)*, **3**, 18–36.

Dunham, R. J., 1970. Stratigraphic reefs versus ecologic reefs, *Am. Assoc. Pet. Geol. Bull.*, **54**, 1931–1932.

Dunham, R. J., 1962. Classification of carbonate rocks according to their depositional texture,in W. E. Ham, ed., Classification of Carbonate Rocks-a symposium, *American Association of Petroleum Geologists Memoir*, **1**, 108–121.

Egemeier,S. J., 1981. Cavern development by thermal waters, *Bull. Nat. Speleolog. Society*, **43**, 31–55.

Embree, P., Burg, J. F., & Backus, M. M., 1963. Wide-band velocity filtering the pie-slice process, *Geophysics*, **28**, 948–974.

Emilio, C., 2002. Coastal Aquifers as important natural hydrological structures, *In : Emilia Bocanerga, Mario Hernandez and Eduardo Usunoff (Editors), Groundwater and human development, IAH Selected Papers on Hydrogeology 6.*

Enos, P. & Sawatsky, L. H., 1981. Pore networks in Holocene carbonate sediments, *Journal of Sedimentary Petrology.*, **51**, 961–986.

Esteban, M. & Klappa, C. F., 1983. Subaerial exposure environments, In : Carbonate Depositional Environment (Ed. by P. A. Scholle, D.G.Bebout, and C.H. Moore), *AAPG Memoir*, **33**, 1–54.

Fanning, K. A., Byme, R. H., Breland, J. A., & Betzer, P. R., 1981. Geothermal springs of the West Florida continental shelf : evidence for dolomitization and radionuclide enrichment, *Bull. Geol. Soc. America*, **52**, 345–354.

Folk, R. L., 1959. Practical petrographic classification of limestones, *Bull. Am. Assoc. Pet. Geol*, **43**, 1–38.

Folk, R. L., 1962. Spectral subdivision of limestone types, in W. E. Ham,ed., Classification of Carbonate Rocks-a symposium, *American Association of Petroleum Geologists Memoir*, **1**, 62–84.

Fomel, S. & Vaillant, L., 2001. Evaluating the Stolt-stretch parameter, *Journal of Seismic Exploration*, **9**, 319–335.

Fontbote, J. M., Obrador,, A., & Pomar, L., 1983. Islas Baleares, in Geologia de Espaa, T.II (Libro Jubilar J.M. Rios) , *Madrid,Comision National de Geologia e instituto Geologico y Minero de Espaa*, pp. 343–391.

Gardner, G. H. F., Gardner, L. W., & Gregory, A. R., 1974. Shallow Formation velocity and density-The diagnostic basics for stratigraphic traps, *Geophysics*, **39**, 770–780.

Gardner, L. W., 1939. An Areal Plan of mapping subsurface structure by refraction shooting, *Geophysics*, **4**, 247–259.

Gazdag, J., 1978. Wave equation migration with the phase-shift method, *Geophysics*, **43**, 23–48.

Groen, J., Velstra, J., & Meesters, A. G. C. A., 2000. Salinization processes in palaeowaters in coastal sediments of Surinam : evidence from $\delta^{37}$Cl analysis and diffusion modelling, *Journal of Hydrology*, **234**, 1–20.

Hagedoorn, J. G., 1959. The plus-minus method of interpreting seismic refraction sections , *Geophys. Prosp*, **7**, 158–182.

Hein, F. J. & Risk, M. J., 1975. Bioerosion of coral heads : inner patch reefs, Florida Reef Tract, *Bull. Mar. Sci.*, **25**, 133–138.

Hill, C. A., 1990. Sulphuric acid speleogenesis of Carlsbad Cavern and its relationship to hydrocarbons, *Bull. Am. Assoc. Petrol. Geologists*, **74**, 1685–1694.

Hill, C. A., 1992. *Sulfuric acid oil-field karst. In : Karst Related Diagenesis and Reservoir Development : Examples from Ordovician-Devonian Age Strata of West Texas and the Mid-Continent (Ed by M.P. Candelaria and C.L. Reed )*, Soc. Econ. Paleont. Min., Publ.

Hinds, R. C., Kuzmiski, R. D., Botha, W. J., & Anderson, N. L., 1989. Vertical and lateral seismic profiles, *Anderson, N.L., Hills, L.V. and Cederwall, D.A., (eds.), Geophysical atlas of western Canadian hydrocarbon pools : Canadian Society of Exploration Geophysicists/Canadian Society of Petroleum Geologists*, pp. 319–344.

Hocke, C. & Fehmers, G., 2002. Fast structural interpretation with structure-oriented filtering, *The Leading Edge*, **21**, 238–243.

Hubral, P., 1983. Computing true amplitude reflections in a laterally inhomogeneous earth , *Geophysics*, **48**, 1051–1062.

Jaeggi, D., 2006. *Multiscalar porosity structure of a Miocene reefal carbonate complex*, Ph.D. thesis, ETH, Zurich.

Jäger, R., Jurgen, M., Höecht, G., & Hubral, P., 2001. Common-reflection-surface stack : Image and attributes, *Geophysics*, **66**, 97–109.

Jäger, R., 1999. *The Common Reflection Surface Stack-Introduction and Application*, Ph.D. thesis, Master's thesis, Universität Karlsruhe.

James, N. P. & Mountjoy, E. W., 1983. Shelf-slope break in fossil carbonate platforms : an overview. In : The Shelfbreak : Critical Interface on Continental Margins (Ed. by D.J. Stanley and G.T. Moore), *Spec. Publ. Soc. Econ.Paleont. Miner.*, **33**, 189–206.

James, N. P., 1962. Reef environment, in P. A. Scholle, D. G. Bebout, and C. H. Moore,eds., Carbonate Depositional Environments, *American Association of Petroleum Geologists Memoir*, **33**, 335–340.

James, N. P. & Ginsburg, R. N., 1979. The seaward margin of belize barrier and atoll reefs : morphology, sedimentology, organism distribution and late quaternary history, *Spec. Publ. Int. Assoc. Sedimentol.*, **3**, 191.

Jan, B. & Helbig, K., 1998. *Shallow high-resolution reflection seismics*, *Handbook of Geophysical Exploration*, vol. 19, Elsevier Science, Amsterdam.

Jefferson, R. W., Steeples, D. W., Black, R. A., & Carr, T., 1998. Effects of soil-moisture content on shallow-seismic data, *Geophysics*, **63**, 1357–1362.

Johnson., S. H., 1976. Interpretation of split-spread refraction data in terms of plane dipping layers, *Geophysics*, **41**, 418–424.

Jones, B. & Pemberton, S. G. J., 1988. Lithophaga borings and their influence on the diagenesis of corals in the Pleistocene Ironshore Formation of Grand Cayman Island, British West Indies, *Palaios.*, **3**, 3–21.

Karsli, H. & Bayrak, Y., 2008. Ground-roll attenuation based on Wiener-filtering and benefits of time-frequency imaging, *The Leading Edge*, **27**, 206–209.

Kendall, R., Side, J., & Ronen, S., 2005. An SVD-polarization filter for ground roll attenuation on multicomponent data, *SEG Expanded Abstracts*, **77**, 928–932.

Khublaryan, M. G., Frolov, A. P., & Yushmanov, I. O., 2008. Seawater intrusion into coastal aquifers , *Water Resour*, **35**, 274–286.

Landa, L. S. & Moor, C. H., 1980. Lithification, micritization and syndepositional diagenesis of biolithites on the Jamaican island slope, *Journal of Sedimentary Petrology.*, **50**, 357–370.

Leon Thomsen., 1986. Weak elastic anisotropy, *Geophysics*, **51**, 1954–1966.

Lighty, R. G., 1983. Preservation of internal reef porosity and diagenetic sealing of submerged early Holocene barrier reef, southeast Florida Shelf. In : Carbonate Cements (Ed. by N. Schneidermann and P.M. Harris)., *Spec. Publ. Soc. Econ.Paleont. Miner*, **36**, 123–151.

Liner, C., Li, C. F., Gersztenkorn, A., & Smythe, J., 2004. Spice : A new general seismic attribute, *SEG Expanded Abstracts*, **72**, 433–436.

Liu, X., 1999. Ground roll suppression using the Karhunen–Loeve transform, *Geophysics*, **64**, 564–566.

Loewentha, D., Lu, L., Robertson, R., & Sherwood, J., 1996. The wave equation applied to migration , *Geophys. Prosp*, **24**, 380–399.

Longman, M. W., 1981. A process approach to recognising facies of reef complexes. in : European fossil reef models, in *(Ed. by D.F. Toomey)*, vol. 30, pp. 9–40.

Loucks, R. G., 1999. Paleocave carbonate reservoirs :origins, burial-depth modifications spatial complexity, and reservoir implications, *Journal of Sedimentary Research*, **83**, 1795–1834.

Lucia, F. J., 1995. Rock-fabric/petrophysical classification of carbonate pore space for reservoir characterization, *Am. Assoc. Pet. Geol. Bull.*, **79**, 1275–1300.

Lumsden, D. N. & Lloyd, R. V., 1997. Three dolomites, *Journal of Sedimentary Research*, **67**, 391–396.

Luo,, Y., Higgs, W. G., & Kowalik, W. S., 1996. Edge detection and stratigraphic analysis using 3d seismic data, *SEG Expanded Abstracts*, **66**, 324–327.

M.A. Slawinski., 2003. *Seismic Waves and Rays in Elastic Media*, Elsevier Science.

Machel, G. G. & Mountjoy, E. W., 1986. Chemistry and Environments of Dolomitization-A Reappraisal, *Earth Science Rev.*, **23**, 175–222.

Mann, J., Müller, T., Höecht, G., & Hubral, P., 1999. Common Reflection Surface stack - a real data example, *J. Appl. Geophys*, **42**, 301–318.

Mann, J., 2002. *Extensions and applications of the Common-Reflection-Surface Stack*, Logos Verlag, Berlin.

Manuel, T. S. & Enders, A. R., 1979. *Deconvolution of Geophysical Time Series in the Exploration for Oil and Natural Gas*, Elsevier Science Amsterdam.

Maragos, J. F., Baines, G. B. K., & Beveridge, P., 1973. Tropical cyclone creates a new land formation of Funafuti Atoll, *Science.*, **181**, 1161–1164.

Marfurt, K. J., Kirlin, R. L., Farmer, S. L., & Bahorich, M. S., 1998. 3-D seismic attributes using a semblance-based coherency algorithm , *Geophysics*, **63**, 1150–1165.

Marfurt, K. J., 2006. Robust estimates of reflector dip and azimuth , *Geophysics*, **71**, 29–40.

Marshall, j. F., 1983. Submarine cementation in a high energy platform reef : One Tree Reef, southern Great Barrier Reef, *Sedim. Geol.*, **53**, 1133–1149.

Melo, P, E. M., Porsani, M. J., & Silva, M. G., 2009. Ground-roll attenuation using a 2D time-derivative filter , *Geophys. Prosp*, **57**, 343–353.

Mike Cox., 1999. *Static corrections for seismic reflection surveys*, Society of Exploration Geophysicist, Tulsa, Ok.

Miller, R, D., 1992. Normal moveout stretch mute on shallow-reflection data, *Geophysics*, **57**, 1502–1507.

Miller, R. D. & Xia, J., 1998. Large near-surface velocity gradients on shallow seismic reflection data, *Geophysics*, **63**, 1384–1356.

Montagne, R. & Vasconcelos, G. L., 2006. Optimized suppression of coherent noise from seismic data using the Karhunen–Loeve transform, *Physical Review*, **74**, 1–9.

Moor, C. H., Graham, E. A., & Lad, L. S., 1976. Sediment transport and dispersal across the deep fore-reef and island slope (-55 m to -305 m), Discovery Bay, Jamaica, *Journal of Sedimentary Petrology.*, **46**, 174–187.

Moor, C. H., 1989. *Carbonate Diagenesis and Porosity*, New York, Elsevier.

Moshier, S. O., 1989. Microporosity in micritic limestones ; a review, *Sediment. Geo.*, **63**, 191–213.

Müller, T. J., Jäger, R., & Höcht, G., 1998. Common reflection surface stacking method - imaging with an unknown velocity model, *SEG Expanded Abstracts*, pp. 1764–1767.

Muller, P., 1989. *Hydrothermal paleokarst of Hungary, In : Paleokarst. A Systematic and Regional Review (Ed ;by P. Bosak, D.C. Ford, J. Glazek and I. Horacek)*, Elsevier Publ. Co., Amsterdam.

Müller, T., 1999. *The common reflection surface stack - seismic imaging without explicit knowledge of the velocity model*, Ph.D. thesis, Der Andere Verlag, BadIburg.

Neidell, N. & Taner, M, T., 1971. Semblance and other coherency measures for multichannel data, *Geophysics*, **36**, 482–497.

Palmer , M. V. & Palmer, A. N., 1989. Paleokarst of the United States , *In : P. Bosak, D.C. Ford, J. Glazek and I. Horacek (Editors)*, *Paleokarst : A Systematic and Regional Review. Elsevier Publ. Co., Amsterdam*, pp. 337–363.

Palmer, A. N., 1995. Geochemical Models for the Origin of Macroscopic Solution Porosity in Carbonate Rocks, In :Unconformities and Porosity in Carbonate Strata (Ed. by D. A. Budd, A H. Saller, and P. M. Harris), *AAPG Memoir*, **63**, 77–101.

Palmer, D., 1980. *The Generalized Reciprocal Method of seismic refraction interpretation*, Society of Exploration Geophysicist, Tulsa, Ok.

Perkins, R. D. & Halsey, S. D., 1971. Geologic significance of microboring fungi and algae in Carolina shelf sediments, *Journal of Sedimentary Petrology.*, **41**, 843–853.

Perroud, H. & Tygel, M., 2004. Nonstretch NMO, *Geophysics*, **69**, 599–607.

Pomar, L., Esteban,, M., Calvet, F., & Baron, A., 1983. La unidad arrecifal del mioceno superior de Mallorca, el terciario de las Baleares (Mallorca-Menorca) , *Guia de las excursiones and congresso nacional de sedimentologia*, *grupo espanol de sedimentologia*, pp. 139–175.

Pomar, L., 1991. Reef geometries, erosion surfaces and high frequency sea-level changes, upper Miocene reef complex, Mallorca, Spain , *Sedimentology*, **38**, 243–270.

Pomar, L. & Ward, W. C., 1981. Reservoir-Scale Heterogeneity in Depositional Packages and Diagenetic Patterns on a Reef-Rimmed Platform, Upper Miocene, Mallorca, Spain, *Bull. Geol. Soc. America*, **3**, 1759–1773.

Pomar, L. & Ward, W. C., 1994. Response of a late Miocene Mediterranean reef platform to high-frequency eustasy , *Geology*, **22**, 131–134.

Pomar, L. & Ward, W. C., 1995. *Sea-level Changes, Carbonate Production and Platform Architecture : The Llucmajor Platform, Mallorca, Spain : in Haq, B. ed. : Chapter 4 in Sequence Stratigraphy and Depositional Response to Eustatic, Tectonic and Climatic Forcing*, Kluwer Academic Press.

R.E.Sheriff. & L.P.Geldart., 2001. *Exploration Seismology*, Cambridge University Press.

Roberts, A., 2001. Curvature attributes and their application to 3D interpreted horizons, *First Break*, **19**, 85–99.

Ronald, C. H., Neil, L. A., & Richard, D. K., 1996. *VSP Interpretive Processing : Theory and Practice*, Society of Exploration Geophysicist, Tulsa, Oklahoma.

Ronen, J. & Claerbout, J. F., 1985. Surface-consistent residual statics estimation by stack-power maximization, *Geophysics*, **50**, 2759–2767.

Schleicher, J., Tygel, M., & Hubral, P., 1993. Parabolic and hyperbolic paraxial two-point traveltimes in 3d media, *Geophys. Prosp,*, **41**, 459–513.

Schroeder, J. H. & Zankl, H., 1974. Dynamic reef formation :a sedimentological concept based on studies of recent bermuda and bahama reefs, in *Proc. 2nd Int. Coral Reef Symp" Brisbane 2*, pp. 413–428.

Scoffin, T. P. & Garrett, P., 1974. Processes in the formation and preservation of internal structure in bermuda patch reefs, in *Proc. 2nd Int. Coral Reef Symp" Brisbane 2*, pp. 429–448.

Shavit, U. & Furman, A., 2001. The location of deep sedimentary sources in the Israeli coastal aquifer, *Journal of Hydrology*, **250**, 63–77.

Smart, P. L. & Whitaker, F. F., 1991. Karst processes, hydrology and porosity evolution, *In : V.P. Wright,M. Esteban and P.L. Smart (Editors), Palaeokarsts and Palaeokarstic Reservoirs. Postgraduate Research Institute for Sedimentology, University of Reading*, pp. 1–55.

Spitzer, R., Nitsche, F. O., & Green, A. G., 2001. Reducing source-generated noise in shallow seismic data using linear and hyperbolic tau-p transformations, *Geophysics*, **66**, 1612–1621.

Steeples, D. W. & Miller, R. D., 1998. Avoiding pitfalls in shallow seismic reflection surveys , *Geophysics*, **63**, 1213–1224.

Stoddart, D. R., 1969. Post-hurricane changes in the British Honduras Reefs and Cays, *Atoll Res. Bull.*, **170**, 1–25.

Stoessell, R. K., Ward, W. C., Ford, B. D., & Schuffert, J. D., 1989. Water chemistry and $CaCo_3$ dissolution in the saline part of the open-flow mixing zone, coastal Yucatan Peninsula, Mexico, *Bull. Geol. Soc. America*, **101**, 159–169.

Stoffa, P., Fokkema, J. T., Freire, R. M., & Kessinger, W. P., 1990. Split-step Fourier migration, *Geophysics*, **55**, 410–421.

Stolt, R. H., 1978. Migration by fourier transform, *Geophysics*, **43**, 23–48.

Taner, M. T., Schuelke, J. S., O'Doherty, R., & Baysal, E., 1994. Seismic attributes revisited, *SEG Expanded Abstracts*, **64**, 1104–1106.

Taner, M. T. & Koehler, F., 1969. Velocity spectra – digital computer derivation and applications of velocity functions, *Geophysics*, **34**, 859–881.

Throne Lay. & Terry C. Wallace., 1995. *Modern Global Seismology*, Academic Press, San Diego.

Tsourlos, P., Ogilvy, R., Meldrum, P., & Williams, G., 2003. Time-lapse monitoring in single boreholes using electrical resistivity tomography , *J. Environ. Eng. Geophysics*, **8**, 1–14.

Tucker, M. E. & Wright, V. P., 1990. *Carbonate Sedimentology*, Blackwell Scientific Publications.

Tufekcic, D., Claerbout, J. F., & Rasperic, Z., 1981. Spectral balancing in the time domain, *Geophysics*, **46**, 1182–1188.

Turhan, T. M., 1997. *Seismic data processing flow in areas of shallow carbonates (in Carbonate Seismology)*, Society of Exploration Geophysicists.

Tygel, M., Müller, T., Hubral, P., & Schleicher, J., 1997. Eigenwave based multiparameter traveltime expansions, *SEG Expanded Abstracts*, **67**, 1770–1773.

Vengosh, A. & Ben-Zvi, A., 1994. Formation of a salt plume in the Coastal Plain of Israel : the Beér Toviyya region, *Journal of Hydrology*, **160**, 21–52.

Vermeer, G. J. O., 1999. Factors affecting spatial resolution, *Geophysics*, **64**, 942–953.

V.Hebert., 2011. *Analyse multi-échelle de la structure d'un réservoir carbonaté littoral : example de la plate-forme du Llucmajor (Majorque Espagne)*, Ph.D. thesis, Université de Montpellier 2.

Vladimir, G. & Ilya, T., 2000. Inversion of azimuthally dependent nmo velocity in transversely isotropic media with a tilted axis of symmetry, *Geophysics*, **65**, 232–246.

Wang, Z. & Nur, A., 1988. Effect of temperature on wave velocity in sandstone and sandstone with heavy hydrocarbon, *SPE Reserv. Eng.*, **3**, 158–164.

Watts, N. R., 1988. Carbonate particulate sedimentation and facies within the Lower Silurian Hogklint patch reefs of Gotland, Sweden, *Sedim. Geol.*, **59**, 93–113.

Winterstein, D. F., 1990. Velocity anisotropy terminology for geophysicists, *Geophysics*, **55**, 1070–1088.

Y. Maria-Sube., 2007. *Structure et hétérogénéité d'une plate-forme récifale Miocène (Majorque) : implication pour les intrusions d'eau sal'ee en zone côtière*, Ph.D. thesis, Université de Montpellier 2.

Yarham, C., Boeniger, U., & Herrmann, F., 2006. Curvelet-based ground roll removal, *SEG Expanded Abstracts*, **76**, 2777–2780.

Yilmaz, O., 2001. *Seismic Data Analysis ; Processing, Inversion and Analysis of Seismic Data*, Society of Exploration Geophysicist, Tulsa, Ok.

# *Annexes*

Two conference papers published in the proceedings of Near Surface of EAGE in 2010 and 2011.

P69

## Static Correction Determination Based on Delay Time Inversion

T. Muhammad* (Université de Pau et des Pays de l'Adour (UPPA)), H. Perroud (Université de Pau et des Pays de l'Adour(UPPA)) & D. Rousset (Université de Pau et des Pays de l'Adour(UPPA))

## SUMMARY

To obtain a high resolution seismic image,static correction plays a vital role.Static correction is applied to mitigate the effect of irregular topography and weathering velocity.Inadequate static correction will result in seismic data smearing and false anomalies.We present a data driven technique that performs the delay time inversion based on the first arrivals for static correction computation.
Based on this technique we do not require the explicit velocity information and the subsurface depth model.So it perform all the
necessary steps for static correction computation in time domain thus prevents from certain errors that might propagate otherwise due to time to depth conversion.We applied the time-delay inversion method on the real field data and compared the results with other methods i.e. delay-time and generalized reciprocal method.Generalized reciprocal method requires the explicit velocity information and optimum distance. Change in
any one of the parameter will change the apparent reflector velocity and depth model. While using delay time inversion we do not require velocity information and optimum parameter.Moreover delay time technique can be generalised to several weathering layers as compared to the generalised reciprocal method which is valid for only one layer.

## Abstract

Static correction is a key factor in high resolution seismic processing that plays a vital role to achieve high quality image. Static correction is applied to counter for the low velocity layer and irregular topography. There are many methods available for static correction computation. These methods are based on first arrival analysis, tomography or hybrid method. We present a technique of static correction computation based on delay-time inversion. Weathering static correction for receivers and sources is computed from inverted delay times. By inversion of delay-time we compute the static correction in time domain and avoid certain errors produced due to time to depth conversion. We compared the results with delay-time computation and generalized reciprocal method (GRM).

## Introduction

Near surface layers, up to certain depth, are composed of unconsolidated loose material. Seismic waves propagating through these shallow unconsolidated layers will take longer time to traverse them. It is important to mitigate this effect. The idea of static correction is to apply the constant time shift to bring the recorded data on a well defined datum by compensating the irregular topography (elevation static) and low velocity or weathering layer correction, its thickness and velocity (weathering static).

What happen if we do not apply the static corrections? This will produce, seismic resolution problem, phase inversion, problem of miss ties with well or different vintage data and false structural or stratigraphic anomalies that will create problem at the final stage of data interpretation. It will smear the quality of processed data due to static anomalies. For shallow reflection survey its importance lies in the fact that time shifts are comparable to the dominant period of reflection.

Static corrections computation based on first arrival include slope-intercept method, time-delay method, plus-minus method, generalized reciprocal method. All these methods have certain advantages and inherent shortcomings. But the legacy of all first arrival based method lies in the accomplishment of Snell's law due to velocity contrast ($V_2 > V_1$).

Delay-time is not an obvious quantity. Referring to Figure1.b, delay times for sources and receivers are $\delta t_{S_i} = (t_{S_iB} - t_{AB})$ and $\delta t_{R_i} = (t_{CR_i} - t_{CD})$ respectively. It can be shown that for a dipping interface delay-time is related to the depth by the relation:

$$\delta t = \frac{Z cos\theta_c cos\varsigma}{V_1} \tag{1}$$

Total travel time is the time taken along the reflector of velocity $V_2$ plus additional source and receiver delay time, given by:

$$t^{obs} = \frac{x_{S_iR_j}}{V_2} + \delta t_{S_i} + \delta t_{R_j} \tag{2}$$

## Delay-time inversion methodology

For delay time inversion first we have to calculate corrected time for different offsets corresponding to different pairs of shot points and receivers. From equation 2 we have:

$$t^{obs} - \frac{x_{S_iR_j}}{V_2} = \delta t_{S_i} + \delta t_{R_j} \tag{3}$$

To calculate the delay time knowledge of $V_2$ (bedrock velocity) is mandatory. We calculate the weathering layer velocity, bedrock velocity, angle and dip of the refractor by *Intercept-Slope Method* (Figure1.a). From Snell's law:

$$V_2 = \frac{V_1}{sin\theta_c} \tag{4}$$

where critical angle, $\theta_c$, is calculated as :

$$\theta_c = \frac{1}{2}(sin^{-1}(\frac{V_1}{V_{22}}) + sin^{-1}(\frac{V_1}{V_{21}})) \tag{5}$$

For dip calculation:

$$\varsigma = \frac{1}{2}(sin^{-1}(\frac{V_1}{V_{22}}) - sin^{-1}(\frac{V_1}{V_{21}}))$$ 

(6)

$V_{21}$ and $V_{22}$ are the bed rock velocities calculated from the pairs of positive and negative offset and corresponding first arrivals respectively.

The system of equation for delay time inversion may be written as:

$$M[\delta t_{S_M|R_N}] = [t_{S_M R_N}]$$ 

(7)

where:

$M$      Matrix based upon shot points and corresponding active geophones for each shot point.

$t$      column vector of corrected time to the corresponding offsets.

$\delta t_{S_{(1,2,3...S_M)}|R_{(1,2,3...R_N)}}$      column vector of delay-times to be determined.

Least square inversion of the above equation is given as:

$$[\delta t_{S_M|R_N}] = (M^T M)^{-1} M^T [t_{S_M R_N}]$$ 

(8)

$M^T$ = Transpose of matrix **M**

The system of equations in matrix form may be written as:

|  | $S_1$ | $S_2$ | $S_3$ | ... | $S_M$ | $R_1$ | $R_2$ | $R_3$ | ... | $R_N$ |
|---|---|---|---|---|---|---|---|---|---|---|
| $S_1$ | 1 | 0 | 0 | 0 | 0 | 1 | 0 | 0 | 0 | 0 |
| $S_1$ | 1 | 0 | 0 | 0 | 0 | 0 | 1 | 0 | 0 | 0 |
| $S_1$ | 1 | 0 | 0 | 0 | 0 | 0 | 0 | 1 | 0 | 0 |
| ... | ... | ... | ... | ... | ... | ... | ... | ... | ... | |
| $S_2$ | 0 | 1 | 0 | 0 | 0 | 0 | 1 | 0 | 0 | 0 |
| $S_2$ | 0 | 1 | 0 | 0 | 0 | 0 | 0 | 1 | 0 | 0 |
| $S_2$ | 0 | 1 | 0 | 0 | 0 | 0 | 0 | 0 | 1 | 0 |
| ... | ... | ... | ... | ... | ... | ... | ... | ... | ... | ... |
| ... | ... | ... | ... | ... | ... | ... | ... | ... | ... | ... |
| ... | ... | ... | ... | ... | ... | ... | ... | ... | ... | ... |
| ... | ... | ... | ... | ... | ... | ... | ... | ... | ... | ... |
| $S_M$ | 0 | 0 | 0 | 0 | 1 | 0 | 0 | 1 | 0 | 0 |
| $S_M$ | 0 | 0 | 0 | 0 | 1 | 0 | 0 | 0 | 1 | 0 |
| $S_M$ | 0 | 0 | 0 | 0 | 1 | 0 | 0 | 0 | 0 | 1 |
| $S_1$ | 1 | 0 | 0 | 0 | 0 | -1 | 0 | 0 | 0 | 0 |
| $S_2$ | 0 | 1 | 0 | 0 | 0 | 0 | -1 | 0 | 0 | 0 |
| $S_3$ | 0 | 0 | 1 | 0 | 0 | 0 | 0 | -1 | 0 | 0 |
| ... | ... | ... | ... | ... | ... | ... | ... | ... | ... | ... |
| ... | ... | ... | ... | ... | ... | ... | ... | ... | ... | ... |
| ... | ... | ... | ... | ... | ... | ... | ... | ... | ... | ... |
| $S_M$ | 0 | 0 | 0 | 0 | 1 | 0 | 0 | 0 | 0 | -1 |

with column vector of unknowns $\begin{pmatrix} \delta t_{S_1} \\ \delta t_{S_2} \\ \delta t_{S_3} \\ ... \\ \delta t_{S_M} \\ -- \\ \delta t_{R_1} \\ \delta t_{R_2} \\ \delta t_{R_3} \\ \delta t_{R_4} \\ \delta t_{R_5} \\ \delta t_{R_6} \\ ... \\ ... \\ ... \\ \delta t_{R_N} \end{pmatrix}$ = $\begin{pmatrix} t_{S_1 R_1} \\ t_{S_1 R_2} \\ t_{S_1 R_3} \\ ... \\ t_{S_2 R_1} \\ t_{S_2 R_2} \\ t_{S_2 R_3} \\ ... \\ ... \\ ... \\ t_{S_M R_1} \\ t_{S_M R_2} \\ t_{S_M R_3} \\ ... \\ t_{S_M R_N} \\ 0 \\ 0 \\ 0 \\ ... \\ ... \\ 0 \end{pmatrix}$

The last lines of matrix M correspond to the hypothesis of spatial consistency, that is source and receiver delay times should be equal when they share the same locations. These extra constraints on the unknown delay times help to stabilize the inversion.

**Application to field data**

We applied the delay time inversion scheme on the 2D seismic line with split-spread acquisition geometry having sources at surface in between receivers. Inter receivers distance is 1 meter while the
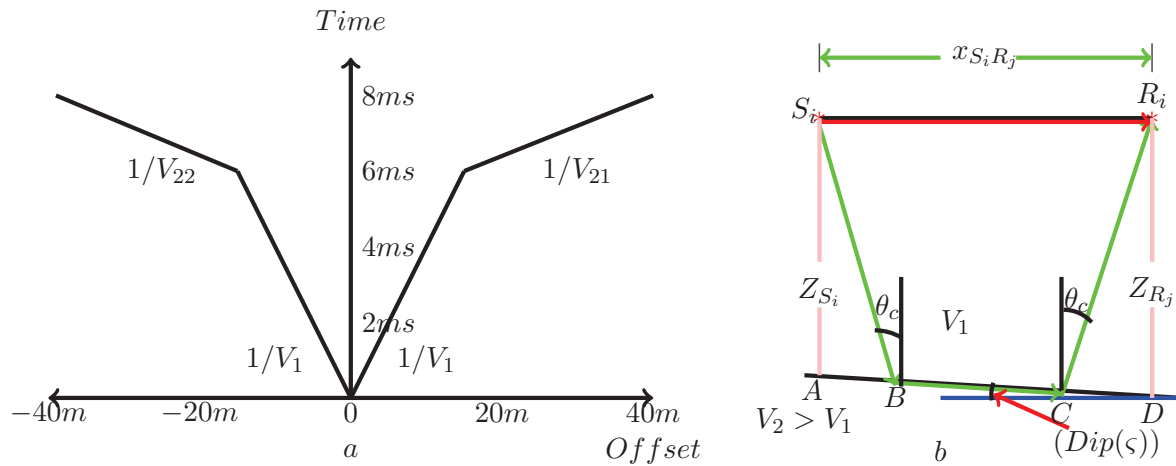
*Figure 1 a) Slope-intercept method   b) Ray paths for delay-time method*

source-receivers offset is 0.5 meter. Figure 2 shows the comparison of observed first arrivals and calculated first arrivals after delay-time inversion.
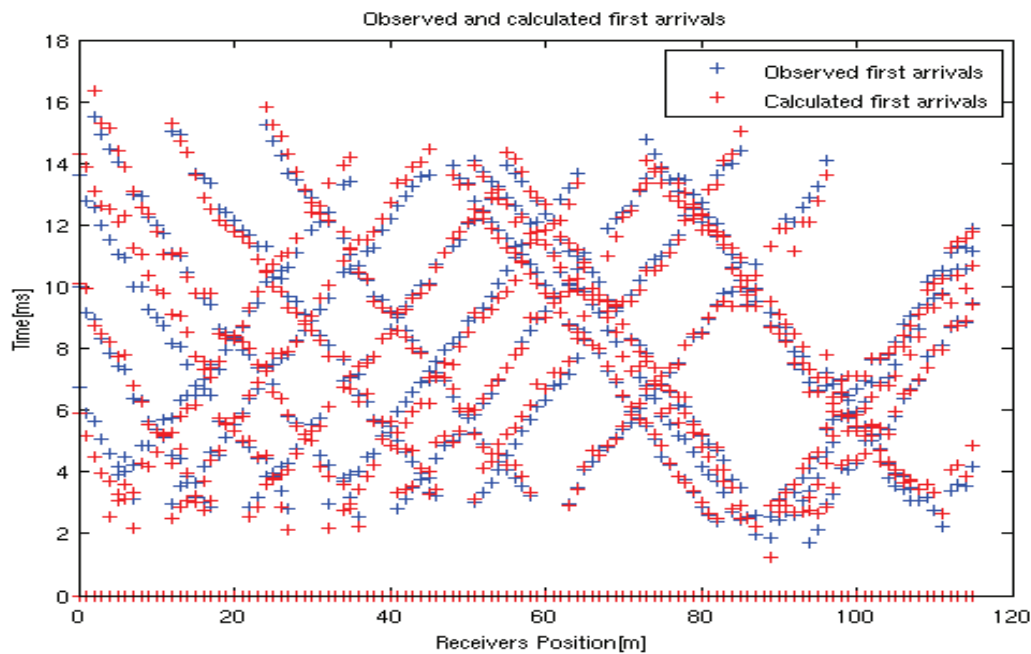


*Figure 2 Comparison of observed and calculated first arrivals after delay time inversion*

After the delay time inversion the receiver delay time is determined for each receiver with picked first arrivals. For missing receivers we applied the cubic spline interpolation. Since the sources are located 0.5m only away from receivers, we assumed that the delay time for source and receivers can be considered as equal. So delay time for sources is calculated from the neighbouring receivers delay times.
To determine the weathering static correction for receivers in terms of receivers delay time we may write:

$$Rwstat_j = \frac{-Z_{R_j}}{V_1} + \frac{Z_{R_j}}{V_2} \tag{9}$$

$$Rwstat_j = \frac{-Z_{R_j}}{V_1} + \frac{Z_{R_j}}{V_1/sin\theta_c} = \frac{-Z_{R_j}}{V_1}(1 - sin\theta_c) \tag{10}$$

$$Rwstat_j = \delta t_{R_j} \frac{1 - sin\theta_c}{cos\theta_c cos\varsigma} \tag{11}$$

So the total static correction for receivers at surface elevation $E_{R_j}$:

$$Rtstat_j = \frac{(E_{datum} - E_{R_j})}{V_2} - \delta t_{R_j} \frac{1 - sin\theta_c}{cos\theta_c cos\varsigma} \tag{12}$$

Similarly the weathering static correction for sources in terms of sources delay time is given by:

$$Swstat_i = \delta t_{S_i} \frac{1 - sin\theta_c}{cos\theta_c cos\varsigma} \tag{13}$$

Hence the total static correction for sources at surface elevation $E_{S_i}$ will be:

$$Ststat_i = \frac{(E_{datum} - E_{S_i})}{V_2} - \delta t_{S_i} \frac{1 - sin\theta_c}{cos\theta_c cos\varsigma} \tag{14}$$

Figure3, shows the comparison of static correction determined by generalized reciprocal, delay-time
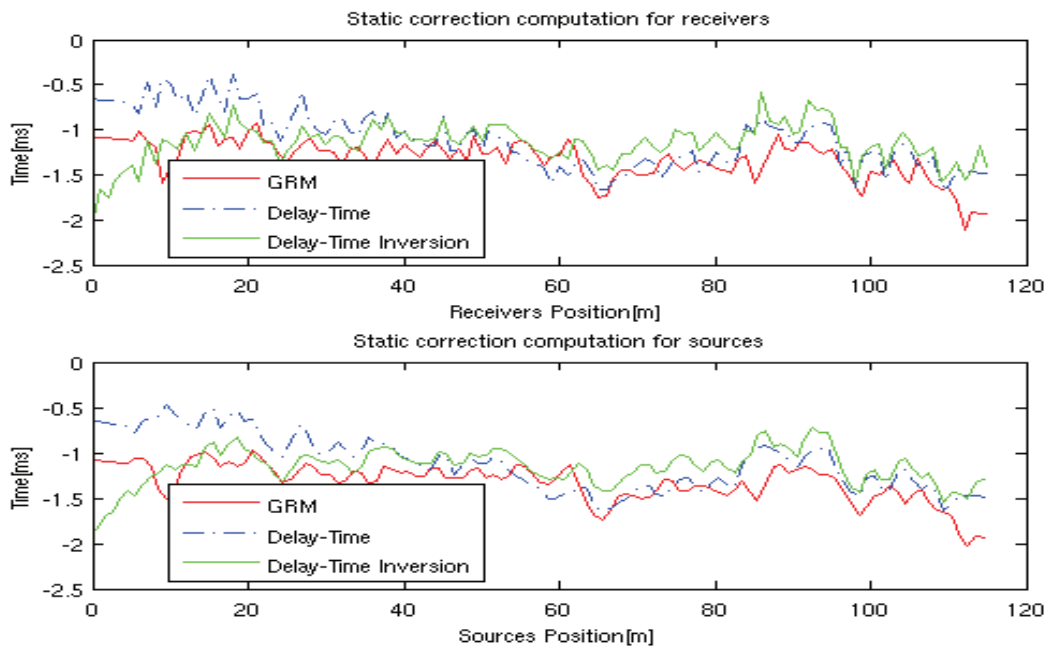


***Figure 3*** *Static corrections for receivers and sources based on GRM, delay-time and delay-time inversion*

and delay-time inversion method. We can observe that the order of magnitude and the general trends are similar but there exist significant differences for some location, that can produce changes in seismic processing results.

**Conclusion**

Time Delay Inversion technique is very simple to apply than GRM. We compared proposed delay-time inversion results with generalised reciprocal method(GRM) applying on the field data. GRM requires regularly spaced first arrival times and optimum distance. The choice of optimum distance is a cumbersome task. But time delay inversion method does not require regularly spaced first arrivals and optimum distance. GRM is applicable for single weathering layer but time delay inversion method can be generalised to several weathering layers. All we need for delay-time inversion is first arrival times arranged in a matrix for sources and corresponding receivers.

**References**
Yilmaz,O.,2001,Seismic data Processing:Society of Exploration Geophysicist

F16

## 3D very High Resolution Shallow Seismic Data from Carbonate Reservoir - A Case Study

M. Toqeer* (Département Géosciences, Université de Pau et des Pays de l'Adour), H. Perroud (Géosciences Université de Montpellier) & D. Rousset (Département Géosciences, Université de Pau et des Pays de l'Adour)

## SUMMARY

Shallow seismic surveys are becoming a considerable way for detecting and characterizing shallow subsurface for environmental, geological, geophysical and geotechnical applications. Shallow 3D seismic survey acquisition and data processing is not an easy task. This is partly due to survey cost and due to near subsurface heterogeneities and several type of noises which partly depends upon the particular site. We present the complete processing and preliminary interpretation results of shallow 3D seismic survey carried out in Campos, Mallorca, Spain.

This project is aimed to characterize the carbonate reservoir down to 100m that is composed of hard carbonate rocks. This rock sequence is karstic and fractured. Due to this factor energy penetration is a problem and severe noises are produced due to diffractions. Furthermore Rayleigh waves pose another serious problem for processing. By efficient processing sequence and application of CRS method zero offset stack data is obtained which is further tuned by post-stack depth migration. The objective is to process the severely noisy data to get the subsurface image for further interpretation and seismic attribute analysis. Here preliminary interpretation results of the data also are presented that will be analysed in detail through seismic attributes.

## Introduction

Seismic reflection survey for shallow investigation is somewhat difficult and cumbersome task due to many factors. These include the near subsurface heterogeneities, noises and near surface low layer velocity, amongst others. To avoid spatial aliasing, averaging and requirement of high fold data to improve S/N ratio increases survey cost. But on the other hand shallow seismic survey deliver better subsurface imaging, detection of small scale objects and characterization of shallow subsurface for geological, environmental and geotechnical purpose. We present the processing result of shallow 3D seismic reflection survey and preliminary interpretation results. This study area is composed of karstic lime stone. Due to hard rock, karstic features and associated system of fractures, diffraction of seismic signals occurs. Additionally Rayleigh waves are generated which are reflective and dispersive to add the complexity in processing. The objective of this study to look for karstic features and other small scale structural heterogeneities. This task is not possible without an efficient processing. Here we present the complete processing results along with preliminary interpretation result to characterize the site. The project is aimed to characterize the carbonate reservoir down to 100m depth.

## Data Acquisition and Processing

For 3D data acquisition 20 in-line and cross-lines of receiver were used. Interline and inter receiver distance was 2m. Total 441 sources (hammer blows) were used. Sources were arranged in 20 parallel lines each line comprising of 21 sources. Inter source distance was 2m. Hence for each source 400 traces were recorded. Figure 1 shows 3D data acquisition geometry along with the CMP fold distribution over the study area. Due to the hard carbonate rock sequence, a large part of the seismic source energy



(a) 3D Acquisition Geometry
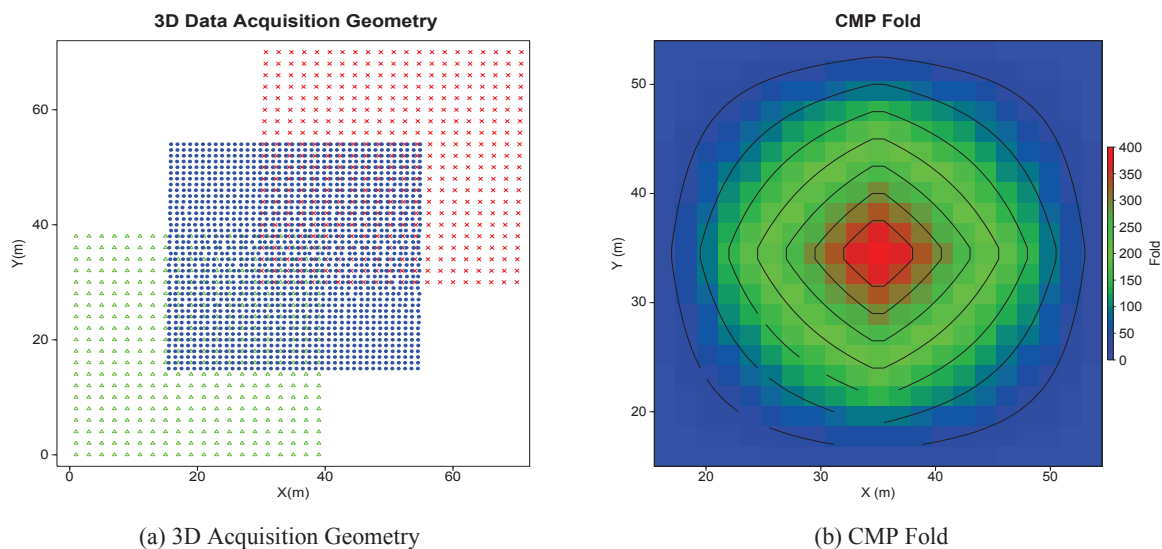
(b) CMP Fold

Figure 1: a) 3D Acquisition geometry. Where green, blue and red color represent receivers, CMP and sources respectively. b) CMP fold distribution over the study area

is converted into wide spread and strong Rayleigh waves that create a serious problem to process the data. Rayleigh waves masked the reflection events. Figure 2a shows the raw shots at increasing distance source point. On these shots one can clearly observe the annoying behaviour of the Rayleigh waves. For first shot the behaviour of the Rayleigh wave is different as compared to the last shot. Rayleigh waves mask the signals in different time windows for different shots. Furthermore, its frequency bandwidth is similar to that of P-wave reflection events and this fact make it difficult to filter the Rayleigh waves. Rayleigh waves velocity change gradually depending on the offset and azimuth from the shot point. Figure 2b shows the effect of low pass filter while the Figure 2c shows the effect of the high

pass filter. For efficient data processing we adopted the following processing steps: After loading the geometry polarity correction was performed for different traces. Trace killing is another step to ensure the good traces. After that static correction is applied. Static correction is of the order of 2ms. Spherical divergence compensation is also applied. To get rid of Rayleigh waves mute is applied in the study area. Rayleigh waves pose a real problem in processing the data. The annoying effects of Rayleigh waves are defined earlier. Rayleigh waves are muted in the selective window because 3D f-k filtering can not filter the Rayleigh waves completely. Further spectral balancing is applied to deconvolve the data. Trace balancing is performed before CRS analysis. Zero offset stack data is obtained by applying CRS (Common



(a) Raw Data        (b) Low Pass Filter        (c) High Pass Filter
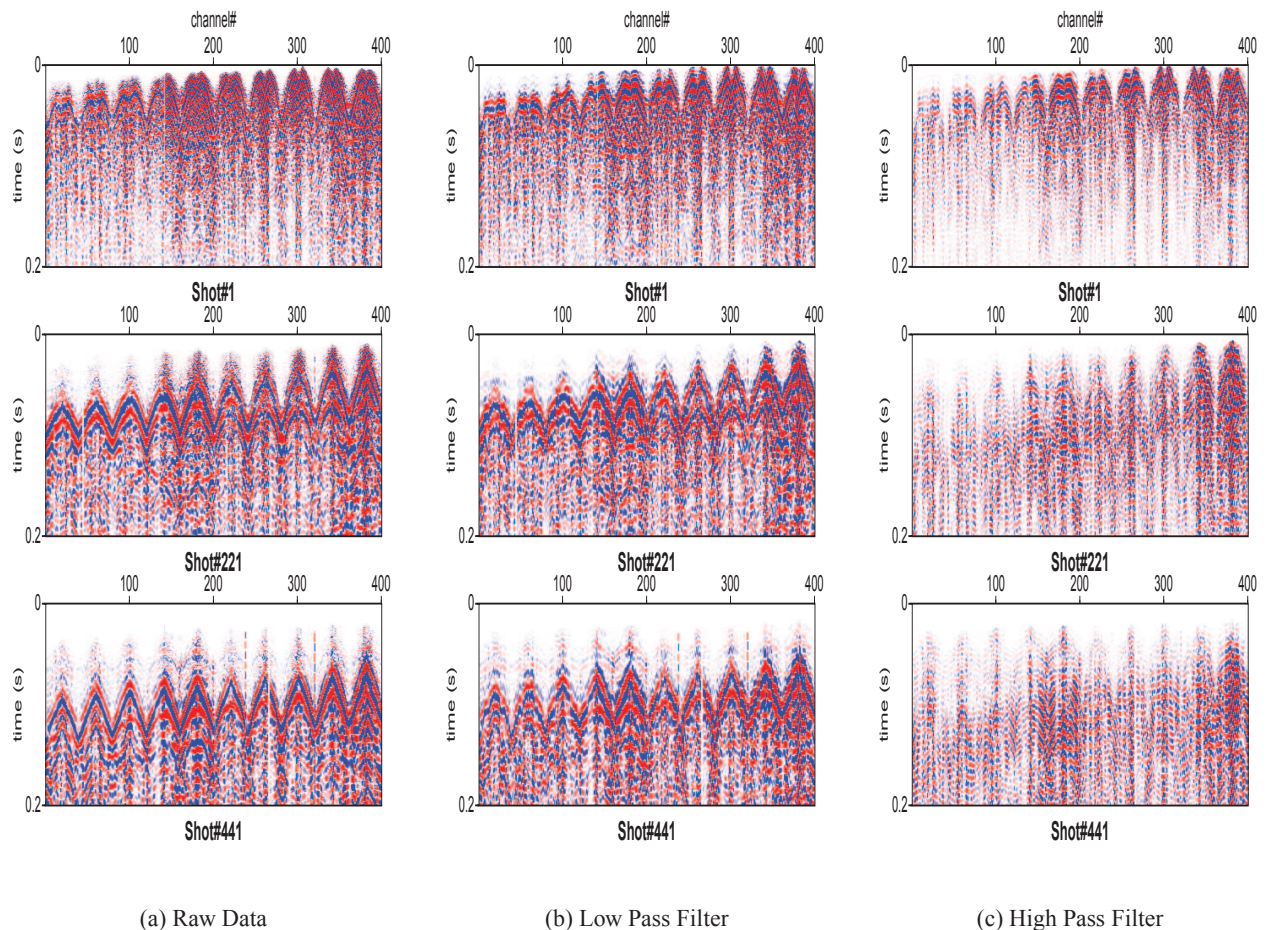
Figure 2: Raw data to show the Rayleigh waves behaviour and application of band pass filtering.

Reflection Surface Stack) method. CRS methods is of great advantage as compared to the conventional velocity analysis. Below is the short description of the CRS method.

CRS technology is based upon the several parameters travel-time equation. It is data driven technique to obtain high resolution, high S/N ratio zero offset stack data that correctly takes into account the location, orientation and curvature of the subsurface reflector. CRS method uses the available data, requires minimum a priori information and is fully data driven. CRS method was proposed by Muller et al.(1998). CRS works with stacking operator and stacking parameters. For 2D zero offset case 3 stacking parameters are required while for 3D zero offset case 8 parameters are required. Further details can be found in Mann et al.(2002). CRS processing leads to considerably improved signal-to-noise (SN) ratio zero offset stack as compared to CMP stack in this complex, heterogeneous area. After the application of CRS method we obtained 3D zero offset stacked cube as show in Figure 3a. To efficiently migrate the data we first applied the deconvolution based on the helix transformation. Deconvolution based on helix transform works through the prediction error filter calculated from the data. For more detail and mathe-

matical derivation readers are refereed to Claebourt.J.F

There are several post stack migration techniques available. We applied the stolt migration (stolt,1978), stolt stretch migration and post-stack depth migration, Split-Step Fourier migration, Stoffa et al.(1990). Only the the migration result of post-stack depth migration is presented here and further interpretation is based on post-stack depth migrated cube. Stolt method assumes a constant velocity for the whole area while stolt stretch migration considers the vertical varying velocity profile. Although the lateral velocity variation is weak in our case study area but still stolt and stolt stretch migration are not efficient because of the structural inhomogeneities while the post-stack depth migration produce reasonable results. This migration technique is applied on the zero offset stack data (Figure 3a) and deconvolved zero offset stack data (Figure 3b). From the Figure 3 one can observe the difference between post-stack depth migrated and deconvolved post-stack depth migrated data. This technique collapse the diffraction and migrate the data very well. From the zero offset depth migrated data (Figure 3c) it is readily seen that after migration many artefacts are produce but if we apply the migration technique after the deconvolution it gives better results (Figure 3d).
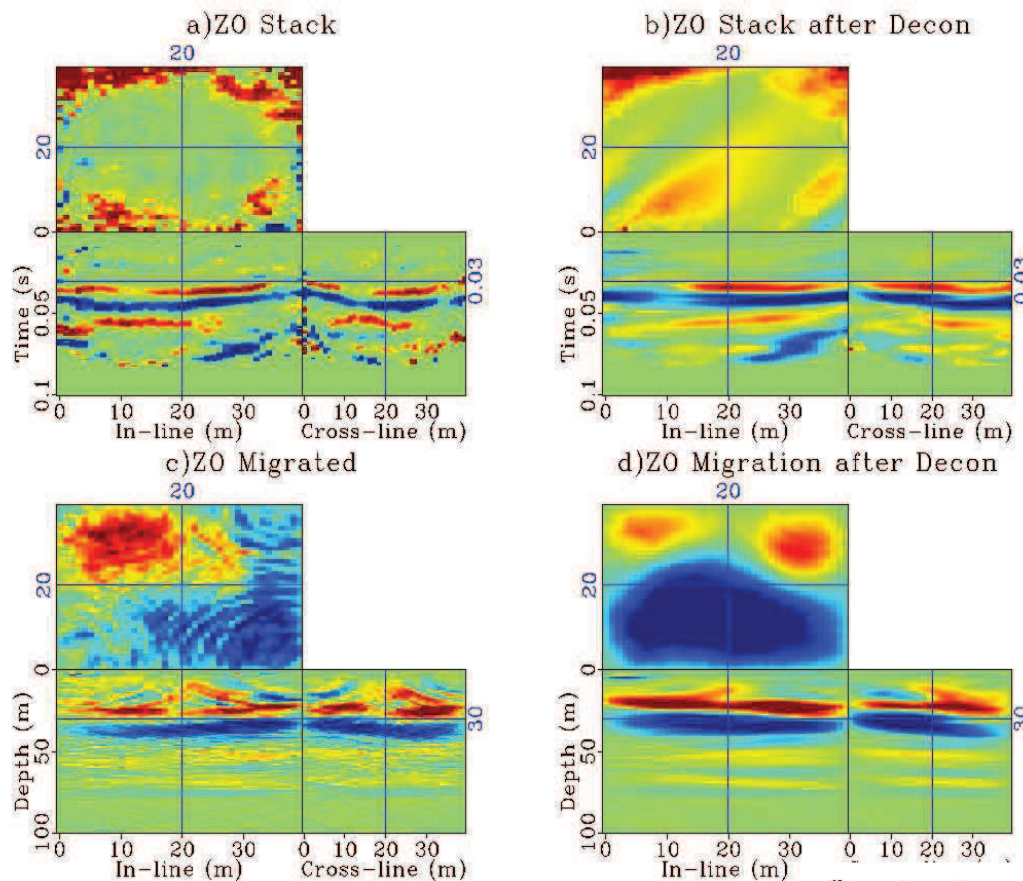


Figure 3: a) Zero Offset stack data. b) Zero Offset stack data after deconvolution. c) Migration of Zero Offset data. d) Migration of deconvolved Zero Offset Data

**Preliminary Interpretation**

Figure 4a shows the in line, cross line and time section. Form the In line and cross line we can see the continuity of the reflections. Figure 4b shows the volume of the data in a particular depth interval along with depth slices, inline and cross lines. This figure clearly demonstrates the continuity of certain features whose position is changing with depth and certain new features that are strictly restricted to particular depths. From this figure the geometry and orientation of these features is also evident. Figure

4c shows the different depth slices sampled at 20 meter interval. These depth slices are individually clipped and symmetrical around zero to better visualize and interpret the features. From these depth slices different striking features are evident. Different cavities and karstic features can be interpreted. These cavities are spatially and vertically restricted. From last depth slice one could interpret the cavities along with the system of fractures.



| (a) | (b) | (c) |
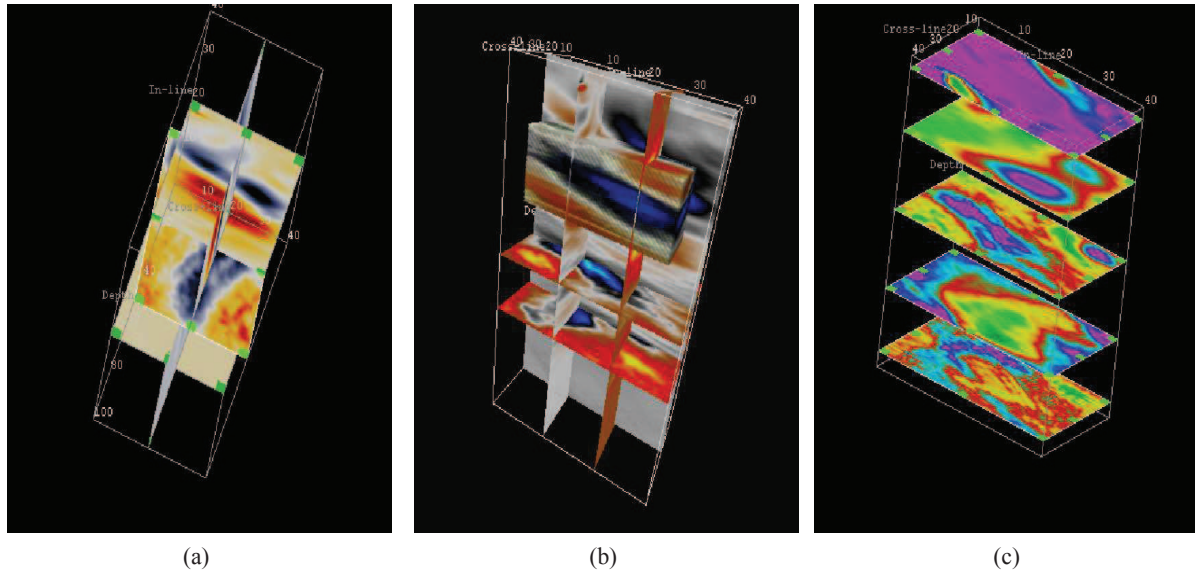
Figure 4: a) 3D Cube .b) 3D cube, Depth slices,cross lines and in lines. c) Depth slices at 20m interval

## CONCLUSION

We presented the processing of very shallow and very noisy data. In our case study the processing was complicated task largely due to the Rayleigh waves and inherent geological features,i.e karst and fractures. The energy penetration is also another problem in this area because of hard rocks and diffracting nature. Thank to the CRS technique that assured the zero offset stack cube despite of aforementioned problems. From the data visualization and it's preliminary interpretation reveals many interesting features i.e karst etc. Further attribute analysis,i.e, Coherency, similarity, curvature, RMS amplitude attributes and spectral decomposition will helpful in revealing the fracture system and other structural features to better characterize the reservoir.

### Acknowledgements

### References

[1] Claerbout,J.F. Geophysical Estimation by Example, (http://sepwww.stanford.edu/sep/prof/index.html)

[2] Mann, J., Bergler, S., Zhang, Y., Chira, P., and Hubral, P. 2002. Generalizations of the Common-Reflection-Surface Stack, EAGE extended abstracts, E023

[3] Muller, T., Jager, R., and Hocht, G. 1998. Common reflection surface stacking method - imaging with an unknown velocity model, SEG meeting Expanded Abstracts,1764-1767

[4] Stolt R.H.1978. Migration by Fourier transform , Geophysics 43,23-48

[5] Stoffa, P. L., J. T. Fokkema, R. M. de Luna Freire, and W. P. Kessinger, 1990. Split-step Fourier migration , Geophysics 55,410–421